Short-range correlations in quark and nuclear matter

Dissertation zur Erlangung des Doktorgrades

der Naturwissenschaftlichen Fakultät
der Justus-Liebig-Universität Gießen

Fachbereich 07 – Mathematik und Informatik,
Physik, Geographie

vorgelegt von

Frank Frömel

aus Altenstadt

Gießen, Juni 2007

Dekan: Prof. Dr. Bernd Baumann
I. Gutachter: Prof. Dr. Ulrich Mosel
II. Gutachter: PD Dr. Stefan Leupold
Tag der mündlichen Prüfung: 18.07.2007

Contents

1 Introduction

We know from our everyday experience that the properties of an object depend on the surrounding environment. Consider, for example, the different weight of an item – or the different resistance to its motion – in air and in water. Such effects, arising from interactions with the medium, play also an important role in microscopic many-body systems. In this thesis, we will explore the influence of dynamical correlations on the properties of quarks and nucleons in quark matter and nuclear matter, respectively. We will focus on the short-range correlations here. In comparison to the well-investigated long-range correlations that determine the bulk properties of the quarks and nucleons – like effective masses and binding energies – they have a more subtle influence on the in-medium properties of the particles.

To illustrate the difference between long- and short-range correlations, we can consider a simple system of interacting "particles" [Buß04]: Persons that stroll along a street in a pedestrian area. The upper panels of Fig. 1.1 show the path of a walker in three situations with a varying number of other pedestrians (late at night, on a regular weekday, and on the Saturday before Christmas). The lower panels indicate the corresponding probabilities to find the walker at a certain (instantaneous) velocity $|\vec{v}\,|$. The first scenario does not require much discussion. Late at night, no other persons are in the street. The walker can move along a straight line with constant velocity. This corresponds to the motion of free particles in the vacuum.

In the second case, a few other pedestrians will be present. This is a typical example for long-range correlations. The spaces between the pedestrians remain large and our walker can see them from far away. Thus, he can adjust his path long before he runs into another person. Compared to the first case, he has to slow down a little. However, he can still walk with a constant velocity along the smoothly curved path. Note that we would obtain the same velocity distribution if there were no other persons but the street had a little slope that slows down the walker. This corresponds to a so-called mean-field approach where the interactions between the particles are absorbed into an effective potential or an effective mass.

The third scenario shows the effect of short-range correlations. On the Saturday before Christmas, the street will be crowded with other pedestrians – moving in non-uniform ways and obstructing the view of the walker. Hence, he cannot plan his path in advance. It becomes necessary for the walker to adjust his velocity (and direction) dynamically. At some times it will be better to stop for a moment, at other times it will be better to rush through a gap. The probability to find the walker at a certain velocity turns from a sharp peak into a broad distribution. It should be clear from our simple example that the magnitude of the broadening, i.e. the importance

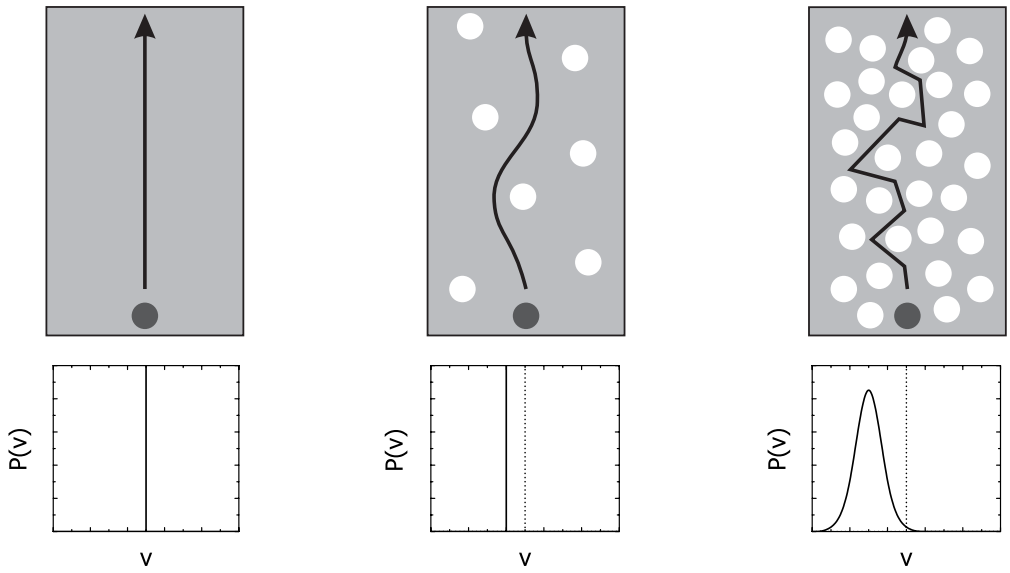

Figure 1.1: A simple example for long- and short-range correlations: The path of a walker through a pedestrian area (upper panels) – late at night (left), at daytime on a regular weekday (middle), and at noon on the Saturday before Christmas (right). White dots stand for other pedestrians. The lower panels indicate the probability to find the walker at a certain (instantaneous) velocity $|\vec{v}\,|$. The dashed lines in the middle and the right panel denote the free case.

of the short-range correlations, depends strongly on the density of the medium. A description of the short-range effects by a simple potential is not feasible. Hence, their investigation will be more complicated than the study of long-range effects.

Of course, the details of the interactions between pedestrians, quarks, or nucleons differ. Nonetheless, the observed effects are universal. In quark matter and nuclear matter, we use spectral functions to describe the properties of the particles. The spectral functions, that determine the probability to find a particle with a given energy at a certain momentum (or vice versa), are closely related to the velocity distributions of the above example: When only long-range correlations between quarks or nucleons are considered, we observe a sharp peak that has no width – a so-called quasiparticle peak – in the spectral function. The position of this peak is shifted with respect to a free particle. Short-range correlations lead to a breakdown of the quasiparticle picture. Interactions, in which the particles exchange energy and momentum, induce the collisional broadening of the peak in the spectral function as illustrated in Fig. 1.1. The existence of states far away from the maximum of the peak will lead to interesting effects that we discuss below.

After we have established the basic concepts, let us take a closer look at quark matter. To our present knowledge, quantum chromodynamics (QCD) is the theory of the strong interaction. All properties of strongly interacting systems should be described by QCD [PS95]. However, QCD does not provide an easy access to the

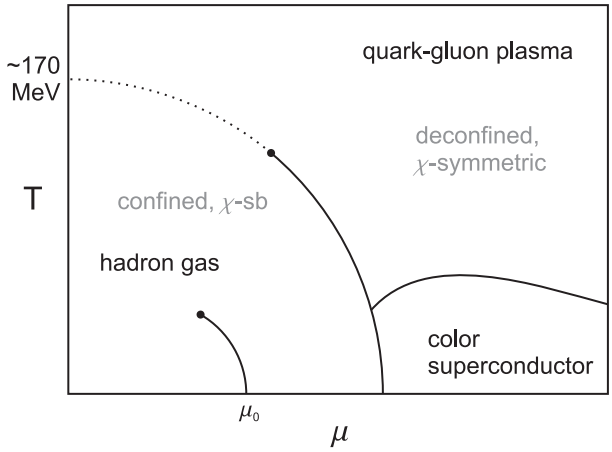

Figure 1.2: The phase diagram of QCD (schematic), taken from [Kar06]. Model calculations indicate that the chiral phase transition is of first order at low temperatures (solid line) and turns into a smooth crossover (dotted line) above a critical point. At large chemical potentials μ and low temperatures T, a color superconducting phase may exist above the chiral phase transition. Below the phase transition, chiral symmetry is broken (χ-sb). The line at low μ ($\sim \mu_0$) and T denotes the liquid–gas phase transition [BBI+95] of normal nuclear matter.

investigation of phenomena at moderate energies: The theory is not directly solvable and it is not possible to perform perturbative calculations since the running coupling of the QCD Lagrangian becomes large at low energies. The numerical realization of QCD in the form of Lattice QCD [Cre83] is technically challenging and – in particular at finite chemical potentials – still limited in its applications [Kar02]. Consequently, effective models have been developed to investigate the low energy phenomenology of QCD and the underlying mechanisms. These effective models treat the quarks usually as quasiparticles, i.e., sharp energy–momentum distributions are assumed. Even when systems with considerable quark densities are explored, the possibility of short-range correlations that lead to a collisional broadening of the quark spectral function is not taken into account.

The Nambu–Jona-Lasinio (NJL) model [NJL61a, NJL61b, Kle92, VW91, HK94] is an effective quark model with a pointlike interaction that has been constructed to resemble the symmetries of QCD. The NJL model is frequently used to explore phenomena related to chiral symmetry – in particular the dynamical breaking of this symmetry at low temperatures and densities and the chiral phase transition at higher temperatures T and/or chemical potentials μ. In the last years, the model has also become very popular to explore the effects of color superconductivity and their impact on the QCD phase diagram at high densities and low temperatures. See, e.g., [RW02, Bub05] for recent reviews. Fig. 1.2 shows a schematic QCD phase diagram. Like many phenomenological models [Kar06], the NJL model in the quasiparticle approximation (Hartree or Hartree–Fock) generates a chiral phase transition that is

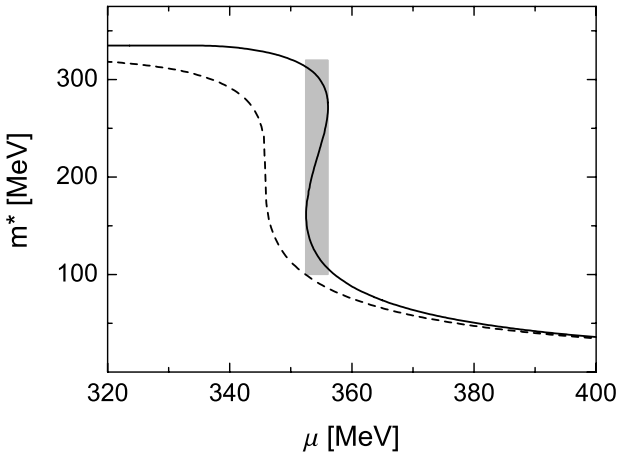

Figure 1.3: The effective quark mass as function of the chemical potential at $T = 0$ in the NJL model. The solid line shows the Hartree–Fock result, the dashed line the result of a calculation with a constant quark width of 28 MeV. The shaded area denotes the region of a first-order phase transition. See the text for details. (Due to the width, the dashed line drops faster at low μ. This means the density $\rho \sim (\mu^2 - m^{*2})^{3/2}$ rises faster than in the quasiparticle calculation. Consequently, the dashed curve drops at a slightly lower μ than the solid curve.)

of first order at low T and high μ and turns into a smooth crossover at high T and low μ.

At zero temperature, just above the chiral phase transition, quark densities a few times larger than normal nuclear matter density ($\rho_0 = 0.17\,\mathrm{fm}^{-3}$) are reached. It is not unlikely that short-range correlations exist at such densities and have considerable influence on the properties of the medium [Pes04]. For example, a simple estimate indicates that the character of the chiral phase transition at low temperatures changes when a small width is added to the quasiparticle quark propagator: The result of such a calculation is shown in Fig. 1.3. The solid line shows the result of a standard Hartree–Fock calculation including a finite current quark mass. In the shaded region, three solutions for the effective mass $m^*(\mu)$ are found for a given value of μ. This is characteristic for a first-order phase transition [PB94]. The upper and the lower solution correspond to minima of the thermodynamical potential (free energy) [SKP99, Kle92] that is shown in Fig. 1.4 and thus are stable. The intermediate solution for m^* is metastable, it corresponds to a maximum of the potential. Somewhere in the shaded region of Fig. 1.3 (lines (b-d) in Fig. 1.4), the two minima have the same value (line (c)). There, the actual phase transition takes place and the system drops from the upper to the lower solution for m^* discontinuously.

The dashed curve in Fig. 1.3 shows a different behavior. It has been obtained after inserting a constant width into the quasiparticle quark propagator. The collisional broadening turns the phase transition into a crossover: The region where multiple

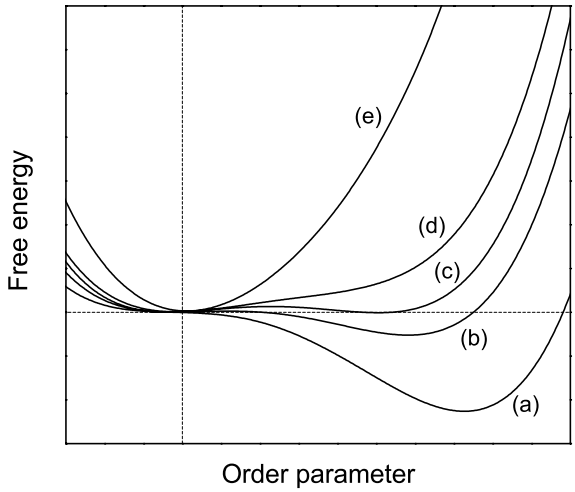

Figure 1.4: The free energy (schematic) as a function of the order parameter in the vicinity of a first-order phase transition [PB94]. The order parameter of the chiral phase transition is the effective mass m^*. The lines (a)-(e) correspond to increasing values of the chemical potential μ (from bottom to top). The phase transition occurs when the two minima of the free energy have the same value, cf. line (c).

solutions for m^* exist has disappeared, the quark mass dropsrapidly but continuously now. In other words, the (quasiparticle) predictions for the character of the chiral phase transition and/or the position of the critical point are considerably modified. Note that the width is just chosen as an arbitrary constant here. Fig. 1.3 is meant as an illustrative example. A more realistic calculation with a self-consistently determined width will be given below.

We have investigated the possibility of short-range effects for the first time in [Frö01, FLM03b, FLM03c]. Our simple but fully self-consistent approach to the NJL model was based on techniques that haven proven to be very successful in the investigation of nuclear matter. To illustrate the importance of short-range correlations, we shall discuss the case of nucleons in some detail before we return to quarks.

For nucleons in nuclear matter, short-range effects are well known and have been the subject of many investigations [DVN05]. In finite nuclei the effects of short-range correlations can be observed in $A(e,e'p)X$ and $A(e,e'pp)X$ experiments (see, e.g., [dWH90] and [CdAPS91]). Theoretically, the effects have been investigated first in sophisticated many-body calculations [RPD89, RDP91, BFF92, BBG$^+$92]. It has been found that a full understanding of nuclear matter and finite nuclei is not possible when the short-range effects are not taken into account. At zero temperature and normal nuclear matter density ρ_0, the effects range on a 10% level. This can, e.g., be seen in the momentum distribution that is shown in Fig. 1.5: Strength is shifted away from the quasiparticle peaks of the spectral function. This leads to a depletion of the occupation probabilites inside the Fermi-sphere (below the Fermi momentum) in

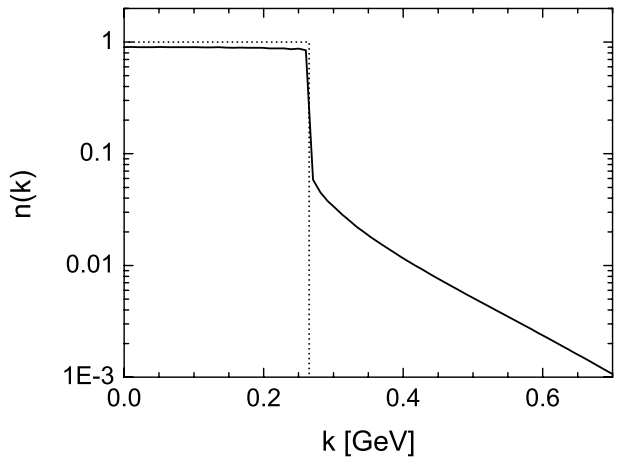

Figure 1.5: The nucleon momentum distribution in cold nuclear matter at saturation density [LLLM02] (solid line). The dotted line indicates the momentum distribution of a system of non-interacting particles (free fermion gas). See the text for details.

comparison to a system of non-interacting particles. The missing strength is shifted to higher momenta by nucleon–nucleon collisions – producing a long tail above the Fermi momentum.

In the last years, the properties of nucleons in (isospin symmetric) nuclear matter have been studied extensively in self-consistent approaches that allow a simultaneous treatment of long- and short-range effects. A recent review can be found in [DB04]. Those approaches solve Dyson–Schwinger equations for the full in-medium nucleon propagator that is dressed with an energy and momentum dependent complex self-energy. Some of the calculations have been performed in T-matrix approaches using realistic NN potentials [Bȯz02, FM03]. Other approaches have been based on very simple interaction models [LEL$^+$00, LLLM02], namely the lowest order diagrams for the collisional self-energy and a pointlike interaction for the short-range part. Note that more recently, those studies have also been extended to asymmetric nuclear matter [Bȯz04, FMR$^+$05, KLM05].

Concerning the short-range effects, the results of the theoretical approaches agree rather well. Already with a pointlike interaction it is possible to reach a good agreement with the more realistic calculations and the experimental data. It is striking that spectral functions, momentum distributions, occupation probabilities, and response functions can be reproduced with the overall strength as the only free parameter. Thus, what matters is not the detailed modeling but the overall strength of the interaction and a reliable description of the collisional phase space [LEL$^+$00].

The density and temperature dependence of the short-range correlations in nuclear matter is of particular interest for various regions of nuclear physics. For example, in heavy ion collisions like those planned at the Compressed Baryonic Matter (CBM)

facility at GSI [GGHM01], densities of several times the nuclear matter saturation density $\rho_0 = 0.16/\,\mathrm{fm}^3$ are reached. Similar conditions are encountered in astrophysical scenarios. When a neutron star is formed in a supernova explosion, temperatures of several tens of MeV and densities far beyond normal nuclear matter density arise. The neutrinos emitted from the nascent neutron star provide important information about the ongoing cooling processes. Nucleon correlations, however, affect the neutrino opacity in dense nuclear matter. The neutrino cross sections can be significantly reduced due to the presence of correlations in the medium [Saw95, RPLP99]. Therefore it is important to take nucleon correlations into account when interpreting the neutrino spectra.

So far, there has been no consistent investigation of the properties of the nucleon spectral function that covers the full temperature and density range of those scenarios. Even though the main focus of the present work is on the short-range correlations in quark matter, we will address this problem in the following – see also [FLM03a]. Therefore, we reconsider the approach to short-range correlations in nuclear matter (at $T = 0$ and saturation density) presented in [LEL$^+$00, LLLM02] and extend it to the more general cases of finite temperatures and densities beyond the nuclear matter equilibrium point.

Such an extension requires a reliable description of the static mean-field self-energy which in [LEL$^+$00, LLLM02] could most conveniently be absorbed into a redefinition of the chemical potential. To obtain consistent results at all T and ρ, an explicit treatment of the density and momentum dependent mean-field, i.e. the long-range part of the nucleon–nucleon interaction, is necessary. The (repulsive) pointlike interaction used to generate the short-range effects cannot describe the long-range interactions in nuclear matter. Thus, we incorporate the static properties of the mean-field into our model by an empirical, Skyrme-type energy-density functional [Sky59, BFvGQ75, VB72].

Alvarez-Ruso et al. [ARFdCO96] have performed calculations similar to ours for densities from half to twice ρ_0 and temperatures up to 20 MeV. In their "semi-phenomenological" approach they have evaluated second order diagrams taking the magnitude of the NN interaction from experiment. However, they did not perform their calculations self-consistently. Note that the basis of their work was also a model for cold nuclear matter [FdCO92]. In the self-consistent T-matrix approach of Bożek [Bòz99], the temperature dependence of the spectral function was investigated up to $T = 20\,\mathrm{MeV}$ while the density dependence has been ignored.

In this work, we go far beyond the temperature and density ranges of the former approaches. To study the role of short-range correlations in supernovae and heavy ion collisions at CBM, we consider temperatures up to 70 MeV and densities from ρ_0 to $3\rho_0$. Note that this is the first time that such a large range is investigated consistently within the same model. The self-consistent calculations will yield interesting results concerning the temperature and density dependence of the short-range correlations in nuclear matter. Some of the results will also be instructive for our investigation of quark matter.

Let us return to quarks now: The success of using pointlike interactions in nuclear matter had motivated our first approach to quark matter [FLM03b]. The NJL model provides a similar interaction for quarks that respects the relevant symmetries of QCD. We have used it in a self-consistent calculation where the collisional self-energy was determined by the direct and the exchange Born diagram, i.e., at a 2-loop level. The results of [FLM03b] have shown that this approach generates rather small collisional widths. The short-range effects are more than one order of magnitude smaller than in nuclear matter. A similar approach to higher order effects in quark matter can be found in [DBM93, DM94] where several NJL inspired interactions are compared. In those works, the collisional self-energy was not determined self-consistently and the calculations were restricted to $\mu = 0$. Nonetheless, the results for the quark width range on the same order of magnitude as in [FLM03b].

A priori, there is of course no reason to expect a certain order of magnitude for the correlations. On the other hand, it is known that a loop-expansion is questionable in the NJL model since the coupling is large. An expansion in the inverse number of colors, $1/N_c$, is preferable [QK94, DSTL95]. While the Born diagrams are the only diagrams in next-to-leading order of the coupling, an infinite number of self-energy diagrams in next-to-leading order of $1/N_c$ exists. Hence, the results of a $1/N_c$ expansion should differ from [FLM03b] and [DBM93, DM94].

In this work, we bring our approach from [FLM03b] to a consistent level in $1/N_c$. We include all quark self-energy diagrams of the next-to-leading order $\mathcal{O}(1/N_c)$ in a self-consistent calculation, not only the Born diagrams. This leads to the introduction of dynamically generated RPA mesons, i.e., in our $SU(2)$ approach states with the quantum numbers of the σ and π. In contrast to the standard Hartree+RPA scheme [Kle92] we do not calculate the RPA polarizations with quasiparticle propagators but with the full in-medium quark propagators. The RPA mesons are part of the self-consistent procedure and their properties are fed back into the quark self-energy. By solving a coupled set of Dyson–Schwinger equations for the quark and meson propagators in an iterative calculation we are able to explore the off-shell effects in quark matter.

$1/N_c$ extensions to the NJL model on the quasiparticle level – using a pole approximation for the dynamically generated mesons and not considering the collisional broadening of the quarks – have been discussed before [QK94, DSTL95, NBC$^+$96]. The purpose of those considerations was to find next-to-leading order corrections to the Hartree+RPA approximation without disturbing the chiral properties of the model. It has been shown in [DSTL95, NBC$^+$96] that the generation of massless pions (Goldstone modes) in a perturbative expansion relies on a careful choice of diagrams for the meson polarizations. Our self-consistent ansatz iterates diagrams up to arbitrary orders in $1/N_c$ but does not generate all contributions of any given order. Thus, the RPA pions become massive in the chirally broken phase. Note that we obtain a reasonable pion mass – in comparison to the Hartree+RPA approximation – above the chiral phase transition. An approach that is self-consistent *and* yields massless pions (in the chiral limit) has not been proposed so far for the NJL model.

The result of our self-consistent calculation could be used as input for an additional formalism which yields realistic pion properties. However, in the approach proposed in [DSTL95] and similarly in [OBW00, vHK02], the Goldstone pions are not fed back into the calculation of the quark properties.

Our approach goes beyond the quasiparticle models of [DSTL95, NBC$^+$96]. We do not only consider the poles of the RPA meson propagators but also the continuum of off-shell states. As we will see later, these states are much more important for the quark properties than the poles. A detailed analysis of the different off-shell contributions to the quark width will show that some of them are sensitive to the pion mass while others are not. Concerning the chirally broken phase, it will turn out that our self-consistent calculation yields a conservative estimate of the short-range correlations in quark matter.

In the present work, as a first step, we ignore diquark condensates and color superconductivity – relevant at high chemical potentials μ and low temperatures T and explore the role of the short-range correlations in the chirally broken and restored phase. We restrict our numerical calculations to a wide range of chemical potentials at zero temperature. Nevertheless, the formalism that is presented here can also be used at finite T. At some places we will use simplifications for $T = 0$. In the present form the method is not applicable to flavor asymmetric matter – we have consequently used all simplifications that are possible in symmetric quark matter. An approach to asymmetric systems would be technically more involved because the up and the down quarks as well as the three pions $\pi^{0,\pm}$ would have to be treated separately. Hence, instead of working with flavor multiplets we would have to change to the basis of particle states which is better suited for flavor asymmetric systems. However, there are no fundamental problems with such an approach. For nuclear matter this has been demonstrated in [KLM05].

This work is structured as follows. In Chapter 2 we briefly present the NJL model and introduce the different approaches to the quark properties – the mean-field Hartree+RPA approximation as well as our self-consistent $\mathcal{O}(1/N_c)$ approach. A review of $1/N_c$ corrections to the NJL model that leave the chiral theorems intact is also included. In the end of the chapter we discuss the structure of the propagators and self-energies in the real-time formalism that we use for our calculations at finite chemical potentials. In Chapter 3 we show how to calculate the quark self-energy and the meson polarizations using the full in-medium propagators. The imaginary parts will be determined in a direct calculation. For the real parts we use dispersion relations. This requires a close inspection of the analytical expressions.

In Chapter 4 we use quasiparticle approximations and simple phase space arguments to explore the structure of the quark width and its density dependence. We also investigate the influence of the RPA pion mass on the on-shell width. The numerical realization of our model is presented in Chapter 5. We show results from calculations with two sets of parametrizations, one with a finite current quark mass m_0 and one with vanishing m_0 (chiral limit). We discuss the influence of the short-range correlations on the properties of the quarks and investigate the density dependence

of the effects. The results for quark matter are compared to calculations for nuclear matter and our former results from [FLM03b].

Our approach to the short-range correlations in nuclear matter at finite temperatures and high densities can be found in Chapter 6. We will compare our results to other models (at $T = 0$ and finite temperatures) and discuss the temperature and density dependence of the short-range correlations. A summary, reviewing the dynamical correlations at the various scales from quark to nuclear matter, is found in the concluding discussion in Chapter 7 where we also give an outlook to future improvements.

2 The formalism

In the following we present the components of our model. We begin with a short introduction to the NJL model and the concept of expansions in the inverse number of colors. After reviewing the standard mean-field approach to quarks and mesons in the NJL model, we construct a fully self-consistent approach to the quark self-energies beyond the mean-field approximation. In the last part of this chapter, we discuss the formal structure of the in-medium propagators and self-energies that enter our calculations.

In the derivation of our model we assume that the system is in thermal equilibrium. For simplicity, we work in the rest frame of the medium. The formalism that we derive here is also suitable for calculations at finite temperatures. However, it is presently restricted to flavor symmetric quark matter. In contrast to our earlier approach to short-range correlations [FLM03b] there is no restriction to the chirally restored phase of the system.

2.1 The NJL interaction

The Nambu–Jona-Lasinio (NJL) model in its original form has been introduced in 1961 [NJL61a, NJL61b]. Inspired by the Bardeen–Cooper–Schrieffer (BCS) theory of superconductivity [BCS57], Nambu and Jona–Lasinio had constructed an effective, local nucleon–nucleon interaction. Quarks and quantum chromodynamics (QCD) were yet unknown at this time.

After the rise of QCD, the need for effective quark interaction models became apparent. The running coupling of QCD becomes small only at large momentum transfers (asymptotic freedom). Thus, the perturbative methods that were developed for quantum electrodynamics (QED) are not applicable in QCD at the length scales and momentum transfers that are typical for hadronic physics. This has led to a reconsideration of the NJL model: The NJL Lagrangian is by design the simplest effective interaction that resembles all relevant symmetries of QCD [Kle92], namely $SU_V(2) \otimes SU_A(2) \otimes U_V(1)$ (for two flavors) while the $U_A(1)$ symmetry is broken,

$$\begin{aligned} SU_V(2):\ \psi \to \psi' = e^{-i\vec{\alpha}\cdot\vec{\tau}/2}\psi \qquad & U_V(1):\ \psi \to \psi' = e^{-i\sigma}\psi \\ SU_A(2):\ \psi \to \psi' = e^{-i\gamma^5\vec{\beta}\cdot\vec{\tau}/2}\psi \qquad & U_A(1):\ \psi \to \psi' = e^{-i\gamma^5\rho}\psi\,, \end{aligned}$$

where the τ_i are the isospin Pauli matrices and $\vec{\alpha}, \vec{\beta}, \sigma, \rho$ are (constant) isospin vectors and numbers. Since the symmetries are among the most important features of QCD,

the NJL interaction has been identified with a low energy approximation to QCD and its degrees of freedom have been reinterpreted as (up and down) quarks.

Detailed investigations of the NJL model in $SU(2)$ and $SU(3)$, i.e. for two and three quark flavors, can be found in the reviews of Klevansky [Kle92], Vogl and Weise [VW91], and Hatsuda and Kunihiro [HK94]. The NJL model is useful in many situations where it is not necessary to treat gluons as explicit degrees of freedom and they can thus be absorbed in an effective $q\bar{q}$ coupling[1]. In particular, it is very popular for the investigation of chiral symmetry (see below) and its dynamical breaking at low temperatures and densities.

In the lowest order mean-field approach – the Hartree+Random Phase Approximation (RPA), see Section 2.3.1 for details – a finite constituent quark mass is generated and breaks chiral symmetry dynamically at low μ and T. Pions that can be identified with the Goldstone modes of the model are found in the RPA approach. At higher μ and/or T, chiral symmetry is restored and the NJL model allows an investigation of the chiral phase transition.

Let us now turn to the details of the NJL interaction. The standard version of the two flavor Lagrangian, including a small current quark mass m_0, is given by

$$\mathcal{L}_{\mathrm{NJL}} = \bar{\psi}\left(i\partial\!\!\!/ - m_0\right)\psi + \mathrm{G}\left[(\bar{\psi}\psi)^2 + (\bar{\psi}i\gamma_5\vec{\tau}\psi)^2\right] , \tag{2.1}$$

where G is the constant coupling strength and the τ_i are the isospin Pauli matrices. Note that the invariance under $SU_V(2)\otimes SU_A(2)$ transformations is equivalent to the invariance under the chiral symmetries $SU_L(2)\otimes SU_R(2)$:

$$\begin{aligned} SU_L(2):\ \psi_L &\to \psi'_L = e^{-i\vec{\sigma}\cdot\vec{\tau}/2}\psi_L\,, \\ SU_R(2):\ \psi_R &\to \psi'_R = e^{-i\vec{\rho}\cdot\vec{\tau}/2}\psi_R\,, \end{aligned}$$

with the left-handed state $\psi_L = \frac{1}{2}(1-\gamma^5)\psi$ and the right-handed state $\psi_R = \frac{1}{2}(1+\gamma^5)\psi$. The term $m_0\bar{\psi}\psi$ is not invariant under these transformations. Hence, chiral symmetry is broken explicitly – to a small extent – when m_0 is set to a finite value. This is, however, a small effect in comparison to the dynamical symmetry breaking that we will discuss below.

Due to the constant coupling, the model cannot be renormalized. Several regularization schemes for the NJL interaction exist, the simplest one is to introduce a (three-)momentum cutoff Λ. The coupling G, the cutoff Λ and the (optional) current quark mass m_0 are the free parameters of the NJL model. Usually their values are fixed such that reasonable results are obtained for the quark condensate and the pion decay constant in vacuum – and for the pion mass in the case $m_0 \neq 0$. We list some typical sets of parameters for mean-field calculations in Table 2.1. The simplicity of

[1] An effective quark interaction without gluons can be motivated by the BCS theory [Kle92]: In the theory of superconductivity, an effective electron–electron interaction is generated – independently of the Coulomb interaction between the electrons – by electron–phonon interactions. Complicated gluon exchange processes could generate, in analogy to this phenomenon, an effective quark–quark interaction.

Table 2.1: Mean-field NJL parameter sets, using a three-momentum cutoff Λ. The values and the naming scheme are consistent with [Kle92] and references therein. Sets I and II include a finite current quark mass m_0. The coupling G is fitted for Hartree calculations. The coupling G_{HF} for the Hartree–Fock approximation is obtained from G by a rescaling factor 12/13. m^* and $\langle\bar{u}u\rangle$ are the effective mass and the quark condensate that are found using the given parameters.

	m_0 [MeV]	$G\Lambda^2$	$G_{HF}\Lambda^2$	Λ [MeV]	m^* [MeV]	$\langle\bar{u}u\rangle^{1/3}$ [MeV]
Set 0	-	2.14	1.98	653	313	-250
Set I	5.5	2.19	2.02	631	336	-247
Set II	5.0	2.17	2.00	925	472	-359

(a) (b)

Figure 2.1: The scalar and the pseudoscalar $q\bar{q}$ vertices of the standard NJL interaction (a) and the $q\bar{q}$-meson vertices of the bosonized NJL interaction (b). The solid dots in (a) represent the coupling constant G. The dashed lines in (b) correspond to dynamically generated σ and π mesons. The coupling constant G does not appear explicitly but is hidden in the meson propagators.

this model leads also to certain shortcomings like the lack of asymptotic freedom and the absence of confinement. The cutoff is sometimes interpreted as a crude implementation of asymptotic freedom. For confinement no such simple emulation exists.

The NJL Lagrangian in the present form provides scalar and pseudoscalar $q\bar{q}$ interaction channels. Fig. 2.1(a) shows the corresponding interaction vertices. After a slight rearrangement, the vertices resemble the quantum numbers of σ, π^0 and π^+, π^- meson exchanges, respectively:

$$\mathcal{L}_{\mathrm{NJL}} = \bar{\psi}\left(i\partial\!\!\!/ - m_0\right)\psi + \sum_l \mathrm{G}(\bar{\psi}\Gamma_l\psi)(\bar{\psi}\tilde{\Gamma}_l\psi)\,, \tag{2.2}$$

with $l = \sigma, 0, +, -$ and

$$\begin{aligned} \Gamma_\sigma &= \tilde{\Gamma}_\sigma = 1\,, \\ \Gamma_0 &= \tilde{\Gamma}_0 = i\gamma_5\tau_3\,, \\ \Gamma_\pm &= \tilde{\Gamma}_\mp = i\gamma_5\tau_\pm = i\gamma_5(\tau_1 \pm i\tau_2)/\sqrt{2}\,. \end{aligned} \tag{2.3}$$

In the last years, the NJL model has been frequently used to investigate the phenomenon of color superconductivity, see [Bub05] and references therein. Therefore, a vertex was added to the Lagrangian that introduces an attractive interaction in the qq channel. We do not consider such an extension to the Lagrangian in the present work. However, it would be a consequent extension of our approach to investigate the structure of the phase diagram in a self-consistent model that also incorporates the effects of color superconductivity.

It is also possible to construct a bosonized version of the NJL Lagrangian [Kle92, HK94, ZW92]. Using the notation of [Reh98] we rewrite the Lagrangian,

$$\begin{aligned}\mathcal{L}_{\mathrm{NJL}} = \bar{\psi}\left(i\partial\!\!\!/ - m_0\right)\psi - \bar{\psi}\left(\sigma\Gamma_\sigma + \pi_0\Gamma_0 + \pi_+\Gamma_- + \pi_-\Gamma_+\right)\psi \\ - \frac{1}{4G}\left(\sigma^2 + \pi_0^2 + 2\pi_+\pi_-\right) ,\end{aligned} \tag{2.4}$$

where the σ and π fields are defined as

$$\begin{aligned}\sigma &= -2G\bar{\psi}\Gamma_\sigma\psi\,, \\ \pi^{0,\pm} &= -2G\bar{\psi}\Gamma_{0,\pm}\psi\,.\end{aligned} \tag{2.5}$$

The new form of the Lagrangian describes an effective quark–meson (σ,π) interaction. The corresponding vertices are shown in Fig. 2.1(b). It should be noted that the Lagrangian (2.4) does not contain a dynamical part for the meson fields. Thus their dynamics are completely determined by that of the quark fields they are generated from. For a discussion on the quantization of (2.4) we refer to [Reh98, ZW92].

2.2 $1/N_c$ expansion in the NJL model

2.2.1 Order counting in $1/N_c$

The NJL model is a strongly interacting theory. It can be seen in Table 2.1 that $G\Lambda^2$ – the relevant quantity to estimate the interaction strength – has a value of approximately 2 for all given parameter sets. Thus, a perturbative expansion in terms of the coupling constant G is not feasible. However, the NJL model is a QCD inspired theory and it is possible to perform an expansion in the inverse number of colors, $1/N_c$. Expansions in $1/N_c$ that go beyond the usual Hartree+RPA approach have been studied in [QK94, DSTL95] on the level of Feynman diagrams. For that purpose, a scheme is developed that allows to determine the order in $1/N_c$ of Feynman diagrams by counting vertices and loops. A factor G is assigned to each interaction vertex and a factor N_c to each closed fermion loop (a loop corresponds to the trace over a quark propagator in color space). In this symbolic notation one sets $GN_c = \mathcal{O}(1)$.

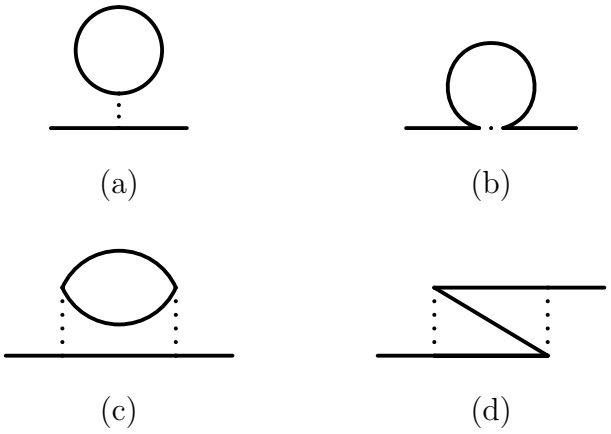

Figure 2.2: The Hartree (a) and Fock (b) self-energies and the direct (c) and exchange (d) diagrams of the Born self-energy. The pointlike interaction vertex has been replaced by a finite interaction line to make the diagrams graphically distinguishable. Due to the closed fermion loop, the Hartree diagram is of order $\mathcal{O}(\mathrm{G}N_c) = \mathcal{O}(1)$ while the Fock diagram is of order $\mathcal{O}(1/N_c)$. The direct Born diagram is also of order $\mathcal{O}(1/N_c)$ since $\mathrm{G}^2 N_c^1 = N_c^{-1}$ (symbolic notation). The exchange diagram does not include a closed fermion loop and is of order $\mathcal{O}(1/N_c^2)$.

The (free) quark propagator is of order unity,

$$\begin{aligned} &\text{——} && \sim \mathcal{O}(1)\,, \\ &\bullet && \sim \mathcal{O}(G) \sim \mathcal{O}(1/N_c)\,, \\ &\bigcirc && \sim \mathcal{O}(N_c)\,. \end{aligned} \tag{2.6}$$

The order of a diagram with n vertices and m loops is then given by $\mathrm{G}^n N_c^m = N_c^{m-n}$. In other words, in the $1/N_c$ expansion the order of a diagram is not determined by the number of vertices or by the number of loops but by the difference of loops and vertices.

2.2.2 Classification of self-energy diagrams

The difference between an expansion in $1/N_c$ and an expansion in the coupling can be easily seen. Fig. 2.2 shows some diagrams that are of first (a,b) and second order (c,d) in the coupling. According to the $1/N_c$ counting scheme, the Hartree diagram (a) is the only contribution of order $\mathcal{O}(1)$ to the quark self-energy. The Fock diagram (b) as well as the direct Born diagram (c) are of order $\mathcal{O}(1/N_c)$. The exchange Born diagram (d) is even of order $\mathcal{O}(1/N_c^2)$. On the other hand, all diagrams in Fig. 2.3 are of the same order, namely $\mathcal{O}(1/N_c)$. There is always one more vertex than there are

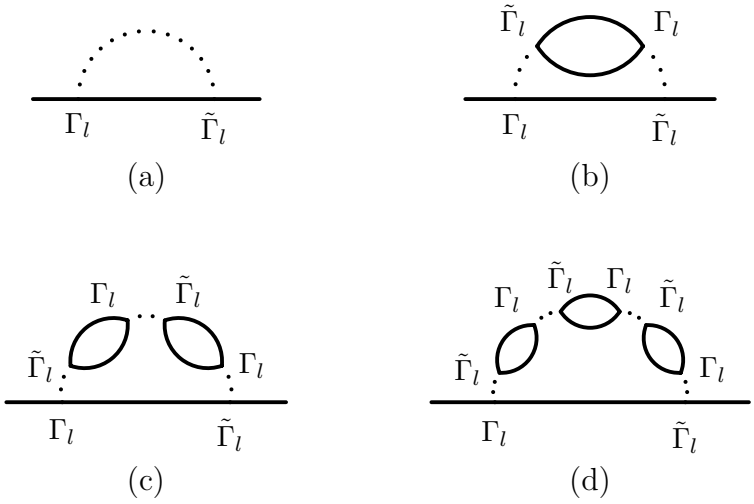

Figure 2.3: Self-energy diagrams of order $\mathcal{O}(1/N_c)$. The pointlike interaction was replaced by an interaction line to show the structure of the diagrams unambiguously. (a) and (b) are the Fock and the direct Born self-energies, respectively. Diagram (c) was constructed by adding one further vertex and quark loop to (b), (d) was constructed by adding two more vertices and quark loops. Further diagrams of higher order in G but of the same order in $1/N_c$ can be constructed by adding more loops and vertices to the chain of loops in (d).

loops. Fig. 2.3(a) and (b) are again the Fock diagram and the direct Born diagram. The other diagrams were constructed by adding pairs of loops and vertices to the Born diagram. Diagrams of any higher order in the coupling while still on the same order in $1/N_c$ can be found by adding further loops to the chain of loops in Fig. 2.3(d). Note that all vertices in such a diagram must be of the same kind (i.e., the same l in the $\Gamma_l, \tilde{\Gamma}_l$ of all vertices) to get a non-trivial contribution to the self-energy.

By dressing the internal quark lines in the diagrams of Fig. 2.2 with the Hartree diagram, further diagrams of the same order as the original diagrams can be constructed. By dressing the quark loop of the Hartree diagram with, e.g., the Fock or the direct Born diagram, diagrams of order $\mathcal{O}(1/N_c)$ can be constructed that are not of the same structure as the diagrams of Fig. 2.3. Such diagrams will later be generated automatically when the free propagators are replaced by dressed ones in a self-consistent calculation. They are not discussed here to avoid double counting.

The counting scheme (2.6) does not work in a strict sense when dressed propagators are considered: The full propagator of a self-consistent calculation can be dressed with self-energies of arbitrary order in $1/N_c$. It remains $\mathcal{O}(1)$ in leading order but gains contributions of higher orders. Consequently, the Feynman diagrams constructed from such propagators will not be purely of a certain order in $1/N_c$. Like the dressed propagators, however, the diagrams maintain a well defined leading order that is identified by the counting scheme. In a self-consistent approach this means that we

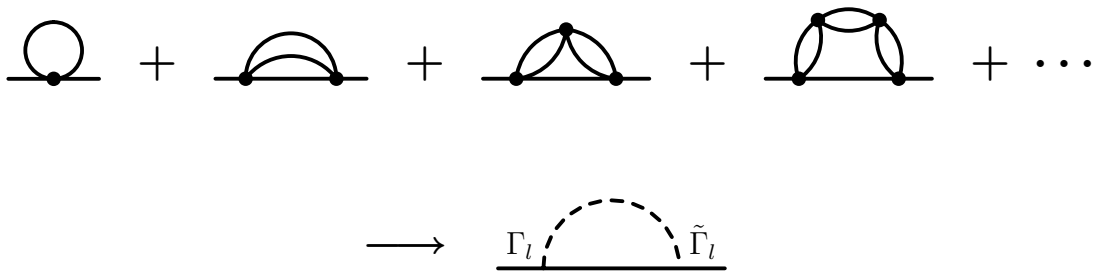

Figure 2.4: The $\mathcal{O}(1/N_c)$ diagrams of the structure shown in Fig. 2.3 are added up in a random phase approximation. An effective meson exchange (dashed line) is generated, the type of the generated meson depends on the chosen $\Gamma_l, \tilde{\Gamma}_l$. As shown in Fig. 2.3, the first diagram of the series is the Fock diagram. The Hartree diagram is of different order and has to be treated separately. In contrast to the Hartree diagram, the non-local meson exchange represents a complex contribution to the quark self-energy.

can select Feynman diagrams by their leading order to find a consistent set of diagrams for any given order. However, every diagram will contribute in subleading orders in a possibly incomplete way. Note that the Hartree approximation constitutes an exception. Since the Hartree self-energy is of order $\mathcal{O}(1/N_c^0)$, the order of a propagator that is dressed only with such diagrams – even iteratively in a self-consistent approach – remains exactly $\mathcal{O}(1)$.

2.2.3 The Random Phase Approximation

Usually, all $\mathcal{O}(1/N_c)$ diagrams of the structure shown in Fig. 2.3 are summed up in a random phase approximation (RPA). The diagrams can be interpreted as contributions to an effective meson exchange as shown in Fig. 2.4. This allows us to treat a whole class of self-energy diagrams in a simple and consistent way. The type of the exchanged meson $(\sigma, \pi^{0,\pm})$ is determined by the choice of $\Gamma_l, \tilde{\Gamma}_l$ (cf. Fig. 2.4). The propagators of the RPA mesons have the following form:

(2.7)

where $(l = \sigma, 0, \pm)$

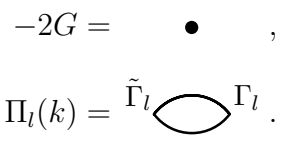

(2.8)

$\Pi_\sigma(k)$ and $\Pi_{0,\pm}(k)$ are the σ and $\pi^{0,\pm}$ polarizations, respectively. They can be interpreted as the fundamental building blocks of the RPA mesons.

Using Eqs. (2.8) and introducing the symbol $\Delta_l(k)$ for the meson propagators, we can rewrite Eq. (2.7),

$$\Delta_l(k) = -2G\left[1 + (-2G)\,\Pi_l(k) + (-2G)\,\Pi_l(k)(-2G)\,\Pi_l(k) + \ldots\right] . \tag{2.9}$$

The rhs. of Eq. (2.9) is a geometric series. Thus, a simple analytic expression for the effective meson propagators is found:

$$\Delta_l(k) = -\frac{2\mathrm{G}}{1 + 2\mathrm{G}\,\Pi_l(k)} . \tag{2.10}$$

It should be noted that the effective propagators do not have explicit kinetic parts of the form $k^2 - M^2$. The dynamics of the effective RPA mesons are completely governed by the underlying $q\bar{q}$ states and are thus hidden in the polarizations.

To illustrate the properties of the RPA mesons, we show the spectral function (cf. Section 2.7) of the RPA pion from a mean-field calculation in Fig. 2.5. We can make out two distinct components of the spectral function that are related to the composition of the RPA propagators (2.7,2.10). The δ-peak is identified with the actual RPA pion. It correspond to a bound $q\bar{q}$ state and is located at a pole of the propagator, i.e., $1+2\mathrm{GRe}\,\Pi_l(k) = 0$. The spectral function is, however, not restricted to this bound state. At energies above $k_0 = \mu+m^*$ ($2m^*$ in the vacuum), contributions from unbound $q\bar{q}$ states (2.7) are picked up – in this region the RPA mesons are not stable but decay into quark–antiquark pairs (see Section 4.5 for details). A wide range of states with a large decay width, the so-called $q\bar{q}$ continuum, is found in the spectral functions above this threshold.

Coming back to the quark self-energy, the diagram in the second line of Fig. 2.4 replaces the diagrams of Fig. 2.3 – and all others of the same structure. Like the Fock and the direct Born diagram, this is a contribution to the quark self-energy of the order $\mathcal{O}(1/N_c)$. A diagram like this is crucial for our approach. Its non-local structure generates a four-momentum dependent contribution to the self-energy. This contribution is complex and its imaginary part will later be identified with the collisional width of the quark spectral function. The $\mathcal{O}(1)$ Hartree diagram and the $\mathcal{O}(1/N_c^2)$ exchange Born diagram are not included in the effective meson exchange. They have to be treated separately, if needed.

2.3 Mean-field approaches

2.3.1 The $\mathcal{O}(1)$ Hartree+RPA approach

The standard approach to quarks and mesons in the NJL model is the Hartree+RPA approximation. It works in leading order of $1/N_c$, i.e. $\mathcal{O}(1)$, for the quarks. The complete Hartree+RPA approximation can be summarized in the two Dyson–Schwinger equations for quarks and mesons that are shown in Fig. 2.6.

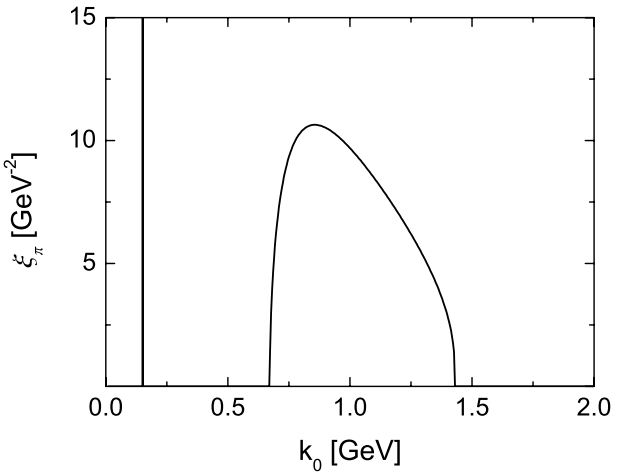

Figure 2.5: The spectral function of the RPA pion in the Hartree+RPA approximation at zero quark density and a constant three-momentum of 50 MeV, using parameter set I of Table 2.1. See Sections 2.3.1 and 2.7 for more details. The peak at $k_0 = 150\,\mathrm{MeV}$ ($m_\pi = 142\,\mathrm{MeV}$) corresponds to bound $q\bar{q}$ states, the broad structure at higher k_0 is the $q\bar{q}$ continuum. Note that ξ_π is antisymmetric in k_0.

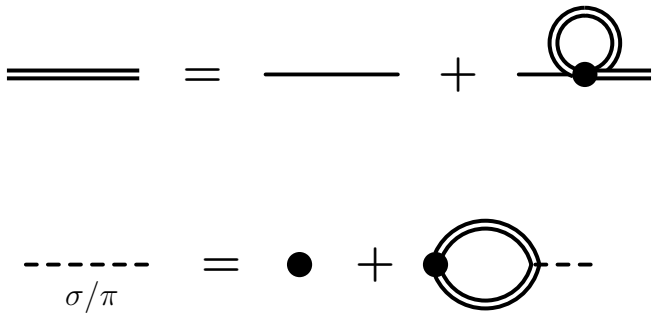

Figure 2.6: The set of Dyson–Schwinger equations corresponding to the Hartree+RPA approximation. The double lines denote quark propagators dressed with the Hartree self-energy. The first line enters the gap equation, the second line describes the RPA construction of the mesons. There is no feedback from the mesons to the quarks in this $\mathcal{O}(1)$ approximation scheme.

A self-consistent Hartree calculation is used to determine the quark properties. Therefore the so-called gap equation (first line of Fig. 2.6) is solved,

$$m^* = m_0 + \Sigma^{\mathrm{H}} = m_0 + 2i\mathrm{G}N_f N_c \int \frac{d^4p}{(2\pi)^4}\,\mathrm{tr}\,\mathrm{S}_{\mathrm{H}}(p)\,, \tag{2.11}$$

where $m^* = m_0 + \Sigma^{\mathrm{H}}$ is the effective quark mass and $\mathrm{S}_{\mathrm{H}}(k)$ the dressed Hartree propagator. "tr" denotes a trace in spinor space here. The meson properties are

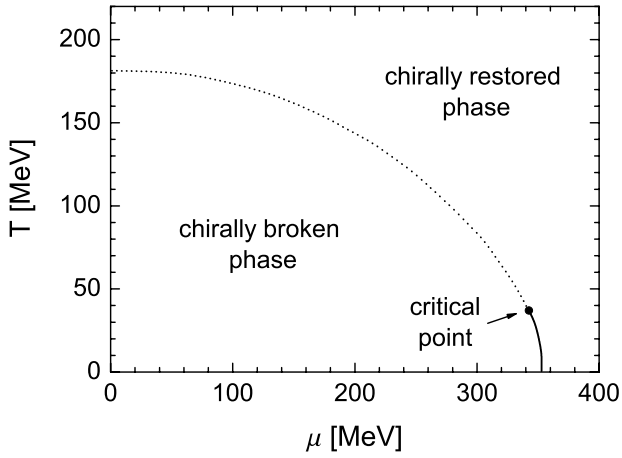

Figure 2.7: The chiral phase transition in the Hartree+RPA approximation, using parameter set I from Table 2.1. The critical point – where the first-order phase transition (solid line) turns into a smooth crossover (dotted line) – is located at $T = 37\,\mathrm{MeV}$ and $\mu = 343\,\mathrm{MeV}$. (Data taken from [Kle92, AY89])

found by calculating the polarizations $\Pi_l(k)$ (second line of Fig. 2.6) using the Hartree propagators,

$$\frac{1}{i}\,\Pi_l(k) = -\int \frac{d^4p}{(2\pi)^4}\,\mathrm{Tr}\left[\tilde{\Gamma}_l\,\mathrm{S_H}(p)\Gamma_l\,\mathrm{S_H}(p-k)\right]\,, \tag{2.12}$$

where "Tr" denotes a trace in color, flavor, and spinor space. Of course, the integrals in both Dyson–Schwinger equations are divergent and have to be regularized. We will come back to that in Section 2.4. Note that some technical details of the Hartree(–Fock)+RPA approximation will be relevant for our extended model. We discuss them in Appendix B.

The Hartree+RPA approach is well established and has been used extensively to investigate quarks and mesons. Constituent quark masses are dynamically generated at low T and μ, a chiral phase transition[2] occurs at a higher chemical potential (or temperature). Fig. 2.7 shows the chiral phase transition line that has been found in a calculation using parameter set I from Table 2.1. The phase transition is of first order [PB94] at low temperatures (and high densities) and turns into a smooth crossover at higher temperatures.

The pions of the Hartree+RPA approximation satisfy the Goldstone theorem. Below the chiral phase transition, they are massless in the chiral limit and light for finite current quark masses. In the chirally restored phase, the pions become massive while the constituent quark mass breaks down. In Fig. 2.8 we show the effective quark mass and density and the RPA sigma and pion masses that are found, again using

[2]The order of the phase transition may depend on the choice of parameters and the regularization scheme [Kle92].

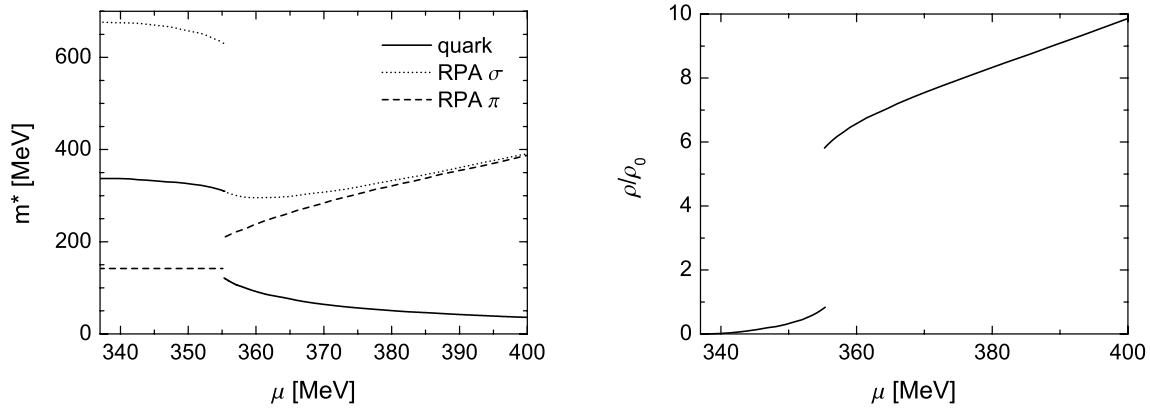

Figure 2.8: The effective quark mass and the RPA sigma and pion masses (left) and the quark density (right) as functions of the chemical potential μ in the Hartree+RPA approximation ($\rho_0 = 0.17\,\mathrm{fm}^{-3}$), using parameter set I from Table 2.1 ($m_0 = 5.5\,\mathrm{MeV}$). A first-order chiral phase transition occurs at $\mu = 355\,\mathrm{MeV}$. (Data taken from [Kle92, AY89])

parameter set I from Table 2.1. We will not investigate the Hartree+RPA approach in more detail at this point. For a thorough analysis we refer to the extensive review articles [Kle92, VW91, HK94].

Considering short-range effects, the Hartree+RPA approach has several shortcomings. First, the Hartree self-energy is time-local. Thus it is real and does not lead to a collisional broadening of the quark spectral function. The quarks remain quasiparticles in this approach. Second, the properties of the RPA mesons have no influence on the quark properties. Such a feedback would – in lowest order – correspond to the self-energy diagram that is shown in Fig. 2.4 or the modified Hartree diagram in Fig. 2.13. Those diagrams are, however, not of leading order in $1/N_c$ and therefore beyond the Hartree+RPA approach. To investigate the effects of short-range correlations it will be necessary to consider diagrams of next-to-leading order, i.e. $\mathcal{O}(1/N_c)$, or higher, for the quark self-energy.

2.3.2 Hartree–Fock, RPA, and Goldstone modes

Let us briefy discuss another mean-field model before we present our approach to short-range effects. Adding the Fock self-energy to the Dyson–Schwinger equations is the simplest way to extend the Hartree+RPA approximation. The resulting approach, to which we will refer as Hartree–Fock+RPA approximation in the following, is shown in Fig. 2.9. The RPA mesons are now generated from quark loops (RPA polarizations) with Hartree–Fock propagators. Since the Fock self-energy is time-local, the quarks remain quasiparticles.

The Hartree–Fock+RPA approximation does not represent a clean $1/N_c$ expansion

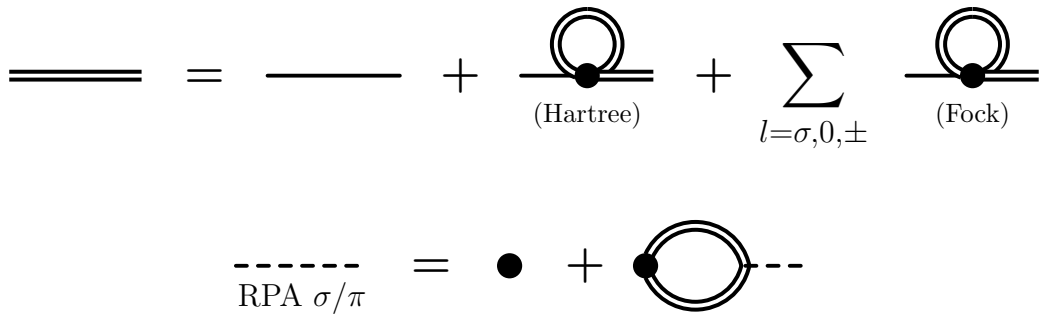

Figure 2.9: The Hartree–Fock+RPA approximation (see Fig. 2.2 for the difference between the Hartree and the Fock diagram). Double lines denote quark propagators dressed with the Hartree and Fock self-eneries. The first line enters the gap equation, the second line describes the RPA construction of the mesons. Like in the Hartree+RPA approach, there is no feedback from the mesons to the quarks.

of the quark self-energy. However, it is useful to illustrate the influence of higher order effects on the Goldstone boson character of the dynamically generated pions: Like in the $\mathcal{O}(1/N_c)$ approach that we present below – and in contrast to the Hartree+RPA approximation – the dressed quark propagators in the RPA polarizations are not purely $\mathcal{O}(1)$. This leads to the automatic generation of higher order contributions to the meson polarizations that are not present in the Hartree+RPA approximation. An explicit calculation, that can be found in Appendix B, shows that the pions generated by the present Hartree–Fock+RPA approximation cannot be identified with Goldstone bosons. Even in the chiral limit, they acquire a considerable mass.

Expecting that a (regular) random phase approximation on the Hartree–Fock level yields the Goldstone modes of the broken chiral symmetry [RS80, BR86, DVN05], this result may come as a surprise. The reason for the breakdown of the chiral properties of the RPA pions is the incomplete $1/N_c$ expansion of the meson polarizations in the Dyson–Schwinger equations of Fig. 2.9. As we will discuss in detail in Section 2.5, the generation of massless pions (in the chiral limit) in a $1/N_c$ expansion of the NJL model depends on a delicate balance [DSTL95]: In each order of $1/N_c$, the contributions from different polarization diagrams must cancel each other. When the Hartree–Fock propagator is inserted into the RPA polarizations, it will automatically generate some higher order contributions to the polarization. This approach does, however, not generate all (relvant) higher order contributions to the polarizations. We illustrate this in Fig. 2.10: Both diagrams are next-to-leading order polarization diagrams – but only diagram (a) is automatically generated by the present Hartree–Fock+RPA scheme. Consequently, the cancellation effect remains incomplete and the chiral properties of the dynamically generated pions are disturbed.

To recover the Goldstone modes, we would have to identify all polarization diagrams

(a) (b)

Figure 2.10: Two examples for next-to-leading order contributions in $1/N_c$ to the meson polarizations. Solid lines denote free quark propagators, dashed lines RPA mesons. The pointlike NJL vertices have been replaced by (dotted) interaction lines. Diagram (a) is automatically generated by the Hartree–Fock approximation of Fig. 2.9 while diagram (b) is not automatically generated.

in next-to-leading and higher orders[3] that are needed to cancel the automatically generated contributions and add them explicitly to the second Dyson–Schwinger equation of Fig. 2.9. We will come back to such an approach in Section 2.5. It is interesting to note that some of the missing higher order diagrams (Fig. 2.10(b), see also Fig. 2.14) have the form of vertex corrections. Those contributions would dynamically adjust the interaction in the (RPA) quark loops. The calculation in Appendix B shows that we could recover the Goldstone modes in our Hartree–Fock+RPA by adjusting the interaction in the second Dyson–Schwinger equation of Fig. 2.9 by a factor $(\Sigma^{\mathrm{H}} + \Sigma^{\mathrm{F}})/\,\Sigma^{\mathrm{H}}$ (the correction $\Sigma^{\mathrm{F}}\,/\,\Sigma^{\mathrm{H}}$ is on the order of $1/N_c$).

We have introduced the Hartree–Fock+RPA approximation here since it demonstrates a general problem of $1/N_c$ extensions beyond the Hartree+RPA approximation. Our $\mathcal{O}(1/N_c)$ approach will generate RPA mesons in the same fashion as the Hartree–Fock+RPA approximation. Hence, we will encounter similar problems with the Goldstone boson character of the RPA pions below. The Hartree–Fock+RPA approximation can then be used as an illustrative example that allows simple (analytical) estimates.

Let us clarify our terminology before we continue: Following the literature that discusses $1/N_c$ extensions of the NJL model, see e.g. [DSTL95], we stay with the term "RPA" for the summation of quark loops where propagators beyond the Hartree approximation are used. Hence, we refer to the mesons that are generated by a Dyson–Schwinger equation like the second one in Fig. 2.9 as RPA mesons – even when the correspondence to a regular random phase approximation is lost and the RPA pions do not satisfy the chiral theorems.

[3]The Hartree–Fock propagator contributes in all orders of $1/N_c$ since the $\mathcal{O}(1/N_c)$ Fock diagram is iterated in the first Dyson–Schwinger equation.

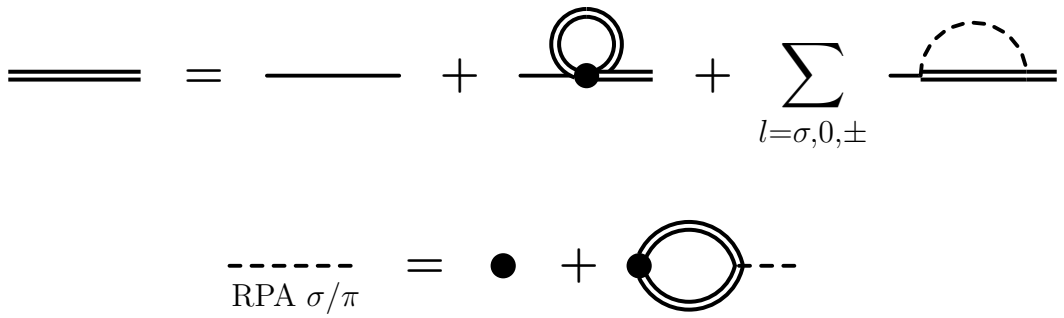

Figure 2.11: The set of Dyson–Schwinger equations corresponding to the fully self-consistent $\mathcal{O}(1/N_c)$ approach. The double lines denote dressed quark propagators. The first line enters the gap equation. The last term on the rhs. generates a feedback of the mesons to the quarks that is not present in the Hartree+RPA approach. The second line describes the RPA like construction of the mesons. Since full propagators with off-shell contributions are used, this goes beyond the standard RPA for quasiparticles.

2.4 The $\mathcal{O}(1/N_c)$ approach

2.4.1 Coupled set of Dyson–Schwinger equations

For our investigation of the short-range correlations in quark matter, we will calculate the quark properties in next-to-leading order[4] $\mathcal{O}(1/N_c)$ in the inverse number of colors. Therefore, the meson exchange diagram shown in Fig. 2.4 is added to the quark self-energy in the first Dyson–Schwinger equation of Fig. 2.6 while the second equation is left unchanged. The new Dyson–Schwinger equations will self-consistently generate all contributions to the self-energy of order $\mathcal{O}(1/N_c)$. As discussed before, this leads to a feedback of the RPA mesons into the quark self-energy. The result is a fully self-consistent model where quark and meson properties depend on each other. Since the meson exchange is a non-local interaction, the quarks will acquire a finite width.

The set of coupled Dyson–Schwinger equations that corresponds to our $\mathcal{O}(1/N_c)$ approach is shown in Fig. 2.11. The self-energy (upper line of Fig. 2.11) that enters the gap equation reads now

$$\Sigma(k) = 2i\mathrm{G}N_f N_c \int \frac{d^4p}{(2\pi)^4}\,\mathrm{tr}\,\mathrm{S}(p) - i\sum_l \int \frac{d^4p}{(2\pi)^4}\Gamma_l\,\mathrm{S}(p)\tilde{\Gamma}_l\,\Delta_l(p-k)\,, \qquad (2.13)$$

where $\mathrm{S}(k)$ denotes the full in-medium quark propagator beyond the Hartree approx-

[4] We have seen in Section 2.2 that the order of diagrams is not well defined in a fully self-consistent approach. Only the leading order of a diagram can be determined. When referring to the order of a diagram in the following, we always refer to the leading order of the diagram. Our approach is of order $\mathcal{O}(1/N_c)$ in the sense that it contains all diagrams of orders $\mathcal{O}(1/N_c)$ and $\mathcal{O}(1)$ for the quark self-energy. Additional diagrams of order $\mathcal{O}(1/N_c^n)$ with $n \geq 2$ are generated iteratively – but not necessarily in a complete way.

imation. The structure of this propagator will be discussed in detail in the next section. $\Delta_l(k)$ is the meson propagator as defined in Eq. (2.10). The RPA polarizationsare calculated using the full quark propagators, as shown in the second line of Fig. 2.11,

$$\frac{1}{i}\,\Pi_l(k) = -\int \frac{d^4p}{(2\pi)^4}\,\mathrm{Tr}\left[\tilde{\Gamma}_l\,\mathrm{S}(p)\Gamma_l\,\mathrm{S}(p-k)\right]\,. \tag{2.14}$$

The quark self-energy has no longer the simple form of an effective mass. Due to the non-local meson exchange, the self-energy becomes complex and four-momentum dependent. In addition, the new diagram in the Dyson–Schwinger equation introduces contributions to the self-energy that have – in contrast to the Hartree self-energy – no Lorentz scalar structure. The quark propagator and the self-energy acquire a more complicated spinor structure. This will be discussed in detail in Sections 2.6 and 2.8. The imaginary part of the self-energy is an effect of the short-range correlations that are now present in the model. It is identified with the collisional width that leads to the broadening of the quark spectral function.

The main drawback of the present approach has already been brought up in Section 2.3.2. Like in the Hartree–Fock+RPA approximation of Fig. 2.9, we do not consider a consistent $1/N_c$ expansion of the meson polarizations here. Hence, the RPA pions will acquire a considerable mass. We will investigate this problem in more detail in Section 2.5. There, we will also discuss methods, i.e. explicit higher order corrections to the meson polarizations, that restore the Goldstone modes of the broken chiral symmetry and thus the correspondence to a (regular) random phase approximation. In our calculations, where we mainly use the RPA mesons to generate all next-to-leading quark self-energy diagrams (we have illustrated the procedure in Fig. 2.4), we will, however, not take such corrections into account.

2.4.2 Regularization scheme

To complete our approach, we have to specify a regularization scheme for the divergent integrals in Eqs. (2.13,2.14). A variety of schemes on different levels of sophistication – from covariant four-momentum cutoffs to the gauge invariant Pauli–Villars scheme – are available for this task. They are discussed in detail, e.g., in [Kle92]. To keep our model numerically simple, we will work with a simple three-momentum cutoff Λ for the time being. Like in [FLM03b] and [DBM93, DM94], we use the cutoff to restrict the three-momentum of each quark in the integrals to values below Λ, i.e., the cutoff is attached to all quark propagators,

$$\mathrm{S}(p) \to \mathrm{S}(p)\Theta(\Lambda - |\vec{p}|)\,.$$

This scheme is sufficient to regularize all integrals in (2.13,2.14). A meson cutoff is implicitly included in this scheme since the quark loop integrals in the polarizations can only yield finite results for three-momenta of the RPA mesons below 2Λ.

As long as the collisional width does not become too large, most of the strength of the quark propagator should remain in the vicinity of the on-shell peaks. Then the three-momentum cutoff serves also as an energy cutoff,

$$|p_0| < E_\Lambda < \sqrt{\Lambda^2 + m^{*2}}\,,$$

where m^* is the effective quark mass. This will not be a sharp cutoff when the peaks have a finite width, but the quark propagators at higher energies will be strongly suppressed in the self-energy and polarization integrals.

Note that the cutoff can also be implemented in other ways. In [DSTL95, NBC$^+$96, OBW00], the restrictions are applied to the integration variables,

$$\int d^4p \to \int d^4p \Theta(\Lambda - |\vec{p}|)\,,$$

after all δ-functions in the integrand have been used to reduce the number of integrals. It is necessary to use two different cutoffs in this case – one for the quark and quark–quark loops and another one for the quark–meson loops in Fig. 2.11. The masses of the quarks and the RPA mesons should not be affected significantly by the two different implementations of the cutoff. They are mainly determined by integrals over single quark propagators (the details will be discussed later) and the cutoff schemes do not differ for such integrals. The quark and meson widths, however, may depend on the way the regularization is implemented.

2.4.3 Further remarks

Of course, an analytic solution of the self-consistency problem presented in Fig. 2.11 and Eqs. (2.13,2.14) is not possible. A solution can only be found in a numerical calculation. Such a calculation is much more involved than the usual Hartree+RPA approach and must be done iteratively. By using full in-medium propagators – including off-shell contributions – we clearly go beyond the standard RPA approach. In contrast to the Hartree+RPA approach where quasiparticle propagators are used, the calculation of the polarizations is part of the self-consistent procedure here. We do not use a pole approximation for the RPA propagators in the calculations. As we will see in the following, the $q\bar{q}$ continuum of the RPA spectral function is an important component of our approach.

At this point, a remark concerning our earlier approach in [FLM03b] is in order. We have not considered dynamically generated mesons there. Instead, the direct and the exchange Born diagrams (cf. Fig. 2.2) were used to construct the collisional quark self-energy. The corresponding Dyson–Schwinger equation is shown in Fig. 2.12. We had restricted ourselves to the chirally restored phase in that approach, hence we did not consider the Hartree and Fock diagrams. In the new approach we use all diagrams of orders $\mathcal{O}(1)$ and $\mathcal{O}(1/N_c)$, not only the direct Born diagram. The exchange Born diagram will be ignored here since it is of order $\mathcal{O}(1/N_c^2)$. In comparison to nuclear

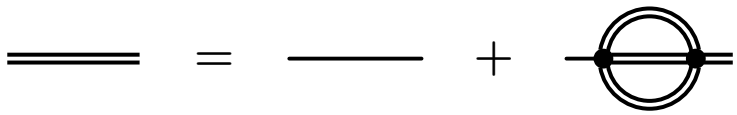

Figure 2.12: The Dyson–Schwinger equation corresponding to the approach to short-range correlations in [FLM03b]. Dynamically generated mesons were not discussed in this approach.

matter we found rather small widths for the quarks in [FLM03b]. By including an infinite number of $\mathcal{O}(1/N_c)$ diagrams in the new approach the importance of collisional broadening will increase significantly.

2.5 $1/N_c$ corrections and chiral symmetry

In the past, there have been several approaches to extend the NJL model beyond the Hartree+RPA approximation [QK94, DSTL95, NBC+96, OBW00]. Chiral symmetry is considered as one of the most important features of the NJL model. Hence, it was the main interest of those works to find next-to-leading order extensions in $1/N_c$ that leave the chiral theorems like the Goldstone theorem, the Goldberger–Treiman relation, and the Gell-Mann–Oakes–Renner relation intact.

To check the chiral theorems on the basis of analytical calculations, the quarks and mesons have been treated only on the quasiparticle level[5] in the considerations of [QK94, DSTL95, NBC+96, OBW00]. Nonetheless, the results are relevant for the present approach – that is technically more involved – and will be reviewed in this section. The study of Dmitrašinović et al. [DSTL95] is of particular interest for us since they have explored the $1/N_c$ expansion on the level of Feynman diagrams, using the counting rules in Eq. (2.6). The basic idea of their approach is to consider the $1/N_c$ extensions as corrections to the Hartree+RPA approximation. The ansatz in [DSTL95] is self-consistent and – like our model – dynamically generates diagrams of arbitrary subleading orders.

Dmitrašinović et al. have shown that the validity of the chiral theorems in a next-to-leading order approximation scheme relies on a delicate balance of the contributions to the meson polarizations (see also [NBC+96]). To ensure that, e.g., the dynamically generated pions become massless in the chiral limit, the polarization diagrams in each order of $1/N_c$ must be chosen such that certain contributions cancel each other. This is a straightforward exercise in leading order: There exists just one diagram, the simple $\mathcal{O}(1)$ quark loop with Hartree propagators. The situation becomes more complicated in higher orders where some of the relevant contributions may be automatically generated while other must be considered explicitly.

[5] For the mesons a pole approximation has been used so that only bound $q\bar{q}$ states were considered but not the $q\bar{q}$ continuum states.

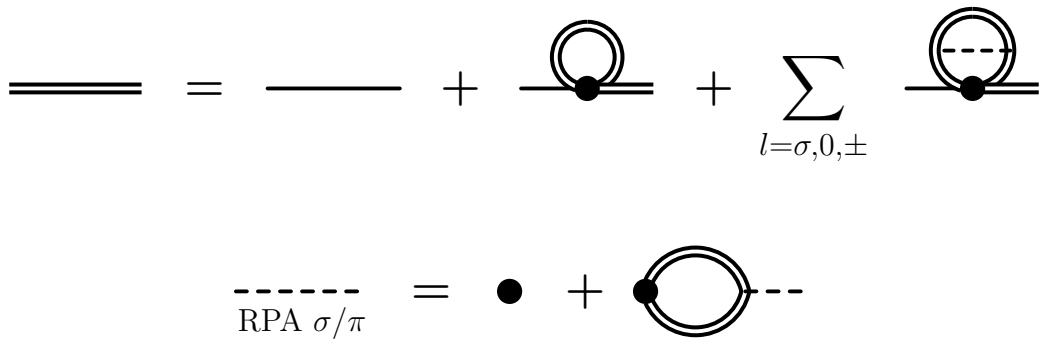

Figure 2.13: The set of coupled Dyson–Schwinger equations that is used by Dmitrašinović et al. [DSTL95] for a self-consistent calculation. One obtains a $1/N_c$ corrected quark propagator and – in comparison to the Hartree+RPA scheme – modified RPA meson propagators.

2.5.1 Chirally invariant $1/N_c$ extensions

The starting point in [DSTL95] are the Dyson–Schwinger equations shown in Fig. 2.13. In comparison to the Hartree+RPA approximation, the equation for the quarks has been extended by an $\mathcal{O}(1/N_c)$ self-energy diagram. This diagram corresponds to a combination of the Hartree diagram and the meson exchange from Fig. 2.4. Since only time-local diagrams[6] are considered, the self-energy remains real and the quarks can be treated as quasiparticles. This is a crucial difference to our approach where the meson exchange diagram of Fig. 2.4 generates (complex) short-range effects.

The two Dyson–Schwinger equations in Fig. 2.13 are coupled by the $\mathcal{O}(1/N_c)$ diagram and must be solved self-consistently. The $1/N_c$ extended quark propagator will not be purely of order $\mathcal{O}(1)$, cf. Section 2.2. When the RPA polarizations are calculated using this propagator, contributions in subleading orders will be automatically generated – in an incomplete way. The cancellation effect described in [DSTL95] remains incomplete beyond leading order and the – in comparison to the Hartree+RPA scheme – modified RPA pions do not satisfy the Goldstone theorem.

To find the physical $1/N_c$ extended mesons, the set (b,c,d) of correctional $\mathcal{O}(1)$ diagrams in Fig. 2.14 must be added to the $\mathcal{O}(N_c)$ RPA polarization (a), see [DSTL95] for details. The self-consistent propagators from the Dyson–Schwinger equations in Fig. 2.13 are used to calculate those diagrams. The propagators of the $1/N_c$ extended mesons are then given by

$$\tilde{\Delta}_l(k) = -\frac{2\mathrm{G}}{1 + 2\mathrm{G}\tilde{\Pi}_l(k)} \,.$$

As shown in [DSTL95], $\tilde{\Delta}_\pi$ is in agreement with the chiral theorems. It is important

[6] In [DSTL95] it is discussed that the meson exchange diagram (cf. Fig. 2.4) is numerically suppressed compared to the modified Hartree diagram in Fig. 2.13. Thus, the four-momentum dependent contribution to the self-energy has been dropped to simplify the calculations there.

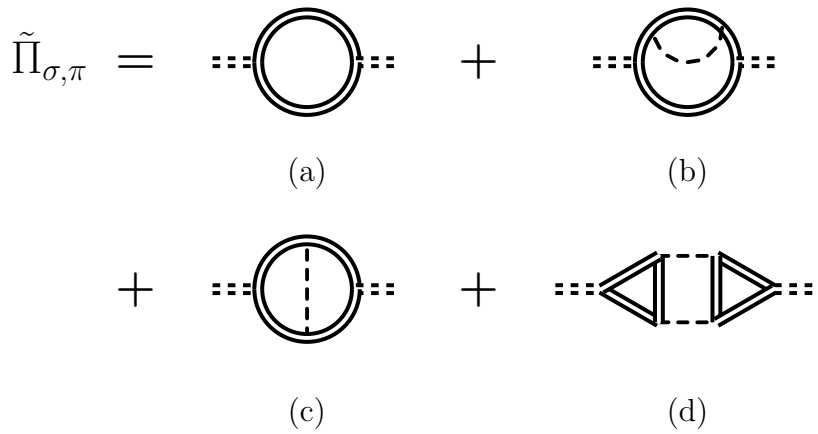

Figure 2.14: The $\mathcal{O}(1)$ extended meson polarizations of [DSTL95]. The three $\mathcal{O}(1)$ diagrams (b,c,d) must be added to the RPA polarization loop (a) to find pions that satisfy the Goldstone theorem in the $1/N_c$ extended model. The diagrams are calculated using the propagators from the Dyson–Schwinger equations in Fig. 2.13. The double dashed lines indicate the $1/N_c$ extended mesons.

to stress that the improved propagators $\tilde{\Delta}_l$ are *not* further modified. It is tempting to reinsert them into the correctional diagrams in a self-consistent procedure, i.e., to replace the single dashed lines in Fig. 2.14 by double dashed lines. This, however, would destroy the chiral properties again. In short: The RPA mesons are calculated self-consistently with the Dyson–Schwinger equations of Fig. 2.13 whereas the physical mesons are determined only afterwards. The properties of the $1/N_c$ extended quarks are determined by the Dyson–Schwinger equations where only the RPA mesons enter, but not the physical mesons. Thus, this scheme is not fully self-consistent – concerning the physical mesons – but it respects the chiral properties.

We will not discuss the chirally invariant $1/N_c$ extensions found in [NBC+96, OBW00, vHK02] in more detail here. We note, however, that similar restrictions apply for them. In all of those schemes it is necessary to perform $1/N_c$ corrections that are not fed back into a self-consistent calculation.

2.5.2 Consequences for the $\mathcal{O}(1/N_c)$ approach

Let us compare the approach of Dmitrašinović et al. to our model. The main difference between our Dyson–Schwinger equations in Fig. 2.11 and those in Fig. 2.13 is that we include the meson exchange diagram from Fig. 2.4 explicitly. The $\mathcal{O}(1/N_c)$ diagram in the Dyson–Schwinger equation for the quarks in Fig. 2.13 is present in our approach, too. It is dynamically generated by the Hartree diagram and the meson exchange diagram. Our Dyson–Schwinger equations also generate the first $\mathcal{O}(1)$ correctional diagram (b) to the polarization in Fig. 2.14. The two vertex corrections (c) and (d) in the second line of Fig. 2.14, however, are not generated. From the discussion in

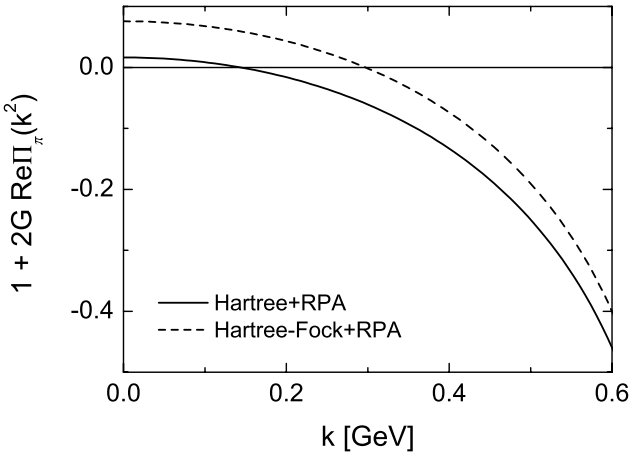

Figure 2.15: The real part of the denominator of the RPA pion propagator in the Hartree+RPA and Hartree–Fock+RPA approximations using parameter set I from Table 2.1 ($m_0 = 5.5\,\mathrm{MeV}$, three-momentum cutoff Λ). The poles of the propagator – and thus the RPA pion mass – are determined by the zeros of this expression. In the vicinity of the zeros the function is rather flat – small fluctuations can thus have significant influence on the mass.

[DSTL95] it is immediately suggestive that the extended RPA pions of our approach will not satisfy the Goldstone theorem.

It is possible to estimate the mass of the RPA pions in our model roughly. Fig. 2.15 shows the real part of the denominator of the RPA pion propagator, $1 + 2G\mathrm{Re}\,\Pi_\pi$, in the Hartree+RPA and Hartree–Fock+RPA approximations. The zeros of this expression determine the poles of the propagator. We see that even small fluctuations in higher orders of $1/N_c$ (that shift the Hartree+RPA curve) can have a significant influence on the mass of the RPA pions. This effect shows up already in the Hartree–Fock+RPA approximation scheme, where the $\mathcal{O}(1/N_c)$ Fock diagram from Fig. 2.2(b) is added to the Dyson–Schwinger equation of Fig. 2.6 – see Appendix B and [Kle92] for details. The shift of 0.08 – as estimated using Eq. (B.8) – raises the RPA pion mass by $\approx 150\,\mathrm{MeV}$. We will come back to this estimate in Section 3.7.

In principle, we can follow the approach of [DSTL95] to fix the chiral properties of our model in next-to-leading order: The Dyson–Schwinger equations that are solved self-consistently as a first step yield (massive) RPA pions. To find the physical pions that satisfy the Goldstone theorem, we have to calculate the vertex corrections (c,d) from Fig. 2.14. For this task, the quark and RPA meson propagators that were determined from the Dyson–Schwinger equations in Fig. 2.11 have to be used.

This simple approach has a drawback: Since the physical mesons are not fed back into the Dyson–Schwinger equations, the quark spectral function will not be affected by the corrections to the pions. The short-range correlations in our model are generated by a meson exchange diagram, cf. Fig. 2.4, where the (intermediate) RPA pions

– that might acquire a considerable mass – and not the physical pions enter. This leaves us with two choices. Either, we find a more involved approach that feeds back the Goldstone modes into the quark self-energies, or we stick to the RPA mesons in the self-consistent calculations. In the latter case, we have to check that the influence of the RPA pion mass on the quark properties does not become too large.

A fully self-consistent approach that yields massless pions has so far not been proposed for the NJL model. (In [Leu07], such a scheme has been proposed which, however, does not work in the vicinity of the chiral phase transition.) Adding the vertex corrections (c,d) from Fig. 2.14 to the Dyson–Schwinger equation for the mesons in Fig. 2.11 should improve – but not fix – the chiral properties of the pions and generate a feedback on the quarks. Such an approach would increase the numerical efforts significantly by involving two- and three-loop diagrams that must be calculated in every iteration. Since the numerical calculations are already rather involved, we do not pursue this strategy any further at the present stage. It indicates, however, how our model can be improved in the future.

This brings us back to the second option, i.e., working with the massive RPA pions in the self-consistent approach as shown in Fig. 2.11. Recall that it is our main interest to determine the extent of short-range correlations in quark matter. We want to investigate the collisional broadening of the quark spectral function and possible changes to the chiral phase transition. We are not primarily interested in the properties of the dynamically generated mesons. As discussed in Section 2.2, we rather use the RPA mesons as a tool to generate the next-to-leading order quark–quark interactions beyond the Hartree level. In other words: we are not too concerned about the chiral properties of the pions as long as the influence on the quark properties remains limited.

The influence of the RPA pion mass on the quark width will be investigated in Chapter 4. We will find there that the off-shell states of the RPA meson propagators – that were not considered in the above discussion but are part of our full calculation – are much more important for the width of the occupied quark states than the bound $q\bar{q}$ states. The $q\bar{q}$ continuum in the timelike region is neither in its thresholds nor in its magnitude affected by the cancellation problems and largely independent of the pion mass, see Figs. 4.4 and 5.8 (concerning the $q\bar{q}$ continuum of the meson propagators, the vertex corrections are only next-to-next-to-leading order corrections of the quark self-energy). The off-shell states in the spacelike region are more sensitive to the RPA pion mass. A higher pion mass will lower the magnitude of the contributions from this region to the quark width. Below the chiral phase transition, our approach without the vertex corrections will thus yield a conservative estimate of the short-range effects. (Above the phase transition, we obtain a pion mass comparable to the Hartree+RPA approximation.)

At the end of this section we note that all corrections that have been considered so far will only restore the chiral theorems in next-to-leading order. Due to the self-consistent nature of our approach we generate diagrams of arbitrary order in a – for the subleading orders – inconsistent way. To satisfy, e.g., the Goldstone theorem in

any higher order it will be necessary to identify the correctional diagrams of that order. This might be possible by using Bethe-Salpeter equations that generate vertex corrections in all orders [vHK02]. The approach introduced by van Hess and Knoll, however, can only be used to correct the meson properties in higher orders after the self-consistent calculation. Hence, it is not suitable to improve the properties of the quarks in our approach and we will not consider it any further.

2.6 Quark fields and propagators

In the previous sections, we have introduced the Dyson–Schwinger equations that define our approach. Before we can actually solve these equations, we have to determine the structure of the propagators, self-energies and polarizations in Fig. 2.11. This will be done in the remaining sections of this chapter.

Let us begin by pointing out that (ground state) perturbation theory as it is found in field theory textbooks (see, e.g., [PS95]) does not work in systems with a finite chemical potential or temperature and systems that are not in thermodynamical equilibrium. The reason for this failure is readily identified: In standard perturbation theory one assumes that the interaction is switched on and off asymptotically so that the system is in the ground state of the free theory $|0\rangle$ for $t \to -\infty$. The ground state of the interacting theory $|\Omega\rangle$ (at $t = 0$) is then related to $|0\rangle$ by the Gell-Mann–Low theorem, $|\Omega\rangle = U(0, -\infty)|0\rangle$, where U is the time evolution operator. Furthermore, the state $U(+\infty, -\infty)|0\rangle$ should be equal to the state $|0\rangle$ up to a phase factor. In the time evolution of many-body systems, however, no state of the future may be identified with a state of the past [Dan84]. This should be clear, in particular, for systems in non-equilibrium. Consequently, the Gell-Mann–Low theorem does not hold and Wick's theorem [PS95] cannot be used to obtain the usual Feynman rules.

To avoid the "problems" with time evolution in a many-body system, it is necessary to modify the Green's function formalism. This has been done, e.g., by Schwinger [Sch61] and Keldysh [Kel64]. They have introduced the closed time-path that is shown in Fig. 2.16. The contour C starts at an early time t_0 (that can be set to $-\infty$) and runs along its chronological branch C_1 to the time t – that must be equal to the largest time that occurs in the calculation – before it returns along its anti-chronological branch C_2 to t_0. The time arguments of operators are then placed on this contour and the regular time ordering of operators along the real time axis is replaced by a path ordering along the contour. In this formalism, the application of Wick's theorem becomes possible again [Dan84] and Feynman rules can be found that are similar to the rules of standard perturbation theory. The main difference is that all time integrals are replaced by integrals along the contour C.

Throughout the present work, we will use this so-called real-time formalism[7] (or

[7] The name real-time formalism emphasizes the most obvious difference to the alternative Green's function formalism that has been introduced by Matsubara [Mat55]. This formalism for systems in thermodynamical equilibrium, that was further developed by Martin and Schwinger [MS59],

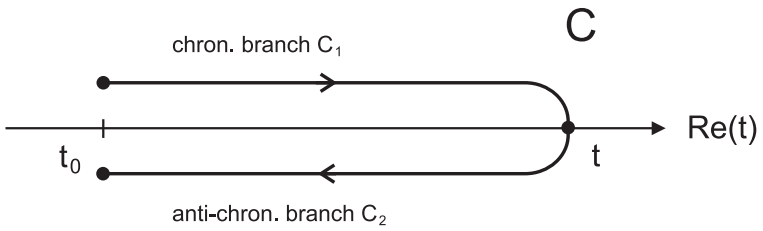

Figure 2.16: The time-path of the real-time formalism [Dan84, BM90, Das97] in the complex plane. Corresponding to their direction in time, the upper and the lower branch are called chronological and anti-chronological branch, respectively. Points on the chronological branch are considered to be earlier than points on the anti-chronological branch of C.

Schwinger–Keldysh formalism) for our calculations. The Feynman rules – in a form that is most suitable for the present approach – can be found in Appendix C. We will not discuss the technical details of the real-time formalism in more detail here. Didactical introductions can be found in [Dan84, BM90, Das97]. Helpful discussions on in-medium Green's functions are also available in [KB62, PLM04] and the transport theoretical approaches to quark matter in [MH94, ZW92, Reh98].

2.6.1 Green's functions on a closed time-path

The fundamental elements of our model are the single-particle Green's functions on the closed time-path contour C that is shown in Fig. 2.16. The path-ordered Green's function is defined as

$$\mathrm{S}^{\mathrm{P}}_{\alpha\beta}(1,2) = -i\left\langle \mathrm{P}[\psi_\alpha(1)\bar{\psi}_\beta(2)]\right\rangle \,, \tag{2.15}$$

where α and β denote the spinor indices of the quark fields. The color and flavor indices have been suppressed here. In symmetric quark matter, the propagator is proportional to unit matrices in flavor and color space. P denotes the path-ordering operator along the contour C,

$$\mathrm{P}[A(1)B(2)] = \Theta_C(t_1,t_2)A(1)B(2) \mp \Theta_C(t_2,t_1)B(2)A(1)\,,$$

where the upper (lower) sign refers to quark (meson) operators and Θ_C is the generalized step function on the time-path,

$$\Theta_C(t_1,t_2) = \begin{cases} 1 & \text{if } t_1 \text{ is later on } C \text{ than } t_2, \\ 0 & \text{if } t_1 \text{ is earlier on } C \text{ than } t_2. \end{cases} \tag{2.16}$$

If both points are on the same branch, P corresponds to the regular time-ordering operator T on the chronological and to the anti-time-ordering operator $\bar{\mathrm{T}}$ on the

allows only imaginary times within a finite interval (see, e.g.,[Das97] for details).

anti-chronological branch,

$$\begin{aligned}\mathrm{T}[A(1)B(2)] &= \Theta(t_1-t_2)A(1)B(2) \mp \Theta(t_2-t_1)B(2)A(1)\,,\\ \bar{\mathrm{T}}[A(1)B(2)] &= \Theta(t_2-t_1)A(1)B(2) \mp \Theta(t_1-t_2)B(2)A(1)\,.\end{aligned}$$

Consequently, $\mathrm{S}^{\mathrm{P}}(1,2)$ reduces to the – time-ordered – causal (Feynman), the anti-causal, or one of the non-ordered Green's functions (or propagators) depending on the positions of t_1 and t_2 on the two branches,

$$\begin{aligned}\mathrm{S}^{\mathrm{c}}_{\alpha\beta}(1,2) &= -i\left\langle \mathrm{T}[\psi_\alpha(1)\bar{\psi}_\beta(2)]\right\rangle && \text{for } t_1,t_2\in C_1\,,\\ \mathrm{S}^{\mathrm{a}}_{\alpha\beta}(1,2) &= -i\left\langle \bar{\mathrm{T}}[\psi_\alpha(1)\bar{\psi}_\beta(2)]\right\rangle && \text{for } t_1,t_2\in C_2\,,\\ \mathrm{S}^{>}_{\alpha\beta}(1,2) &= -i\left\langle \psi_\alpha(1)\bar{\psi}_\beta(2)\right\rangle && \text{for } t_1\in C_2, t_2\in C_1\,,\\ \mathrm{S}^{<}_{\alpha\beta}(1,2) &= i\left\langle \bar{\psi}_\beta(2)\psi_\alpha(1)\right\rangle && \text{for } t_1\in C_1, t_2\in C_2\,.\end{aligned} \tag{2.17}$$

In our approach, it will be more convenient to work with the retarded and advanced propagators $\mathrm{S}^{\mathrm{ret,av}}$ instead of the (anti-)time-ordered $\mathrm{S}^{\mathrm{c,a}}$. The reasons will become clear in the following. $\mathrm{S}^{\mathrm{ret,av}}$ are, e.g., closely related to the spectral function and are easier to handle at finite densities. $\mathrm{S}^{\mathrm{c,a}}$ and $\mathrm{S}^{\mathrm{ret,av}}$ are related to each other via the non-ordered propagators $\mathrm{S}^{\gtrless}$,

$$\begin{aligned}\mathrm{S}^{\mathrm{ret}}(1,2) &= \Theta(t_1-t_2)[\mathrm{S}^{>}(1,2)-\mathrm{S}^{<}(1,2)] = \mathrm{S}^{\mathrm{c}}(1,2)-\mathrm{S}^{<}(1,2)\,,\\ \mathrm{S}^{\mathrm{av}}(1,2) &= \Theta(t_2-t_1)[\mathrm{S}^{<}(1,2)-\mathrm{S}^{>}(1,2)] = \mathrm{S}^{\mathrm{c}}(1,2)-\mathrm{S}^{>}(1,2)\,.\end{aligned} \tag{2.18}$$

Note that $\mathrm{S}^{\mathrm{ret}}$ and S^{av} are complex conjugates of each other,

$$\mathrm{S}^{\mathrm{ret}}(1,2)^* = \mathrm{S}^{\mathrm{av}}(1,2)\,. \tag{2.19}$$

For our calculations it will be advantageous to work in momentum space. The propagators in coordinate space can be transformed to momentum space by means of a Wigner transformation

$$\bar{F}(X,k) = \int d^4u e^{iku} F(X+u/2, X-u/2)\,. \tag{2.20}$$

Formally, the transformed two-point functions depend on the four-momentum k and the space-time coordinate X. In this work we will consider only infinite systems in thermal equilibrium. Our results will be independent of the position in the medium. Hence, we can drop the X dependence of the functions in the following.

2.6.2 Lorentz structure

The relativistic, fermionic propagators have a matrix structure in spinor space. The most general form of this Lorentz structure is found by writing down the Green's

functions in terms of the 16 linearly independent products of the Dirac γ matrices (Clifford algebra),

$$\begin{array}{llll} \mathbb{1}_{4\times4} & \text{(scalar)}, & \gamma^5 & \text{(pseudoscalar)}, \\ \gamma^\mu & \text{(vector)}, & \gamma^\mu\gamma^5 & \text{(axial vector)}, \\ \sigma^{\mu\nu} & \text{(tensor)}, & & \end{array}$$

where $\sigma^{\mu\nu} = \frac{i}{2}[\gamma^\mu, \gamma^\nu]$. To obtain a Lorentz invariant propagator, γ^μ, $\gamma^\mu\gamma^5$, and $\sigma^{\mu\nu}$ have to be contracted with four-vectors. This can be either k^μ, the four-momentum of the considered state, or n^μ, the four-momentum of the medium. In the rest frame of the medium ($n_\mu = (n_0, 0)$) we find

$$\begin{aligned} \mathrm{S}(k) = {} & \mathrm{S}_s(k)\cdot\mathbb{1}_{4\times4} + \mathrm{S}_p(k)\cdot\gamma^5 \\ & + \mathrm{S}_k(k)\cdot k_\mu\gamma^\mu + \mathrm{S}_n(k)\cdot n_0\gamma^0 \\ & + \mathrm{S}_a^k(k)\cdot k_\mu\gamma^\mu\gamma^5 + \mathrm{S}_a^n(k)\cdot n_0\gamma^0\gamma^5 \\ & + \mathrm{S}_t(k)\cdot n_0 k_i\sigma^{0i} + \mathrm{S}_\epsilon(k)\cdot n^0 k^i\epsilon_{0ijk}\sigma^{jk}\,, \end{aligned} \tag{2.21}$$

where we have used $\sigma^{\mu\mu} = 0$ and $k_\mu k_\nu\sigma^{\mu\nu} = 0$. Since we consider only flavor symmetric quark matter in this work, $\mathrm{S}_s \cdots \mathrm{S}_\epsilon$ are scalar functions that do not have a structure in flavor space.

Note that $\mathrm{S}_s \cdots \mathrm{S}_\epsilon$ do not depend on the four components of k independently but are functions of k_0 and $|\vec{k}\,|$ in the present case: Lorentz invariance demands that the functions depend only on the Lorentz scalars k^2 and $k_\mu n^\mu = k_0 n_0$ (rest frame of the medium). In other words, $\mathrm{S}_s \cdots \mathrm{S}_\epsilon$ depend separately on $k^2 = k_0^2 - \vec{k}$ and k_0 – this can be reexpressed by a dependence on k_0 and $|\vec{k}\,|$. It is not too surprising that the functions are invariant under rotations when the medium is at rest.

Symmetry arguments help us to simplify the Lorentz structure in (2.21) since they rule out many of the possible terms. This has been studied in very much detail in Section 4.3 and Appendix B of [Frö01]: Our approach should be invariant under parity and time-reversal transformations since we consider an infinite medium in equilibrium and the strong interaction which obeys these symmetries. The symmetry transformations are given explicitly by [PS95]

$$\begin{array}{ll} P\psi(x_0,\vec{x}\,)P = \eta\gamma^0\psi(x_0,-\vec{x}\,) & \qquad\qquad T\psi(x_0,\vec{x}\,)T = (-\gamma^1\gamma^3)\psi(-x_0,\vec{x}\,) \\ P\bar{\psi}(x_0,\vec{x}\,)P = \eta^*\psi(x_0,-\vec{x}\,)\gamma^0 & \text{and} \qquad T\bar{\psi}(x_0,\vec{x}\,)T = \psi(-x_0,\vec{x}\,)(\gamma^1\gamma^3)\,, \end{array}$$

where P and T are the parity and time-reversal operators, respectively (η is a possible phase with $\eta^2 = \pm1$, $\eta\eta^* = 1$). For the transformation of the fermion propagators ($\sim \psi\bar{\psi}$, cf. (2.15)) in momentum space, we obtain the following relations [Frö01]

$$\begin{aligned} P\,\mathrm{S}(k_0,\vec{k}\,)P &= \gamma^0\,\mathrm{S}(k_0,-\vec{k}\,)\gamma^0\,, \\ T\,\mathrm{S}(k_0,\vec{k}\,)T &= (-\gamma^1\gamma^3)\,\mathrm{S}(k_0,-\vec{k}\,)(\gamma^1\gamma^3)\,. \end{aligned} \tag{2.22}$$

The pseudoscalar, axial vector, and ϵ-tensor terms in (2.21) are not invariant under the parity transformation, the tensor term is not invariant under the time reversal transformation of (2.22). Hence, the Lorentz structure of the propagators reduces to three independent components [Frö01, BD65] in the rest frame of a strongly interacting medium in thermodynamical equilibrium:

$$\mathrm{S}(k) = \mathrm{S}_s(k)\,\mathbb{1}_{4\times4} + \mathrm{S}_0(k)\,\gamma_0 - \mathrm{S}_v(k)\,\vec{e}_k\cdot\vec{\gamma} = \mathrm{S}_s(k) + \mathrm{S}_\mu(k)\,\gamma^\mu\,, \tag{2.23}$$

with $\vec{e}_k = \vec{k}/|\vec{k}\,|$ and $\mathrm{S}^i(k) = \mathrm{S}_v(k)e^i_k$. Note that S_k and S_n of (2.21) have been recombined to $\mathrm{S}_0 = \mathrm{S}_k\,k_0 + \mathrm{S}_n\,n_0$ and $\mathrm{S}_v = \mathrm{S}_k\,|\vec{k}\,|$. The sign convention in (2.23) differs from [FLM03b] where S_v had the opposite sign.

The three functions S_s, S_0, and S_v can always be extracted from the full propagators $\mathrm{S}_{\alpha\beta}$ using

$$\mathrm{S}_s(k) = \frac{\mathrm{tr}\,\mathrm{S}(k)}{4}\,,\quad \mathrm{S}_0(k) = \frac{\mathrm{tr}[\gamma_0\,\mathrm{S}(k)]}{4}\,,\quad \mathrm{S}_v(k) = \frac{\mathrm{tr}[\vec{e}_k\cdot\vec{\gamma}\,\mathrm{S}(k)]}{4}\,. \tag{2.24}$$

Recall our convention from Section 2.3.1. "tr" denotes a trace in spinor space only while the symbol "Tr" is used for a full trace in color, flavor, and spinor space.

2.6.3 Quark spectral function

The spectral function $\mathcal{A}(k)$ corresponds to the density of states at a given energy k_0 and momentum $\vec{k}$. As the definitions in (2.17) show, the non-ordered propagators $i\,\mathrm{S}^>(1,1)$ and $-i\,\mathrm{S}^<(1,1)$ are related to the density of the free and the populated states in the medium, respectively [Dan84]:

$$\begin{aligned} i\,\mathrm{Tr}\,\gamma_0\,\mathrm{S}^>(1,1) &= \left\langle \psi_\alpha(1)\psi^\dagger_\alpha(1)\right\rangle\,,\\ -i\,\mathrm{Tr}\,\gamma_0\,\mathrm{S}^<(1,1) &= \left\langle \psi^\dagger_\alpha(1)\psi_\alpha(1)\right\rangle\,. \end{aligned} \tag{2.25}$$

Thus, we can introduce the spectral function in terms of these propagators,

$$\mathcal{A}(k) = i\,[\mathrm{S}^>(k) - \mathrm{S}^<(k)] = -2\mathrm{Im}\,\mathrm{S}^{\mathrm{ret}}(k)\,. \tag{2.26}$$

Using the hermitian conjugate $\gamma_0 F^\dagger \gamma_0$, we define real and imaginary part here as [FLM03b, BD65]

$$\mathrm{Re}F = \frac{1}{2}(F + \gamma_0 F^\dagger\gamma_0) \qquad \text{and} \qquad \mathrm{Im}F = \frac{1}{2i}(F - \gamma_0 F^\dagger\gamma_0)\,,$$

respectively. This definition makes sure that

$$\mathrm{Im}\,\mathrm{S} = (\mathrm{Im}\,\mathrm{S}_s)\,\mathbb{1}_{4\times4} + (\mathrm{Im}\,\mathrm{S}_\mu)\,\gamma^\mu\,,$$

i.e. $\gamma_\mu = \mathrm{Re}\gamma_\mu$ in this formalism – see Appendix A. For Lorentz scalar functions there is no difference to the normal definition.

The spectral function inherits the Lorentz structure of the Green's functions,

$$\mathcal{A}(k) = \mathcal{A}_s(k)\mathbb{1}_{4\times4} + \mathcal{A}_0(k)\gamma_0 - \mathcal{A}_v(k)\vec{e}_k\cdot\vec{\gamma} = \mathcal{A}_s(k) + \mathcal{A}_\mu(k)\gamma^\mu\,. \tag{2.27}$$

The Lorentz components of $\mathcal{A}$ are purely real scalar functions. They are "normalized" as shown in Appendix D,

$$\int_{-\infty}^{+\infty}\frac{dp_0}{2\pi}\mathcal{A}_0(p) = 1\,,\quad \int_{-\infty}^{+\infty}\frac{dp_0}{2\pi}\mathcal{A}_s(p) = 0\,,\quad \int_{-\infty}^{+\infty}\frac{dp_0}{2\pi}\mathcal{A}_v(p) = 0\,. \tag{2.28}$$

The fermionic phase space distribution function $\mathrm{n_F}(k)$ determines the probability that a state with four-momentum k is populated. In thermodynamical equilibrium, $\mathrm{n_F}(k)$ depends only on k_0 and not on k_i. It is given by

$$\mathrm{n_F}(k_0) = \frac{1}{e^{(k_0-\mu)/T}+1} \quad\xrightarrow{T=0}\quad \Theta(\mu-k_0)\,. \tag{2.29}$$

At zero temperature, all states below the chemical potential μ are occupied while all states with energies above μ are free. The distribution function can be used to express the propagators $\mathrm{S}^{\gtrless}(k)$ in terms of the spectral function [KB62],

$$\mathrm{S}^{>}(k) = -i\mathcal{A}(k)[1-\mathrm{n_F}(k_0)]\,, \tag{2.30}$$

$$\mathrm{S}^{<}(k) = i\mathcal{A}(k)\mathrm{n_F}(k_0)\,. \tag{2.31}$$

In other words, the density of the occupied states is given by the density of all states multiplied with the occupation probability while the density of the free states is given by multiplying with the probability that the states are not populated.

A few helpful relations between the different kinds of propagators and the spectral function exist. They can be derived from Eqs. (2.18,2.19) and Eqs. (2.26,2.30,2.31). We list them here for further reference:

$$\begin{aligned}
\mathrm{S^c}(k) &= \mathrm{S^{ret}}(k) + \mathrm{S}^{<}(k) = \mathrm{S^{ret}}(k) + i\mathcal{A}(k)\mathrm{n_F}(k_0)\,,\\
&= \mathrm{S^{av}}(k) + \mathrm{S}^{>}(k) = \mathrm{S^{av}}(k) - i\mathcal{A}(k)[1-\mathrm{n_F}(k_0)]\,,\\
\mathrm{S}^{<}(k) &= [\mathrm{S^{av}}(k) - \mathrm{S^{ret}}(k)]\mathrm{n_F}(k_0)\,,\\
\mathrm{Re\,S^{ret,av}}(k) &= \frac{1}{2}[\mathrm{S^{ret}}(k) + \mathrm{S^{av}}(k)]\,,\\
\mathrm{Im\,S^{ret,av}}(k) &= \mp\frac{i}{2}([\mathrm{S^{ret}}(k) - \mathrm{S^{av}}(k)]\,.
\end{aligned} \tag{2.32}$$

2.6.4 Real and imaginary parts of the propagators

For a system in thermodynamical equilibrium, the retarded and advanced propagators in momentum space are given by

$$\mathrm{S^{ret,av}}(k) = \frac{1}{\not{k} - m_0 - \Sigma^{\mathrm{ret,av}}(k)}\,, \tag{2.33}$$

where $\Sigma^{\mathrm{ret,av}}(k) = \Sigma_s^{\mathrm{ret,av}}(k) + \Sigma_\mu^{\mathrm{ret,av}}(k)\gamma^\mu$ are the retarded and the advanced self-energy, respectively. They have the same Lorentz structure as the propagators, cf. (2.23). The form of the propagators in (2.33) resembles that of the time-ordered propagators $\mathrm{S}^{\mathrm{c,a}}$ in vacuum. In contrast to the time-ordered propagators, however, $\mathrm{S}^{\mathrm{ret,av}}$ keep the simple form in the presence of a medium while the (anti-)time-ordered propagators gain extra terms [Das97]. Consequently, the retarded and advanced propagators and the spectral function are much easier to handle in calculations at finite μ.

Introducing the – four-momentum dependent and complex – effective masses $\tilde{m}^{\mathrm{ret,av}}$ and the effective four-momenta $\tilde{k}^{\mathrm{ret,av}}$,

$$\begin{aligned} \tilde{k}_\mu^{\mathrm{ret,av}} &= k_\mu - \Sigma_\mu^{\mathrm{ret,av}}(k)\,, \\ \tilde{m}^{\mathrm{ret,av}}(k) &= m_0 + \Sigma_s^{\mathrm{ret,av}}(k)\,, \end{aligned} \tag{2.34}$$

Eq. (2.33) becomes

$$\mathrm{S}^{\mathrm{ret,av}}(k) = \frac{1}{\tilde{\not{k}}^{\mathrm{ret,av}} - \tilde{m}^{\mathrm{ret,av}}(k)} = \frac{\tilde{\not{k}}^{\mathrm{ret,av}} + \tilde{m}^{\mathrm{ret,av}}(k)}{\tilde{k}^2_{\mathrm{ret,av}} - \tilde{m}^2_{\mathrm{ret,av}}(k)}\,. \tag{2.35}$$

For our calculations it will be necessary to disentangle the real and the imaginary parts of the propagators, e.g., to determine the spectral function. Both, the numerator and the denominator on the rhs. of Eq. (2.35) are complex since the self-energies $\Sigma^{\mathrm{ret,av}}(k)$ are complex quantities. The real and the imaginary part of the denominator can be identified with

$$\mathcal{P}(k) = \mathrm{Re}\tilde{k}^2 - \mathrm{Re}\tilde{m}(k)^2 - \left[\mathrm{Im}\,\Sigma_\mu^{\mathrm{ret}}(k)\mathrm{Im}\,\Sigma_{\mathrm{ret}}^{\mu}(k) - \mathrm{Im}\,\Sigma_s^{\mathrm{ret}}(k)^2\right]\,, \tag{2.36}$$

$$\mathcal{W}(k) = -2\left[\mathrm{Re}\tilde{k}_\mu\mathrm{Im}\,\Sigma_{\mathrm{ret}}^{\mu}(k) + \mathrm{Re}\tilde{m}(k)\mathrm{Im}\,\Sigma_s^{\mathrm{ret}}(k)\right] \tag{2.37}$$

for the retarded propagator and

$$\mathcal{P}^{\mathrm{av}}(k) = \mathcal{P}(k)\,, \quad \mathcal{W}^{\mathrm{av}}(k) = -\,\mathcal{W}(k)$$

for the advanced propagator. We have used $\Sigma^*_{\mathrm{ret}}(k) = \Sigma^{\mathrm{av}}(k)$ here. Note that $\mathrm{Re}\tilde{m} = \mathrm{Re}\tilde{m}^{\mathrm{ret,av}}$ and $\mathrm{Re}\tilde{k} = \mathrm{Re}\tilde{k}^{\mathrm{ret,av}}$. The expansion with the complex conjugates of the denominators yields [Hen92]

$$\mathrm{S}^{\mathrm{ret,av}}(k) = \frac{\left(\tilde{\not{k}}^{\mathrm{ret,av}} + \tilde{m}^{\mathrm{ret,av}}(k)\right)\left(\mathcal{P}(k) \mp i\,\mathcal{W}(k)\right)}{\mathcal{P}^2(k) + \mathcal{W}^2(k)}\,. \tag{2.38}$$

The upper sign in the numerator refers to the retarded and the lower sign to the advanced propagator, respectively. In both cases the same functions $\mathcal{P}$ and $\mathcal{W}$ – defined in terms of retarded self-energies – are used.

The zeros of the function $\mathcal{P}(k)$ determine the position of the poles of the propagator. $\mathcal{W}(k)$ – originating from the imaginary part of the denominator – generates

the collisional and decay width of the propagators. In the following, we refer to the broadened poles as on-shell peaks. The on-shell energy $k_0^{\rm os}(\vec{k}\,)$ and the on-shell momentum $\vec{k}_{\rm os}(k_0)$ are found by solving one of the equations

$$\mathcal{P}\left(k_0^{\rm os}(\vec{k}\,),\vec{k}\right)=0\,,\quad \mathcal{P}\left(k_0,\vec{k}_{\rm os}(k_0)\right)=0\,. \tag{2.39}$$

It should be noted that $\mathcal{P}$ and $\mathcal{W}$ both depend on the full complex self-energy and not only the real or imaginary part. As we will see later, the imaginary part does not become too large in the on-shell region. Hence, the influence of the quadratic $\mathrm{Im}\,\Sigma^{\rm ret}$ terms in (2.36) will be limited. In a quasiparticle model like the Hartree+RPA approach one has $\mathrm{Im}\,\Sigma^{\rm ret}=0$ and $\mathrm{Re}\,\Sigma^{\rm ret}=\Sigma^{\rm mf}$. Thus $\mathcal{W}_{\rm qp}$ is zero and $\mathcal{P}$ reduces to $\mathcal{P}_{\rm qp}(k)=k^2-(m_0+\Sigma^{\rm mf})^2=k^2-m^{*2}$, where m^* is a real valued, momentum independent effective mass.

The real and the imaginary part of the propagators can be easily extracted from Eq. (2.38),

$$\begin{aligned}
\mathrm{Re}\,\mathrm{S}^{\rm ret,av}(k)&=\frac{\mathrm{Re}\tilde{m}\,\mathcal{P}+\mathrm{Im}\,\Sigma_s^{\rm ret}\,\mathcal{W}}{\mathcal{P}^2+\mathcal{W}^2}+\frac{\mathrm{Re}\tilde{k}_\mu\,\mathcal{P}-\mathrm{Im}\,\Sigma_\mu^{\rm ret}\,\mathcal{W}}{\mathcal{P}^2+\mathcal{W}^2}\gamma^\mu\,,\\
\mathrm{Im}\,\mathrm{S}^{\rm ret,av}(k)&=\pm\frac{\mathrm{Im}\,\Sigma_s^{\rm ret}\,\mathcal{P}-\mathrm{Re}\tilde{m}\,\mathcal{W}}{\mathcal{P}^2+\mathcal{W}^2}\mp\frac{\mathrm{Im}\,\Sigma_\mu^{\rm ret}\,\mathcal{P}+\mathrm{Re}\tilde{k}_\mu\,\mathcal{W}}{\mathcal{P}^2+\mathcal{W}^2}\gamma^\mu\,,
\end{aligned}$$

where we have used $\Sigma^*_{\rm ret}(k)=\Sigma^{\rm av}(k)$ again. The Lorentz components of the quark spectral function $\mathcal{A}=-2\mathrm{Im}\,\mathrm{S}^{\rm ret}$ are identified as

$$\begin{aligned}
\mathcal{A}_s(k)&=2\frac{\mathrm{Re}\tilde{m}\,\mathcal{W}-\mathrm{Im}\,\Sigma_s^{\rm ret}\,\mathcal{P}}{\mathcal{P}^2+\mathcal{W}^2}\,,\\
\mathcal{A}_\mu(k)&=2\frac{\mathrm{Re}\tilde{k}_\mu\,\mathcal{W}+\mathrm{Im}\,\Sigma_\mu^{\rm ret}\,\mathcal{P}}{\mathcal{P}^2+\mathcal{W}^2}\,.
\end{aligned} \tag{2.40}$$

In the absence of a finite current quark mass m_0, the Lorentz scalar component S_s – and thus also $\Sigma_s^{\rm ret}$ – vanishes when chiral symmetry is restored. The Lorentz structure is then simplified even further[8]. Using $m_0=\Sigma^{\rm mf}=\Sigma_s^{\rm ret}(k)=\tilde{m}^{\rm ret}(k)=0$ – yields

$$\begin{aligned}
\mathcal{A}_s^c(k)&=0\,,\\
\mathcal{A}_\mu^c(k)&=2\frac{\mathrm{Re}\tilde{k}_\mu\,\mathcal{W}_c+\mathrm{Im}\,\Sigma_\mu^{\rm ret}\,\mathcal{P}_c}{\mathcal{P}_c^2+\mathcal{W}_c^2}
\end{aligned}$$

with $\mathcal{P}^c(k)=\mathrm{Re}\tilde{k}^2-\mathrm{Im}\,\Sigma_\mu^{\rm ret}\,\mathrm{Im}\,\Sigma^\mu_{\rm ret}$ and $\mathcal{W}^c(k)=-2\mathrm{Re}\tilde{k}_\mu\mathrm{Im}\,\Sigma^\mu_{\rm ret}$. This result is equivalent to the expressions used in [FLM03b], taking the difference in the sign convention into account.

[8] In case of a small but finite m_0 chiral symmetry is restored only approximately. S_s and $\Sigma_s^{\rm ret}$ will become small but do not vanish entirely.

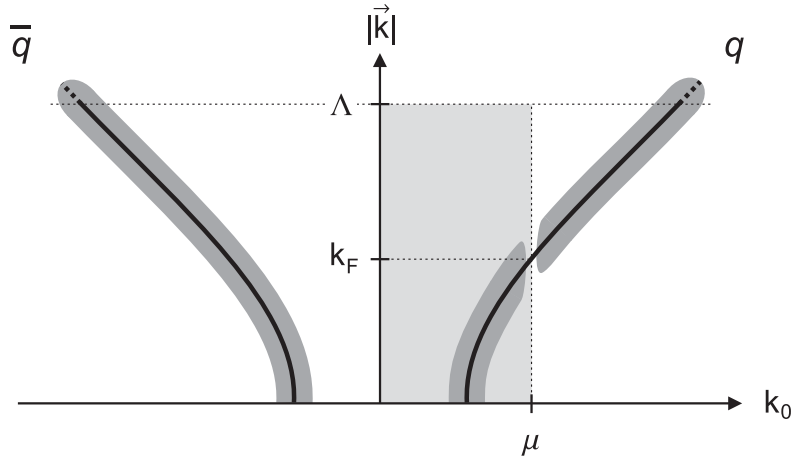

Figure 2.17: Structure of the quark spectral function $\mathcal{A}(k_0, \vec{k})$ in the energy–momentum plane (schematic). The displayed features are universal for all Lorentz components. The solid lines and the dark shaded regions denote the location of the broadened quark and antiquark on-shell peaks. (μ and k_F are the chemical potential and the corresponding Fermi momentum. Λ is the three-momentum cutoff of the NJL model.) See the text for details.

2.6.5 Spectral function in the energy–momentum plane

Let us briefly review the most important features of the quark spectral function. In Fig. 2.17, we show a schematic plot of $\mathcal{A}(k)$ in the energy–momentum plane. The position of the on-shell states – determined by $\mathcal{P}(k) = 0$ ($k_0 \approx \pm[\vec{k}^2 + m^{*2}]^{1/2}$) – is indicated by the solid lines. We find on-shell states at positive and negative energies that will later be identified with quark and antiquark states, respectively (see Section 4.1.1). The dark shaded regions denote the broadening of the quasiparticle peaks, induced by the collisional and decay width $\mathcal{W}(k)$ of our approach (in a realistic calculation, off-shell states exist also outside the shaded regions). Only at the chemical potential μ, the width will drop to zero and the quarks turn into quasiparticles – this will be discussed in detail at the end of Section 3.3 and in Chapter 4.

At zero temperature, the populated states of the medium are located within the light shaded region in Fig. 2.17: All states at energies below the chemical potential μ are populated with quarks (Fermi sea). States at negative energies, however, are reinterpreted as free antiquark states (see Appendix E for the exact definition of quark and antiquark states). We obtain the quark density by integrating the spectral function in the shaded region over energy and momentum, cf. Eq. (3.9). Due to the cutoff of the NJL model, states at three-momenta $|\vec{k}\,| > \Lambda$ will not contribute to the density. Note that the spectral function does not vanish at momenta above the cutoff. Because of the chosen regularization scheme (see Section 2.4.2), however, the spectral function at larger momenta will not contribute to any self-energy or polarization integral.

Fig. 2.17 also shows that the three-momentum cutoff Λ constitutes an effective energy cutoff. For energies $|k_0| > E_\Lambda$, where

$$E_\Lambda = k_0^{\rm os}(\Lambda) \qquad \left(E_\Lambda \approx \sqrt{\Lambda^2 + m^{*2}}\right) ,$$

the on-shell peaks are located (at momenta) above the cutoff. Since most of the spectral strength is concentrated within the vicinity of the on-shell peaks, the spectral function will not yield large contributions to self-energy and polarization integrals at higher energies than E_Λ. The off-shell components of the spectral function at large energies (and $|\vec{k}\,| < \Lambda$) are not affected by the regularization scheme – see Fig. 2.17. Hence, the effective energy cutoff is not as strict as the three-momentum cutoff that suppresses *all* contributions from $|\vec{k}\,| > \Lambda$.

The Fermi momentum k_F can be identified with the three-momentum at which the on-shell states cross the chemical potential, i.e.,

$$k_F = |\vec{k}_{\rm os}(\mu)| \qquad \left(k_F \approx \sqrt{\mu^2 - m^{*2}}\right) .$$

In a mean-field approach, where the full strength of the spectral function is located in sharp quasiparticle peaks (solid lines in Fig. 2.17), no populated states exist above the Fermi momentum. Due to collisional broadening of the peaks, this is not the case in our approach. We can see in the schematic plot of Fig. 2.17 that populated off-shell states exist at $|\vec{k}\,| > k_F$. This brings us to the momentum distribution of the medium, cf. Fig. 1.5 (nuclear matter). The momentum distribution $n(|\vec{k}\,|)$ is found by integrating the spectral function over the energy of the populated states at fixed momentum – see Eq. (5.4) and Appendix E. In contrast to the momentum distribution of a free Fermi gas (quasiparticles, dotted line in Fig. 1.5), we will find a high momentum tail (solid line in Fig. 1.5) in the momentum distribution of our approach. This tail is generated by the populated off-shell states above k_F.

2.7 Meson propagators and spectral functions

At the bosonization of the NJL Lagrangian in Eq. (2.4) we have introduced meson fields (2.5). For the path-ordered σ and $\pi^{0,\pm}$ Green's functions in terms of the fields we find [Reh98]:

$$\begin{aligned} \Delta_\sigma^{\rm P}(1,2) &= -i\left\{\langle {\rm P}[\sigma(1)\sigma(2)]\rangle - \langle\sigma(1)\rangle\,\langle\sigma(2)\rangle\right\} , \\ \Delta_{0,\pm}^{\rm P}(1,2) &= -i\left\{\left\langle {\rm P}[\pi^{0,+}(1)\pi^{0,-}(2)]\right\rangle - \left\langle\pi^{0,+}(1)\right\rangle\left\langle\pi^{0,-}(2)\right\rangle\right\} . \end{aligned} \tag{2.41}$$

The causal, anti-causal, and non-ordered meson Green's functions $\Delta^{\rm c,a,\gtrless}$ are found in analogy to the quark propagators in (2.17). The meson Green's functions are scalar functions and have no Lorentz structure. Like for the quarks, the retarded and

advanced propagators are defined as

$$\Delta^{\rm ret}(1,2) = \Theta(t_1-t_2)[\Delta^{>}(1,2)-\Delta^{<}(1,2)] = \Delta^{\rm c}(1,2)-\Delta^{<}(1,2)\,,$$
$$\Delta^{\rm av}(1,2) = \Theta(t_2-t_1)[\Delta^{<}(1,2)-\Delta^{>}(1,2)] = \Delta^{\rm c}(1,2)-\Delta^{>}(1,2)\,.$$

We have dropped the indices $\sigma, 0, \pm$ here since the definition is the same for all mesons.

In analogy to Eq. (2.26), the σ and $\pi^{0,\pm}$ spectral functions are introduced in terms of the non-ordered propagators $\Delta^{\gtrless}$,

$$\xi(k) = i\,[\Delta^{>}(k)-\Delta^{<}(k)] = -2{\rm Im}\,\Delta^{\rm ret}(k)\,.$$

The bosonic phase space distribution function $\mathrm{n_B}$ in thermodynamical equilibrium,

$$\mathrm{n_B}(k_0) = \frac{1}{e^{k_0/T}-1} \quad \xrightarrow{T=0} \quad -\Theta(-k_0)\,, \tag{2.42}$$

is – like $\mathrm{n_F}$ – a simple step function at zero temperature. We can use $\mathrm{n_B}$ to express the non-ordered propagators $\Delta^{\gtrless}$ in terms of the spectral functions [KB62],

$$\Delta^{>}(k) = -i\xi(k)[1+\mathrm{n_B}(k_0)]\,, \tag{2.43}$$
$$\Delta^{<}(k) = -i\xi(k)\mathrm{n_B}(k_0)\,. \tag{2.44}$$

Note the subtle differences to the relations for the quarks in Eqs. (2.30,2.31). The distributions $\mathrm{n_F}(k_0)$ in the quark relations correspond to $-\mathrm{n_B}(k_0)$ in (2.43,2.44), i.e., Pauli blocking is replaced by Bose enhancement.

The relations between the different kinds of quark propagators and the spectral function (2.32) exist in equivalent form for the meson propagators. We summarize them here since they will be helpful in the later sections.

$$\begin{aligned}
\Delta^{\rm c}(k) &= \Delta^{\rm ret}(k)+\Delta^{<}(k) = \Delta^{\rm ret}(k) - i\xi(k)\mathrm{n_B}(k_0)\,,\\
&= \Delta^{\rm av}(k)+\Delta^{>}(k) = \Delta^{\rm av}(k) - i\xi(k)[1+\mathrm{n_B}(k_0)]\,,\\
\Delta^{<}(k) &= [\Delta^{\rm ret}(k)-\Delta^{\rm av}(k)]\mathrm{n_B}(k_0)\,,\\
{\rm Re}\,\Delta^{\rm ret,av}(k) &= \frac{1}{2}[\Delta^{\rm ret}(k)+\Delta^{\rm av}(k)]\,,\\
{\rm Im}\,\Delta^{\rm ret,av}(k) &= \mp\frac{i}{2}([\Delta^{\rm ret}(k)-\Delta^{\rm av}(k)]\,.
\end{aligned} \tag{2.45}$$

In Section 2.2, the RPA meson propagators were determined in terms of the NJL coupling and the polarizations, cf. Eq. (2.10),

$$\Delta_l^{\rm ret}(k) = -\frac{2{\rm G}}{1+2{\rm G}\,\Pi_l^{\rm ret}(k)}\,, \tag{2.46}$$

where $l=\sigma,0,\pm$ denotes the type of the meson and $\Pi_l^{\rm ret}(k)$ is the corresponding polarization. Since $\Delta^{\rm ret}$ and $\Pi^{\rm ret}$ are scalar functions, we can easily disentangle the real and the imaginary part of the retarded propagators,

$$\Delta_l^{\rm ret}(k) = -\frac{\frac{1}{2{\rm G}}+{\rm Re}\,\Pi_l^{\rm ret}(k) - i{\rm Im}\,\Pi_l^{\rm ret}(k)}{\left(\frac{1}{2{\rm G}}+{\rm Re}\,\Pi_l^{\rm ret}(k)\right)^2+{\rm Im}\,\Pi_l^{\rm ret}(k)^2}\,. \tag{2.47}$$

The spectral function $\xi = -2\mathrm{Im}\,\Delta^{\mathrm{ret}}$ is then identified with

$$\xi_l(k) = \frac{-2\mathrm{Im}\,\Pi_l^{\mathrm{ret}}(k)}{\left(\frac{1}{2\mathrm{G}} + \mathrm{Re}\,\Pi_l^{\mathrm{ret}}(k)\right)^2 + \mathrm{Im}\,\Pi_l^{\mathrm{ret}}(k)^2}\,. \tag{2.48}$$

Instead of a term of the form $k^2 - m^2$ we find a term $\frac{1}{2\mathrm{G}} + \mathrm{Re}\,\Pi^{\mathrm{ret}}$ that determines the dynamics, i.e. the pole structure, of the RPA propagators. The imaginary part of the polarization generates the width of on-shell peaks. In contrast to the quark case, the meson spectral functions are not normalized to a certain value. This can be explained by the fact that no explicit coupling factors enter the quark–meson interaction vertices, cf. Eq. (2.4). The effective coupling is hidden in the RPA meson propagators. Hence, the RPA spectral function can be interpreted as the product of a normalized spectral function and the effective quark–meson coupling.

2.8 Self-energy, polarizations and widths

2.8.1 Quark self-energy

In the real-time formalism, the single-particle quark self-energy is defined on the same closed time-path contour as the Green's function $\mathrm{S}^{\mathrm{P}}(1,2)$ [Dan84, BM90, Das97]. When the times t_1 and t_2 are located on fixed branches of the contour in Fig. 2.16, the path-ordered self-energy $\Sigma^{\mathrm{P}}(1,2)$ reduces – like the Green's function – to the causal (Feynman) self-energy Σ^{c}, the anti-causal self-energy Σ^{a}, or one of the collisional (non-ordered) self-energies $\Sigma^{\gtrless}$, cf. (2.15) and (2.17).

The self-energies on the contour are not independent of each other. The time-ordered self-energy $\Sigma^{\mathrm{c}}(1,2)$ can be split up into the collisional self-energies $\Sigma^{\gtrless}$ and a time-local mean-field part $\Sigma^{\mathrm{mf}} \sim \delta(t_1 - t_2)$,

$$\Sigma^{\mathrm{c}}(1,2) = \Sigma^{\mathrm{mf}}(1,2) + \Theta(t_1 - t_2)\,\Sigma^{>}(1,2) + \Theta(t_2 - t_1)\,\Sigma^{<}(1,2)\,.$$

The mean-field self-energy contains the long-range effects that can be described by the motion of non-interacting particles in a mean-field potential. In the present $\mathcal{O}(1/N_c)$ approach to the NJL model, the mean-field self-energy is identified with the Hartree self-energy Σ^{H} of the Dyson–Schwinger equation (2.13) that is shown in the first line of Fig. 2.11. It is mainly responsible for the dynamical generation of the constituent quark mass. Note that the Fock diagram, typically a mean-field self-energy, is part of the RPA meson exchange. We must take this into account later when we calculate the real part of the self-energy. The collisional self-energies $\Sigma^{\gtrless}$ contain the short-range effects that arise from decays and particle collisions in the medium. They correspond to the meson exchange diagram in the Dyson–Schwinger equation. In the Hartree+RPA approximation, the self-energy in the gap equation (2.11) is purely time-local. Collisional self-energies are not present in that approach.

In Section 2.6 we have already encountered the retarded and advanced self-energies $\Sigma^{\text{ret,av}}$. They are defined in analogy to the Green's functions $\text{S}^{\text{ret,av}}$ (2.18),

$$\begin{aligned} \Sigma^{\text{ret}}(1,2) &= \Sigma^{\text{mf}}(1,2) + \Theta(t_1 - t_2)\,[\Sigma^{>}(1,2) - \Sigma^{<}(1,2)]\;, \\ \Sigma^{\text{av}}(1,2) &= \Sigma^{\text{mf}}(1,2) + \Theta(t_2 - t_1)\,[\Sigma^{<}(1,2) - \Sigma^{>}(1,2)]\;. \end{aligned} \tag{2.49}$$

The Wigner transformed (2.20) self-energy $\Sigma^{\text{ret}}(k)$ enters the retarded quark propagator $\text{S}^{\text{ret}}(k)$ (2.33) and thus the spectral function $\mathcal{A}(k) = -2\text{Im}\,\text{S}^{\text{ret}}(k)$ (2.40). The real part of $\Sigma^{\text{ret}}(k)$ represents in-medium corrections to the four-momenta and the masses of the quarks in the spectral function, as one can see in Eqs. (2.34) and (2.36,2.38). Note that the collisional corrections to the mass are usually smaller than the mean-field self-energy.

The imaginary part of $\Sigma^{\text{ret}}(k)$ is responsible for the collisional broadening of the quark states. As we can see in Eqs. (2.37,2.38), the width in the quark spectral function is determined by the Lorentz components of $-2\text{Im}\,\Sigma^{\text{ret}}(k)$. In momentum space, we find $-2\text{Im}\,\Sigma^{\text{ret}}(k) = i\,\Sigma^{>}(k) - i\,\Sigma^{<}(k)$ [Dan84] – a relation similar to (2.26). As we will discuss in Chapter 4 in more detail, the self-energies $i\,\Sigma^{>}(k)$ and $-i\,\Sigma^{<}(k)$ are identical to the total collision rates for scattering out of and into of the configuration $(k_0, \vec{k}\,)$, respectively [KB62, FLM03b]. Therefore, we can define the quark width Γ – the overall measure for changes of a configuration – by the sum of the two collisional self-energies,

$$\Gamma(k) = i\,\Sigma^{>}(k) - i\,\Sigma^{<}(k) = -2\text{Im}\,\Sigma^{\text{ret}}(k)\,. \tag{2.50}$$

The relation on the rhs. of (2.50) is of course nothing but the optical theorem [PS95] that relates the imaginary part of a Feynman amplitude ($\text{Im}\,\Sigma^{\text{ret}}$) to a total cross section or collision rate ($i\,\Sigma^{>} - i\,\Sigma^{<}$). The relevant scattering and decay processes can be identified with the help of cutting – or Cutkosky – rules [PS95, Das97]: A total collision rate is found by cutting the Feynman diagram in all possible ways, putting the cut propagators on-shell, and integrating over the four-momenta of the cut propagators. When we cut the meson exchange diagram in Fig. 2.11, we find processes like $q \to q\pi$ and $q\bar{q} \to \sigma$ that contribute to the loss rate $i\,\Sigma^{>}$ and the gain rate $-i\,\Sigma^{<}$. We will examine the structure of these processes in more detail in Chapter 4. An overview of all contributing processes can be found in Fig. 4.3.

Using the definition of the on-shell energy $k_0^{\text{os}}(\vec{k}\,)$ and the on-shell momentum $\vec{k}_{\text{os}}$ in (2.39) we can also introduce on-shell self-energies and a on-shell width,

$$\begin{aligned} \Sigma_{\text{os}}(k_0) &= \Sigma(k_0, \vec{k}_{\text{os}}(k_0))\,, \quad \Gamma_{\text{os}}(k_0) = \Gamma(k_0, \vec{k}_{\text{os}}(k_0))\,, \\ \Sigma_{\text{os}}(\vec{k}\,) &= \Sigma(k_0^{\text{os}}(\vec{k}\,), \vec{k}\,)\,, \qquad \Gamma_{\text{os}}(\vec{k}\,) = \Gamma(k_0^{\text{os}}(\vec{k}\,), \vec{k}\,)\,. \end{aligned} \tag{2.51}$$

Note that the definitions hold for all kinds of self-energies (Σ^{c}, Σ^{ret}, etc.).

It follows from Eq. (2.33) that the quark self-energies and the width must have the same Lorentz structure as the propagators,

$$\begin{aligned} \Sigma(k) &= \Sigma_s(k)\,\mathbb{1}_{4\times4} + \Sigma_0(k)\,\gamma_0 - \Sigma_v(k)\,\vec{e}_k\cdot\vec{\gamma} = \Sigma_s(k) + \Sigma_\mu(k)\,\gamma^\mu\,, \\ \Gamma(k) &= \Gamma_s(k)\,\mathbb{1}_{4\times4} + \Gamma_0(k)\,\gamma_0 - \Gamma_v(k)\,\vec{e}_k\cdot\vec{\gamma} = \Gamma_s(k) + \Gamma_\mu(k)\,\gamma^\mu\,, \end{aligned} \tag{2.52}$$

with the scalar functions $\Sigma_{s,0,v}$ and $\Gamma_{s,0,v}$ which are functions of k_0 and $|\vec{k}\,|$ only. Relations similar to Eqs. (2.24) can be used to extract the Lorentz components from complicated expressions for Σ or Γ:

$$\Sigma_s(k) = \frac{\mathrm{tr}\,\Sigma(k)}{4}\,, \quad \Sigma_0(k) = \frac{\mathrm{tr}[\gamma_0\,\Sigma(k)]}{4}\,, \quad \Sigma_v(k) = \frac{\mathrm{tr}[\vec{e}_k\cdot\vec{\gamma}\,\Sigma(k)]}{4}\,, \tag{2.53}$$

and correspondingly for $\Gamma_{s,0,v}$.

2.8.2 RPA meson polarization

We turn now to the polarizations of the RPA mesons. Much of the above discussion for the quark self-energy holds also for the polarizations. Thus, we can be rather brief in the following. As one can see in Eq. (2.8), the RPA polarizations do not include time-local mean-field contributions. Thus, the time-ordered polarization Π_l^{c} can be expressed solely in terms of the collisional polarizations $\Pi_l^{\gtrless}$,

$$\Pi_l^{\mathrm{c}}(1,2) = \Theta(t_1-t_2)\,\Pi_l^{>}(1,2) + \Theta(t_2-t_1)\,\Pi_l^{<}(1,2)\,.$$

The retarded polarization is then given by

$$\Pi^{\mathrm{ret}}(1,2) = \Theta(t_1-t_2)\,[\Pi^{>}(1,2) - \Pi^{<}(1,2)]\ .$$

Like the collisional self-energies $\Sigma^{\gtrless}$, the polarizations $i\,\Pi^{>}$ and $-i\,\Pi^{<}$ can be identified with total collision rates. We find processes like $\pi \to q\bar{q}$, $\sigma q \to q$, etc., when we cut the polarization diagram in Fig. 2.14 (see Section 4.5 for details). In analogy to the quark case and in accordance with the structure of the RPA propagators and spectral functions (2.47,2.48), we introduce the RPA meson widths

$$\Gamma_l(k) = [i\,\Pi_l^{>}(k) - i\,\Pi_l^{<}(k)]/(2k_0) = -\mathrm{Im}\,\Pi_l^{\mathrm{ret}}(k)/k_0\,. \tag{2.54}$$

The additional factor $1/k_0$ in comparison to (2.50) is required to get the dimension of the widths right. The factor $1/2$ is conventional. It ensures that the non-relativistic limit of this definition is identical to the widths from non-relativistic models [Leu01, Y$^+$06].

3 Calculation of self-energies and polarizations

In this chapter we show in detail how to calculate the quark self-energy and the RPA meson polarizations in our self-consistent approach (cf. Fig. 2.11), using the full in-medium propagators. After a short review of the mean-field self-energy we will demonstrate how the quark and meson widths can be calculated via the collisional self-energies $\Sigma^{\gtrless}$ and polarizations $\Pi^{\gtrless}$. In the last part of this chapter, the calculation of the real parts of the retarded self-energy and the RPA polarizations via dispersion integrals will be discussed. Note that the Feynman rules of the real-time formalism for the quark–quark interaction (2.1) and the quark–meson interaction (2.4) can be found in Appendix C.

3.1 Mean-field self-energy

With mean-field self-energy we refer here to the components of the full quark self-energy that are calculated from typical mean-field diagrams like the Hartree or the Fock diagram. This does not imply that a quasiparticle approximation is used. The diagrams are calculated with full in-medium propagators including a collisional width.

3.1.1 Hartree self-energy

In our $\mathcal{O}(1/N_c)$ approach of Fig. 2.11, the Hartree diagram Σ^{H} takes the role of the mean-field self-energy Σ^{mf},

$$-i\,\Sigma^{\mathrm{H}} = 2i\mathrm{G}\sum_{l}\int\frac{d^4p}{(2\pi)^4}\Gamma_l\,\mathrm{Tr}[i\,\mathrm{S}^{\mathrm{c}}(p)\tilde{\Gamma}_l]\cdot(-1) = 2\mathrm{G}\int\frac{d^4p}{(2\pi)^4}\,\mathrm{Tr}\,\mathrm{S}^{\mathrm{c}}(p)\,, \tag{3.1}$$

where "Tr" denotes a trace in color, flavor, and spinor space. A cutoff must be used to regularize the integral. Only the isospin scalar NJL vertex ($l = \sigma$) contributes to the Hartree self-energy since $\mathrm{Tr}\,\gamma_5 = \mathrm{Tr}\,\gamma_\mu\gamma_5 = 0$, cf. Eqs. (2.3,2.23). With $\mathrm{S}^{\mathrm{c}}(k) = \mathrm{S}^{\mathrm{ret}}(k) + \mathrm{S}^{<}(k)$, cf. (2.32) and using Eq. (D.5) we get

$$-i\,\Sigma^{\mathrm{H}} = 2\mathrm{G}\int\frac{d^4p}{(2\pi)^4}\,\mathrm{Tr}\,\mathrm{S}^{<}(p)\,.$$

We can work out the trace since the Lorentz structure of the propagator is known (2.23),

$$-i\,\Sigma^{\mathrm{H}} = 8\mathrm{G}N_f N_c \int \frac{d^4p}{(2\pi)^4}\,\mathrm{S}_s^<(p) = 8i\mathrm{G}N_f N_c \int \frac{d^4p}{(2\pi)^4}\mathcal{A}_s(p)\mathrm{n_F}(p_0)\,. \tag{3.2}$$

The mean-field self-energy provided by the Hartree diagram has a very simple Lorentz structure – only the Lorentz scalar part is finite. This result is independent of the presence of a medium.

3.1.2 Fock self-energy

The Fock self-energy is part of the RPA meson exchange diagram and should be treated in that framework. Since it will later be necessary to isolate a Fock-like term from the real part of the collisional self-energy, an explicit discussion is in order. In particular, the Lorentz structure of the Fock self-energy will be of interest later. The Feynman rules (Appendix C.2.2) yield

$$-i\,\Sigma^{\mathrm{F}} = -2\mathrm{G}\sum_l \int \frac{d^4p}{(2\pi)^4}\Gamma_l\,\mathrm{S^c}(p)\tilde{\Gamma}_l\,. \tag{3.3}$$

The time-ordered propagator can be decomposed into its real and imaginary part,

$$\mathrm{S^c}(k) = \mathrm{S^{ret}}(k) + \mathrm{S}^<(k) = \mathrm{Re}\,\mathrm{S^{ret}}(k) - \frac{i}{2}\mathcal{A}(k)[1-2\mathrm{n_F}(k_0)]\,.$$

From Eq. (D.4) follows that the k_0 integral over $\mathrm{Re}\,\mathrm{S^{ret}}(k)$ vanishes. With

$$\sum_l \Gamma_l\mathcal{A}(k)\tilde{\Gamma}_l = \mathcal{A}(k) - 3[\mathcal{A}_s(k) - \mathcal{A}_\mu(k)\gamma^\mu] = -2\mathcal{A}_s(k) + 4\mathcal{A}_\mu(k)\gamma^\mu\,,$$

the Fock self-energy becomes

$$\Sigma^{\mathrm{F}} = 2\mathrm{G}\int \frac{d^4p}{(2\pi)^4}\,[\mathcal{A}_s(p) - 2\mathcal{A}_\mu(p)\gamma^\mu]\,[1-2\mathrm{n_F}(p_0)]\,. \tag{3.4}$$

The Lorentz components Σ_s^{F} and Σ_0^{F} can be directly read off from Eq. (3.4). We use the normalization of the spectral function (D.6) to simplify Σ_s^{F},

$$\begin{aligned}\Sigma_s^{\mathrm{F}} &= -4\mathrm{G}\int \frac{d^4p}{(2\pi)^4}\mathcal{A}_s(p)\mathrm{n_F}(p_0)\,,\\ \Sigma_0^{\mathrm{F}} &= -4\mathrm{G}\int \frac{d^4p}{(2\pi)^4}\mathcal{A}_0(p)[1-2\mathrm{n_F}(p_0)]\,.\end{aligned} \tag{3.5}$$

The integrand of Eq. (3.4) contains a factor $\vec{p}\cdot\vec{\gamma}$ – with the three-momentum $\vec{p}$ of the integration variables instead of the external $\vec{k}$. Thus, the rule of Eq. (2.24) has to be

used to extract Σ_v^{F}. Using again the normalization of the spectral function (D.6), we find

$$\Sigma_v^{\mathrm{F}} = 8\mathrm{G} \int \frac{d^4p}{(2\pi)^4} \cos\vartheta \mathcal{A}_v(p) \mathrm{n_F}(p_0) \,,$$

where $e_k^i e_p^j \,\mathrm{tr}\,\gamma^i\gamma^j = -4\vec{e}_k \cdot \vec{e}_p = -4\cos\vartheta$ has been used to find Σ_v^{F}. Since $\mathcal{A}_v(p) = \mathcal{A}_v(p_0, |\vec{p}\,|)$ and $\int_{-1}^{+1} d\cos\vartheta \cos\vartheta = 0$, Σ_v^{F} can be simplified even further,

$$\Sigma_v^{\mathrm{F}} = 0 \,. \tag{3.6}$$

We can conclude that the Lorentz structure of the Fock self-energy is more complicated than that of the Hartree self-energy. Only Σ_v^{F} vanishes for all μ and T. At zero temperature we have $[1 - 2\mathrm{n_F}(p_0)] = \mathrm{sgn}(p_0 - \mu)$. $\mathcal{A}_0$ is symmetric in p_0 in the vacuum. Thus, Σ_0^{F} vanishes for $\mu = 0$ and becomes finite only in the presence of a medium. Σ_s^{F} is the only component that can be finite for all μ and T. It is proportional to Σ^{H}, cf. (3.2,3.5),

$$\Sigma_s^{\mathrm{F}} = \frac{1}{2N_f N_c} \Sigma^{\mathrm{H}} \,. \tag{3.7}$$

In the Hartree–Fock approximation, Σ_0^{F} is usually absorbed into a redefined chemical potential [Kle92]. In this case, the mean-field self-energy remains Lorentz scalar and is given by $\Sigma^{\mathrm{mf}} = \Sigma^{\mathrm{H}} + \Sigma_s^{\mathrm{F}}$. Of course, this is a purely technical measure and has no influence on the results.

3.2 Quark condensate and quark density

The definitions of the quark condensate and the quark density are closely related to the mean-field self-energy. Hence, we take a brief look at them at this point. In isospin symmetric quark matter we have

$$\langle \bar{u}u \rangle = \langle \bar{d}d \rangle = \frac{1}{2} \langle \bar{\psi}\psi \rangle = -\frac{i}{2} \int \frac{d^4p}{(2\pi)^4} \,\mathrm{Tr}\,\mathrm{S^c}(p) \,.$$

Comparing this expression to Eq. (3.1) yields $\langle \bar{\psi}\psi \rangle = -1/(2\mathrm{G})\,\Sigma^{\mathrm{H}}$. Thus, we get for the quark condensate

$$\langle \bar{u}u \rangle^{1/3} = -\left(\frac{1}{4\mathrm{G}} \Sigma^{\mathrm{H}} \right)^{\frac{1}{3}} \,. \tag{3.8}$$

The quark number density $\rho(\mu, T)$ is related to $\langle \psi_\alpha^\dagger \psi_\alpha \rangle = -i \,\mathrm{Tr}\,\gamma_0\,\mathrm{S^<}(1,1)$, cf. (2.25). Using Eq. (2.31), this means that the density can be calculated by integrating over $\mathrm{Tr}\,\gamma_0 \mathcal{A}(p) \mathrm{n_F}(p_0)$ – the spectral function weighted with the occupation probability.

The density is given by the number of quarks minus the number of antiquarks in the system. We show in Appendix E that the calculation of this difference becomes very sensitive to numerical fluctuations in the presence of short-range correlations. Thus, we do not introduce the exact definition of the density here, but a numerically stable approximation that works well at zero temperature: We identify the quarks – in contrast to antiquarks – with the states that have a positive effective energy $\mathrm{Re}\tilde{p}_0$ (see the schematic plot in Fig. 2.17) and integrate only over those states,

$$\begin{aligned}\rho(\mu) &= \int_\Lambda \frac{d^3p}{(2\pi)^3} \int\limits_{Re\tilde{p}_0=0}^{\infty} \frac{dp_0}{2\pi} \mathrm{n_F}(p_0)\,\mathrm{Tr}\,\gamma_0 \mathcal{A}(p) \\ &= 4N_f N_c \int_\Lambda \frac{d^3p}{(2\pi)^3} \int\limits_{Re\tilde{p}_0=0}^{\infty} \frac{dp_0}{2\pi} \mathrm{n_F}(p_0) \mathcal{A}_0(p)\,. \end{aligned} \tag{3.9}$$

As for the self-energies, the integrals in (3.9) have to be regularized by a cutoff. Note that $\mathcal{A}_0$ is the only Lorentz component of $\mathcal{A}$ that remains finite in the non-relativistic limit. The exact definition of the density (E.14) and a discussion on the quality of the approximation used in (3.9) can be found in Appendix E.

In the quasiparticle approximation, the peaks of $\mathcal{A}_0$ become δ-functions, see (4.1). The integral in the last term of (3.9) can then be easily calculated ($T = 0$). We find

$$\rho_{\mathrm{qp}}(\mu) = N_f N_c/(3\pi^2) k_F^3\,, \tag{3.10}$$

where $k_F = \sqrt{\mu^2 - m^{*2}}$ is the quasiparticle Fermi momentum.

3.3 Collisional self-energies and quark widths

The diagrams that correspond to the collisional self-energies $\Sigma^{\gtrless}(k)$ are shown explicitly in Fig 3.1. Using the Feynman rules of the real-time formalism (see Appendix C.2.3) we find

$$-i\,\Sigma^{\gtrless}(k) = \sum_l \int \frac{d^4p}{(2\pi)^4} \Gamma_l\, \mathrm{S}^{\gtrless}(p) \tilde{\Gamma}_l\, \Delta_l^{\lessgtr}(p-k)\,. \tag{3.11}$$

It is possible to calculate the sum over the different kinds of mesons after replacing Γ_l and $\tilde{\Gamma}_l$ according to Eq. (2.3). In flavor symmetric quark matter, the isospin matrices τ_i commute with the quark propagators. For the γ_5 matrices we have $\{\gamma_5, \gamma_\mu\} = 0$. Shifting around the matrices yields

$$\begin{aligned}-i\,\Sigma^{\gtrless}(k) = &\int \frac{d^4p}{(2\pi)^4} \left(\mathrm{S}_s^{\gtrless}(p) + \mathrm{S}_\mu^{\gtrless}(p)\gamma^\mu\right) \Delta_\sigma^{\lessgtr}(p-k) \\ &+ \int \frac{d^4p}{(2\pi)^4} \left(-\mathrm{S}_s^{\gtrless}(p) + \mathrm{S}_\mu^{\gtrless}(p)\gamma^\mu\right) \\ &\quad \times \left[\Delta_0^{\lessgtr}(p-k) + (1+\tau_3)\,\Delta_+^{\lessgtr}(p-k) + (1-\tau_3)\,\Delta_-^{\lessgtr}(p-k)\right]\,, \end{aligned}$$

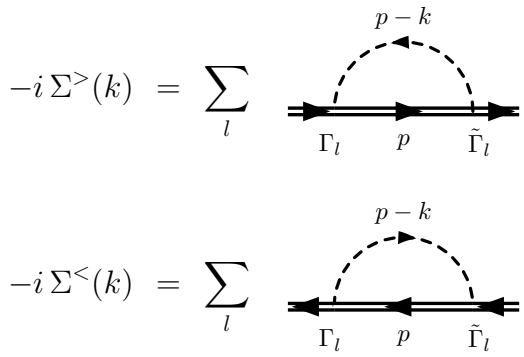

Figure 3.1: The collisional quark self-energies $\Sigma^{>}$ and $\Sigma^{<}$. The directed quark and meson lines correspond to the non-ordered propagators $\mathrm{S}^{\gtrless}$ and $\Delta^{\gtrless}$, respectively. $l = \sigma, 0, \pm$ denotes the different kinds of RPA mesons.

where we have used $(\gamma_5)^2 = \mathbb{1}_{4\times4}$ and $\tau^i\tau^j = \delta^{ij}\mathbb{1}_{2\times2} + i\epsilon^{ijk}\tau^k$ (see Appendix A). The contributions from the three different RPA pions are equivalent up to the different propagators $\Delta_0^{\gtrless}$, $\Delta_\pm^{\gtrless}$ and the isospin factors

$$\mathbb{1} = \begin{pmatrix} 1 & 0 \\ 0 & 1 \end{pmatrix}, \qquad \mathbb{1} + \tau_3 = \begin{pmatrix} 2 & 0 \\ 0 & 0 \end{pmatrix}, \qquad \mathbb{1} - \tau_3 = \begin{pmatrix} 0 & 0 \\ 0 & 2 \end{pmatrix}.$$

This difference is important in asymmetric quark matter. In symmetric quark matter, however, we have $\Delta_0 = \Delta_+ = \Delta_-$ since the polarizations $\Pi_{0,\pm}$ are equal. This is shown explicitly in Section 3.4, Eqs. (3.20,3.21). It is not necessary to treat the different pions separately here[1]. Instead, the contributions to the quark self-energy can be added up, $\Sigma^{\gtrless} = \Sigma_\sigma^{\gtrless} + 3\,\Sigma_\pi^{\gtrless}$, after introducing the universal RPA pion propagators $\Delta_\pi^{\gtrless}$,

$$-i\,\Sigma^{\gtrless}(k) = \int \frac{d^4p}{(2\pi)^4} \Big[\mathrm{S}_s^{\gtrless}(p) \left\{ \Delta_\sigma^{\lessgtr}(p-k) - 3\,\Delta_\pi^{\lessgtr}(p-k) \right\} + \mathrm{S}_\mu^{\gtrless}(p)\gamma^\mu \left\{ \Delta_\sigma^{\lessgtr}(p-k) + 3\,\Delta_\pi^{\lessgtr}(p-k) \right\} \Big] . \tag{3.12}$$

It is a straightforward exercise to extract the Lorentz components $\Sigma_s^{\gtrless}$ and $\Sigma_0^{\gtrless}$ from Eq. (3.12). $\Sigma_v^{\gtrless}$ has to be extracted using Eq. (2.53),

$$-i\,\Sigma_v^{\gtrless}(k) = \int \frac{d^4p}{(2\pi)^4} \cos\vartheta\, \mathrm{S}_v^{\gtrless}(p) \left\{ \Delta_\sigma^{\lessgtr}(p-k) + 3\,\Delta_\pi^{\lessgtr}(p-k) \right\} , \tag{3.13}$$

where ϑ is the angle between the three-momenta $\vec{k}$ and $\vec{p}$.

To determine $\mathrm{Im}\,\Sigma^{\mathrm{ret}}$ and the quark width, it is convenient to replace the propagators in (3.12) by spectral functions and distribution functions according to Eqs.

[1]Note that we use the same (averaged) current quark mass for up and down quarks in (2.1), i.e. isospin symmetry is exact in our approach.

(2.30,2.31) and (2.43,2.44). We get

$$\begin{aligned} i\,\Sigma^{>}(k) = \int \frac{d^4p}{(2\pi)^4}[1-\mathrm{n_F}(p_0)]\mathrm{n_B}(p_0-k_0) \\ \times\left[\mathcal{A}_s(p)\left\{\xi_\sigma(p-k)-3\xi_\pi(p-k)\right\}\right. \\ \left.+\mathcal{A}_\mu(p)\gamma^\mu\left\{\xi_\sigma(p-k)+3\xi_\pi(p-k)\right\}\right] \end{aligned} \tag{3.14}$$

and

$$\begin{aligned} -i\,\Sigma^{<}(k) = \int \frac{d^4p}{(2\pi)^4}\mathrm{n_F}(p_0)[1+\mathrm{n_B}(p_0-k_0)] \\ \times\left[\mathcal{A}_s(p)\left\{\xi_\sigma(p-k)-3\xi_\pi(p-k)\right\}\right. \\ \left.+\mathcal{A}_\mu(p)\gamma^\mu\left\{\xi_\sigma(p-k)+3\xi_\pi(p-k)\right\}\right]\,. \end{aligned} \tag{3.15}$$

The quark width is given by the sum of the two collisional self-energies as shown in Eq. (2.50), $\Gamma = -2\mathrm{Im}\,\Sigma^{\mathrm{ret}} = i\,\Sigma^{>} - i\,\Sigma^{<}$. We find for the Lorentz components

$$\Gamma_{s,\mu}(k) = \int \frac{d^4p}{(2\pi)^4}[\mathrm{n_F}(p_0)+\mathrm{n_B}(p_0-k_0)]\mathcal{A}_{s,\mu}(p)\left[\xi_\sigma(p-k)\mp 3\xi_\pi(p-k)\right]\,, \tag{3.16}$$

where the upper sign in the integrand refers to the Lorentz scalar and the lower sign to the Lorentz vector component. $\mathcal{A}_i(p)$ should be read as $\mathcal{A}_v(p)\cos\vartheta e_k^i$ when determining Γ_v, cf. Eq. (3.13).

For $T=0$, $\mathrm{n_F}$ and $\mathrm{n_B}$ become simple step functions (2.29,2.42). This can be used to combine the distribution functions with the limits of the p_0 integration,

$$\int_{-\infty}^{+\infty} dp_0[\mathrm{n_F}(p_0)+\mathrm{n_B}(p_0-k_0)]\cdots \quad \xrightarrow{T=0} \quad \int_{k_0}^{\mu} dp_0\cdots \tag{3.17}$$

One sees immediately that the width becomes zero for $k_0=\mu$ in this case: states at the Fermi energy $(\mu,\vec{k}\,)$ are stable (quasiparticles). Because of Pauli blocking it is impossible to scatter into our out of those states. For finite temperature this restriction is less strict. At low temperatures, however, the quark width will remain small for energies in the vicinity of the chemical potential. Due to the structure of the integration limits it can also be expected that certain Lorentz components of the width change their sign at $k_0=\mu$.

3.4 Collisional polarizations and RPA meson widths

Fig. 3.2 shows the diagrams corresponding to the collisional polarizations $\Pi_l^{\gtrless}(k)$. From the Feynman rules, we obtain for these diagrams

$$-i\,\Pi_l^{\gtrless}(k) = -\int \frac{d^4p}{(2\pi)^4}\,\mathrm{Tr}\left[\tilde{\Gamma}_l\,\mathrm{S}^{\gtrless}(p)\Gamma_l\,\mathrm{S}^{\lessgtr}(p-k)\right]\,, \tag{3.18}$$

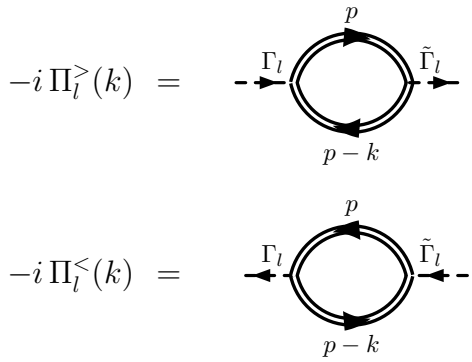

Figure 3.2: The collisional meson polarizations $\Pi^>$ and $\Pi^<$. The directed quark and meson lines correspond to the non-ordered propagators $\mathrm{S}^{\gtrless}$ and $\Delta^{\gtrless}$, respectively. $l = \sigma, 0, \pm$ denotes the different kinds of RPA mesons.

where $l = \sigma, 0, \pm$ denotes the different kinds of RPA mesons. The trace in Eq. (3.18) can be worked out after inserting the different $\Gamma_l, \tilde{\Gamma}_l$ pairs from Eqs. (2.3) explicitly. Using the Lorentz structure of the quark propagators (2.23) we find for $l = \sigma$

$$-i\,\Pi_\sigma^{\gtrless}(k) = -4N_f N_c \int \frac{d^4p}{(2\pi)^4} \left[\mathrm{S}_s^{\gtrless}(p)\,\mathrm{S}_s^{\lessgtr}(p-k) + \mathrm{S}_\mu^{\gtrless}(p)\,\mathrm{S}_{\lessgtr}^{\mu}(p-k) \right] , \tag{3.19}$$

with

$$\mathrm{S}_\mu^{\gtrless}(p)\,\mathrm{S}_{\lessgtr}^{\mu}(p-k) = \mathrm{S}_0^{\gtrless}(p)\,\mathrm{S}_0^{\lessgtr}(p-k) - \mathrm{S}_v^{\gtrless}(p)\,\mathrm{S}_v^{\lessgtr}(p-k)\vec{e}_p \cdot \vec{e}_{p-k}\,.$$

In flavor symmetric quark matter the isospin matrices τ_i commute with the quark propagators. Since $\tau_\mp \tau_\pm = 1 \pm \tau_3$ and $\mathrm{tr}\,\tau_3 = 0$, the same result is found for all pions ($l = 0, \pm$),

$$-i\,\Pi_\pi^{\gtrless}(k) = -4N_f N_c \int \frac{d^4p}{(2\pi)^4} \left[-\mathrm{S}_s^{\gtrless}(p)\,\mathrm{S}_s^{\lessgtr}(p-k) + \mathrm{S}_\mu^{\gtrless}(p)\,\mathrm{S}_{\lessgtr}^{\mu}(p-k) \right] . \tag{3.20}$$

From Eq. (2.10) and $\Pi_0^{\gtrless} = \Pi_+^{\gtrless} = \Pi_-^{\gtrless}$ follows that

$$\Delta_0^{\gtrless}(k) = \Delta_+^{\gtrless}(k) = \Delta_-^{\gtrless}(k)\,. \tag{3.21}$$

Thus, we can introduce a universal pion propagator Δ_π, as already done in Eq. (3.12). Of course, this simplification of the formalism is only possible in flavor symmetric systems. In flavor asymmetric matter the quark propagators have a non-trivial structure in flavor space and will not commute with the isospin matrices τ_i. Different results will then be found for the polarizations of π^0, π^+, and π^-.

We can replace the quark propagators in Eqs. (3.19) and (3.20) by spectral functions and distribution functions $\mathrm{n_F}$. This yields

$$\begin{aligned} i\,\Pi_{\sigma,\pi}^{>}(k) = 4N_f N_c \int \frac{d^4p}{(2\pi)^4} &[1 - \mathrm{n_F}(p_0)]\mathrm{n_F}(p_0 - k_0) \\ &\times [\pm\mathcal{A}_s(p)\mathcal{A}_s(p-k) + \mathcal{A}_\mu(p)\mathcal{A}^\mu(p-k)] \end{aligned}$$

and

$$-i\,\Pi^{<}_{\sigma,\pi}(k) = -4N_f N_c \int \frac{d^4p}{(2\pi)^4} \mathrm{n_F}(p_0)[1-\mathrm{n_F}(p_0-k_0)] \\ \times [\pm\mathcal{A}_s(p)\mathcal{A}_s(p-k) + \mathcal{A}_\mu(p)\mathcal{A}^\mu(p-k)] \ ,$$

where the upper signs in the integrands refer to the sigma polarizations and the lower sign to the pion polarizations. The widths of the RPA mesons are then found with the help of Eq. (2.54), $k_0\Gamma_l(k) = -\mathrm{Im}\,\Pi^{\mathrm{ret}}_l(k) = [i\,\Pi^{>}_l(k) - i\,\Pi^{<}_l(k)]/2$,

$$\Gamma_{\sigma,\pi}(k) = \frac{2N_f N_c}{k_0} \int \frac{d^4p}{(2\pi)^4} [\mathrm{n_F}(p_0-k_0) - \mathrm{n_F}(p_0)] \\ \times [\pm\mathcal{A}_s(p)\mathcal{A}_s(p-k) + \mathcal{A}_\mu(p)\mathcal{A}^\mu(p-k)] \ . \tag{3.22}$$

Note that the integral is antisymmetric in k. To see that, we have to perform the substitution $p \to p - \frac{1}{2}k$,

$$\int \frac{d^4p}{(2\pi)^4} [\mathrm{n_F}(p_0-\tfrac{1}{2}k_0) - \mathrm{n_F}(p_0+\tfrac{1}{2}k_0)] \\ \times \left[\pm\mathcal{A}_s(p+\tfrac{1}{2}k)\mathcal{A}_s(p-\tfrac{1}{2}k) + \mathcal{A}_\mu(p+\tfrac{1}{2}k)\mathcal{A}^\mu(p-\tfrac{1}{2}k)\right] \ .$$

Obviously, the first part of the integrand is antisymmetric while the second part is symmetric in k. It follows from the first part that the integral is antisymmetric in k_0. This is not surprising since the widths depend only on k_0 and $|\vec{k}\,|$. The factor $1/k_0$ in front of the integral in (3.22) turns the antisymmetry into a symmetry for $\Gamma_{\sigma,\pi}(k)$.

For $T = 0$ the distribution function $\mathrm{n_F}$ becomes a simple step function (2.29). This can be used to rewrite the p_0 integration,

$$\int_{-\infty}^{+\infty} dp_0 [\mathrm{n_F}(p_0-k_0) - \mathrm{n_F}(p_0)] \cdots \quad \xrightarrow{T=0} \quad \int_{\mu}^{\mu+k_0} dp_0 \cdots \ . \tag{3.23}$$

3.5 Dispersion integrals

In the previous sections we have shown how to calculate the mean-field self-energy and the imaginary parts of the retarded self-energy and polarizations. The properties of the quark and RPA meson spectral functions are predominantly determined by these quantities. The imaginary parts describe the effects of collisional broadening. The mean-field self-energy, on the other hand, is the main contribution to the effective quark mass and thus determines also the properties of the chiral phase transition. Nonetheless, for a complete description of the spectral functions it is also necessary to consider the contributions to $\mathrm{Re}\,\Sigma^{\mathrm{ret}}$ and $\mathrm{Re}\,\Pi^{\mathrm{ret}}_l$ that arise from the diagrams shown in Fig. 3.3.

Figure 3.3: Diagrams that yield complex contributions to the time-ordered and retarded quark self-energies and RPA meson polarizations.

In the NJL model, cutoffs are used to regularize momentum integrals. Besides other effects, such cutoffs yield a violation of analyticity – i.e., the analytic connection between the real and the imaginary parts of the complex self-energy and the RPA polarizations is destroyed. This gives us two choices for our calculation. The first choice is to sacrifice analyticity and to calculate both, the real and the imaginary parts, using the Feynman rules of the real-time formalism. As a consequence, some properties of the spectral functions – like the normalization of $\mathcal{A}(k)$ (2.28) – would be lost. The second choice is to calculate only the real or the imaginary parts directly and to use dispersion integrals to determine their counterparts. This approach ensures that analyticity is preserved. However, even without cutoffs the results from a dispersion integral might differ from a direct calculation. This point is discussed in Appendix F. Note that the mean-field self-energy is time-local (see Section 2.8.1) in coordinate space and thus energy independent in momentum space, cf. Eq. (3.1). Consequently, Σ^{mf} is purely real and has no influence on the analyticity of the full quark self-energy. It can be calculated separately in both cases.

Our main interest in the present work is to investigate the collisional broadening of the spectral functions. For the self-consistent approach it is more reasonable to preserve analyticity – and thus, e.g., the proper normalization of the quark spectral function – than to calculate the real parts of the diagrams in Fig. 3.3 directly. Therefore, we will calculate only $\mathrm{Im}\,\Sigma^{\mathrm{ret}}$ and $\mathrm{Im}\,\Pi_l^{\mathrm{ret}}$ from the Feynman rules as shown in Sections 3.3 and 3.4. The real parts are determined by the dispersion relations

$$\begin{aligned} \mathrm{Re}\,\Sigma^{\mathrm{ret}}(k_0,\vec{k}\,) &= \Sigma^{\mathrm{mf}} + \frac{1}{2\pi}\;\mathcal{P}\int\limits_{-\infty}^{+\infty} dp_0 \frac{\Gamma(p_0,\vec{k}\,)}{k_0-p_0} + \text{const.}\,, \\ \mathrm{Re}\,\Pi_l^{\mathrm{ret}}(k_0,\vec{k}\,) &= \frac{1}{\pi}\,\mathcal{P}\int\limits_{0}^{\infty} dp_0^2 \frac{p_0\Gamma_l(p_0,\vec{k}\,)}{k_0^2-p_0^2} + \text{const.} \end{aligned} \tag{3.24}$$

In the second line we have used the antisymmetry of $p_0\Gamma_l$ that has been mentioned after Eq. (3.22).

Constant – or at least energy independent – contributions to $\mathrm{Re}\,\Sigma^{\mathrm{ret}}$ and $\mathrm{Re}\,\Pi_l^{\mathrm{ret}}$ do not interfere with analyticity and cannot be calculated from dispersion integrals. Those shifts may have significant influence on the quark or meson properties and should not be ignored. For example, the masses of the RPA pions depend strongly on the inclusion of such constant terms, cf. Fig. 2.15. We must calculate them separately

and add them to the dispersion integrals, as shown in (3.24). To identify the energy independent terms[2], a closer investigation of the real parts that are given by the Feynman rules is necessary.

The Feynman rules provide no direct access to the retarded self-energy and polarizations [Dan84, Das97] since – in coordinate space – the positions of the time coordinates on the two branches of the time-path contour in Fig. 2.16 are not well-defined, cf. (2.18). To search for constant terms, we can start from the time-ordered self-energy Σ^{c} and polarizations Π_l^{c}. They are related to Σ^{ret} and Π_l^{ret} in a simple way [Das97]:

$$\begin{aligned}
\mathrm{Re}\,\Sigma^{\mathrm{c}}(k) &= \mathrm{Re}\,\Sigma^{\mathrm{ret}}(k)\,, \\
\mathrm{Re}\,\Pi_l^{\mathrm{c}}(k) &= \mathrm{Re}\,\Pi_l^{\mathrm{ret}}(k)\,, \\
\mathrm{Im}\,\Sigma^{\mathrm{c}}(k) &= [1-2\mathrm{n_F}(k_0)]\mathrm{Im}\,\Sigma^{\mathrm{ret}}(k)\,, \\
\mathrm{Im}\,\Pi_l^{\mathrm{c}}(k) &= [1+2\mathrm{n_B}(k_0)]\mathrm{Im}\,\Pi_l^{\mathrm{ret}}(k)\,,
\end{aligned} \tag{3.25}$$

with the zero temperature limits $1-2\mathrm{n_F}(k_0) \to \mathrm{sgn}(k_0-\mu)$ and $1+2\mathrm{n_B}(k_0) \to \mathrm{sgn}(k_0)$. Note that $1-2\mathrm{n_F}(k_0) = \tanh(\beta(k_0-\mu)/2)$ and $1+2\mathrm{n_B}(k_0) = \coth(\beta k_0/2)$, cf. Eqs. (G.2,G.4). The imaginary parts of Σ^{ret} and Π_l^{ret} that are found in this approach should of course be equivalent to the widths that we have found earlier (3.16,3.22). In fact, this will be demonstrated below.

3.6 Real parts of the RPA meson polarizations

In the following we will examine the complex polarizations, not only the real parts, to identify constant contributions to $\mathrm{Re}\,\Pi_l^{\mathrm{ret}}$. Therefore, we will construct an expression for the retarded polarizations that contains only retarded and advanced propagators. From that expression we will also construct the meson widths to check our result from Section 3.4. In this section we will frequently use the relations between the different kinds of propagators ($\mathrm{S}^{\mathrm{c}}, \mathrm{S}^{\mathrm{ret}}, \mathrm{S}^{\gtrless}$) that are summarized in Eqs. (2.32) without further reference.

3.6.1 Time-ordered and retarded polarizations

The time-ordered polarizations of the RPA mesons (cf. Fig. 3.3) are given by

$$-i\,\Pi_l^{\mathrm{c}}(k) = -\int \frac{d^4p}{(2\pi)^4}\,\mathrm{Tr}\left[\tilde{\Gamma}_l\,\mathrm{S}^{\mathrm{c}}(p)\Gamma_l\,\mathrm{S}^{\mathrm{c}}(p-k)\right]\,. \tag{3.26}$$

[2]The Fock self-energy that is hidden in the RPA meson exchange is an example for such a term. Since the Fock self-energy is – like the Hartree self-energy – constant and purely real, it cannot be calculated dispersively from the imaginary part of the collisional self-energy.

We can replace the time-ordered propagators by retarded and non-ordered propagators, $\mathrm{S}^{\mathrm{c}}(k) = \mathrm{S}^{\mathrm{ret}}(k) + \mathrm{S}^{<}(k)$. This yields

$$-i\,\Pi_l^{\mathrm{c}}(k) = -\int \frac{d^4p}{(2\pi)^4}\,\mathrm{Tr}\Big[\tilde{\Gamma}_l\,\mathrm{S}^{\mathrm{ret}}(p)\Gamma_l\,\mathrm{S}^{\mathrm{ret}}(p-k) + \tilde{\Gamma}_l\,\mathrm{S}^{\mathrm{ret}}(p)\Gamma_l\,\mathrm{S}^{<}(p-k) + \tilde{\Gamma}_l\,\mathrm{S}^{<}(p)\Gamma_l\,\mathrm{S}^{\mathrm{ret}}(p-k) + \tilde{\Gamma}_l\,\mathrm{S}^{<}(p)\Gamma_l\,\mathrm{S}^{<}(p-k)\Big]\,. \tag{3.27}$$

The first part of this integral, $\int \tilde{\Gamma}_l\,\mathrm{S}^{\mathrm{ret}}\,\Gamma_l\,\mathrm{S}^{\mathrm{ret}}$, is zero: Since the poles of both retarded propagators are located in the same half plane [Das97], the p_0 integral can be closed along a contour in the other half plane so that no poles are included. More details can be found in Appendix D. After inserting $\mathrm{S}^{\mathrm{ret}}(k) = \mathrm{Re}\,\mathrm{S}^{\mathrm{ret}}(k) - \frac{i}{2}\mathcal{A}(k)$ and $\mathrm{S}^{<}(k) = i\mathcal{A}(k)\mathrm{n}_{\mathrm{F}}(k_0)$, the polarizations Π_l^{c} can be split up into their real and imaginary parts:

$$\mathrm{Re}\,\Pi_l^{\mathrm{c}}(k) = \int \frac{d^4p}{(2\pi)^4}\,\mathrm{Tr}\Big[\tilde{\Gamma}_l \mathrm{Re}\,\mathrm{S}^{\mathrm{ret}}(p)\Gamma_l\mathcal{A}(p-k)\mathrm{n}_{\mathrm{F}}(p_0-k_0) + \tilde{\Gamma}_l\mathcal{A}(p)\Gamma_l\mathrm{Re}\,\mathrm{S}^{\mathrm{ret}}(p-k)\mathrm{n}_{\mathrm{F}}(p_0)\Big]\,, \tag{3.28}$$

$$\mathrm{Im}\,\Pi_l^{\mathrm{c}}(k) = \frac{1}{2}\int \frac{d^4p}{(2\pi)^4}[\mathrm{n}_{\mathrm{F}}(p_0) - \mathrm{n}_{\mathrm{F}}(p_0-k_0)][1+2\mathrm{n}_{\mathrm{B}}(k_0)] \times \mathrm{Tr}\Big[\tilde{\Gamma}_l\mathcal{A}(p)\Gamma_l\mathcal{A}(p-k)\Big]\,, \tag{3.29}$$

where we have used the relation

$$\mathrm{n}_{\mathrm{F}}(p) + \mathrm{n}_{\mathrm{F}}(p-k) - 2\mathrm{n}_{\mathrm{F}}(p)\mathrm{n}_{\mathrm{F}}(p-k) = [\mathrm{n}_{\mathrm{F}}(p-k) - \mathrm{n}_{\mathrm{F}}(p)][1+2\mathrm{n}_{\mathrm{B}}(k)]$$

in the derivation of the imaginary parts. The proof for this relation can be found in Appendix G. $\mathrm{Re}\,\Pi_l^{\mathrm{ret}}(k)$ and $\mathrm{Im}\,\Pi_l^{\mathrm{ret}}(k)$ can be directly read off from Eqs. (3.28) and (3.29) with the help of the relations in (3.25). Note that the result for $\mathrm{Im}\,\Pi_l^{\mathrm{ret}}(k)$ that we have found here is identical to the result for the meson widths in Eq. (3.22) that was found from the collisional polarizations, $i[\Pi^{>}(k) - \Pi^{<}(k)]/2k_0$.

The real and imaginary parts of Π_l^{ret} can be combined to obtain an expression for the complex polarization $\Pi_l^{\mathrm{ret}}(k)$:

$$\Pi_l^{\mathrm{ret}}(k) = \int \frac{d^4p}{(2\pi)^4}\,\mathrm{Tr}\Big[\tilde{\Gamma}_l[\mathrm{Re}\,\mathrm{S}^{\mathrm{ret}}(p) - \frac{i}{2}\mathcal{A}(p)]\Gamma_l\mathcal{A}(p-k)\mathrm{n}_{\mathrm{F}}(p_0-k_0) + \tilde{\Gamma}_l\mathcal{A}(p)\Gamma_l[\mathrm{Re}\,\mathrm{S}^{\mathrm{ret}}(p-k) + \frac{i}{2}\mathcal{A}(p-k)]\mathrm{n}_{\mathrm{F}}(p_0)\Big]\,.$$

Using $\mathrm{S}^{*}_{\mathrm{ret}}(k) = \mathrm{S}^{\mathrm{av}}(k)$ and making the replacement $i\mathcal{A}(k)\mathrm{n}_{\mathrm{F}}(k_0) = \mathrm{S}^{<}(k)$, we find a more compact form,

$$\Pi_l^{\mathrm{ret}}(k) = -i\int \frac{d^4p}{(2\pi)^4}\,\mathrm{Tr}\Big[\tilde{\Gamma}_l\,\mathrm{S}^{\mathrm{ret}}(p)\Gamma_l\,\mathrm{S}^{<}(p-k) + \tilde{\Gamma}_l\,\mathrm{S}^{<}(p)\Gamma_l\,\mathrm{S}^{\mathrm{av}}(p-k)\Big]\,. \tag{3.30}$$

3.6.2 Decomposition of the RPA polarizations

The purpose of the following – rather technical – manipulations is to isolate the non-dispersive part of $\mathrm{Re}\,\Pi^{\mathrm{ret}}$. First, we bring the integrands in Eqs. (3.27) and (3.30) into a more symmetric form by shifting the integration variable by $\frac{1}{2}k$, i.e., $p \to p - \frac{1}{2}k$. In addition, we introduce the shorthand notation[3], cf. (2.34),

$$\begin{aligned} \mathrm{S}_{\pm}^{\gtrless,\mathrm{ret,av}} &= \mathrm{S}^{\gtrless,\mathrm{ret,av}}(p_{\pm}) & \tilde{p}_{\pm,\mu}^{\mathrm{ret,av}} &= p_{\mu}^{\pm} - \Sigma_{\mu}^{\mathrm{ret,av}}(p_{\pm}) \\ \mathrm{n}_{\mathrm{F}}^{\pm} &= \mathrm{n}_{\mathrm{F}}(p_0^{\pm}) & \tilde{m}_{\pm}^{\mathrm{ret,av}} &= m_0 + \Sigma_s^{\mathrm{ret,av}}(p_{\pm})\,, \end{aligned}$$

where $p_{\pm} = p \pm \frac{1}{2}k$. This yields the more compact form

$$\begin{aligned} \Pi_l^{\mathrm{ret}}(k) &= -i \int \frac{d^4p}{(2\pi)^4}\, \mathrm{Tr}\left[\tilde{\Gamma}_l\, \mathrm{S}_+^{\mathrm{ret}}\, \Gamma_l\, \mathrm{S}_-^{<} + \tilde{\Gamma}_l\, \mathrm{S}_+^{<}\, \Gamma_l\, \mathrm{S}_-^{\mathrm{av}}\right], \\ \Pi_l^{\mathrm{c}}(k) &= -i \int \frac{d^4p}{(2\pi)^4}\, \mathrm{Tr}\left[\tilde{\Gamma}_l\, \mathrm{S}_+^{\mathrm{ret}}\, \Gamma_l\, \mathrm{S}_-^{\mathrm{ret}} + \tilde{\Gamma}_l\, \mathrm{S}_+^{\mathrm{ret}}\, \Gamma_l\, \mathrm{S}_-^{<} + \tilde{\Gamma}_l\, \mathrm{S}_+^{<}\, \Gamma_l\, \mathrm{S}_-^{\mathrm{ret}} + \tilde{\Gamma}_l\, \mathrm{S}_+^{<}\, \Gamma_l\, \mathrm{S}_-^{<}\right]. \end{aligned}$$

Next, we replace the non-ordered propagators in the integrands by $\mathrm{S}_{\pm}^{<} = [\mathrm{S}_{\pm}^{\mathrm{av}} - \mathrm{S}_{\pm}^{\mathrm{ret}}]\mathrm{n}_{\mathrm{F}}^{\pm}$ to get expressions for the polarizations $\Pi^{\mathrm{c,ret}}$ that contain only retarded and advanced propagators. We find

$$\begin{aligned} \Pi_l^{\mathrm{ret}}(k) = -i \int \frac{d^4p}{(2\pi)^4}\, \mathrm{Tr}\Big[&-\tilde{\Gamma}_l\, \mathrm{S}_+^{\mathrm{ret}}\, \Gamma_l\, \mathrm{S}_-^{\mathrm{ret}}\, \mathrm{n}_{\mathrm{F}}^{-} + \tilde{\Gamma}_l\, \mathrm{S}_+^{\mathrm{av}}\, \Gamma_l\, \mathrm{S}_-^{\mathrm{av}}\, \mathrm{n}_{\mathrm{F}}^{+} \\ &+ \tilde{\Gamma}_l\, \mathrm{S}_+^{\mathrm{ret}}\, \Gamma_l\, \mathrm{S}_-^{\mathrm{av}} \left\{\mathrm{n}_{\mathrm{F}}^{-} - \mathrm{n}_{\mathrm{F}}^{+}\right\}\Big], \end{aligned} \tag{3.31}$$

and

$$\begin{aligned} \Pi_l^{\mathrm{c}}(k) = -i \int \frac{d^4p}{(2\pi)^4}\, \mathrm{Tr}\Big[&\tilde{\Gamma}_l\, \mathrm{S}_+^{\mathrm{ret}}\, \Gamma_l\, \mathrm{S}_-^{\mathrm{ret}}(1-\mathrm{n}_{\mathrm{F}}^{+})(1-\mathrm{n}_{\mathrm{F}}^{-}) + \tilde{\Gamma}_l\, \mathrm{S}_+^{\mathrm{av}}\, \Gamma_l\, \mathrm{S}_-^{\mathrm{av}}\, \mathrm{n}_{\mathrm{F}}^{+}\mathrm{n}_{\mathrm{F}}^{-} \\ &+ \tilde{\Gamma}_l\, \mathrm{S}_+^{\mathrm{ret}}\, \Gamma_l\, \mathrm{S}_-^{\mathrm{av}}(1-\mathrm{n}_{\mathrm{F}}^{+})\mathrm{n}_{\mathrm{F}}^{-} + \tilde{\Gamma}_l\, \mathrm{S}_+^{\mathrm{av}}\, \Gamma_l\, \mathrm{S}_-^{\mathrm{ret}}\, \mathrm{n}_{\mathrm{F}}^{+}(1-\mathrm{n}_{\mathrm{F}}^{-})\Big]. \end{aligned} \tag{3.32}$$

The integrand of Π_l^{c} has an interesting structure. Each propagator $\mathrm{S}^{\mathrm{ret}}$ is connected to a factor $(1 - \mathrm{n}_{\mathrm{F}})$ and each propagator S^{av} to a factor n_{F}. We will come back to that aspect later.

At first glance the new expressions for Π_l^{ret} and Π_l^{c} look more complicated than the ones in Eqs. (3.27,3.30). However, they are a good starting point for our search for the energy independent components of $\mathrm{Re}\,\Pi_l^{\mathrm{c,ret}}(k)$. Eqs. (3.31,3.32) contain only retarded and advanced quark propagators in the integrals. Those propagators have a structure that – even in an interacting medium – resembles the structure of the free propagators. Thus, an investigation similar to the Hartree+RPA approach at $T = \mu = 0$ – see Appendix B and [Kle92] for details – is possible.

[3] Note that the effective masses that are defined here are complex and four-momentum dependent. The mean-field self-energy Σ^{mf} is included in $\Sigma_s^{\mathrm{ret,av}}$, cf. Eq. (2.49).

The full in-medium quark propagators are given explicitly in Eq. (2.35). Instead of inserting the explicit forms of the retarded and advanced propagators into the integrands of Eqs. (3.31) or (3.32) right away, we will investigate the more general expression $\mathrm{Tr}\,\tilde{\Gamma}_l\,\mathrm{S}_+\,\Gamma_l\,\mathrm{S}_-$ first. In this trace, S_+ and S_- each represent either a retarded or an advanced propagator. Thus the indices $\pm$ do not only mark the four-momentum but implicitly also the kind (ret, av) of the propagators and the self-energies contained in them. Later we can derive expressions for specific combinations of retarded and advanced propagators from this general form. Inserting the explicit forms of the propagators (2.35) and the matrices $\tilde{\Gamma}_l, \Gamma_l$ into the general trace, we get

$$\mathrm{Tr}\,\tilde{\Gamma}_{\sigma,\pi}\,\mathrm{S}_+\,\Gamma_{\sigma,\pi}\,\mathrm{S}_- = 4N_f N_c \frac{\tilde{p}_\mu^+ \tilde{p}_-^\mu \pm \tilde{m}_+ \tilde{m}_-}{(\tilde{p}_+^2 - \tilde{m}_+^2)(\tilde{p}_-^2 - \tilde{m}_-^2)}\,. \tag{3.33}$$

In the numerator, the upper sign refers to the σ and the lower sign to the π case, respectively. We find the same result for all pions $(0, \pm)$ in isospin symmetric matter, thus Γ_π is used here as a shorthand notation for $\Gamma_{0,\pm}$. Note that the numerator would take the simpler form $p^2 - \frac{1}{4}k^2 \pm m^{*2}$ in the Hartree approximation, cf. (B.1), where $\Sigma_s^{\mathrm{ret,av}}(k) = \Sigma^{\mathrm{mf}}$ and $\Sigma_{0,v}^{\mathrm{ret,av}} = 0$.

We can rewrite the denominator of Eq. (3.33) in terms of partial fractions,

$$\frac{1}{(\tilde{p}_+^2 - \tilde{m}_+^2)(\tilde{p}_-^2 - \tilde{m}_-^2)} = \left[\frac{1}{\tilde{p}_+^2 - \tilde{m}_+^2} + \frac{1}{\tilde{p}_-^2 - \tilde{m}_-^2}\right](\tilde{p}_+^2 + \tilde{p}_-^2 - \tilde{m}_+^2 - \tilde{m}_-^2)^{-1}\,. \tag{3.34}$$

The inverse of the second factor on the rhs. can also be isolated in the numerator of (3.33),

$$\tilde{p}_\mu^+ \tilde{p}_-^\mu \pm \tilde{m}_+ \tilde{m}_- = \frac{1}{2}[\tilde{p}_+^2 + \tilde{p}_-^2 - \tilde{m}_+^2 - \tilde{m}_-^2] - \frac{1}{2}[(\tilde{p}_+ - \tilde{p}_-)^2 - (\tilde{m}_+ \pm \tilde{m}_-)^2]\,. \tag{3.35}$$

Combining the two expressions (3.34) and (3.35) we obtain for the general trace:

$$\begin{aligned}&\mathrm{Tr}\,\tilde{\Gamma}_{\sigma,\pi}\,\mathrm{S}_+\,\Gamma_{\sigma,\pi}\,\mathrm{S}_- \\ &\quad = \frac{1}{2}N_f N_c\,\mathrm{tr}\left[\frac{\mathrm{S}_+}{\tilde{m}_+} + \frac{\mathrm{S}_-}{\tilde{m}_-}\right] - 2N_f N_c \frac{(\tilde{p}_+ - \tilde{p}_-)^2 - (\tilde{m}_+ \pm \tilde{m}_-)^2}{(\tilde{p}_+^2 - \tilde{m}_+^2)(\tilde{p}_-^2 - \tilde{m}_-^2)}\,,\end{aligned} \tag{3.36}$$

where we have used Eq. (2.35) to rewrite the first term on the rhs.,

$$\frac{1}{\tilde{p}^2 - \tilde{m}^2} = \frac{1}{4\tilde{m}}\,\mathrm{tr}\,\frac{\not{\tilde{p}} + \tilde{m}}{\tilde{p}^2 - \tilde{m}^2} = \frac{1}{4\tilde{m}}\,\mathrm{tr}\,\mathrm{S}(p)\,.$$

3.6.3 The non-dispersive part of the RPA polarizations

The first part of the rhs. of Eq. (3.36) corresponds to a constant contribution to the real parts of the meson polarizations. It has the same value for all RPA mesons. It can generate a pion mass and thus may spoil the Goldstone boson character of the

RPA pions. The second part of the rhs. of Eq. (3.36) is complex. The real part can in principle be calculated from a dispersion integral. Energy independent shifts that might arise from this term – depending on how the dispersion integral is calculated – will be discussed later.

Inserting the first term on the rhs. of (3.36) into the retarded polarizations (3.31), i.e., identifying the propagators $\mathrm{S}_\pm$ with the different combinations of retarded and advanced propagators, yields for the non-dispersive, constant part of the meson polarizations

$$\Pi_\mathrm{n} = -\frac{i}{2} N_f N_c \int \frac{d^4p}{(2\pi)^4} \,\mathrm{tr}\left[\frac{\mathrm{S}_+^\mathrm{av}}{\tilde{m}_+^\mathrm{av}}\mathrm{n}_\mathrm{F}^+ - \frac{\mathrm{S}_+^\mathrm{ret}}{\tilde{m}_+^\mathrm{ret}}\mathrm{n}_\mathrm{F}^+ + \frac{\mathrm{S}_-^\mathrm{av}}{\tilde{m}_-^\mathrm{av}}\mathrm{n}_\mathrm{F}^- - \frac{\mathrm{S}_-^\mathrm{ret}}{\tilde{m}_-^\mathrm{ret}}\mathrm{n}_\mathrm{F}^-\right] .$$

In the integrand, four of the initial eight terms have canceled each other. The same result would be found by inserting the first term on the rhs. of (3.36) into the integral for $\Pi_l^\mathrm{c}(k)$, with the help of (D.5). After splitting up the integrand into a "+" and a "−" part and applying the substitutions $p \to p \pm \frac{1}{2}k$, we get

$$\Pi_\mathrm{n} = -iN_f N_c \int \frac{d^4p}{(2\pi)^4} \,\mathrm{tr}\left[\frac{\mathrm{S}^\mathrm{av}(p)}{\tilde{m}^\mathrm{av}} - \frac{\mathrm{S}^\mathrm{ret}(p)}{\tilde{m}^\mathrm{ret}}\right] \mathrm{n}_\mathrm{F}(p_0) .$$

Note that $\mathrm{S}^\mathrm{av} - \mathrm{S}^\mathrm{ret} = -2\mathrm{Im}\,\mathrm{S}^\mathrm{ret} = \mathcal{A}$. In contrast to the mean-field case, this relation cannot be used directly here, cf. Eq. (B.4), since the effective masses $\tilde{m}^\mathrm{ret}$ and $\tilde{m}^\mathrm{av}$ are not equal. Replacing the propagators by the explicit expressions (2.35) again and using $\tilde{p}^*_\mathrm{ret} = \tilde{p}_\mathrm{av}$, $\tilde{m}^*_\mathrm{ret} = \tilde{m}_\mathrm{av}$ leads to

$$\Pi_\mathrm{n} = -4iN_f N_c \int \frac{d^4p}{(2\pi)^4}(-2i)\mathrm{Im}\frac{1}{\tilde{p}^2_\mathrm{ret} - \tilde{m}^2_\mathrm{ret}}\mathrm{n}_\mathrm{F}(p_0) . \tag{3.37}$$

In a pure mean-field calculation, this integral would closely resemble the Hartree self-energy Σ^H and could be replaced accordingly, cf. (B.4,B.5). A similar approach is possible in the full calculation. The mean-field self-energy – that is identical to the Hartree self-energy here – is given by Eq. (3.2). Using $\mathcal{A}(k) = -2\mathrm{Im}\,\mathrm{S}^\mathrm{ret}(k)$ and working out the trace yields

$$\Sigma^\mathrm{mf} = -2\mathrm{G}\int \frac{d^4p}{(2\pi)^4}\,\mathrm{Tr}\,\mathcal{A}(p)\mathrm{n}_\mathrm{F}(p_0) = 16\mathrm{G}N_f N_c \int \frac{d^4p}{(2\pi)^4}\mathrm{Im}\frac{\tilde{m}^2_\mathrm{ret}}{\tilde{p}^2_\mathrm{ret} - \tilde{m}^2_\mathrm{ret}}\mathrm{n}_\mathrm{F}(p_0) .$$

Introducing $\Sigma^s_\mathrm{const.}$, the sum of all constant contributions to $\Sigma_s^\mathrm{c,ret}$, we can split up the integral

$$\begin{aligned}\Sigma^\mathrm{mf} = 16\mathrm{G}N_f N_c(m_0 + \Sigma^s_\mathrm{const.}) \int \frac{d^4p}{(2\pi)^4}\mathrm{Im}\frac{1}{\tilde{p}^2_\mathrm{ret} - \tilde{m}^2_\mathrm{ret}}\mathrm{n}_\mathrm{F}(p_0) \\ +16\mathrm{G}N_f N_c \int \frac{d^4p}{(2\pi)^4}\mathrm{Im}\frac{\Sigma_s^\mathrm{ret}(p) - \Sigma^s_\mathrm{const.}}{\tilde{p}^2_\mathrm{ret} - \tilde{m}^2_\mathrm{ret}}\mathrm{n}_\mathrm{F}(p_0) .\end{aligned} \tag{3.38}$$

The mean-field self-energy $\Sigma^{\rm mf}$ is the largest constant contribution to $\Sigma_s^{\rm c,ret}$ when chiral symmetry is spontaneously broken. We will show in Section 3.8 how to calculate the other components of $\Sigma^s_{\rm const.}$.

The first integral in (3.38) is equivalent to the one in Eq. (3.37). Thus we get for the non-dispersive part of the RPA polarizations

$$\Pi_{\rm n} = -\frac{1}{2{\rm G}}\frac{\Sigma^{\rm mf}}{m_0+\Sigma^s_{\rm const.}} + \frac{8N_fN_c}{m_0+\Sigma^s_{\rm const.}}\int\frac{d^4p}{(2\pi)^4}{\rm Im}\frac{\Sigma_s^{\rm ret}(p)-\Sigma^s_{\rm const.}}{\tilde p^2_{\rm ret}-\tilde m^2_{\rm ret}}{\rm n_F}(p_0)\,. \tag{3.39}$$

The second term results from using full propagators. In the Hartree(–Fock) approximation, where $\Sigma_s^{\rm ret}(k) = \Sigma^{\rm H}(+\Sigma^{\rm F})$, this term will vanish. Note that the value of $\Sigma^s_{\rm const.}$ can in principle be freely chosen. The first term of (3.39) corresponds to the result of the Hartree(–Fock) approximation (B.5) when $\Sigma^s_{\rm const.}$ is set to $\Sigma^{\rm H}(+\Sigma^{\rm F})$.

3.6.4 The dispersive part of the RPA polarizations

We turn now to the second part of Eq. (3.36). Inserting this expression into Eq. (3.31), i.e. identifying the $\rm S_\pm$ with the different combinations of retarded and advanced propagators, we find for the dispersive part of the retarded polarizations

$$\begin{aligned}\Pi^{\rm ret}_{{\rm d},l}(k) = 2iN_fN_c\int\frac{d^4p}{(2\pi)^4}\Bigg[&-\frac{(\tilde p^{\rm ret}_+-\tilde p^{\rm ret}_-)^2-(\tilde m^{\rm ret}_+\pm\tilde m^{\rm ret}_-)^2}{(\tilde p^{\rm ret\,2}_+-\tilde m^{\rm ret\,2}_+)(\tilde p^{\rm ret\,2}_--\tilde m^{\rm ret\,2}_-)}{\rm n_F^-}\\ &+\frac{(\tilde p^{\rm av}_+-\tilde p^{\rm av}_-)^2-(\tilde m^{\rm av}_+\pm\tilde m^{\rm av}_-)^2}{(\tilde p^{\rm av\,2}_+-\tilde m^{\rm av\,2}_+)(\tilde p^{\rm av\,2}_--\tilde m^{\rm av\,2}_-)}{\rm n_F^+}\\ &+\frac{(\tilde p^{\rm ret}_+-\tilde p^{\rm av}_-)^2-(\tilde m^{\rm ret}_+\pm\tilde m^{\rm av}_-)^2}{(\tilde p^{\rm ret\,2}_+-\tilde m^{\rm ret\,2}_+)(\tilde p^{\rm av\,2}_--\tilde m^{\rm av\,2}_-)}({\rm n_F^- - n_F^+})\Bigg]\,,\end{aligned} \tag{3.40}$$

and in the same way for the time-ordered polarizations

$$\begin{aligned}\Pi^{\rm c}_{{\rm d},l}(k) = 2iN_fN_c\int\frac{d^4p}{(2\pi)^4}\Bigg[&\frac{(\tilde p^{\rm ret}_+-\tilde p^{\rm ret}_-)^2-(\tilde m^{\rm ret}_+\pm\tilde m^{\rm ret}_-)^2}{(\tilde p^{\rm ret\,2}_+-\tilde m^{\rm ret\,2}_+)(\tilde p^{\rm ret\,2}_--\tilde m^{\rm ret\,2}_-)}({\rm 1-n_F^+})({\rm 1-n_F^-})\\ &+\frac{(\tilde p^{\rm av}_+-\tilde p^{\rm av}_-)^2-(\tilde m^{\rm av}_+\pm\tilde m^{\rm av}_-)^2}{(\tilde p^{\rm av\,2}_+-\tilde m^{\rm av\,2}_+)(\tilde p^{\rm av\,2}_--\tilde m^{\rm av\,2}_-)}{\rm n_F^+n_F^-}\\ &+\frac{(\tilde p^{\rm ret}_+-\tilde p^{\rm av}_-)^2-(\tilde m^{\rm ret}_+\pm\tilde m^{\rm av}_-)^2}{(\tilde p^{\rm ret\,2}_+-\tilde m^{\rm ret\,2}_+)(\tilde p^{\rm av\,2}_--\tilde m^{\rm av\,2}_-)}({\rm 1-n_F^+}){\rm n_F^-}\\ &+\frac{(\tilde p^{\rm av}_+-\tilde p^{\rm ret}_-)^2-(\tilde m^{\rm av}_+\pm\tilde m^{\rm ret}_-)^2}{(\tilde p^{\rm av\,2}_+-\tilde m^{\rm av\,2}_+)(\tilde p^{\rm ret\,2}_--\tilde m^{\rm ret\,2}_-)}{\rm n_F^+}({\rm 1-n_F^-})\Bigg]\,.\end{aligned} \tag{3.41}$$

Due to the mixture of retarded and advanced quantities and the Fermi distributions, a simplification of these integrals seems rather complicated. However, at least for $T = 0$ it is possible to bring the integrand in Eq. (3.41) into a much simpler form.

Besides the distribution functions, the four terms in the integrand differ only in the retarded and advanced quark self-energies that are part of the effective masses and momenta. Using (3.25) and $\Sigma^*_{\rm ret}(k) = \Sigma^{\rm av}(k)$ we find

$$\mathrm{Im}\,\Sigma^{\rm c}(k) = [1 - 2\mathrm{n_F}(k_0)]\mathrm{Im}\,\Sigma^{\rm ret}(k) = -[1 - 2\mathrm{n_F}(k_0)]\mathrm{Im}\,\Sigma^{\rm av}(k)\,.$$

For $T = 0$, the factor $1 - 2\mathrm{n_F}(k_0)$ reduces to a simple sign function $\mathrm{sgn}(k_0 - \mu)$. This means that the time-ordered imaginary parts are identical to the retarded ones for $k_0 > \mu$ and identical to the advanced ones for $k_0 < \mu$. Since the real parts of $\Sigma^{\rm c,ret,av}$ are identical (3.25) for all k_0 we get

$$\begin{aligned} \Sigma^{\rm c}(k)\mathrm{n_F}(k_0) &\overset{T=0}{=} \Sigma^{\rm av}(k)\mathrm{n_F}(k_0)\,, \\ \Sigma^{\rm c}(k)[1 - \mathrm{n_F}(k_0)] &\overset{T=0}{=} \Sigma^{\rm ret}(k)[1 - \mathrm{n_F}(k_0)]\,. \end{aligned} \tag{3.42}$$

In the integrand of Eq. (3.41) every retarded quantity is connected to a factor $(1 - \mathrm{n_F})$ while every advanced quantity comes with a factor $\mathrm{n_F}$. In combination with (3.42) it follows that all retarded and advanced quantities can be replaced by time-ordered ones – at $T = 0$ the Fermi distributions ensure that only the energy ranges in which those quantities are identical contribute to the integral. Each of the four terms in the integrand covers a distinct energy range. After the replacement $\mathrm{ret}, \mathrm{av} \to \mathrm{c}$, those terms can be added up and we find

$$\Pi^{\rm c}_{{\rm d},l}(k) \overset{T=0}{=} 2iN_fN_c \int \frac{d^4p}{(2\pi)^4} \frac{(\tilde{p}^{\rm c}_+ - \tilde{p}^{\rm c}_-)^2 - (\tilde{m}^{\rm c}_+ \pm \tilde{m}^{\rm c}_-)^2}{(\tilde{p}^{\rm c\ 2}_+ - \tilde{m}^{\rm c\ 2}_+)(\tilde{p}^{\rm c\ 2}_- - \tilde{m}^{\rm c\ 2}_-)}\,. \tag{3.43}$$

Before we continue, it is important to recall that the constant (i.e., energy independent) terms which are not covered by dispersive integrals can be isolated in the $k_0 \to \pm\infty$ limit, cf. Appendix F. The numerator of the integrand in (3.43) hides some of its features in the present form. By inserting the effective masses and momenta explicitly, we find for the σ and the π case

$$\begin{aligned} (\tilde{p}_+ - \tilde{p}_-)^2 - (\tilde{m}_+ + \tilde{m}_-)^2 &= k^2 - 4M^2 - 2k_\mu \Delta\,\Sigma^\mu + \Delta\,\Sigma_\mu\,\Delta\,\Sigma^\mu\,, \\ (\tilde{p}_+ - \tilde{p}_-)^2 - (\tilde{m}_+ - \tilde{m}_-)^2 &= k^2 - \Delta\,\Sigma_s^2 - 2k_\mu \Delta\,\Sigma^\mu + \Delta\,\Sigma_\mu\,\Delta\,\Sigma^\mu\,, \end{aligned} \tag{3.44}$$

with $\Delta\,\Sigma^{s,\mu} = \Sigma^{s,\mu}_+ - \Sigma^{s,\mu}_-$ and $M = m_0 + \frac{1}{2}(\Sigma^s_+ + \Sigma^s_-)$. It can be seen that the numerators depend on the integration variables p_0 and $\vec{p}$ only in the arguments of the self-energies. Up to the $\Delta\,\Sigma$ terms, the expressions in (3.44) have a structure similar to the mean-field results $k^2 - 4m^{*2}$ and k^2, cf. (B.2).

At large k_0^2, the imaginary parts as well as the four-momentum dependent dispersive real parts of the self-energies will vanish due to the cutoff of the model. Only the mean-field self-energy and the three-momentum dependent, real shifts to the dispersion integrals remain finite, i.e., $\Sigma^s_\pm \to \Sigma^{\rm mf} + \Sigma^{\rm F}_{{\rm eff},s}(|\vec{p}_\pm|)$ and $\Sigma^\mu_\pm \to \Sigma^{\rm F}_{{\rm eff},\mu}(|\vec{p}_\pm|)$. Here $\Sigma^{\rm F}_{\rm eff}$ is the effective Fock self-energy that is defined below in Eq. (3.60). It will be discussed in detail in Section 3.8.

Thus, the p_0 dependence of (3.44) is completely lost in the high-energy limit $k_0^2 \to \infty$. The k_0 dependent part of the numerators reduces to $k^2 - 2k_\mu \Delta\,\Sigma^\mu$. The term $2k_\mu \Delta\,\Sigma^\mu$ – that is not present in the mean-field approach – does not contribute to the integral in Eq. (3.43) as can be seen as follows: When k_0^2 becomes large, the $\vec{p}$ dependence of the denominators in (3.43) can be ignored. The three-momentum integrals can then be applied to the numerator alone. Since $\Delta\,\Sigma^\mu \to \Sigma^{\rm F}_{{\rm eff},\mu}(|\vec{p}_+|) - \Sigma^{\rm F}_{{\rm eff},\mu}(|\vec{p}_-|)$ we find

$$\begin{aligned} k_0 \left[\int d^3p\, \Sigma^{\rm F}_{{\rm eff},0}(|\vec{p}_+|) - \int d^3p\, \Sigma^{\rm F}_{{\rm eff},0}(|\vec{p}_-|) \right] &= 0\,, \\ \vec{k}\cdot \left[\int d^3p\, \Sigma^{\rm F}_{{\rm eff},v}(|\vec{p}_+|)\vec{e}_+ - \int d^3p\, \Sigma^{\rm F}_{{\rm eff},v}(|\vec{p}_-|)\vec{e}_- \right] &= 0\,, \end{aligned} \tag{3.45}$$

by a shift of the integration variables in the first ($\vec{p} \to \vec{p}_+$) and the second integral ($\vec{p} \to \vec{p}_-$) of each line. Hence, the energy dependence of the numerators in (3.44) is – as in the mean-field case – given by

$$(\tilde{p}_+ - \tilde{p}_-)^2 - (\tilde{m}_+ \pm \tilde{m}_-)^2 \quad \xrightarrow{k_0^2 \to \infty} \quad k_0^2 + \mathcal{O}(k_0^0)\,. \tag{3.46}$$

Note that the second term, $\mathcal{O}(k_0^0)$, is still $\vec{p}_\pm$ dependent. We will come back to that point in Section 3.8.

Exactly the same result (3.46) is found for the two more general expressions in Eqs. (3.40,3.41). The various numerators in those integrals can also be brought into the form (3.44). At large k_0^2, where the self-energies are purely real, the distinction between retarded and advanced self-energies becomes irrelevant in the numerators. Thus, shifts like in (3.45) can be applied and the energy dependence (3.46) is found for the numerators of (3.40,3.41), too.

At large energies it is also possible to reduce the number of terms in the integrals (3.40,3.41). For $k_0^2 \to \infty$ we have either $\tilde{p}_- < \mu < \tilde{p}_+$ ($k_0 \to +\infty$) or $\tilde{p}_+ < \mu < \tilde{p}_-$ ($k_0 \to -\infty$). Hence, the distribution functions become

$$\begin{aligned} {\rm n}_{\rm F}^+ = 0,\ {\rm n}_{\rm F}^- = 1 \quad \text{for} \quad k_0 \to +\infty\,, \\ {\rm n}_{\rm F}^+ = 1,\ {\rm n}_{\rm F}^- = 0 \quad \text{for} \quad k_0 \to -\infty\,. \end{aligned}$$

This means that only the term $\sim (1-{\rm n}_{\rm F}^+){\rm n}_{\rm F}^-$ or the term $\sim {\rm n}_{\rm F}^+(1-{\rm n}_{\rm F}^-)$ can contribute to the integral in (3.41). In (3.40) either the terms $\sim {\rm n}_{\rm F}^+$ or the terms $\sim {\rm n}_{\rm F}^-$ must be zero. Eq. (D.7) provides an argument why the remaining one of the first two terms in Eq. (3.40) should be zero, too: The denominators of these terms correspond to those of two retarded or two advanced propagators. Thus all poles of each term are located in the same half plane. For ${\rm n}_{\rm F}^\mp \to 1$ in the $k_0 \to \pm\infty$ limit, it is possible to close the p_0 integral in the opposite half plane, cf. Fig. D.1. Consequently, only the third term yields finite contributions to the integral of Eq. (3.40) at high energies.

Before we study the denominators in Eqs. (3.40,3.41) and (3.43) in more detail, we briefly comment on the $k \to 0$ behavior of the numerators. It should be noted

that the integrand of Eq. (3.43) vanishes for $k \to 0$ in the pion case. This can easily be seen in (3.43) since $\tilde{p}^{\rm c}_+ = \tilde{p}^{\rm c}_-$ and $\tilde{m}^{\rm c}_+ = \tilde{m}^{\rm c}_-$ for $k \to 0$. In Eqs. (3.40,3.41) the terms that contain either only retarded or only advanced self-energies will vanish in the same way. The remaining mixed terms become zero already for $k_0 = 0$, due to the distribution functions: When $p_0^+ = p_0^- = p_0$, the distributions $(\mathrm{n}_{\rm F}^- - \mathrm{n}_{\rm F}^+)$ in the third term of (3.40) cancel each other. In (3.41), the factors $(1-\mathrm{n}_{\rm F}^{\pm})\mathrm{n}_{\rm F}^{\mp}$ could only be finite for $p_0 < \mu$ *and* $p_0 > \mu$ at the same time. The $k \to 0$ behavior will be important below when we discuss the pion mass.

We turn our attention now to the denominator of (3.43) and introduce the integral

$$\mathrm{I}(k) = \int \frac{d^4p}{(2\pi)^4} \frac{1}{(\tilde{p}_+^{\rm c\,2} - \tilde{m}_+^{\rm c\,2})(\tilde{p}_-^{\rm c\,2} - \tilde{m}_-^{\rm c\,2})} \,. \tag{3.47}$$

Note that the *imaginary* part of I corresponds to the *real* part of $\Pi^{\rm c,ret}$. In the mean-field approximation, the real and the imaginary part of $\mathrm{I}(k)$ can be calculated analytically when a simple cutoff scheme is used. In Appendix B a retarded version of $\mathrm{I}(k)$ is introduced by $\mathrm{ReI}^{\rm ret}(k) = \mathrm{ReI}(k)[1 + 2\mathrm{n_B}(k_0)]$, $\mathrm{ImI}^{\rm ret}(k) = \mathrm{ImI}(k)$. It is shown that $\mathrm{ImI}^{\rm ret}(k)$ calculated from a dispersion integral is identical to the imaginary part of $\mathrm{I}(k)$ obtained from the direct calculation. No constant shifts must be added to the dispersion integral.

The complex self-energies that enter the denominator of (3.47) in the full calculation do not introduce additional poles to the integrand of $\mathrm{I}(k)$. They remain small and vanish or become real and energy independent for energies a few times larger than the cutoff Λ. Thus, the full calculation does not introduce additional shifts to the dispersion relation and – like in the mean-field case – the relation

$$\mathrm{ImI}^{(\rm ret)}(k_0, \vec{k}\,) = \frac{1}{\pi}\, \mathcal{P} \int_0^\infty dp_0^2 \frac{\mathrm{ReI}^{\rm ret}(p_0, \vec{k}\,)}{k_0^2 - p_0^2} \tag{3.48}$$

should hold. The complex integral $\mathrm{I}^{\rm ret}(k)$ of the full calculation can be found by replacing the numerators of all terms in the integrand of Eq. (3.40) by 1

$$\begin{aligned} \mathrm{I}^{\rm ret}(k) = \int \frac{d^4p}{(2\pi)^4} \Bigg[& -\frac{1}{(\tilde{p}_+^{\rm ret\,2} - \tilde{m}_+^{\rm ret\,2})(\tilde{p}_-^{\rm ret\,2} - \tilde{m}_-^{\rm ret\,2})} \mathrm{n}_{\rm F}^- \\ & + \frac{1}{(\tilde{p}_+^{\rm av\,2} - \tilde{m}_+^{\rm av\,2})(\tilde{p}_-^{\rm av\,2} - \tilde{m}_-^{\rm av\,2})} \mathrm{n}_{\rm F}^+ \\ & + \frac{1}{(\tilde{p}_+^{\rm ret\,2} - \tilde{m}_+^{\rm ret\,2})(\tilde{p}_-^{\rm av\,2} - \tilde{m}_-^{\rm av\,2})} (\mathrm{n}_{\rm F}^- - \mathrm{n}_{\rm F}^+) \Bigg] \,. \end{aligned} \tag{3.49}$$

In Eqs. (2.36,2.37) the symbols $\mathcal{P}$ and $\mathcal{W}$ for the real and the imaginary parts of the propagators have been introduced. Using these symbols we find for the real part of

$\mathrm{I}^{\mathrm{ret}}$ explicitly

$$\mathrm{ReI}^{\mathrm{ret}}(k) = \int \frac{d^4p}{(2\pi)^4} \frac{2\,\mathcal{W}_+\,\mathcal{W}_-}{(\mathcal{P}_+^2+\mathcal{W}_+^2)(\mathcal{P}_-^2+\mathcal{W}_-^2)} (\mathrm{n}_{\mathrm{F}}^- - \mathrm{n}_{\mathrm{F}}^+)\,.$$

It can be checked that the same result is found by replacing the numerator in Eq. (3.43) by 1 to get $\mathrm{I}(k)$ and using $\mathrm{ReI}^{\mathrm{ret}}(k) = \mathrm{ReI}(k)[1+2\mathrm{n}_{\mathrm{B}}(k_0)]$ to find $\mathrm{ReI}^{\mathrm{ret}}(k)$.

Eq. (3.48) does not translate directly to the polarizations. The numerators (3.44) in the integral for $\Pi^{\mathrm{ret}}_{\mathrm{d},l}(k)$ are more complicated than the trivial ones in (3.49). In particular, a factor k^2 occurs which, of course, changes the $k^2 \to \infty$ behavior. This factor will generate a k_0 independent shift if it is included in the dispersion integral (cf. Appendix B):

$$\begin{aligned} k^2\mathrm{ImI}^{(\mathrm{ret})}(k_0,\vec{k}\,) &= \frac{k^2}{\pi}\,\mathcal{P}\int_0^\infty dp_0^2 \frac{\mathrm{ReI}^{\mathrm{ret}}(p_0,\vec{k}\,)}{k_0^2-p_0^2} \\ &= \frac{1}{\pi}\int_0^\infty dp_0^2 \mathrm{ReI}^{\mathrm{ret}}(p_0,\vec{k}\,) + \frac{1}{\pi}\,\mathcal{P}\int_0^\infty dp_0^2 \frac{(p_0^2-\vec{k}^2)\mathrm{ReI}^{\mathrm{ret}}(p_0,\vec{k}\,)}{k_0^2-p_0^2}\,. \end{aligned} \tag{3.50}$$

Note that the numerator in the last term of (3.50) is just $p^2\mathrm{ReI}^{\mathrm{ret}}(p)$ for $\vec{p}=\vec{k}$, i.e., it is a dispersion for $k^2\mathrm{I}(k)$ instead of $\mathrm{I}(k)$ alone. On account of (3.44) this is just one of the terms which appear in (3.43).

The other terms in the numerators of (3.43) should not generate additional shifts: They are either constant or – as we have discussed earlier – well behaved functions that vanish for large k_0. Hence, the integrals, cf. (3.44),

$$\begin{aligned} \mathrm{J}_\sigma(k) &= \int \frac{d^4p}{(2\pi)^4} \frac{4M^2 + 2k_\mu \Delta\,\Sigma^\mu - \Delta\,\Sigma_\mu\,\Delta\,\Sigma^\mu}{(\tilde{p}_+^{\mathrm{c}\,2} - \tilde{m}_+^{\mathrm{c}\,2})(\tilde{p}_-^{\mathrm{c}\,2} - \tilde{m}_-^{\mathrm{c}\,2})}\,, \\ \mathrm{J}_\pi(k) &= \int \frac{d^4p}{(2\pi)^4} \frac{\Delta\,\Sigma_s^2 + 2k_\mu \Delta\,\Sigma^\mu - \Delta\,\Sigma_\mu\,\Delta\,\Sigma^\mu}{(\tilde{p}_+^{\mathrm{c}\,2} - \tilde{m}_+^{\mathrm{c}\,2})(\tilde{p}_-^{\mathrm{c}\,2} - \tilde{m}_-^{\mathrm{c}\,2})}\,, \end{aligned} \tag{3.51}$$

will satisfy corresponding dispersion relations without shifts (3.48) as $\mathrm{I}(k)$. The integrals $\mathrm{J}^{\mathrm{ret}}_{\sigma,\pi}(k)$ are constructed in analogy to $\mathrm{I}^{\mathrm{ret}}(k)$ (3.49) by inserting (3.44) into the numerators of Eq. (3.40) and removing the k^2 terms.

$\Pi^{\mathrm{ret}}_{\mathrm{d},l}$ can be decomposed into

$$\Pi^{\mathrm{ret}}_{\mathrm{d}\sigma,\pi}(k) = 2iN_fN_c[k^2\mathrm{I}^{\mathrm{ret}}(k) - \mathrm{J}^{\mathrm{ret}}_{\sigma,\pi}(k)]\,. \tag{3.52}$$

The dispersion relation for $\Pi^{\mathrm{ret}}_{\mathrm{d},l}$ is then given by the dispersion relations for $k^2\mathrm{I}^{\mathrm{ret}}(k)$ and $\mathrm{J}^{\mathrm{ret}}_{\sigma,\pi}(k)$ that have already been discussed. A shift proportional to the one found in (3.50) will be the only correction to the dispersion integral over $\mathrm{Im}\,\Pi^{\mathrm{ret}}_{\mathrm{d},l}$. Using $\Gamma_l(k) = -\mathrm{Im}\,\Pi^{\mathrm{ret}}_l(k)/k_0$ we find

$$\mathrm{Re}\,\Pi^{\mathrm{ret}}_{\mathrm{d},l}(k) = \frac{1}{\pi}\,\mathcal{P}\int_0^\infty dp_0^2 \frac{p_0\Gamma_l(p_0,\vec{k}\,)}{k_0^2-p_0^2} - \frac{2N_fN_c}{\pi}\int_0^\infty dp_0^2 \mathrm{ReI}^{\mathrm{ret}}(p_0,\vec{k}\,)\,. \tag{3.53}$$

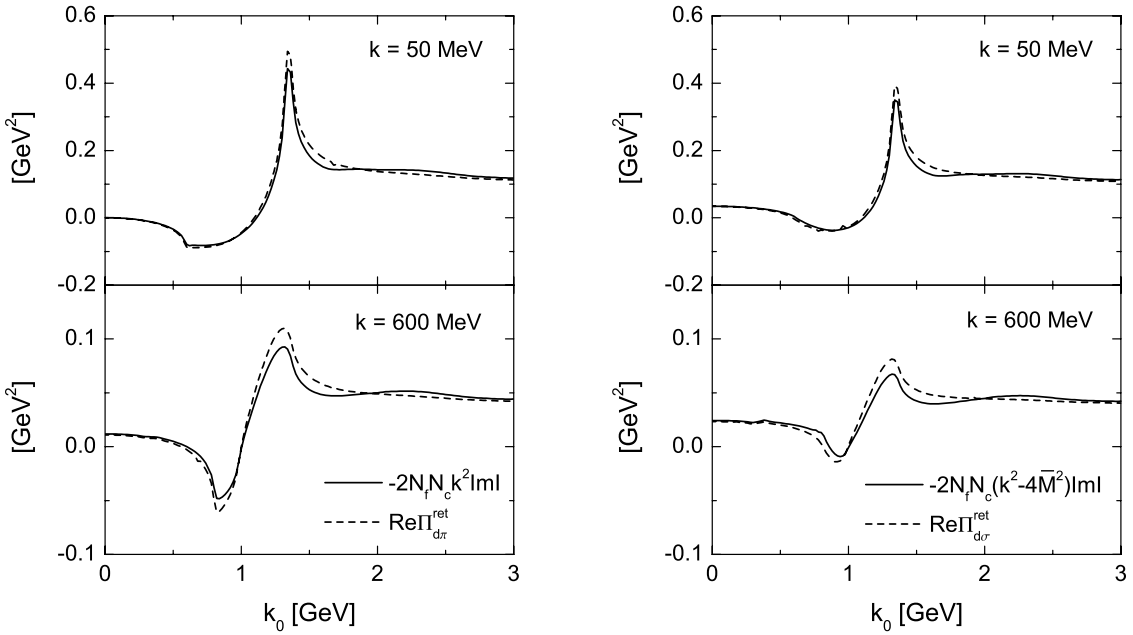

Figure 3.4: The functions $-2N_f N_c k^2 \mathrm{Im}\mathrm{I}(k)$ and $-2N_f N_c (k^2 - 4\bar{M}^2)\mathrm{Im}\mathrm{I}(k)$, cf. (3.48) and (3.52), in comparison to $\mathrm{Re}\,\Pi^{\mathrm{ret}}_{\mathrm{d},\pi}$ and $\mathrm{Re}\,\Pi^{\mathrm{ret}}_{\mathrm{d},\sigma}$ (3.53), respectively, as cuts at two different three-momenta. The results have been obtained in a full $\mathcal{O}(1/N_c)$ calculation in the chirally broken phase ($\rho = 0.06\rho_0$, $\rho_0 = 0.17\,\mathrm{fm}^{-3}$), using parameter set 0 of Table 5.1.

Eventually, the dispersion relation for the retarded RPA polarizations – including all k_0 independent shifts – is found by combining the results from Eqs. (3.39) and (3.53):

$$\mathrm{Re}\,\Pi^{\mathrm{ret}}_l(k) = \Pi_{\mathrm{n}} + \mathrm{Re}\,\Pi^{\mathrm{ret}}_{\mathrm{d},l}(k)\,. \tag{3.54}$$

These are the real parts which enter our numerical calculations.

To study the influence of the functions $\mathrm{J}^{\mathrm{ret}}_{\sigma,\pi}$ on $\mathrm{Re}\,\Pi^{\mathrm{ret}}_l$, we show the result of a full $\mathcal{O}(1/N_c)$ calculation in Fig. 3.4. In the left panel we compare $-2N_f N_c k^2 \mathrm{Im}\mathrm{I}(k)$ to the real part of $\Pi^{\mathrm{ret}}_{\mathrm{d},\pi}(k)$ for two constant three-momenta. The difference between the curves is given by $\mathrm{J}^{\mathrm{ret}}_{\pi}$, cf. Eq. (3.52). It can be clearly seen that $k^2\mathrm{Im}\mathrm{I}$ dominates the structure of $\Pi^{\mathrm{ret}}_{\mathrm{d},\pi}$, in particular at the lower three-momentum. This is not surprising since $\mathrm{J}^{\mathrm{ret}}_{\pi}$ would be zero in a mean-field calculation. As we have discussed before, the functions $-2N_f N_c k^2 \mathrm{Im}\mathrm{I}(k)$ and $\mathrm{Re}\,\Pi^{\mathrm{ret}}_{\mathrm{d},\pi}(k)$ approach the same limits for $k_0^2 \to \infty$. Note that the minima and the maxima of the functions correspond to the thresholds where phase space opens and – due to the quark cutoff Λ – closes for the states of the $q\bar{q}$ continuum. See Section 5.3 for details.

In the right panel of Fig. 3.4 we compare the function $-2N_f N_c (k^2 - 4\bar{M}^2)\mathrm{Im}\mathrm{I}(k)$ to the real part of $\Pi^{\mathrm{ret}}_{\mathrm{d},\sigma}(k)$, cf. (3.47,3.51) and (3.52). The real and constant mass $\bar{M}$

is defined here as $\bar{M} = m_0 + \mathrm{Re}\,\Sigma^{\mathrm{ret}}_{\mathrm{os},s}(\vec{k}=0)$, i.e., in terms of the on-shell self-energy (2.51) of a quark at rest. The expression $-2N_fN_c(k^2-4\bar{M}^2)\mathrm{ImI}(k)$ resembles the mean-field result for $\mathrm{Re}\,\Pi^{\mathrm{ret}}_{\mathrm{d},\sigma}(k)$ in (B.4). As we can see, the differences between the curves in Fig. 3.4 are – like in the pion case – small. The terms in $\mathrm{J}^{\mathrm{ret}}_\sigma$ that go beyond the mean-field approximation do not become very large. For $k_0^2\to\infty$, $-2N_fN_c(k^2-4\bar{M}^2)\mathrm{ImI}(k)$ and $\mathrm{Re}\,\Pi^{\mathrm{ret}}_{\mathrm{d},\sigma}(k)$ approach the same limits. They are identical to the limits of $-2N_fN_ck^2\mathrm{ImI}(k)$ and $\mathrm{Re}\,\Pi^{\mathrm{ret}}_{\mathrm{d},\pi}(k)$.

3.7 Masses of the RPA mesons

As discussed in Sections 2.2 and 2.5, we use the RPA mesons mainly as a tool to generate the next-to-leading order quark–quark interactions. Nonetheless, it is interesting to explore the properties of the mesons in the $\mathcal{O}(1/N_c)$ approach. Quasiparticle approaches [DSTL95, NBC+96, OBW00] have shown that the RPA pions, i.e. the bound $q\bar{q}$ states, may loose their Goldstone boson character in $1/N_c$ extensions of the NJL model, see the discussion in Sections 2.3.2 and 2.5 for details. In Appendix B, that is briefly summarized below, we demonstrate how this effect arises on the mean-field level.

The poles of the retarded RPA propagators are given by the zeros of $1+2\mathrm{G}\mathrm{Re}\,\Pi^{\mathrm{ret}}_l$, cf. (2.46). In the Hartree+RPA approximation (see (B.6) and (B.11) in Appendix B below), the term $1+2\mathrm{G}\,\Pi_{\mathrm{n}} = (m^*-\Sigma^{\mathrm{mf}})/m^*$ becomes zero in the chiral limit ($m_0=0$), cf. (B.7). The poles are then determined by $\mathrm{Re}\,\Pi^{\mathrm{ret}}_{\mathrm{d},\pi}\sim k^2\mathrm{ImI}(k)$ and $\mathrm{Re}\,\Pi^{\mathrm{ret}}_{\mathrm{d},\sigma}\sim(k^2-4m^{*2})\mathrm{ImI}(k)$. Hence, the RPA pions are massless and the RPA sigma has a mass of $2m^*$. For finite m_0, $1+2\mathrm{G}\,\Pi_{\mathrm{n}}$ will become finite, too. Only a small shift will be generated, however, so that the pion remains light. This can be seen in Fig. 2.15.

Let us turn now from the Hartree+RPA approximation to our full calculation. We will discuss the terms $\Pi^{\mathrm{ret}}_{\mathrm{d},l}$ and $1+2\mathrm{G}\,\Pi_{\mathrm{n}}$, cf. (3.39) and (3.53), separately. The properties of $\Pi^{\mathrm{ret}}_{\mathrm{d},l}$ should not change too much in the $\mathcal{O}(1/N_c)$ approach. The decomposition $\Pi^{\mathrm{ret}}_{\mathrm{d}\sigma,\pi}(k) = 2iN_fN_c[k^2\mathrm{I}^{\mathrm{ret}}(k)-\mathrm{J}^{\mathrm{ret}}_{\sigma,\pi}(k)]$ shows that the dominant part of $\Pi^{\mathrm{ret}}_{\mathrm{d}\pi}$ vanishes for $k^2=0$ – it can be seen in Eq. (3.50) that this still holds when the real part is calculated from a dispersion relation. Due to the self-energies in the numerators it is difficult to check the behavior of $\mathrm{J}^{\mathrm{ret}}_\pi(k)$ for $k^2=0$ analytically. The numerical result in Fig. 3.4 confirms our observation that $\mathrm{J}^{\mathrm{ret}}_\pi(k)$ vanishes for $k\to0$. A closer inspection of the $|\vec{k}\,|=600\,\mathrm{MeV}$ cut shows, that the curves for $k^2\mathrm{ImI}$ and $\Pi^{\mathrm{ret}}_{\mathrm{d},\pi}(k)$ are not equal at $k_0=600\,\mathrm{MeV}$. We can conclude that $\mathrm{J}^{\mathrm{ret}}_\pi(k^2=0)$ does – in general – not vanish. Nonetheless, the numerical result indicates that it remains very small.

The most important term in the numerator of $\mathrm{J}^{\mathrm{ret}}_\sigma(k)$ is $M^2=[m_0+\frac{1}{2}(\Sigma^s_+ + \Sigma^s_-)]^2$. The largest contribution to the real part of $\Sigma^s_\pm$ is the constant $\mathcal{O}(1)$ Hartree self-energy Σ^{mf}. The contributions from the meson exchange diagram are suppressed in $1/N_c$. This is confirmed by our numerical calculation, cf. Fig. 5.13. We find that $\Sigma^{\mathrm{mf}}\approx 0.8\,\mathrm{Re}\,\Sigma^{\mathrm{ret}}_s$ on the mass shell. Splitting up M^2 and moving the constant

term $\bar{M}^2 = (m_0 + \mathrm{Re}\,\Sigma^{\mathrm{ret}}_{\mathrm{os},s}(\vec{k}=0))^2$ in front of the integral in $\mathrm{J}^{\mathrm{ret}}_\sigma$ yields a term $\sim [k^2 - 4\bar{M}^2]\,\mathrm{I}^{\mathrm{ret}}(k)$ in $\Pi^{\mathrm{ret}}_{\mathrm{d}\sigma}(k)$. This term resembles the mean-field result. Its zero at $k^2 = 4\bar{M}^2$ should determine the RPA sigma mass roughly. The remaining terms in the numerator of $\mathrm{J}^{\mathrm{ret}}_\sigma$ are small in comparison to $4\bar{M}^2$ and should provide only small corrections.

In our $\mathcal{O}(1/N_c)$ approach – as in the Hartree–Fock+RPA approximation[4] of Fig. 2.9 (see Appendix B for details) – the term $1+2\mathrm{G}\,\Pi_{\mathrm{n}}$ will not vanish for $m_0 = 0$. Eq. (3.39) yields

$$1 + 2\mathrm{G}\,\Pi_{\mathrm{n}} = \frac{m_0 + \Sigma^s_{\mathrm{const.}} - \Sigma^{\mathrm{mf}}}{m_0 + \Sigma^s_{\mathrm{const.}}} + \frac{16\mathrm{G}N_fN_c}{m_0 + \Sigma^s_{\mathrm{const.}}} \int \frac{d^4p}{(2\pi)^4} \mathrm{Im} \frac{\Sigma^{\mathrm{ret}}_s(p) - \Sigma^s_{\mathrm{const.}}}{\tilde{p}^2_{\mathrm{ret}} - \tilde{m}^2_{\mathrm{ret}}} \mathrm{n_F}(p_0)\,. \tag{3.55}$$

The first term corresponds to the mean-field result (B.8). Since this term is easier to handle, it is reasonable to chose the value of $\Sigma^s_{\mathrm{const.}}$ as large as possible. The role of the second term is then minimized. When $\Sigma^s_{\mathrm{const.}}$ is chosen so that it contains all constant contributions to the real part of Σ^{ret}_s, it will not be equal to Σ^{mf}. Next-to-leading order terms like Σ^{F} will also contribute on a $20-25\%$ level, cf. Fig. 5.13. Using the numerical result $0.75\,\Sigma^s_{\mathrm{const.}} \approx \Sigma^{\mathrm{mf}}$ leads to a value of $0.15 - 0.2$ for the first term of (3.55). Thus, this shift is larger than in the Hartree–Fock+RPA approximation (B.8), where it has a value of $1/(2N_fN_c+1) \approx 0.08$ in the chiral limit.

The second term of (3.55) appears only in the full calculation, where the self-energy becomes complex and four-momentum dependent. This term cannot be easily estimated. The importance of the term clearly depends on the structure of Σ^{ret}_s. A closer analysis of the collisional self-energies can be found in Chapter 4. Note that the term will not vanish at zero chemical potential. Decay processes like $q \to qq\bar{q}$ and $\bar{q} \to \bar{q}\bar{q}q$ (cf. Fig. 4.3) can occur even in the vacuum (for $|k_0| \gtrsim 3m^*$). This will not lead to large quark widths in the vicinity of the on-shell peaks. The dispersion integrals, however, pick up those off-shell contributions so that they have some influence on the real part of Σ^{ret}_s in the on-shell region.

The exact size of $1 + 2\mathrm{G}\,\Pi_{\mathrm{n}}$ can only be determined in a numerical calculation. As we will see in Section 5.3, a value of ≈ 0.2 is found numerically in our approach (cf. Fig. 5.9). The second term of (3.55) remains small for the suggested choice of $\Sigma^s_{\mathrm{const.}}$. A cancellation of the two terms in (3.55) does not occur. Therefore, the RPA pion remains massive even in the chiral limit – this resembles qualitatively the Hartree–Fock+RPA approximation discussed in Appendix B. Quantitatively, the effect even exceeds the Hartree–Fock+RPA result.

The large shift raises the question which influence the RPA pion mass has on the quark properties in our self-consistent calculation – recall the discussion in Section 2.5.

[4] The reason for the breakdown of the chiral properties of the present RPA pions – that are not expected in a regular random phase approximation on the Hartree–Fock level [RS80, BR86, DVN05] – is the incomplete $1/N_c$ expansion of the meson polarization in higher orders of $1/N_c$ that we have discussed in Section 2.5.

We will address this problem in Section 4. There, it will be found that the off-shell states of the pion spectral function – and not the bound $q\bar{q}$ states – have the largest influence on the quark self-energy. The $q\bar{q}$ continuum states in the timelike region are not generated by poles of the pion propagator but by large decay widths. They are largely independent of the RPA pion mass and differ within reasonable limits in the $\mathcal{O}(1/N_c)$ and the Hartree+RPA approaches, cf. Figs. 4.4 and 5.8. The large RPA pion mass will, however, lead to a suppression of the contributions from the spacelike region to the quark width. Our analysis in Section 4 indicates that the differences to a calculation with a more realistic pion mass range below one order of magnitude for those contributions. We can conclude that our approach will – on average – underestimate the short-range effects in the chirally broken phase.

3.8 Real parts of the quark self-energy

Like the meson polarizations, the quark self-energy may contain k_0 independent contributions to the real part that cannot be calculated dispersively. For the quarks, the search for such components is not as important as for the mesons. The quark mass is determined predominantly by the $\mathcal{O}(1)$ mean-field self-energy Σ^{mf} that we calculate separately. The constant terms that arise from the $\mathcal{O}(1/N_c)$ meson exchange diagram in Fig. 3.3 as shifts to the dispersion integral should be significantly smaller than Σ^{mf} – the numerical confirmation can be found in Fig. 5.13.

In this section we will use the relations between the different kinds of propagators ($\mathrm{S}^{\mathrm{c}}, \mathrm{S}^{\mathrm{ret}}, \mathrm{S}^{\gtrless}$ and $\Delta^{\mathrm{c}}, \Delta^{\mathrm{ret}}, \Delta^{\gtrless}$) that are summarized in Eqs. (2.32) and (2.45) without further reference. Using the Feynman rules of the real-time formalism (see Appendix C), we find for the time-ordered self-energy of the quarks (cf. Fig. 3.3)

$$-i\,\Sigma^{\mathrm{c}}(k) = -i\,\Sigma^{\mathrm{mf}} + \sum_l \int \frac{d^4p}{(2\pi)^4} \Gamma_l\, \mathrm{S}^{\mathrm{c}}(p) \tilde{\Gamma}_l\, \Delta_l^{\mathrm{c}}(p-k)\,. \tag{3.56}$$

The structure of the integrand is similar to the integrand of the RPA polarizations in Eq. (3.26). An investigation of (3.56) in the same way as in Section 3.6 is, however, not possible as we will show now.

In Section 3.6 the explicit structure of the quark propagator in momentum space was utilized to decompose and simplify the integrand. The effective propagator $\Delta_l^{\mathrm{c}}(k)$ of the RPA mesons is defined in terms of the polarizations and the NJL coupling constant,

$$\Delta_l^{\mathrm{c}}(k) = -\frac{2\mathrm{G}}{1 + 2\mathrm{G}\,\Pi_l^{\mathrm{c}}(k)}\,. \tag{3.57}$$

The structure of this propagator is completely different from the quark propagator. Thus most of the methods that were used in Section 3.6 are not applicable here. It

is not feasible to replace the RPA propagator Δ_l^{c} by a standard meson propagator

$$\mathrm{D}_l^{\mathrm{c}}(k) = \frac{1}{k^2 - m^2 - \Pi_l^{\mathrm{c}}(k)}$$

in Eq. (3.56) since the properties of Δ_l^{c} and $\mathrm{D}_l^{\mathrm{c}}$ differ – especially in the high-energy properties. However, in the following we will use one of the differences to identify a constant contribution to the quark self-energy.

3.8.1 Decomposition of the self-energy

In the limit of $k_0^2 \to \infty$ a standard meson propagator D^{c} would obviously vanish. In our effective propagators, the polarization should be – up to constant terms – suppressed by the cutoff. Therefore, the effective propagator will approach a finite value. This can be seen in Eq. (3.57). If we assumed that the meson polarizations would become zero at large k_0^2, Δ^{c} would approach a value of $-2\mathrm{G}$. However, the results of Section 3.6 suggest that the real parts of the polarizations do not necessarily vanish since a constant contribution Π_{n} (3.39) exists. It is also possible that $\Pi_{\mathrm{d},l}^{\mathrm{c}}$ remains finite. The $k_0^2 \to \infty$ limit of this term can even be $|\vec{k}\,|$ dependent.

We split up the RPA propagator into an energy independent part $\Delta^{\infty}(|\vec{k}\,|)$ that corresponds to the limit at high k_0^2 and an effective propagator $\underline{\Delta}_l^{\mathrm{c}}$ that will vanish for $k_0^2 \to \infty$,

$$\Delta_l^{\mathrm{c}}(k) = \Delta^{\infty}(|\vec{k}\,|) + \underline{\Delta}_l^{\mathrm{c}}(k)\,. \tag{3.58}$$

The same decomposition can be done for the retarded and advanced propagators. Since Δ^{∞} is real, the imaginary parts of the propagators are not affected by the decomposition. Consequently, we find for the spectral functions $\xi_l(k) = -2\mathrm{Im}\,\underline{\Delta}_l^{\mathrm{ret}}(k)$ and – using Eqs. (2.43,2.44) – for the non-ordered propagators $\Delta_l^{\gtrless}(k) = \underline{\Delta}_l^{\gtrless}(k)$.

Inserting the decomposed RPA propagator into the time-ordered quark self-energy (3.56) yields

$$\begin{aligned}\Sigma^{\mathrm{c}}(k) - \Sigma^{\mathrm{mf}} = &\sum_l \int \frac{d^4p}{(2\pi)^4} i\Gamma_l\, \mathrm{S}^{\mathrm{c}}(p)\Gamma_l\, \Delta^{\infty}(|\vec{p} - \vec{k}\,|) \\ &+ \sum_l \int \frac{d^4p}{(2\pi)^4} i\Gamma_l\, \mathrm{S}^{\mathrm{c}}(p)\tilde{\Gamma}_l\, \underline{\Delta}_l^{\mathrm{c}}(p-k)\,.\end{aligned} \tag{3.59}$$

The first integral is a k_0 independent contribution to the real part of the self-energy. Thus, it is not covered by the dispersion integral and must be calculated separately. In the simplest case, $\Delta^{\infty} = -2\mathrm{G}$, this term becomes just the constant Fock self-energy, cf. Eq. (3.3). This is not surprising since the – purely real – Fock diagram is part of the effective meson exchange shown in Fig. 2.4. Because of its structure, we

will refer to the first term of (3.59) as an effective Fock self-energy in the following,

$$\Sigma^{\mathrm{F}}_{\mathrm{eff}}(|\vec{k}\,|) = \sum_l \int \frac{d^4p}{(2\pi)^4} i\Gamma_l \, \mathrm{S}^{\mathrm{c}}(p)\Gamma_l \, \Delta^{\infty}(|\vec{p}-\vec{k}\,|)\,. \tag{3.60}$$

Some properties of the real Fock self-energy Σ^{F} have been discussed in Section 3.1. The Lorentz structure of $\Sigma^{\mathrm{F}}_{\mathrm{eff}}$ can be determined with the help of Eq. (3.4) from that section,

$$\begin{aligned}
\Sigma^{\mathrm{F}}_{\mathrm{eff},s}(|\vec{k}\,|) &= 2\int \frac{d^4p}{(2\pi)^4}\, \Delta^{\infty}(|\vec{p}-\vec{k}\,|)\mathcal{A}_s(p)\mathrm{n_F}(p_0)\,,\\
\Sigma^{\mathrm{F}}_{\mathrm{eff},0}(|\vec{k}\,|) &= 2\int \frac{d^4p}{(2\pi)^4}\, \Delta^{\infty}(|\vec{p}-\vec{k}\,|)\mathcal{A}_0(p)[1-2\mathrm{n_F}(p_0)]\,,\\
\Sigma^{\mathrm{F}}_{\mathrm{eff},v}(|\vec{k}\,|) &= -4\int \frac{d^4p}{(2\pi)^4}\, \Delta^{\infty}(|\vec{p}-\vec{k}\,|)\cos\vartheta\mathcal{A}_v(p)\mathrm{n_F}(p_0)\,,
\end{aligned} \tag{3.61}$$

where we have used the normalization of the spectral function (D.6). In contrast to the component Σ^{F}_v of the real Fock self-energy, the Lorentz component $\Sigma^{\mathrm{F}}_{\mathrm{eff},v}$ does not necessarily vanish. Only when Δ^{∞} is a constant, the symmetry of the integrand can be used to get rid of the integral. The arguments concerning the μ dependence of Σ^{F} at the end of Section 3.1, however, hold also for the Lorentz components of $\Sigma^{\mathrm{F}}_{\mathrm{eff}}$.

3.8.2 Dispersion relation

As discussed before, a search for constant shifts to the dispersion integral in the second term on the rhs. of Eq. (3.59) is complicated. We just give a plausibility argument here, why such shifts should not occur. In general, the existence of constant shifts is related to the level of divergence of the integrand in the dispersion integral. The RPA polarizations (3.56) include two quark propagators $\sim p_\pm/p_\pm^2$ (for large k^2). This gives rise to a term $\sim k^2$ in the numerator of the integrand. We have shown in Eq. (3.50) how the inclusion of the factor k^2 in the dispersion integral for $\mathrm{Re}\,\Pi^{\mathrm{ret}}_l$ generates a constant term. The other terms in the numerator of (3.56) are of lower order in k and do not generate such shifts. In contrast to the polarizations, the self-energy integral in (3.59) contains only one quark propagator and one effective meson propagator $\underline{\Delta}^{\mathrm{c}}_l$. Assuming that $\underline{\Delta}^{\mathrm{c}}_l(p\pm k) \sim 1/(p\pm k)^2$ for large k^2 – like for the standard propagator $\mathrm{D}^{\mathrm{c}}_l$ – the last integrand of (3.59) does not contain a factor k^2 in the numerator. The denominator, on the other hand, resembles that of the polarizations. Consequently, the imaginary part of the quark self-energy (3.59) is of lower order in k than the imaginary parts of the RPA polarizations. We can expect that the dispersion integral for $\mathrm{Re}\,\Sigma^{\mathrm{ret}}$ does not include a shift similar to the one in (3.50)[5].

[5] If any shifts exist that we overlook by applying this argument, they should be small compared to the Hartree self-energy. They would arise from the collisional self-energies that are of higher order in $1/N_c$.

The complete dispersion relation for the real part of the retarded quark self-energy is then given by

$$\mathrm{Re}\,\Sigma^{\mathrm{ret}}(k_0,\vec{k}\,) = \Sigma^{\mathrm{mf}} + \Sigma^{\mathrm{F}}_{\mathrm{eff}}(\vec{k}\,) + \frac{1}{2\pi}\;\mathcal{P}\int_{-\infty}^{+\infty} dp_0 \frac{\Gamma(p_0,\vec{k}\,)}{k_0 - p_0}\,. \tag{3.62}$$

The Lorentz components $\mathrm{Re}\,\Sigma^{\mathrm{ret}}_s$, $\mathrm{Re}\,\Sigma^{\mathrm{ret}}_0$, and $\mathrm{Re}\,\Sigma^{\mathrm{ret}}_v$ can be found in the usual way (2.53). Note that all components depend on $|\vec{k}\,|$ only, not on the full three-momentum $\vec{k}$.

A remarkable interplay between the quark and the meson properties can be observed here. For $k_0^2 \to \infty$, where the dispersion integral vanishes, $\mathrm{Re}\,\Sigma^{\mathrm{ret}}$ approaches the $|\vec{k}\,|$ dependent, finite value of $\Sigma^{\mathrm{mf}} + \Sigma^{\mathrm{F}}_{\mathrm{eff}}(\vec{k}\,)$. The momentum dependence is introduced by the high-energy limit of the effective meson propagator, cf. (3.58,3.60). The momentum dependent limit of the meson propagator, on the other hand, is generated by the effective Fock self-energy that enters Eqs. (3.44,3.46). This self-consistent effect is not present in the Hartree(–Fock)+RPA approximations since the meson polarizations are not fed back into the quark self-energy. There, the $k_0^2 \to \infty$ limits of $\mathrm{Re}\,\Sigma^{\mathrm{ret}}$ and $\mathrm{Re}\,\Pi^{\mathrm{ret}}$ are both constant in $\vec{k}$, cf. Eqs. (3.2,3.4) and (B.17).

In Fig. 3.5 we show the results of a full $\mathcal{O}(1/N_c)$ calculation in the chirally broken phase. The solid lines correspond to $\mathrm{Re}\,\Sigma^{\mathrm{ret}}(k) - \Sigma^{\mathrm{mf}}$, cf. (3.62). The full structure of those curves will become clearer when the quark width is discussed, see Section 5.2 (Fig. 5.3). We will not discuss the details here. As we can see, the real parts approach the effective Fock self-energy at large $|k_0|$. In other words, the dispersive contributions to the real part of Σ^{ret} vanish – as desired – for $k_0^2 \to \infty$. Note that the scalar and the γ_0-component are of similar size in the chirally broken phase while the $\vec{\gamma}$-component is much smaller. The scalar component shrinks considerably in the chirally restored phase – it would be zero if we had chosen a parameter set in the chiral limit ($m_0 = 0$) – while the other components keep their magnitude.

The results for the Lorentz components of $\Sigma^{\mathrm{F}}_{\mathrm{eff}}$ are in agreement with the considerations in this section and in Section 3.1. The scalar component drops by a factor of 3 due to the restoration of chiral symmetry. The γ_0-component is very small at the lower density and increases at higher ρ. It grows by a factor of 5 in Fig. 3.5. In contrast to the regular Fock self-energy of Section 3.1, $\Sigma^{\mathrm{F}}_{\mathrm{eff},v}$ has a small, finite value since Δ^{∞} is not a constant. The value of $\Sigma^{\mathrm{F}}_{\mathrm{eff},v}$ is, however, almost density independent.

3.8.3 Quark width

At the end of this section, we check that the imaginary part of Σ^{ret} that can be calculated from Eq. (3.59) corresponds to the quark width that we have found in Eq. (3.16): Replacing the time-ordered propagators in Eq. (3.59) by $\mathrm{S}^{\mathrm{c}}(k) = \mathrm{S}^{\mathrm{ret}}(k) +$

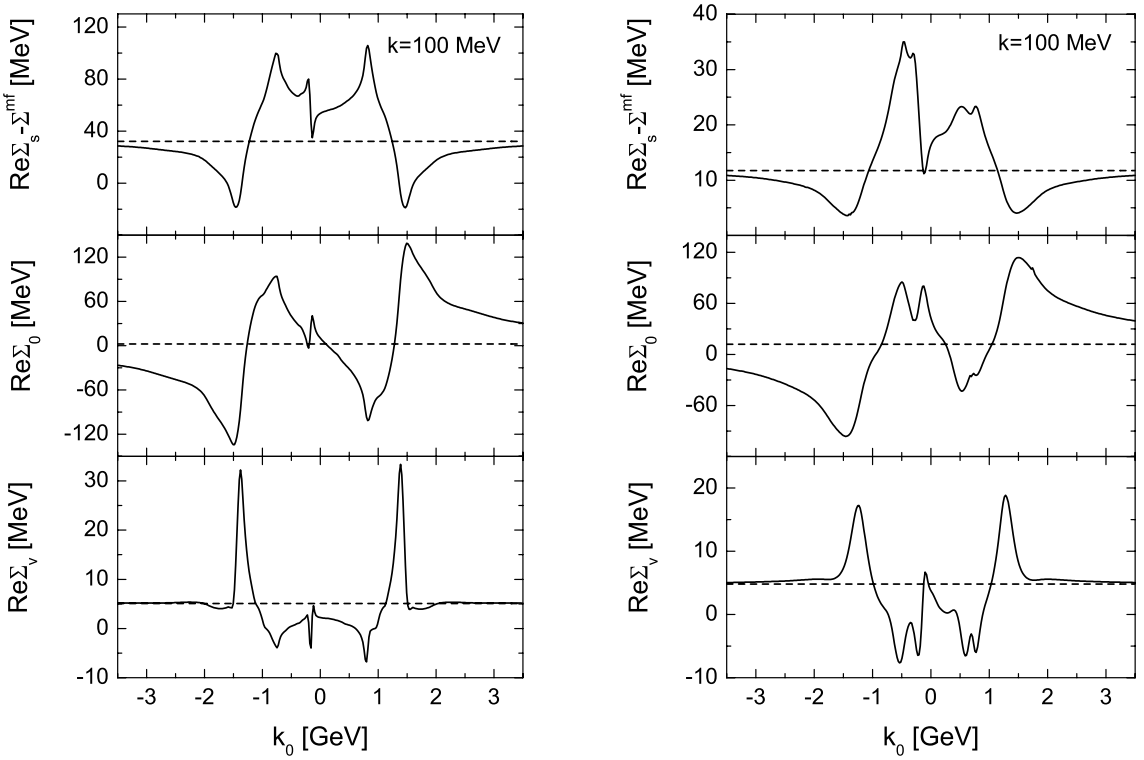

Figure 3.5: The Lorentz components of the real part of the retarded quark self-energy $\Sigma^{\rm ret}$ at a fixed three-momentum of 100 MeV (solid lines). The dashed lines indicate the Lorentz components of the effective Fock self-energy $\Sigma^{\rm F}_{\rm eff}$ (3.61). The $\mathcal{O}(1/N_c)$ results have been obtained for a quark density of $\rho_0 = 0.17\,{\rm fm}^{-3}$ (chirally broken phase, $\mu = 325\,{\rm MeV}$) in the left and of $4.5\rho_0$ (chirally restored phase, $\mu = 332\,{\rm MeV}$) in the right panel. Parameter set I of Table 5.1 has been used in the calculations.

$i\mathcal{A}(k){\rm n_F}(k_0)$ and $\underline{\Delta}^{\rm c}(k) = \underline{\Delta}^{\rm ret}(k) - i\xi(k){\rm n_B}(k_0)$ yields

$$\begin{aligned}{\rm Re}\,\Sigma^{\rm c}(k) - \Sigma^{\rm F}_{\rm eff}(|\vec{k}\,|) = \sum_l \int \frac{d^4p}{(2\pi)^4} \Big[&\Gamma_l {\rm Re}\,{\rm S}^{\rm ret}(p)\tilde{\Gamma}_l \xi(p-k){\rm n_B}(p_0-k_0) \\ &-\Gamma_l \mathcal{A}(p)\tilde{\Gamma}_l {\rm Re}\,\underline{\Delta}^{\rm ret}_l(p-k){\rm n_F}(p_0)\Big] \end{aligned} \tag{3.63}$$

and

$$\begin{aligned}{\rm Im}\,\Sigma^{\rm c}(k) = -\frac{1}{2}\sum_l \int \frac{d^4p}{(2\pi)^4} &[{\rm n_F}(p_0) + {\rm n_B}(p_0-k_0)][1-2{\rm n_F}(k_0)] \\ &\times \Gamma_l \mathcal{A}(p)\tilde{\Gamma}_l \xi_l(p-k)\,, \end{aligned} \tag{3.64}$$

where we have used

$$2{\rm n_F}(p){\rm n_B}(p-k) + {\rm n_F}(p) - {\rm n_B}(p-k) = -[{\rm n_F}(p) + {\rm n_B}(p-k)][1-2{\rm n_F}(k)]\,.$$

A proof for the this relation is given in Appendix G. We can directly read off the imaginary part of $\Sigma^{\rm ret}$ from Eq. (3.64) with the help of (3.25), $\mathrm{Im}\,\Sigma^{\rm c}(k) = [1 - 2\mathrm{n_F}(k_0)]\mathrm{Im}\,\Sigma^{\rm ret}(k)$. After working out the Lorentz structure as shown in Section 3.3, we can see that this expression is in fact identical to the width (3.16).

Taking the real and the imaginary part of $\Sigma^{\rm ret}$ that we obtain from Eqs. (3.63,3.64) and combining them, it is also possible to find a compact form for the complex self-energy $\Sigma^{\rm ret}$,

$$\Sigma^{\rm ret}(k) - \Sigma^{\rm F}_{\rm eff}(|\vec{k}\,|) = \sum_l \int \frac{d^4p}{(2\pi)^4} i\Gamma_l \left[\mathrm{S}^<(p)\,\underline{\Delta}_l^{\rm av}(p-k) + \mathrm{S}^{\rm ret}(p)\,\Delta^<(p-k)\right]\tilde{\Gamma}_l\,. \tag{3.65}$$

4 Quark and meson scattering

The quark width $\Gamma = i\,\Sigma^{>} - i\,\Sigma^{<}$ is generated by the next-to-leading order interactions of the quarks in the medium. When the width has been introduced in Section 2.8, we have discussed that the collisional self-energies $i\,\Sigma^{>}$ and $-i\,\Sigma^{<}$ are identical to the total collision rates for scattering out of and into of a quark state with four-momentum $k = (k_0, \vec{k}\,)$ [KB62]. Due to the variety of contributing scattering and decay processes, the collision rates – and thus the width – have a complicated structure and a non-trivial energy dependence [Wel83]. For each of the contributing scattering and decay processes, phase space opens and closes at a certain energy k_0. Finding those thresholds will lead to a qualitative understanding of the structure of the quark width. Therefore, we will investigate the collision rates in this chapter on the level of the Hartree+RPA approximation at zero temperature – the quarks are quasiparticles and the Fermi and Bose distributions are simple step functions in this case.

We will also discuss the density dependence of the individual processes and check which of the processes contribute to the width of the on-shell states. For completeness, we will investigate the – much simpler – structure of the RPA meson widths in the last section of this chapter. The results of this chapter will be helpful later when the results of the full calculation are discussed. In addition, they allow us to estimate the influence of a too large RPA pion mass on the quark properties.

4.1 Mean-field spectral functions

4.1.1 Quark spectral function

We begin our analysis with a short discussion of the spectral functions. In the Hartree approximation, the quark spectral function $\mathcal{A}$ consists of two quasiparticle peaks, one at positive and one at negative energies k_0 (see the schematic plot in Fig. 2.17),

$$\mathcal{A}(k) = 2\pi(\not{k} + m^*)\frac{1}{2E_k}[\delta(k_0 - E_k) - \delta(k_0 + E_k)]\,, \tag{4.1}$$

where[1] $E_k = (\vec{k}^2 + m^{*2})^{1/2}$ and $m^* = m_0 + \Sigma^{\mathrm{H}}$. Note that the Lorentz component $\mathcal{A}_0(k)$ is symmetric in k_0 while $\mathcal{A}_s(k)$ and $\mathcal{A}_v(k)$ are antisymmetric. The Lorentz structure has no influence on the thresholds of the scattering processes. On the

[1] In the Hartree–Fock approximation, the definition of m^* changes to $m^* = m_0 + \Sigma^{\mathrm{H}} + \Sigma_s^{\mathrm{F}}$ and k_0 has to be replaced by $\tilde{k}_0 = k_0 - \Sigma_0^{\mathrm{F}}$ on the rhs. of (4.1). $\vec{k}$ remains unchanged since $\Sigma_v^{\mathrm{F}} = 0$, cf. (3.6).

mean-field level, the contributions to the collision rates differ only in sign. Hence, we will mostly ignore the Lorentz structure and restrict ourselves to the γ_0-components of $\mathcal{A}$ and $\Sigma^{\gtrless}, \Gamma$ here.

In the following, we will interpret the quark states $k = (k_0, \vec{k})$ at negative k_0 as antiquark states $\bar{k} = (\bar{k}_0, \vec{k}) = (-k_0, \vec{k})$ that have a positive energy $\bar{k}_0 = |k_0|$. The two peaks of the spectral function can then be identified with a quark peak at $k_0 = E_k$ and an antiquark peak at $\bar{k}_0 = E_k$. An antiquark corresponds to a hole in the populated quark states. Since the chemical potential is always positive in our calculations, all quark states at negative energies are populated – there are no holes in the Dirac sea. Consequently, there are no antiquarks in the medium at $T = 0$. Note that we discuss the distinction between quarks and antiquarks in more detail in Appendix E – in the context of the correct definition of the quark density. In the presence of short-range correlations, the border between the quark and the antiquark states will be slightly shifted (see Fig. E.1).

4.1.2 RPA meson spectral functions

Each of the meson spectral functions $\xi_{\sigma,\pi}$ (2.48) consists of two components – see Fig. 2.5 – that we will treat separately. The actual RPA mesons are generated by bound $q\bar{q}$ states. They correspond to poles of the RPA propagators and show up as peaks (at positive and negative energies) in the σ and π spectral functions. Since the mesons are their own antiparticles, we will not refer to the peaks at negative energies as antiparticle peaks. However, we will refer to a meson with negative energy k_0 as a meson with positive energy $\bar{k}_0 = |k_0|$ in the following. The RPA propagators have been constructed from $q\bar{q}$ scattering processes (2.7). Thus, the spectral functions include also broad ranges of – unbound – $q\bar{q}$ continuum states, cf. Sections 2.2 and 4.5. The so-called $q\bar{q}$ continuum is located at $|k_0| > \mu + m^*$, i.e., above the threshold for the decay of a meson into a quark–antiquark pair. Landau damping[2] [KG06] generates further contributions at spacelike four-momenta ($k_0^2 < \vec{k}^2$). In those regions, the spectral functions are characterized by large meson widths $\Gamma_{\sigma,\pi}$ and not by poles of the propagators.

The RPA pion peaks are located below the $q\bar{q}$ decay threshold – even in the Hartree–Fock+RPA approximation where the RPA pions are not the Goldstone modes. Hence, they will generate pronounced contributions to the collision rates that can be easily distinguished from the $q\bar{q}$ continuum contributions. The RPA sigma peaks are – due to the large mass of the bound state – located above the $q\bar{q}$ decay threshold. Thus, the peaks are rather broad. For our qualitative investigation of the collision rates, we will not disentangle the peak and the continuum component of the σ spectral function. It is sufficient to investigate the continuum contributions in this case.

For the quasiparticle component of the RPA pion spectral function we can use an

[2] At spacelike four-momenta, scattering processes of the structure $\pi q \to q$ contribute to the RPA polarizations, see Section 4.5 for details.

expression similar to (4.1),

$$\xi_\pi(k) \sim \delta(k_0 - E_k^\pi) - \delta(k_0 + E_k^\pi)\,, \tag{4.2}$$

where $E_k^\pi = (\vec{k}^2 + m_\pi^2)^{1/2}$. m_π is the effective RPA pion mass that is determined by the poles of the RPA propagator. Since we are presently only interested in energy thresholds and not in the absolute magnitude of the contributions, it is not necessary to specify ξ_π in more detail. We also do not specify the off-shell components of the RPA spectral functions here. To investigate the off-shell contributions to the collision rates, we will rewrite the self-energies $\Sigma^{\gtrless}$ in Section 4.2.2 so that the incoming and outgoing mesons are replaced by $q\bar{q}$ pairs.

4.2 Thresholds

We turn now to the collisional self-energies. After slightly rearranging the rhs. of Eq. (3.11) we find

$$-i\,\Sigma^{\gtrless}(k) = \sum_l \int \frac{d^4p}{(2\pi)^4}\frac{d^4r}{(2\pi)^4}(2\pi)^4\delta^4(k-p+r)\Gamma_l\,\mathrm{S}^{\gtrless}(p)\tilde{\Gamma}_l\,\Delta_l^{\lessgtr}(r)\,. \tag{4.3}$$

In this form, the self-energies can be immediately identified with total collision rates: The δ-function in the integrand ensures energy and momentum conservation in the processes $kr \rightleftarrows p$. Recall that the non-ordered propagators $-i\,\mathrm{S}^<(p) = \mathcal{A}(p)\mathrm{n_F}(p_0)$ and $i\,\mathrm{S}^>(p) = \mathcal{A}(p)[1-\mathrm{n_F}(p_0)]$ are just the densities of the populated and the free quark states (2.25). The meson propagators $i\,\Delta^>(r)$ and $i\,\Delta^<(r)$ can be interpreted accordingly, cf. (2.43,2.44). Hence, the loss rate $i\,\Sigma^>(k)$ corresponds to a quark with four-momentum k that is added to the system and scatters off a meson with four-momentum r into a free quark state p. The gain rate $-i\,\Sigma^<(k)$, on the other hand, corresponds to decays of a quark p from the medium into a quark with four-momentum k and a meson with four-momentum r. Total collision rates are found by integrating over the four-momenta p and r of the scattering partners and the available final states.

It is important to note that incoming quarks with negative energy correspond to outgoing antiquarks – and vice versa – in the scattering processes [Wel83]. This can be seen in the argument of the energy conserving δ-function $\delta(k_0 - p_0 + r_0)$ that yields the condition $k_0 + r_0 = p_0$. When all energies are positive, this corresponds to the processes $kr \rightleftarrows p$. Since the energy of an antiquark is not given by k_0 but by $\bar{k}_0 = -k_0$, the condition from the δ-function should be reinterpreted as $r_0 = \bar{k}_0 + p_0$ when k_0 is negative. This corresponds to the processes $r \rightleftarrows \bar{k}p$, where the incoming k has been turned into an outgoing $\bar{k}$. Using the same argument as for the quarks, an incoming meson with negative energy r_0 is reinterpreted as an outgoing meson with positive energy $\bar{r}_0 = -r_0$.

4.2.1 Processes with bound $q\bar{q}$ states

To investigate the contributions from the RPA pion peaks to the collision rates, we replace the quark and meson propagators in (4.3) by the spectral functions (4.1,4.2) and the appropriate distribution functions, cf. (3.14,3.15). This generates four terms with different combinations of the quasiparticle peaks for each of the two self-energies $\Sigma^{\gtrless}$. At zero temperature, some of those terms are ruled out by the combination of δ- and step functions in the propagators. Since $\mathrm{n_B}(q_0) = -\Theta(-q_0)$, only the negative energy peak of $\Delta^<$ can contribute to $\Sigma^>$ and only the positive energy peak of $\Delta^>$ can contribute[3] to $\Sigma^<$. Correspondingly, the antiquark peak in $\mathrm{S}^>$ cannot contribute to $\Sigma^>$ since the factor $[1 - \mathrm{n_F}(p_0)] = \Theta(p_0 - \mu)$ allows only positive energies $p_0 > \mu$. In total we find

$$i\,\Sigma_0^>(k) \sim \int_\Lambda d^3p\ \delta(k_0 - E_p - E^\pi_{p-k})\,[1 - \mathrm{n_F}(E_p)]\,\mathrm{n_B}(E_p - k_0) \tag{4.4}$$

and

$$\begin{aligned} -i\,\Sigma_0^<(k) \sim &\int_\Lambda d^3p\ \delta(k_0 - E_p + E^\pi_{p-k})\,\mathrm{n_F}(E_p)\,[1 + \mathrm{n_B}(E_p - k_0)] \\ &+ \int_\Lambda d^3p\ \delta(k_0 + E_p + E^\pi_{p-k})\ [1 + \mathrm{n_B}(-E_p - k_0)]\,. \end{aligned} \tag{4.5}$$

There is one process that contributes to $i\,\Sigma^>$ and – taking into account that k_0 can be positive or negative in the first term of (4.5) – three processes that contribute to $-i\,\Sigma^<$. In the last term of (4.5), the Bose distribution demands $k_0 < -E_p$. Hence, the integral will only be finite for negative k_0.

All four processes are shown diagrammatically in Fig. 4.1. The first line shows the only process that contributes to the loss rate $i\,\Sigma^>$ (4.4). The processes that contribute to the gain rate $-i\,\Sigma^<$ (4.5) can be found in the second line. Process (b) contributes to the gain rate at positive k_0. The processes (c) and (d) are the contributions at negative k_0, $-i\,\Sigma^<$ is then an antiquark loss rate. Note that (b) and (c) differ only by the sign of k_0, both are represented by the first line of (4.5).

With the help of Eqs. (4.4) and (4.5), we can determine the energy thresholds of the processes in Fig. 4.1. Besides energy and momentum conservation, the integrands of (4.4) and (4.5) include the following constraints: Incoming quarks from the medium must have a positive energy below the chemical potential. Outgoing quarks, on the other hand, must have an energy higher than μ – due to Pauli blocking. Outgoing antiquarks and mesons must have a positive energy, but are not Pauli blocked. We also have to consider that the (anti-)quark three-momentum $\vec{p}$ is regularized by the cutoff Λ of the model. Since the quasiparticle spectral function $\mathcal{A}$ provides a sharp

[3] Since only the negative energy peak of $\Delta^<$ and only the positive energy peak of $\Delta^>$ contribute, both propagators can be identified with outgoing RPA mesons in the collision rates. This corresponds to the fact that there are no mesons in the medium for $T = 0$.

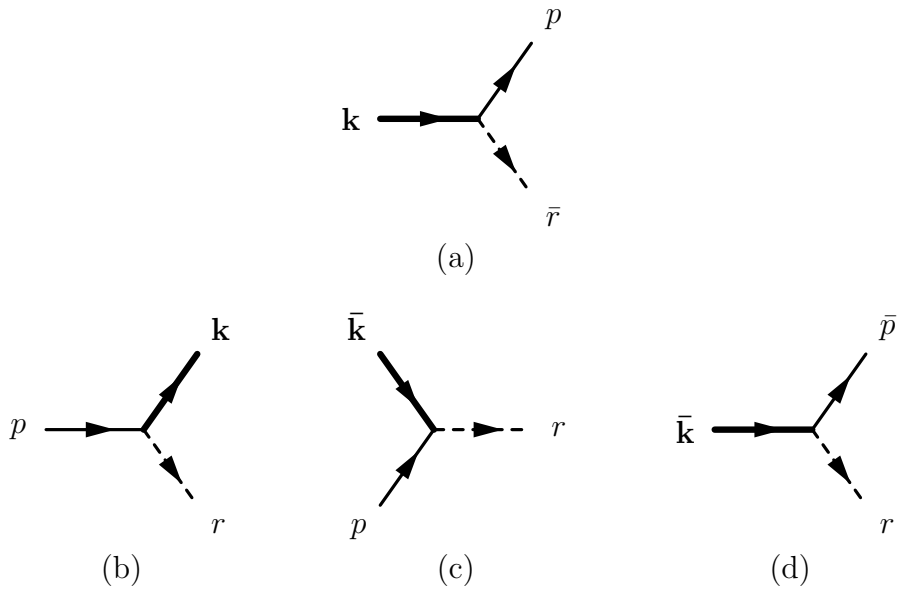

Figure 4.1: Scattering processes corresponding to the collisional self-energies $\Sigma^{\gtrless}(k)$ in the form of Eq. (4.3). The thick lines carry the external four-momentum k. k, p denote quarks with four-momenta $(k_0, \vec{k}\,)$, etc. (with $k_0, p_0 > 0$), and $\bar{k}, \bar{p}$ antiquarks with four-momentum $(-k_0, \vec{k}\,)$, etc. (with $k_0, p_0 < 0$). $\bar{r}$ denotes a meson with four-momentum $(-r_0, \vec{r}\,)$, where $r_0 < 0$. See the text for details.

relation between the energy and the momentum of a quark or antiquark, the energies p_0 and $\bar{p}_0$ are restricted to values below $E_\Lambda = \sqrt{\Lambda^2 + m^{*2}}$.

In Table 4.1 we summarize the energy thresholds that have been found for the processes of Fig. 4.1. We will now review how these thresholds have been determined. Note that the thresholds in Table 4.1 are not always the strictest limits that can be found. However, for our purpose – to understand the structure of the quark width and to identify the contributions from individual scattering and decay processes – they are perfectly suitable.

Processes (a) and (d)

The lowest limit for k_0 in the quark decay (a) is obviously $\mu + m_\pi$. An RPA pion must be created and the outgoing quark needs – due to Pauli blocking – an energy p_0 above the Fermi energy. Our implementation of the NJL cutoff induces an upper limit for the process. Phase space closes at $k_0^{\max} = E_\Lambda + E^\pi_{\Lambda-k}$, where we have introduced $E^\pi_{\Lambda-k} = [(\Lambda + |\vec{k}\,|)^2 + m_\pi^2]^{1/2}$.

The lower limit $\mu + m_\pi$ is rather loose since it does not take the three-momenta of the outgoing states into account. Using the condition for four-momentum conservation

Table 4.1: Energy thresholds of the processes shown in Fig. 4.1, see the text for details. The thresholds in the two lower rows are given for $\bar{k}_0 = -k_0$. Note that m_π is the pion mass that is determined by the poles of the RPA propagator.

Process	Thresholds
(a)	$\left.\begin{array}{c}\mu + m_\pi \\ \sqrt{\vec{k}^2 + (m^* + m_\pi)^2}\end{array}\right\} < k_0 < E_\Lambda + E^\pi_{\Lambda-k}$
(b),(c) $(m^* > m_\pi)$	$\mu - \sqrt{(\lvert\vec{k}\,\rvert + k_F)^2 + m_\pi^2} < k_0 < \left\{\begin{array}{c}\mu - m_\pi \\ \sqrt{\vec{k}^2 + (m^* - m_\pi)^2}\end{array}\right.$
(b),(c) $(m^* < m_\pi)$	$\sqrt{(\lvert\vec{k}\,\rvert - k_F)^2 + m_\pi^2} - \mu < \bar{k}_0 < \left\{\begin{array}{c}E^\pi_{\Lambda+k_F} - \mu \\ \sqrt{\vec{k}^2 + (m^* - m_\pi)^2}\end{array}\right.$
(d)	$\sqrt{\vec{k}^2 + (m^* + m_\pi)^2} < k_0 < E_\Lambda + E^\pi_{\Lambda-k}$

from the δ-function in Eq. (4.4),

$$k_0 = E_p + E^\pi_{p-k} = \sqrt{\vec{p}^{\,2} + m^{*2}} + \sqrt{(\vec{p} - \vec{k}\,)^2 + m_\pi^2}\,, \tag{4.6}$$

we can find a more rigorous limit. Note that k_0 will drop for increasing $\cos\vartheta_{p,k}$ when $|\vec{p}|$ is kept fixed. Our search for minima of k_0 can thus be restricted to the case $\cos\vartheta_{p,k} = 1$. We find the extrema of $k_0|_{\cos\vartheta=1}$ by solving

$$\left.\frac{dk_0}{d|\vec{p}\,|}\right|_{\cos\vartheta=1} = 0\,.$$

A short calculation yields a single solution that corresponds to a minimum of k_0,

$$|\vec{p}\,|_{\min} = \frac{m^*}{m^* + m_\pi}|\vec{k}\,| \qquad \Rightarrow \qquad k_0^{\min} = \sqrt{\vec{k}^2 + (m^* + m_\pi)^2}\,. \tag{4.7}$$

Eq. (4.7) constitutes a purely kinematical threshold that must be satisfied for all $\vec{k}$. It does not take Pauli blocking into account. For small $\vec{k}$, the value of $|\vec{p}\,|_{\min}$ will drop below the Fermi momentum $k_F = [\mu^2 - m^{*2}]^{1/2}$. This is, of course, forbidden by Pauli blocking for the outgoing quark in process (a). We note that the function

$k_0|_{\cos\vartheta=1}$ has only one minimum (4.7) and increases monotonously for $|\vec{p}\,| > |\vec{p}\,|_{\min}$. Thus, for $|\vec{p}\,|_{\min} < k_F$ the effective minimum of k_0 is located at the lowest allowed three-momentum, $|\vec{p}\,| = k_F$,

$$k_0^{\min}\big|_{|\vec{p}\,|_{\min}<k_F} = \mu + \sqrt{(|\vec{k}\,| - k_F)^2 + m_\pi^2} \quad > \mu + m_\pi\,. \tag{4.8}$$

This expression can be easily interpreted. The outgoing quark has the lowest possible four-momentum $p = (\mu, k_F)$ while the outgoing RPA pion has a three-momentum of $|\vec{r}\,| = |\vec{k}\,| - k_F$ and the corresponding on-shell energy.

The two conditions (4.7) and (4.8) complement each other. The kinematical constraint (4.7) must hold for all $\vec{k}$. The Pauli blocking related condition (4.8) must hold only for certain values of $\vec{k}$ in its $|\vec{k}\,|$ dependent form. In the simpler form $k_0 > m^* + m_\pi$, however, it must hold for all $\vec{k}$, too. Therefore, we replace the full expression of (4.8) by its $|\vec{k}\,|$ independent form in Table 4.1. Note that (4.8) ensures that process (a) can occur only at energies k_0 above the chemical potential μ. The limit (4.7) includes the condition $k_0 > E_k + m_\pi$. Thus, process (a) is not allowed when the incoming quark k is on-shell. The larger m_π becomes, the further away k_0 must be from the on-shell region.

The thresholds for the antiquark decay (d) are very similar to those of the quark decay (a). The upper limit is given by $\bar{k}_0 < E_\Lambda + E^\pi_{\Lambda-k}$. The lower limit is equivalent to (4.7), i.e., $\bar{k}_0 > [\vec{k}^2 + (m^* + m_\pi)^2]^{1/2}$. Since the outgoing antiquark is not Pauli blocked, there are no further restrictions. Like in process (a), the incoming antiquark $\bar{k}$ cannot be on-shell. Note that the lower limit reduces to the total mass of the outgoing states, $m^* + m_\pi$, for $\vec{k} = 0$.

Processes (b) and (c)

The two processes (b) and (c) correspond both to the integral in the first line of Eq. (4.5). They differ only by the sign of k_0 (outgoing quark or incoming antiquark). Hence, we determine common thresholds for both processes from (4.5). When the lower limit for k_0 is negative and the upper limit is positive, one process turns smoothly into the other one. The collision rate does not drop to zero at the transition from (b) to (c) at $k_0 = 0$. Note that it is also possible that both thresholds have the same sign. For example, energy conservation demands that the condition $k_0 < \mu - m_\pi$ is always satisfied. This means that the integral in (4.5) is only finite for negative energies k_0 when m_π becomes larger than μ. Process (b) is then forbidden.

For a thorough investigation of the thresholds we turn again to the condition for four-momentum conservation. For the two processes (b) and (c) it is given by the argument of the δ-function in the first line of Eq. (4.5),

$$k_0 = E_p + E^\pi_{p-k} = \sqrt{\vec{p}^{\,2} + m^{*2}} - \sqrt{(\vec{p} - \vec{k}\,)^2 + m_\pi^2}\,. \tag{4.9}$$

For fixed $|\vec{p}\,|$, k_0 increases with increasing $\cos\vartheta_{p,k}$. Hence, the upper limit of k_0

corresponds to the maximum of $k_0|_{\cos\vartheta=1}$. A short calculation yields

$$\left.\frac{dk_0}{d|\vec{p}|}\right|_{\cos\vartheta=1} = 0 \qquad \Rightarrow \qquad |\vec{p}|_{\text{ext}} = \frac{m^*}{m^* - m_\pi}|\vec{k}\,|\,. \tag{4.10}$$

This result needs some comment: First, $|\vec{p}|_{\text{ext}}$ is only positive for $m^* > m_\pi$. Since we demand $|\vec{p}| \geq 0$, $|\vec{p}|_{\text{ext}}$ is (physically) not a reasonable solution for $m^* < m_\pi$. Second, $|\vec{p}|_{\text{ext}}$ corresponds not necessarily to a maximum of k_0 – note the relative minus sign between the two terms on the rhs. of Eq. (4.9). A closer inspection shows that k_0 has in fact a maximum at $|\vec{p}|_{\text{ext}}$ for $m^* > m_\pi$ but a minimum for $m^* < m_\pi$.

Inserting $|\vec{p}|_{\text{ext}}$ into (4.9) yields the maximum of k_0 for $m^* > m_\pi$,

$$k_0^{\max}|_{m^*>m_\pi} = \sqrt{\vec{k}^2 + (m^* - m_\pi)^2}\,. \tag{4.11}$$

As we can see in (4.10), the value of $|\vec{p}|_{\text{ext}}$ may exceed the Fermi momentum k_F for large $\vec{k}$. However, in a medium of quasiparticles there are only populated states up to the Fermi momentum. Since $k_0|_{\cos\vartheta=1}$ has only one maximum, it will drop monotonously for decreasing $|\vec{p}| < |\vec{p}|_{\text{ext}}$. The effective maximum of k_0 is then located at the largest allowed three-momentum, $|\vec{p}| = k_F$,

$$k_0^{\max}|^{|\vec{p}|_{\text{ext}}>k_F}_{m^*>m_\pi} = \mu - \sqrt{(|\vec{k}\,| - k_F)^2 + m_\pi^2} \quad < \mu - m_\pi\,. \tag{4.12}$$

Like for process (a), we have found two complementary conditions, (4.11) and (4.12), for the case $m^* > m_\pi$. Both are listed in Table 4.1, (4.12) in the more general form $k_0 < \mu - m_\pi$ that is $|\vec{k}\,|$ independent. Note that the value of $k_0^{\max}$ from (4.11) is always positive. The kinematical constraint includes the condition $k_0 < E_k$ and forbids that the incoming quark of process (b) is on-shell. The threshold from (4.12) is always smaller than the chemical potential μ. It may become negative for large $\vec{k}$. Process (b) is then forbidden. It follows from the rhs. of (4.12) that the condition

$$\sqrt{k_F^2 + m^*} = \mu < \sqrt{(|\vec{k}\,| - k_F)^2 + m_\pi^2} \tag{4.13}$$

must be satisfied to obtain a negative $k_0^{\max}$. This means that $|\vec{k}\,|$ must be larger than $2k_F$.

Let us now turn to the maximum of k_0 for $m^* < m_\pi$. The three-momentum $|\vec{p}|_{\text{ext}}$ from (4.10) corresponds to a minimum of k_0 at negative $|\vec{p}|$ in this case. For $|\vec{p}| > |\vec{p}|_{\text{ext}}$, k_0 will rise monotonously since $|\vec{p}|_{\text{ext}}$ is the only extremum. Thus, we find the effective maximum of $k_0|_{m^*<m_\pi}$ at the largest allowed value for $|\vec{p}|$. This is again $|\vec{p}| = k_F$. We obtain

$$k_0^{\max}|_{m^*<m_\pi} = \mu - \sqrt{(|\vec{k}\,| - k_F)^2 + m_\pi^2}\,.$$

$k_0^{\max}$ must be negative for all $|\vec{k}\,|$ when $m_\pi > \mu$, cf. (4.13). Process (b) is then completely suppressed. For $m^* < m_\pi < \mu$, $k_0^{\max}$ will be positive only in a small range

of three-momenta $|\vec{k}\,|$ in the vicinity of the Fermi momentum. Therefore, we list $k_0^{\max}$ for $m^* < m_\pi$ in Table 4.1 not as a maximum of the quark energy k_0 but as a minimum of the antiquark energy $\bar{k}_0 = -k_0$.

After we have determined the upper thresholds (in k_0) for the processes (b) and (c), we have to find the lower thresholds. This can be done in an analogous way. Since k_0 of (4.9) drops for fixed $|\vec{p}|$ when $\cos\vartheta_{p,k}$ decreases, the lower limit of k_0 corresponds to the minimum of $k_0|_{\cos\vartheta=-1}$. We find

$$\left.\frac{dk_0}{d|\vec{p}\,|}\right|_{\cos\vartheta=-1} = 0 \qquad \Rightarrow \qquad |\vec{p}\,|_{\rm ext} = -\frac{m^*}{m^* - m_\pi}|\vec{k}\,| \,. \tag{4.14}$$

Recall our comments below Eq. (4.10). $|\vec{p}\,|_{\rm ext}$ is now only positive for $m^* < m_\pi$. It corresponds to a minimum of k_0 in this case but to a maximum of k_0 for $m^* > m_\pi$. When $|\vec{p}\,|_{\rm ext}$ is inserted into (4.9), the minimum of k_0 for $m^* < m_\pi$ is obtained,

$$k_0^{\min}\big|_{m^*<m_\pi} = -\sqrt{\vec{k}^2 + (m^* - m_\pi)^2}\,. \tag{4.15}$$

The value of $|\vec{p}\,|_{\rm ext}$ in (4.14) may become larger than k_F. Thus, we have to consider again that the maximum momentum of an incoming quark from the medium is the Fermi momentum. $|\vec{p}\,|_{\rm ext}$ denotes the position of the only minimum of $k_0|_{\cos\vartheta=-1}$, hence k_0 must rise for decreasing $|\vec{p}\,| < |\vec{p}\,|_{\rm ext}$. We find the effective minimum of k_0 at $|\vec{p}\,| = k_F$, the largest allowed value of $|\vec{p}\,|$,

$$k_0^{\min}\big|_{m^*<m_\pi}^{|\vec{p}\,|_{\rm ext}>k_F} = \mu - \sqrt{(|\vec{k}\,| + k_F)^2 + m_\pi^2} \quad > \mu - E^\pi_{\Lambda+k_F}\,, \tag{4.16}$$

with $E^\pi_{\Lambda+k_F} = [(\Lambda + k_F)^2 + m_\pi^2]^{1/2}$. The rhs. of (4.16) is – like the rhs. of (4.15) – negative for all $|\vec{k}\,|$ as long as $m^* < m_\pi$. In Table 4.1, the two complementary conditions of (4.15) and (4.16) are listed as upper limits of the antiquark energy $\bar{k}_0$, using the $|\vec{k}\,|$ independent form $\bar{k}_0 < E^\pi_{\Lambda+k_F} - \mu$ for (4.16).

Finally, we have to determine the lower limit of k_0 for $m^* > m_\pi$. The negative $|\vec{p}\,|_{\rm ext}$ corresponds to a maximum of k_0 in this case. Since this is the only maximum of $k_0|_{\cos\vartheta=-1}$, k_0 will drop monotonously for increasing $|\vec{p}\,| > |\vec{p}\,|_{\rm ext}$. We find the effective minimum of k_0 – once again – at the largest allowed value for $|\vec{p}\,|$, i.e., the Fermi momentum,

$$k_0^{\min}\big|_{m^*>m_\pi} = \mu - \sqrt{(|\vec{k}\,| + k_F)^2 + m_\pi^2}\,.$$

The sign of this limit is not fixed. When m_π is almost as large as m^*, $k_0^{\min}|_{m^*>m_\pi}$ will be positive only for small $\vec{k}$ and negative otherwise – cf. (4.13) and replace k_F by $-k_F$. However, if m_π is much smaller than m^*, the limit $k_0^{\min}|_{m^*>m_\pi}$ will be only negative for large $|\vec{k}\,|$ – for massless pions, the condition is $|\vec{k}\,| > \mu - k_F$.

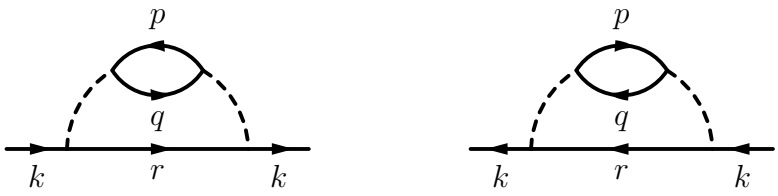

Figure 4.2: Self-energy diagrams corresponding to $-i\,\Sigma^{>}$ (left) and $-i\,\Sigma^{<}$ (right) in the rewritten form of Eq. (4.17).

4.2.2 Quark–quark scattering and decay processes

The continuum of off-shell states in the RPA spectral functions can, of course, not be represented by quasiparticles. To investigate the contributions from the time- and spacelike off-shell states to the collision rates $\Sigma^{\gtrless}$ in a similar way as the contributions from the bound $q\bar{q}$ states, we will rewrite the integrals. Thereby we replace the outgoing mesons by – quasiparticle – quark–antiquark pairs. Using the relation $\Delta_l^{\gtrless} = \Delta_l^{\rm ret}\,\Pi_l^{\gtrless}\,\Delta_l^{\rm av}$ [ZW92, GL98, CSHY85] in Eq. (4.3) we find

$$-i\,\Sigma^{\gtrless}(k) = -i\sum_l \int \frac{d^4p}{(2\pi)^4}\frac{d^4q}{(2\pi)^4}\frac{d^4r}{(2\pi)^4}(2\pi)^4\delta^4(k+p-q-r) \qquad (4.17)$$
$$\times\,\Gamma_l\,{\rm S}^{\gtrless}(r)\tilde{\Gamma}_l\,\Delta_l^{\rm ret}(r-k)\,{\rm Tr}\left[\tilde{\Gamma}_l\,{\rm S}^{\lessgtr}(p)\Gamma_l\,{\rm S}^{\gtrless}(q)\right]\Delta_l^{\rm av}(r-k)\,.$$

Diagrammatically, the self-energies have then the form that is shown in Fig. 4.2. Cutting those diagrams yields scattering and decay processes of the structure $qq \to qq$, $q \to qq\bar{q}$, etc. The energy thresholds of these processes are generated by the incoming and outgoing (anti-)quarks that are explicitly given by the propagators $\mathrm{S}^{\gtrless}$. Hence, we can ignore the off-shell structure of the meson propagators in (4.17). It is also not necessary to distinguish between σ and π contributions at this point – they differ only in magnitude but not in the k_0 thresholds.

Note that (4.17) and the diagrams in Fig. 4.2 resemble the approach of [FLM03b], where we have calculated the collisional self-energies from the Born diagrams that are shown in Fig. 2.2. Here, however, the bare NJL coupling G^2 is replaced by the propagators of the dynamically generated RPA mesons, $\Delta^{\rm ret}\,\Delta^{\rm av} = |\,\Delta^{\rm ret}\,|^2$. To recover the direct Born diagram of [FLM03b], we can use the expansion of the meson propagator that is shown in (2.7).

Replacing the quark propagators in (4.17) by the mean-field spectral functions (4.1) and Fermi distributions, we find

$$i\,\Sigma_0^{>}(k) \sim \int_\Lambda d^3p d^3q\;\delta(k_0+E_p-E_q-E_{k+p-q})\,{\rm n_F}(E_p)\,[1-{\rm n_F}(E_q)]\,[1-{\rm n_F}(E_{k+p-q})]$$
$$+\int_\Lambda d^3p d^3q\;\delta(k_0-E_p-E_q-E_{k+p-q})\,[1-{\rm n_F}(E_q)]\,[1-{\rm n_F}(E_{k+p-q})] \qquad (4.18)$$

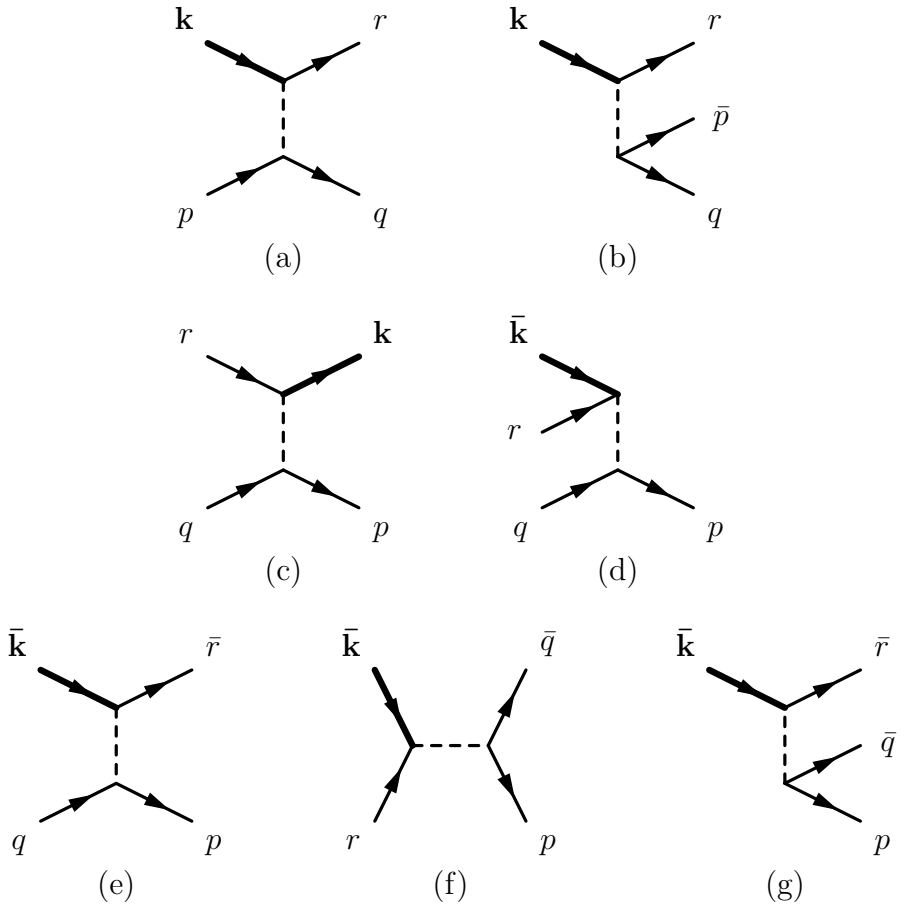

Figure 4.3: Scattering processes corresponding to the collisional self-energies $\Sigma^{\gtrless}(k)$ in the form of Eq. (4.17). The thick lines carry the external four-momentum k. k, p, q, r denote quarks with four-momenta $(k_0, \vec{k}\,)$, etc. (with $k_0, p_0, q_0, r_0 > 0$), and $\bar{k}, \bar{p}, \bar{q}, \bar{r}$ antiquarks with four-momentum $(-k_0, \vec{k}\,)$, etc. (with $k_0, p_0, q_0, r_0 < 0$). See the text for details.

and

$$\begin{aligned} -i\,\Sigma_0^<(k) \sim & \int_\Lambda d^3p d^3q\ \delta(k_0 + E_p - E_q - E_{k+p-q})\,[1 - \mathrm{n_F}(E_p)]\,\mathrm{n_F}(E_q)]\,\mathrm{n_F}(E_{k+p-q}) \\ & + \int_\Lambda d^3p d^3q\ \delta(k_0 + E_p - E_q + E_{k+p-q})\,[1 - \mathrm{n_F}(E_p)]\,\mathrm{n_F}(E_q)] \\ & + \int_\Lambda d^3p d^3q\ \delta(k_0 + E_p + E_q - E_{k+p-q})\,[1 - \mathrm{n_F}(E_p)]\,\mathrm{n_F}(E_{k+p-q}) \\ & + \int_\Lambda d^3p d^3q\ \delta(k_0 + E_p + E_q + E_{k+p-q})\,[1 - \mathrm{n_F}(E_p)]\,. \end{aligned} \tag{4.19}$$

The corresponding processes are shown in Fig. 4.3. Again, many of the formally possible processes are ruled out by the distribution functions (no incoming antiquarks).

Table 4.2: Energy thresholds of the processes shown in Fig. 4.3, see the text for details. The thresholds of the antiquark processes (e), (f), and (g) are given for $\bar{k}_0 = -k_0$.

Process	Thresholds				
(a)	μ	$<$	k_0	$<$	$2E_\Lambda - m^*$
(b)	$\left.\begin{array}{r} 2\mu + m^* \\ \sqrt{\vec{k}^2 + (3m^*)^2} \end{array}\right\}$	$<$	k_0	$<$	$3E_\Lambda$
(c),(d)	$2\mu - \sqrt{(\lvert\vec{k}\rvert + 2k_F)^2 + m^{*2}}$	$<$	k_0	$<$	μ
(e),(f)	m^*	$<$	$\bar{k}_0$	$<$	$2E_\Lambda - m^*$
(g)	$\left.\begin{array}{r} \mu + 2m^* \\ \sqrt{\vec{k}^2 + (3m^*)^2} \end{array}\right\}$	$<$	$\bar{k}_0$	$<$	$3E_\Lambda$

For simplicity, we do not display u-channel processes in Fig. 4.3. They have the same energy thresholds as the shown t-channel processes and thus do not provide additional information. Of course, both channels are included in the full calculation of the quark width.

The processes in Fig. 4.3 are arranged in the same order as the integrals in (4.18) and (4.19). The first line of Fig. 4.3 shows the two contributions to the loss rate $i\,\Sigma^>(k)$. In the second line of Fig. 4.3 we find the only process that contributes to the gain rate $-i\,\Sigma^<$ for positive k_0 and one of the contributions for negative k_0. Note that the processes (c) and (d) both correspond to the first line of (4.19). The processes in the third line of Fig. 4.3 are the remaining contributions to $-i\,\Sigma^<$ for negative k_0 (antiquark loss rate).

The thresholds for the processes can be found by applying the same constraints to the incoming and outgoing quarks as in the analysis of the processes in Fig. 4.1. We have summarized all thresholds in Table 4.2. In the following, we will briefly describe how they have been determined. We will not do this on the same level of detail as in the previous section. Instead, we refer to [Frö01] where a thorough analysis of the processes from Fig. 4.3 can be found for massless quarks.

Processes (a), (e), and (f)

Phase space opens for process (a) at $k_0 = \mu$ since each of the outgoing quarks q and r needs a minimum energy of μ while the incoming quark p of the medium can only provide a maximum energy of μ. Note that this threshold is independent of $|\vec{k}\,|$, see [Frö01]. Due to the cutoff, phase space closes again at an energy of $k_0 = 2E_\Lambda - m^*$.

Since we ignore the existence of bound $q\bar{q}$ states in the meson spectral functions at this point, the t-channel process (e) and the s-channel process (f) have identical limits. The allowed energy range for the two processes, $m^* < \bar{k}_0 < 2E_\Lambda - m^*$, is similar to that for process (a). Only μ is replaced by m^* in the lower limit, since one of the outgoing states is now an antiquark.

Processes (b) and (g)

The quark decay (b) involves two outgoing quarks and one antiquark. Hence, this process is only allowed for energies $k_0 > 2\mu + m^*$. The upper threshold is given by $k_0 = 3E_\Lambda$. We can derive a second condition for the minimum of k_0 by noting the similarity of process (b) to process (a) of Fig. 4.1. When we identify the outgoing states q and $\bar{p}$ with a single state that has a mass of at least $2m^*$, we find – in analogy to (4.7) – the kinematical condition

$$k_0 > \sqrt{\vec{k}^2 + (3m^*)^2}\,. \tag{4.20}$$

The expression in (4.20) and the condition $k_0 > 2\mu + m^*$ complement each other since (4.20) does not respect Pauli blocking. Note that we will not go through the tedious exercise of finding a condition similar Eq. (4.8) here. For our purposes this will not be necessary.

The antiquark decay (g) has limits that are very similar to those of process (b). The upper threshold is identical, $\bar{k}_0 = 3E_\Lambda$. The lower threshold is given by a combination of Pauli blocking and energy conservation, $\bar{k}_0 > \mu + 2m^*$ (two antiquarks and one quark are produced), and the kinematical constraint $\bar{k}_0 > [\vec{k}^2 + (3m^*)^2]^{1/2}$.

Processes (c) and (d)

We turn now to the processes (c) and (d). Like the processes (b) and (c) of Fig. 4.1, those processes turn seamlessly into each other at $k_0 = 0$. Hence, we find common thresholds for both processes. The upper threshold is easily found. Since the two incoming quarks from the medium can provide a maximum total energy of 2μ and the outgoing quark p requires a minimum energy of μ, the upper k_0 limit is given – independently of $|\vec{k}\,|$ – by the chemical potential μ.

Finding the lower limit of the two processes is more complicated. Energy conservation demands

$$k_0 = E_q + E_r - E_p = \sqrt{\vec{q}^{\,2} + m^{*2}} + \sqrt{\vec{r}^{\,2} + m^{*2}} - \sqrt{(\vec{q} + \vec{r} - \vec{k}\,)^2 + m^{*2}}\,, \tag{4.21}$$

where we have used $\vec{p} = \vec{q} + \vec{r} - \vec{k}$. The minimum of k_0 surely corresponds to the case

where $\cos\vartheta_{q,k} = \cos\vartheta_{r,k} = -1$, i.e.,

$$k_0 > \sqrt{\vec{q}^2 + m^{*2}} + \sqrt{\vec{r}^2 + m^{*2}} - \sqrt{(|\vec{q}| + |\vec{r}| + |\vec{k}\,|)^2 + m^{*2}}\,. \tag{4.22}$$

We will now search for a miminum of k_0 at fixed $|\vec{r}|$ and $|\vec{k}\,|$. The second term on the rhs. of (4.22) is then just a constant that has no influence on the location of the minimum. A short calculation yields

$$\left.\frac{dk_0}{d|\vec{q}|}\right|_{\cos\vartheta=-1} = \frac{|\vec{q}|}{\sqrt{|\vec{q}|^2 + m^{*2}}} - \frac{|\vec{q}| + s}{\sqrt{(|\vec{q}| + s)^2 + m^{*2}}}\,, \tag{4.23}$$

where $s = |\vec{r}| + |\vec{k}\,|$. The derivative has no zeros for finite values of $|\vec{q}|$. This is not surprising: At fixed $|\vec{r}|$, the properties of (4.21) should be similar to those of Eq. (4.9). As we have seen in (4.14), the minimum of the rhs. of (4.9) is located at $|\vec{p}|_{\rm ext} = -m^*/(m^* - m_\pi)|\vec{k}\,|$. Since we consider the case $m_\pi \to m^*$ here, the value of $|\vec{p}|_{\rm ext}$ diverges. Nonetheless, we can show that the derivative of k_0 is negative for all (positive) values of $|\vec{q}|$. Rewriting the rhs. of (4.23) yields

$$\left.\frac{dk_0}{d|\vec{q}|}\right|_{\cos\vartheta=-1} = \frac{|\vec{q}|\left[\sqrt{(|\vec{q}| + s)^2 + m^{*2}} - \sqrt{(|\vec{q}| + s)^2 + m^{*2}\frac{(|\vec{q}|+s)^2}{|\vec{q}|^2}}\right]}{\sqrt{|\vec{q}|^2 + m^{*2}}\sqrt{(|\vec{q}| + s)^2 + m^{*2}}}\,. \tag{4.24}$$

Since $(|\vec{q}| + s)^2/|\vec{q}|^2 \geq 1$ (for positive $|\vec{q}|$), we find that the numerator of (4.24) is in fact negative. We come back to the special case $m^* = 0$ below.

It follows from (4.24) that k_0 must drop monotonously for increasing $|\vec{q}|$. Due to the symmetry of the rhs. of (4.22) in $|\vec{q}|$ and $|\vec{r}|$, we find the same result for the $|\vec{r}|$ dependence when $|\vec{q}|$ is kept fixed. Consequently, the minimum of k_0 is located where $|\vec{q}|$ and $|\vec{r}|$ both reach the largest allowed values. In the processes (c) and (d), q and r are quarks from the medium. The upper limit for their momentum is the Fermi momentum $k_F = [\mu^2 - m^{*2}]^{1/2}$. For the minimum of k_0 this means

$$k_0^{\rm min} = 2\mu - \sqrt{(|\vec{k}\,| + 2k_F)^2 + m^{*2}}\,. \tag{4.25}$$

The sign of $k_0^{\rm min}$ is not fixed. In the chirally broken phase, where μ is much larger than k_F, $k_0^{\rm min}$ will become only negative when $|\vec{k}\,|$ is large. For moderate values of $|\vec{k}\,|$ it will be positive. Process (d) is then forbidden. For massless quarks, (4.22) and (4.25) turn into $k_0^{\rm min} = -|\vec{k}\,|$. The derivative of k_0 vanishes in this case, cf. (4.24). Note that the condition $k_0 > -|\vec{k}\,|$ is included in (4.25) for finite m^*, too.

To conclude this section, we list some typical values for the thresholds of all processes in Table 4.3. This should provide a better feeling for the (numerical) position of the thresholds. The values in Table 4.3 are based on the results for m^* and m_π of two calculations in the Hartree+RPA approximation. Since a parameter set with a finite current quark mass has been used, the RPA pions are not massless in the chirally broken phase and the quarks are not massless in the chirally restored phase.

Table 4.3: Typical values for the energy thresholds of the processes from Figs. 4.1 and 4.3 at $|\vec{k}\,| = 100\,\mathrm{MeV}$ in the Hartree+RPA approximation, using parameter set I from Table 2.1. The left column corresponds to $\mu = 352\,\mathrm{MeV}$ ($\rho = 0.44\rho_0$) in the chirally broken phase ($m^* = 320\,\mathrm{MeV}$, $m_\pi = 142\,\mathrm{MeV}$, $E_\Lambda = 707\,\mathrm{MeV}$). The right column corresponds to $\mu = 355\,\mathrm{MeV}$ ($\rho = 5.8\rho_0$) in the chirally restored phase ($m^* = 121\,\mathrm{MeV}$, $m_\pi = 211\,\mathrm{MeV}$, $E_\Lambda = 642\,\mathrm{MeV}$).

Process		Thresholds [MeV]								
		ch. broken phase					ch. restored phase			
Fig. 4.1	(a)	494	$<$	k_0	$<$	1452	566	$<$	k_0	$<$ 1403
	(b),(c)	67	$<$	k_0	$<$	210	-135	$<$	k_0	$<$ 40
	(d)	472	$<$	$\bar{k}_0$	$<$	1452	347	$<$	$\bar{k}_0$	$<$ 1403
Fig. 4.3	(a)	352	$<$	k_0	$<$	1095	355	$<$	k_0	$<$ 1164
	(b)	1024	$<$	k_0	$<$	2122	831	$<$	k_0	$<$ 1928
	(c),(d)	196	$<$	k_0	$<$	352	-67	$<$	k_0	$<$ 355
	(e),(f)	320	$<$	$\bar{k}_0$	$<$	1095	121	$<$	$\bar{k}_0$	$<$ 1164
	(g)	991	$<$	$\bar{k}_0$	$<$	2122	597	$<$	$\bar{k}_0$	$<$ 1928

4.3 Density dependence

The self-energy integrals in Eqs. (4.3) and (4.17) allow us to make some estimates on the density dependence of the scattering processes in Figs. 4.1 and 4.3. Therefore, we have to consider two effects: Each incoming quark from the medium can be identified with a four-momentum integral over $\mathrm{S}^<$ for positive energies. This is of course nothing but the quark density (3.9). Hence, every incoming quark from the medium introduces a linear density dependence into the corresponding collision rate – at least as long as $\mu < E_\Lambda$. The incoming quark states are, however, linked to the density of the outgoing states by energy and momentum conservation. This counteracts the increase of the correlations. Each outgoing quark – not counting the quark with the external four-momentum k – corresponds to an integral over $\mathrm{S}^>$, i.e., the density of the free quark states that are located at $\mu < k_0 < E_\Lambda$. Pauli blocking forbids scattering into the populated quark states at $0 < k_0 < \mu$. The cutoff of the model, on the other hand, suppresses scattering into quark states with energies above E_Λ. Thus, the density of the free quark states decreases when the chemical potential rises. Outgoing antiquarks and mesons are not Pauli blocked. The antiquarks, however, are also regularized by the cutoff.

4.3.1 Saturation effects

It follows from these considerations that we will not observe an unlimited growth of the collision rates – and of the short-range correlations. Processes that have a total incoming energy that is too small or too large to be absorbed by the available final states, cannot contribute to the collision rates. We will investigate this effect in a similar calculation for nucleons in nuclear matter in Chapter 6. There, we will observe a saturation of the correlations at a density of $2-3$ times normal nuclear matter density, see Figs. 6.16 and 6.18. We have also performed nuclear matter calculations without Pauli blocking to verify its responsibility for the saturation. In fact, the collision rates show no saturation in that case. This is illustrated in Fig. 6.20.

There is an important difference between the effects of Pauli blocking and the cutoff. Pauli blocking becomes effective as soon as a medium is present. Even if the chemical potential is low, some final states that could – kinematically – be reached by the incoming quarks will be suppressed. The influence of Pauli blocking remains small at low quark densities but it increases continuously when the chemical potential rises. The cutoff, on the other hand, acts only on outgoing states with a large energy. As long as the total energy of the initial states is too low to reach such final states, the cutoff has no influence on the collision rates. Depending on the considered process, the cutoff may be only relevant if μ – the maximum energy of the quarks from the medium – and/or k_0 are large.

To illustrate the difference between Pauli blocking and the cutoff, we use the scattering process in Fig. 4.3(c) as an example. Pauli blocking sets a lower limit for the energy of the outgoing quark with four-momentum p. If the total energy of the incoming quarks $q_0 + r_0$ is lower than $\mu + k_0$, the process is forbidden and does not contribute to the total collision rate, i.e., the width. If we put the external four-momentum on-shell, we find the threshold $q_0 + r_0 > \mu + m^*$. The minimum total energy of the two incoming quarks is just $2m^*$. The chemical potential μ is larger than m^* at finite densities. Thus, the minimum total energy that can be absorbed by the final states is higher than the minimum total energy that the incoming states provide. The Pauli blocking effect sets in at $\mu = m^*$, i.e., at vanishing quark density. The cutoff effect becomes relevant when the total energy of the incoming quarks in Fig. 4.3(c) exceeds $E_\Lambda + k_0$. The maximum total energy of the incoming quarks is 2μ. Hence, the cutoff will suppress contributions to the collision rates for $2\mu > E_\Lambda + k_0$. Since $k_0 > 0$ for the given process, we find the condition $\mu > E_\Lambda/2$. If the chemical potential stays below this threshold, the cutoff is irrelevant since the final states with energies beyond the cutoff cannot be reached kinematically. The suppression effect sets in above this limit.

It should be noted that $E_\Lambda = [\Lambda^2 + m^{*2}]^{1/2}$ is – due to the density dependence of the effective quark mass – density dependent itself. The value does not change too much within the chirally broken or the restored phase. At the phase transition, however, it drops significantly while μ increases smoothly[4]. In the Hartree approximation,

[4] In terms of the three-momentum, the limits exchange their behavior. The cutoff remains fixed

cf. Fig. 2.8, we find values of $E_\Lambda = 703\,\mathrm{MeV}$ and $E_\Lambda = 642\,\mathrm{MeV}$ right below and above the phase transition at $\mu = 355\,\mathrm{MeV}$, using parameter set I from Table 2.1. The smaller E_Λ may enhance the saturation effect instantaneously. Coming back to the example from above we find that the chemical potential is very close to $E_\Lambda/2$ in the chirally broken phase. Hence, the cutoff effect should not be too important. Above the phase transition, however, the chemical potential is clearly beyond this limit. Therefore, we can expect that the density dependence of this and of some of the other scattering processes changes significantly at the phase transition.

4.3.2 Density dependence of the individual processes

The density dependence of the processes in Fig. 4.1 can be readily understood from the considerations above. The decays (a) and (d) do not involve incoming quarks from the medium. Hence, there is no density dependent increase of the decay rates. Due to Pauli blocking, the decay rate of (a) should slowly decrease while the decay rate of (d) remains constant until the cutoff effect sets in. The processes (b) and (c) should show a linear density dependence because of the incoming quark from the medium. Pauli blocking and the cutoff have no direct influence on these processes – unless μ exceeds E_Λ, then the density of the incoming quarks becomes constant.

The analysis of the processes in Fig. 4.3 is a little more complicated since more states are involved. The decay processes (b) and (g) are both subject to Pauli blocking. Since there are no incoming quarks from the medium, their collision rates will decrease when the density increases. The collision rates of the processes (a) and (e,f) will increase linearly at low quark densities[5]. When the density becomes larger, the increase will slow down since the importance of Pauli blocking rises – for (a) even stronger than for (e,f) since two outgoing quarks are involved. When the cutoff effect becomes relevant, too, it may even be possible that the collision rates decrease again. The processes (c,d) of Fig. 4.3 include two incoming quarks from the medium. Hence, the corresponding collision rates should rise quadratically at low densities. Since only one outgoing quark state is involved, the saturation effect should turn out to be much weaker than in the case of processes (a) and (e,f). We will come back to these points below in Chapter 5.

at the phase transition while the Fermi momentum $k_F = \sqrt{\mu^2 - m^{*2}}$ increases when the mass drops.

[5] From nuclear matter, we know the relation $\Gamma = \rho\sigma v$ (σ is the total cross section and v the relative velocity of the collision partners). This is a low-density approximation for the width generated by collisions with the structure of process (a). When we discuss our results, we will check up to which densities this approximation can be used in the present approach.

4.4 On-shell width

In the previous sections, we have identified the thresholds and the density dependence of all processes that contribute to the quark width. Now we will take a closer look at the processes that contribute to the on-shell width of the quarks and antiquarks. Since the on-shell peaks dominate the structure of the quark spectral function, these processes have the largest influence on the properties of the medium. This investigation is of particular interest for the present $\mathcal{O}(1/N_c)$ approach. The thresholds of the processes that involve bound $q\bar{q}$ states (Fig. 4.1) depend on the RPA pion mass, cf. Table 4.1. As we already know, the RPA pion mass of our approach will be larger than that of the physical pions in the chirally broken phase. Hence, the processes of Fig. 4.1 will in our approach contribute to the width in other regions than in a calculation with a more reasonable pion mass. Furthermore, we will see below that the magnitude of the contributions from some of the processes in Fig. 4.3 depends on the pion mass. This will have some impact on the on-shell width and thus on the properties of the medium.

4.4.1 Relevant processes

The momentum dependent on-shell energy is given by $E_k = [\vec{k}^2 + m^{*2}]^{1/2}$. A scattering or decay process may contribute to the on-shell width if E_k is located within its thresholds. Due to the cutoff, we restrict ourselves here to $|\vec{k}\,| < \Lambda$. We begin our investigation with the processes of Fig. 4.3. As Table 4.2 shows, the processes (a), (c), and (e,f) will contribute to the on-shell width of all free quark states, all populated quark states, and all antiquark states, respectively. The processes (b), (d), and (g), on the other hand, do not reach the on-shell regions when the (anti-)quarks have a finite mass. The lower kinematical limit $[\vec{k}^2 + (3m^*)^2]^{1/2}$ of the processes (b) and (g) will be significantly larger than E_k when the (anti-)quarks are massive. Process (d) is only allowed for $\bar{k}_0 < |\vec{k}\,|$. Hence, it cannot contribute to the on-shell width of the antiquarks.

For massless quarks, the upper threshold of process (d) and the lower kinematical limits of (b) and (g) will be located exactly at the on-shell energy E_k. However, phase space for the decay processes just opens at this point. Contributions to the on-shell width will thus not be generated. The phase space volume that is available for the decays will be large only at some distance from the on-shell regions. For processes (b) and (g) we have also to consider the additional conditions from Pauli blocking, $k_0 > 2\mu + m^*$ and $\bar{k}_0 > \mu + 2m^*$. Those thresholds will – at least for moderate $|\vec{k}\,|$ – prevent the processes from reaching the on-shell regions when the quark mass vanishes.

We note that this picture will not change substantially when the collisional broadening of the quark spectral function is taken into account. The thresholds of Table 4.2 will then be softened and phase space opens already below the given limits. However, this is only a small effect. If the (on-shell) width of the quarks does not become too

large – and this will be the result of our full calculation, see Fig. 5.17 – the thresholds are still rather strict. The phase space volume that is available for decays may not be zero at the on-shell position, but it remains small in comparison to off-shell regions where the main contributions from the processes can be found.

We turn now to the processes of Fig. 4.1 that involve bound $q\bar{q}$ states. The processes (a), (b), and (d) behave similar to (b) and (g) of Fig. 4.3. When m_π is finite, the lower threshold $[\vec{k}^2 + (m^* + m_\pi)]^{1/2}$ $(> E_k)$ of (a) and (d) and the upper threshold $[\vec{k}^2 + (m^* - m_\pi)]^{1/2}$ $(< E_k)$ of process (b) – the $m^* < m_\pi$ limit is even stricter – will keep these processes away from the on-shell regions. Note that this holds for all values of m^*. The complementary conditions from Pauli blocking prevent the processes (a) and (b) even from entering the off-shell regions in the vicinity of the Fermi energy μ.

When the RPA pion mass vanishes, the processes (a), (b), and (d) will reach the on-shell regions. Their thresholds are then located at $k_0 = E_k$ and $\bar{k}_0 = E_k$. Due to the same arguments as before, there will be no contributions to the on-shell width on the quasiparticle level – phase space just opens at E_k. Small contributions are possible when the collisional broadening of the spectral functions is taken into account. These contributions could play a role at very low densities. The three decay processes can occur in vacuum and are not very density dependent. Thus, their (small) contributions to the on-shell width may exceed those of the strongly density dependent on-shell processes (a), (c), and (e,f) of Fig. 4.3. We will come back to that point in Section 4.4.3.

Process (c) of Fig. 4.1 is the only process including a bound $q\bar{q}$ state that may contribute to the (antiquark) on-shell width. When the RPA pion mass is larger than the quark mass, the upper limit $\bar{k}_0 < [\vec{k}^2 + (m^* - m_\pi)^2]^{1/2}$, may become larger than the on-shell energy $E_k = [\vec{k}^2 + m^{*2}]^{1/2}$. As we can see, the exact condition is $m_\pi \geq 2m^*$. In the chirally restored phase, m_π will easily exceed this limit. The incoming quark and the incoming antiquark of process (c) can then form an RPA pion when they are *both* on-shell. Note that the condition of Eq. (4.16) – in the $|\vec{k}\,|$ dependent form – is stricter than the kinematical constraint at large $\vec{k}$. Above a certain value of $|\vec{k}\,|$, on-shell contributions are forbidden. In the chirally broken phase, the physical pions are significantly lighter than the quarks. In this case – where $m^* > m_\pi/2$ – process (c) is not allowed when k is on-shell. The RPA pions of our approach are much heavier than the physical pions in the chirally broken phase. Nonetheless, their mass stays well below $2m^*$. They are not heavy enough to generate contributions to the on-shell width of the antiquarks.

Let us summarize what we have found so far: The on-shell width of the quarks is generated by the processes (a) and (c) of Fig. 4.3 while the antiquark on-shell width is mainly generated by the processes (e,f). All those processes do not involve bound $q\bar{q}$ states. In the chirally restored phase, there may also be contributions from process (c) of Fig. 4.1 to the antiquark on-shell width at low momenta. The remaining processes may come close to the on-shell regions when either m_π (Fig. 4.1) or m^* (Fig. 4.3) drops to zero. But even in these cases, the processes will not be able to generate

considerable contributions to the on-shell width.

As we have seen in Section 4.3, the processes (a), (c), and (e,f) of Fig. 4.3 are strongly density dependent. All four processes need a scattering partner from the medium and can only occur at finite quark densities. Thus, we can expect that the on-shell width remains small in the chirally broken phase where the density is low. The on-shell width of the antiquarks (e,f) and of the quark states above the chemical potential (a) should show a linear density dependence. For the on-shell width of the populated quark states – generated by the scattering process (c) of Fig. 4.3 – even a quadratic density dependence can be expected. At the higher densities of the chirally restored phase, the saturation effects that we have discussed in Section 4.3.1 will limit the growth of the on-shell width. Only the contributions from process (c) of Fig. 4.1 should keep their linear density dependence at high densities.

4.4.2 Role of the RPA pion mass

The analysis of the thresholds has shown that the on-shell quark width in the chirally broken phase is determined by the processes of Fig. 4.3. The thresholds of these processes – involving only the off-shell components of the RPA pion propagator – are independent of the RPA pion mass, cf. Table 4.2. The scattering and decay processes involving bound $q\bar{q}$ states do not contribute to the collision rates in the on-shell region, even when the pions have a reasonable mass. As the kinematical thresholds in Table 4.1 show, the gap between the on-shell energy and the thresholds of the processes involving bound $q\bar{q}$ states is on the order of m_π. Considering a realistic pion mass of 140 MeV, this gap is much larger than the typical width of the on-shell peaks that we will find in our calculations.

In the chirally broken phase, the on-shell width of the antiquarks is also free of contributions from processes with bound $q\bar{q}$ states – no matter if the pions have a realistic mass or are heavier. As we have seen in Section 4.4.1, process (c) of Fig. 4.1 generates contributions to the antiquark on-shell width when $m_\pi > 2m^*$. The RPA pions of the $\mathcal{O}(1/N_c)$ approach as well as the physical pions will exceed this limit only in the chirally restored phase. Since the masses of $\mathcal{O}(1/N_c)$ RPA pions and Hartree+RPA pions are much closer to each other in the chirally restored phase (see Section 5.3), such on-shell contributions are no artifact of the present approach.

Another interesting observation holds for all populated on- and off-shell quark states: The processes that may contribute to the quark width in the region $0 < k_0 < \mu$ – process (b) of Fig. 4.1 and (c) of Fig. 4.3 – do not include incoming or outgoing antiquark states. Even when process (c) of Fig. 4.1 contributes to the antiquark on-shell width, this will have no *direct* influence on the quark states. The properties of the antiquarks are only fed back indirectly into properties of the quarks in this region via the components of the RPA spectral function. The processes that generate the width of the antiquark states, on the other hand, involve incoming and outgoing quark states.

So far, we have not considered the influence of the pion mass on the magnitude of

the various contributions to the on-shell width. In the processes of Fig. 4.3, we do not probe the on-shell region of the RPA pion propagator (i.e., the bound $q\bar{q}$ states). However, the propagator may also depend on the pion mass in its off-shell regions. Thus, it is not unlikely that the pion mass has influence on the on-shell quark width even though the width is generated by the "correct" processes.

As we have seen above, the collision rates (4.17) involve a factor $\mathrm{S}^{\mathrm{ret}}(k_\pi)\,\mathrm{S}^{\mathrm{av}}(k_\pi) = |\,\Delta^{\mathrm{ret}}(k_\pi)|^2$, where $k_\pi = r - k$ is the four-momentum of the exchanged meson. Working out the trace in Eq. (4.17) for quasiparticle propagators (see Appendix B) yields an additional factor $(r-k)^2$. Hence, we can relate the magnitude of the contributions from the individual processes[6] in Fig. 4.3 to the quark width to a factor $k_\pi^2|\,\Delta^{\mathrm{ret}}(k_\pi)|^2$. Comparing the result for this factor from our calculations to the result of the Hartree+RPA approximation – where the dynamically generated pions have a reasonable mass in the chirally broken phase – will allow us to estimate the m_π dependence of the quark width in our approach.

For a more detailed investigation, we have to split up the processes in Fig. 4.3 into the t-channel processes (a,c,e) and the s-channel process (f). In the s-channel process – like in the decays (b,d,g) that do not contribute to the on-shell width – the meson carries a timelike four-momentum that must exceed $k_\pi^2 > (m^* + \mu)^2 > (2m^*)^2$. In other words, the magnitude of the scattering rate is sensitive to the $q\bar{q}$ continuum of the RPA spectral functions. Instead of the full term $k_\pi^2|\,\Delta^{\mathrm{ret}}(k_\pi)|^2$, we show numerical results for the $q\bar{q}$ continuum of the RPA pion spectral function in the Hartree+RPA approximation and in the $\mathcal{O}(1/N_c)$ approach in Fig. 4.4 (see also Fig. 5.8 where the widths are compared). Note that $|\,\Delta_\pi\,|^2 = \xi_\pi/(k_0\Gamma_\pi)$. The differences in size and shape of the continuum are within reasonable limits – we are comparing a leading order to a next-to-leading order scheme here. A significant m_π dependence of the $q\bar{q}$ continuum cannot be observed. This means that the magnitude of the contributions from process (f) to the on-shell quark width is – like the thresholds – independent of the large RPA pion mass (in the chirally broken phase) of our $\mathcal{O}(1/N_c)$ approach. We note that the same is true for the contributions of the decays (b,d,g) to the off-shell quark width.

We turn now to t-channel processes (a,c,e) where the mesons must carry a spacelike four-momentum (see [Y+06] for the kinematics). Typically, one would expect that the range of the meson-exchange interaction in these processes scales with the inverse mass of the exchanged meson, i.e. $R \sim 1/m_\pi$. The simple estimate $\Gamma \sim \rho\sigma v$, $\sigma \sim \pi R^2$ suggests a quadratic m_π dependence of the quark width, $\Gamma \sim 1/m_\pi^2$. Since the RPA pions of our $\mathcal{O}(1/N_c)$ approach are approximately three times heavier than physical pions in the chirally broken phase, this means that the contributions from the processes (a,c,e) to the on-shell quark width could be suppressed by one order of magnitude. The off-shell properties of the dynamically generated mesons in our

[6] Recall that the RPA mesons enter the Lagrangian (2.4) without an explicit quark–meson coupling. In contrast to regular mesons, the coupling strength is part of the "normalization" of the RPA meson spectral functions.

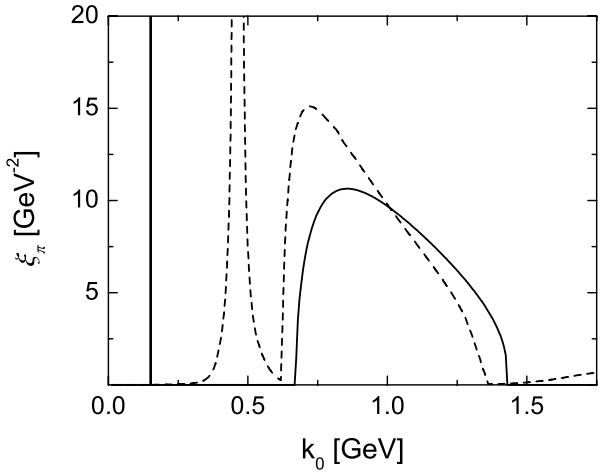

Figure 4.4: The RPA pion spectral function at a constant three-momentum of 50 MeV. The solid line shows the result of the Hartree+RPA approximation in vacuum ($m^* = 336\,\mathrm{MeV}$), the dashed line the result of the $\mathcal{O}(1/N_c)$ approach at a density of $0.05\rho_0$ ($m^* = 326\,\mathrm{MeV}$). Parameter set I of Tables 2.1 and 5.1 has been used.

approach differ, however, from those of regular mesons (recall the discussion from Section 3.8). Thus, we cannot directly transfer this estimate to our approach.

To check the real m_π dependence of the collision rates, we compare numerical results for $k_\pi^2 |\,\Delta^{\mathrm{ret}}(k_\pi)|^2$ from our $\mathcal{O}(1/N_c)$ approach to results from the Hartree+RPA approximation in Fig. 4.5. As we can see, the curves differ in fact by approximately one order of magnitude at low values of $-k_\pi^2$. At higher $-k_\pi^2$, the differences become smaller and, eventually, our approach yields larger results than the Hartree–Fock+RPA approximation.

In the collision rates corresponding to the processes (a,c,e), we integrate over the four-momentum r – and thus over the four-momentum of the exchanged meson $k_\pi = r - k$. In those integrals, we are not sensitive to the full k_π^2 range shown in Fig. 4.5. The limits of the relevant k_π^2 region are fixed by kinematics [Y$^+$06]. The lower limit is determined by the maximum three-momenta (and energies) of the two incoming particles in the collision,

$$k^2_{\pi,\mathrm{min}} = -2\left(E_1 E_2 - \vec{p}_1 \cdot \vec{p}_2 - m^{*2}\right) , \tag{4.26}$$

with $E_{1,2} = \sqrt{\vec{p}^{\,2}_{1,2} + m^{*2}}$. The upper limit is always $k^2_{\pi,\mathrm{min}} = 0$ since we consider scattering partners of equal mass.

In process (c), we integrate over the three-momenta $\vec{r}$ and $\vec{q}$ of the incoming particles. Using their upper limits k_F in (4.26), we obtain values of $k^2_{\pi,\mathrm{min}} = -0.14\,\mathrm{GeV}^2$ and $k^2_{\pi,\mathrm{min}} = -0.18\,\mathrm{GeV}^2$ at densities of ρ_0 and $1.8\rho_0$, respectively[7]. Hence, we can

[7]Note that the chiral phase transition is located slightly above $1.8\rho_0$ in our approach.

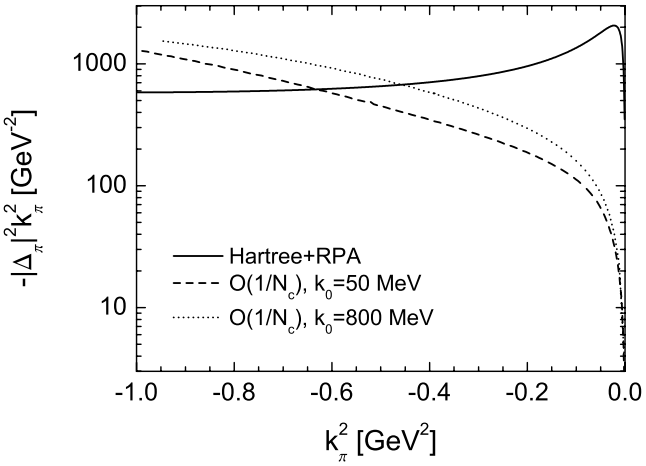

Figure 4.5: The function $-|\Delta_\pi(k_\pi)|^2 k_\pi^2$ for spacelike values of the four-momentum k_π. The solid line shows the result of the Hartree+RPA approximation in vacuum ($m^* = 336\,\mathrm{MeV}$), the dashed and dotted lines the result of the $\mathcal{O}(1/N_c)$ approach at a density of $0.05\rho_0$ ($m^* = 326\,\mathrm{MeV}$). Parameter set I of Tables 2.1 and 5.1 has been used. The function $-|\Delta_\pi(k_\pi)|^2 k_\pi^2$ depends not purely on k_π^2 in our approach since we work in a finite medium and consider a three-momentum cutoff in the calculations. Thus, we show two curves for spacelike k_π^2 at different (fixed) k_0^π.

conclude that the on-shell width of the populated quark states – that is solely generate by process (c) – is suppressed by approximately one order of magnitude in the chirally broken phase.

In processes (a) and (e), one of the incoming three-momenta is given by the external three-momentum $|\vec{k}\,|$. The second three-momentum is again limited to k_F. Thus, the limit $k^2_{\pi,\mathrm{min}}$ for these processes is $|\vec{k}\,|$ dependent. For $|\vec{k}\,| = k_F$, we obtain the same limits as for process (c). For $|\vec{k}\,| = \Lambda$, the value of $k^2_{\pi,\mathrm{min}}$ drops to $-0.54\,\mathrm{GeV}^2$ at a density of ρ_0 and to $-0.59\,\mathrm{GeV}^2$ at a density of $1.8\rho_0$. These results show that the on-shell quark width of the free quark states and the antiquark states is also suppressed by the large RPA pion mass. At higher momenta $|\vec{k}\,|$ – when the scattering processes almost reach the k_π^2 region where our approach yields larger values than the Hartree+RPA approximation – the suppression will range well below one order of magnitude.

Recall that the t-channel process (e) and the s-channel process (f) contribute to the on-shell width in the same energy region. The contributions of process (f) are not suppressed by the pion mass. However, the factor $|\Delta_\pi(k_\pi)|^2 k_\pi^2$ has a value of $\approx 100\,\mathrm{GeV}^2$ near the lower threshold of the $q\bar{q}$ continuum and drops to $\approx 10\,\mathrm{GeV}^2$ at the upper threshold. Comparing these values to the curves in Fig. 4.5 shows that process (e) yields larger contributions to the quark width even though it is suppressed

by m_π. Only when the external four-momentum k is small, the contributions from process (f) may be larger.

This brings us to the end of our analysis of the m_π dependence of the on-shell quark width. We have obtained two important results in this section. First, we have found that our approach generates the on-shell quark width from the "correct" processes, i.e. from the same processes as an approach with a more reasonable pion mass (in the chirally broken phase) – this is important for the structure of the width and its density dependence. However, the contributions from most of these processes are suppressed by the too large RPA pion mass. The naive estimate that the collision rates scale with $1/m_\pi^2$ yields an upper limit for this suppression. On average, the influence of the pion mass on the on-shell width ranges below one order of magnitude. In summary, this means that our approach represents a conservative approximation of the short-range effects in quark matter. A calculation with a more realistic pion mass should lead to stronger short-range correlations.

Let us clarify once again that all these considerations affect only our results in the chirally broken phase. Above the phase transition, the RPA pion mass of our approach will be close to the pion mass of the Hartree+RPA approximation. Thus, there will be no suppression of the quark width in the chirally restored phase. We also note that the decays of Fig. 4.3 contribute to the (off-shell) quark width at the correct energies and with the correct strength in the chirally broken phase. The contributions from the processes in Fig. 4.1 are shifted due to the large pion mass but should also have the correct size. In other words, not all contributions to the quark width are suppressed by the RPA pion mass.

4.4.3 Effects of higher order corrections

For completeness, we will discuss the influence of the correctional diagrams (c,d) of Fig. 2.14. A self-consistent inclusion of these diagrams in the calculation would fix the pion mass in next-to-leading-order and shift the limits of the processes in Fig. 4.1 closer to the Hartree+RPA values. More important than this shift, the contributions from the t-channel processes of Fig. 4.3 to the on-shell width will rise. Since the chiral properties of the pions remain disturbed in higher orders, the RPA pion will still be heavier than physical pions. Thus, the influence on the on-shell width will be weaker than suggested by Fig. 4.5 for the Hartree+RPA approximation.

In addition to the above effects, the polarization of Fig. 2.14 will yield an extended set of self-energy diagrams similar to those in Fig. 4.2 – recall that we have used the relation $\Delta_l^{\gtrless} = \Delta_l^{\mathrm{ret}}\,\Pi_l^{\gtrless}\,\Delta_l^{\mathrm{av}}$ to rewrite the collisional self-energies. The diagrams can be cut and identified with scattering rates. The rates that are constructed from the correctional diagrams (c)-(d), however, are suppressed in $1/N_c$ in comparison to the ones in Fig. 4.3. They represent only next-to-leading order contributions to the quark width.

We note that the m_π dependence of the thresholds in Table 4.1 may lead to some differences between calculations with massive and with massless RPA pions in the

chirally broken phase. For those differences it is irrelevant if the massive pions have a mass of 140 MeV or are heavier. As the estimates of Section 4.3 indicate – and the results of the full $\mathcal{O}(1/N_c)$ calculation will show (see Section 5.2.2) – the decay processes (a) and (d) of Fig. 4.1 generate much larger contributions to the collision rates at low densities than the (on-shell) processes (a), (c) and (e,f) of Fig. 4.3. We have seen in the previous section that the decay processes (a) and (d) of Fig. 4.1 may generate small contributions to the on-shell width when $m_\pi = 0$. Even though the contributions are small in comparison to the off-shell contributions of the same processes, they may be larger than the contributions of the (true) on-shell processes.

When they move closer to the on-shell region, the large contributions of the decay processes to the off-shell width may also have some influence on the results – even when the on-shell width itself does not change too much. To illustrate the possible consequences, we refer to the left panel of Fig. 5.3 that shows a similar effect. In the $\mathcal{O}(1/N_c)$ approach, the contributions from process (c) of Fig. 4.1 come already rather close to the on-shell region of the antiquarks in the chirally broken phase. They generate the small peak in the width at low negative k_0. This peak is reflected in the spectral function by a significant structure, right next to the antiquark on-shell peak.

The decay processes (a) and (d) of Fig. 4.1 are less density dependent than process (c). Thus, they generate larger off-shell contributions at low densities – they can be identified with the shoulders on the large bumps in the left panel of Fig. 5.3. When those processes move closer to the on-shell regions – which happens when m_π becomes small compared to the quark width – the impact will surely be more extreme than that of process (c) in Fig. 5.3. It is important to stress that the pions must be (almost) massless to observe the just discussed effect. The mass of the physical pions, $m_\pi \approx 140\,\text{MeV}$, is considerably larger than the typical on-shell quark width in our approach, cf. Fig. 5.15.

We come to the end of our quasiparticle analysis of the contributions to the quark width. The investigation of the thresholds and the density dependence of the individual processes in Sections 4.2 and 4.3, respectively, will be very helpful for the understanding of the results of our full $\mathcal{O}(1/N_c)$ calculations.

4.5 RPA meson width

In the previous sections of this chapter, we have discussed the various contributions to the quark width in much detail. The structure of the RPA meson width is much simpler. We know already from Section 3.4 that the width is antisymmetric in k_0. There are only two processes at positive energies and two equivalent processes at negative energies that generate the RPA meson widths. For completeness, we will identify these processes and determine their thresholds in this section. Since the processes involve no incoming or outgoing RPA meson states from the medium, it will not be necessary to split them up into contributions from bound $q\bar{q}$ states and the off-shell regions.

The starting point of our analysis are the collisional polarizations. In analogy to (4.3), we rearrange the rhs. of Eq. (3.18),

$$-i\,\Pi_l^{\gtrless}(k) = -\int \frac{d^4p}{(2\pi)^4}\frac{d^4q}{(2\pi)^4}(2\pi)^4\delta^4(k-p+q)\,\mathrm{Tr}\left[i\tilde{\Gamma}_l i\,\mathrm{S}^{\lessgtr}(p) i\Gamma_l i\,\mathrm{S}^{\gtrless}(q)\right] .$$

Replacing the quark propagators by the quasiparticle spectral function of (4.1) and the appropriate distribution functions yields

$$\begin{aligned} i\,\Pi_l^{>}(k) \sim &\int_\Lambda d^3p\;\delta(k_0 - E_p - E_{p-k})\;[1-\mathrm{n_F}(E_p)] \\ &+ \int_\Lambda d^3p\;\delta(k_0 - E_p + E_{p-k})\,[1-\mathrm{n_F}(E_p)]\,\mathrm{n_F}(E_p-k_0) \end{aligned} \tag{4.27}$$

and

$$\begin{aligned} -i\,\Pi_l^{<}(k) \sim &\int_\Lambda d^3p\;\delta(k_0 + E_p + E_{p-k})\;[1-\mathrm{n_F}(-E_p-k_0)] \\ &+ \int_\Lambda d^3p\;\delta(k_0 - E_p + E_{p-k})\,\mathrm{n_F}(E_p)\,[1-\mathrm{n_F}(E_p-k_0)]\,. \end{aligned} \tag{4.28}$$

We note that $i\,\Pi_l^{>}(k)$ is only finite for $k_0 > 0$: In the first line of (4.27), the δ-function sets the condition $k_0 = E_p + E_{p-k}$, where $E_p \geq 0$ and $E_{p-k} \geq 0$. In the second line, the distribution functions demand $E_p > \mu$ and $E_p - k_0 < \mu$. The collisional polarization $-i\,\Pi_l^{<}(k)$, on the other hand, is finite only for negative k_0. The processes that correspond to the integrals in Eqs. (4.27) and (4.28) are shown in Fig. 4.6. In the first line we find the two contributions to $i\,\Pi_l^{>}$ and in the second line the two contributions to $-i\,\Pi_l^{<}$.

Table 4.4 summarizes the thresholds that are found for the processes of Fig. 4.6. Obviously, the processes (a) and (b) are very similar to the processes (c) and (d), respectively. Therefore, the thresholds are symmetric in k_0 ($\bar{k}_0$). Processes (a) and (c) describe the decay of an RPA meson into a quark–antiquark pair. They generate the $q\bar{q}$ continuum at energies k_0 and $\bar{k}_0$ above $\mu + m^*$. Since the two processes do not involve incoming quarks, they may occur in vacuum (where μ must be replaced by m^*). The processes (b) and (d) contribute to the RPA meson widths at spacelike four-momenta. These processes – that are only possible at finite quark densities – can be identified with Landau damping [KG06].

We will now discuss how the thresholds of Table 4.4 have been determined. This is a rather simple task. The processes of Fig. 4.4 are variations of the processes of Figs. 4.1 and 4.3 that we have already investigated in the Sections 4.2.1 and 4.2.2.

Processes (a) and (c)

Kinematically, process (a) of Fig. 4.6 is similar to process (a) of Fig. 4.1. The processes differ only in the mass of the outgoing state that turns from a bound $q\bar{q}$ state into a

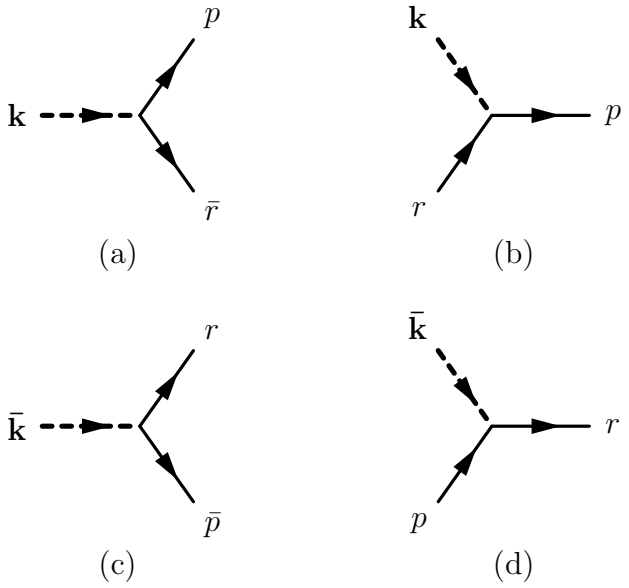

Figure 4.6: Scattering processes corresponding to the collisional RPA polarizations $\Sigma^{\gtrless}(k)$ of Eqs. (4.27) and (4.28). (a), (b) contribute to $i\,\Pi^{>}(k)$ and (c), (d) to $-i\,\Pi^{<}(k)$. The dashed meson lines carry the external four-momentum k ($\bar{k}$). See the text for details.

quark or antiquark. In process (a), four-momentum conservation is given by, cf. (4.6),

$$k_0 = E_p + E_{p-k} = \sqrt{\vec{p}^{\,2} + m^{*2}} + \sqrt{(\vec{p} - \vec{k}\,)^2 + m^{*2}}\,. \tag{4.29}$$

In analogy to (4.7), we find

$$|\vec{p}\,|_{\min} = \frac{1}{2}|\vec{k}\,| \qquad \Rightarrow \qquad k_0^{\min} = \sqrt{\vec{k}^{\,2} + 4m^{*2}}\,. \tag{4.30}$$

This is the lower kinematical limit for this process. For $|\vec{k}\,| < 2k_F$, the value of $|\vec{p}\,|_{\min}$ will drop below the Fermi momentum. This is forbidden by Pauli blocking for the outgoing quark state in process (a). In this case, the effective minimum of k_0 is – like in (4.8) – located at the lowest allowed value for $|\vec{p}\,|$,

$$k_0^{\min}\big|_{|\vec{p}\,|_{\min} < k_F} = \mu + \sqrt{(|\vec{k}\,| - k_F)^2 + m^{*2}} \quad > \mu + m^*\,. \tag{4.31}$$

The conditions in (4.30) and (4.31) complement each other. Hence, we list them both in Table 4.4. Due to the NJL cutoff, there exists also an upper threshold for process (a). The three-momentum of the outgoing quark and the outgoing antiquark must not exceed the cutoff Λ. Hence, phase space closes for this process at $k_0 = E_\Lambda + E_{\Lambda-k}$.

The upper and lower energy limits for process (c) of Fig. 4.6 can be obtained completely analogously. We find thresholds in terms of $\bar{k}_0$ instead of k_0 that are

Table 4.4: Energy thresholds of the processes shown in Fig. 4.6, see the text for details. The thresholds in the two lower rows are given for $\bar{k}_0 = -k_0$.

Process	Thresholds				
(a)	$\left.\begin{array}{c}\mu + m^* \\ \sqrt{\vec{k}^2 + 4m^{*2}}\end{array}\right\}$	$<$	k_0	$<$	$E_\Lambda + E_{\Lambda - k}$
(b)	0	$<$	k_0	$<$	$\sqrt{(\lvert\vec{k}\,\rvert + k_F)^2 + m^{*2}} - \mu$
(c)	$\left.\begin{array}{c}\mu + m^* \\ \sqrt{\vec{k}^2 + 4m^{*2}}\end{array}\right\}$	$<$	$\bar{k}_0$	$<$	$E_\Lambda + E_{\Lambda - k}$
(d)	0	$<$	$\bar{k}_0$	$<$	$\sqrt{(\lvert\vec{k}\,\rvert + k_F)^2 + m^{*2}} - \mu$

equivalent to (4.30) and (4.31). In contrast to processes (a) and (d) of Fig. 4.1, Pauli blocking has the same influence on the two processes (a) and (c) of Fig. 4.6.

Processes (b) and (d)

In process (b) of Fig. 4.6, four-momentum conservation is given by

$$k_0 = \sqrt{\vec{p}^2 + m^{*2}} - \sqrt{(\vec{p} - \vec{k})^2 - m^{*2}}\,. \tag{4.32}$$

Pauli blocking demands that the three-momentum of the outgoing quark exceeds the Fermi momentum, i.e., $|\vec{p}\,| > k_F$. The three-momentum of the incoming quark, on the other hand, must be smaller than the Fermi momentum, $|\vec{p} - \vec{k}\,| < k_F$. This yields immediately that the minimum of k_0 in process (b) must be positive for all values of $\vec{k}$.

There exists also a stricter condition for $k_0^{\min}$ that depends on $|\vec{k}\,|$. We will not determine it here since it is not of relevance for our further studies. We just note that for $|\vec{k}\,| > 2k_F$, the three-momentum $|\vec{p} - \vec{k}\,|$ will exceed the Fermi momentum for any value of $\cos\vartheta_{p,k}$. In this case, the processes (b) and (d) will be completely suppressed by Pauli blocking.

As we can see in (4.32), k_0 will be increasing with increasing $\cos\vartheta_{p,k}$ at fixed $|\vec{p}\,|$. Thus, we have to search for the upper threshold of processes (b) for $\cos\vartheta_{p,k} = 1$. Kinematically, process (b) is very similar to process (c) of Fig. 4.1. Up to the mass of the outgoing state – the meson turns into a quark – Eq. (4.32) is identical to (4.9). It follows from Eqs. (4.10) and (4.14) that k_0 ($\bar{k}_0$) has no minima or maxima at finite

$|\vec{p}|$, when the masses of the incoming and outgoing states p and r are equal.

Like in Section 4.2.2, where the $|\vec{q}|$ dependence of process (d) from Fig. 4.3 has been discussed, we will show now that $k_0|_{\cos\vartheta=1}$ rises monotonously for increasing $|\vec{p}|$. A short calculation yields, cf. (4.23),

$$\left.\frac{dk_0}{d|\vec{p}|}\right|_{\cos\vartheta=1} = \frac{|\vec{p}|}{\sqrt{|\vec{p}|^2+m^{*2}}} - \frac{|\vec{p}|-|\vec{k}\,|}{\sqrt{(|\vec{p}|-|\vec{k}\,|)^2+m^{*2}}}\,. \tag{4.33}$$

To determine the sign of the derivative, we rewrite the rhs. of (4.33) in analogy to (4.24),

$$\left.\frac{dk_0}{d|\vec{p}|}\right|_{\cos\vartheta=1} = \frac{|\vec{p}|\left[\sqrt{r^2+m^{*2}} - \mathrm{sgn}(r)\sqrt{r^2+m^{*2}\frac{r^2}{|\vec{p}|^2}}\right]}{\sqrt{|\vec{p}|^2+m^{*2}}\sqrt{r^2+m^{*2}}}\,, \tag{4.34}$$

where $r = |\vec{p}| - |\vec{k}\,|$. In this form we can easily see that the derivative of k_0 is positive for all values of $|\vec{p}|$ and $|\vec{k}\,|$. Thus, $k_0|_{\cos\vartheta=1}$ must – as predicted – increase monotonously when $|\vec{p}|$ increases.

To find the effective maximum of k_0, we have to determine the largest value of $|\vec{p}|$ that is allowed by Pauli blocking in process (b). The outgoing quark must have a three-momentum that exceeds the Fermi momentum, i.e., $|\vec{p}| > k_F$. The three-momentum of the incoming quark from the medium, on the other hand, must be smaller than the Fermi momentum. For $\cos\vartheta_{p,k} = 1$ this means $|\vec{p}| - |\vec{k}\,| < k_F$. Thus, the maximum value of $|\vec{p}|$ is limited to $k_F + |\vec{k}\,|$. Inserting this result into (4.32) yields

$$k_0^{\max} = \sqrt{(|\vec{k}\,|+k_F)^2+m^{*2}} - \mu\,.$$

For massless quarks, this condition reduces to $k_0 < |\vec{k}\,|$. When m^* is finite, the condition is even stricter. Thus, process (a) may only contribute to the RPA meson width at spacelike four-momenta.

The lower and the upper threshold of process (d) can be found completely analogously. They are – in terms of $\bar{k}_0$ instead of k_0 – identical to those of process (b). We note that the RPA meson widths drops to zero at $k_0 = 0$. In contrast to the processes (b) and (c) of Fig. 4.1, the two processes (b) and (d) do not turn seamlessly into each other.

5 Numerics and results

5.1 Details of the calculation

Using the present $\mathcal{O}(1/N_c)$ approach, we have performed numerical calculations for flavor symmetric quark matter in thermodynamical equilibrium. We have investigated a wide range of chemical potentials μ, allowing for quark matter both, in the chirally broken and restored phase. The calculations have been restricted to zero temperature.

5.1.1 NJL parameter sets

In the calculations, we use two different NJL parameter sets – one that breaks chiral symmetry explicitly with a small current quark mass m_0 and one in the chiral limit ($m_0 = 0$). The two parameter sets are similar to those in Table 2.1, but not identical. Using the Hartree–Fock parameter sets 0 and I from Table 2.1 would lead, e.g., to results for the quark condensate that are too large. Hence, we had to readjust the parameters.

In the Hartree approximation, the coupling constant G and the cutoff Λ are fitted to the quark condensate and the pion decay constant – if a finite current quark mass m_0 is desired, its value is used to adjust the pion mass in vacuum. Presently, we do not calculate the $1/N_c$ corrected physical pions (Goldstone modes) and have no access to their mass and the pion decay constant. Therefore, we proceeded in a way analogous to the transition from the Hartree to the Hartree–Fock approximation in [Kle92]: We kept the values of the parameters Λ and m_0 in Table 2.1 fixed and readjusted only the coupling G so that a reasonable value for the quark condensate $\langle \bar{u}u \rangle$, cf. Eq. (3.8), was obtained.

We have found that lowering the couplings of the Hartree parameter sets 0 and I from Table 2.1 by 22% leads to appropriate results for the quark condensate. Let us point out that the attempt to fix the too large RPA pion mass of the $\mathcal{O}(1/N_c)$ approach by adjusting m_0 would be futile. As we can see in Appendix B, the mass is generated – largely independent of m_0 – by Σ^{F} (or $\Sigma^{\mathrm{F}}_{\mathrm{eff}}$), cf. Eq. (B.8).

The readjusted NJL parameters for the $\mathcal{O}(1/N_c)$ approach and the corresponding vacuum results for the effective quark mass and the quark condensate are shown in Table 5.1. See Eq. (5.1) for the definition of m^* in the $\mathcal{O}(1/N_c)$ approach. Note that G enters the definition of the Hartree self-energy (3.2) explicitly as a linear factor. Lowering the coupling by 22% should lead to a comparable reduction of Σ^{H} – the G dependence is not strictly linear due to the self-consistent nature of the definition.

Table 5.1: Parameter sets for the self-consistent $\mathcal{O}(1/N_c)$ approach. Λ is a three-momentum cutoff. The parametrizations are based on the Hartree parameter sets in Table 2.1. In comparison to Table 2.1 the couplings were reduced by 22% to readjust the quark condensate. m^* and $\langle\bar{u}u\rangle^{1/3}$ are the vacuum results for the effective mass (5.1) and the quark condensate (3.8) that are found with those parameters.

	m_0 [MeV]	$G\Lambda^2$	Λ [MeV]	m^* [MeV]	$\langle\bar{u}u\rangle^{1/3}$ [MeV]
Set 0	-	1.68	653	308	-248
Set I	5.5	1.72	631	326	-244

The effective masses of Tables 2.1 and 5.1, however, differ by only 3%. The real part of the collisional self-energy replaces most of the missing contributions from Σ^{H}.

5.1.2 Iterative procedure

The coupled Dyson–Schwinger equations from Fig. 2.11 are solved in an iterative procedure. To initialize the calculations, we use a Hartree propagator that is modified by adding a small width. The effective quark mass that enters this propagator can either be chosen by hand or calculated by solving the simpler Dyson–Schwinger equation of the Hartree(+RPA) approximation in the first line of Fig. 2.6. With this propagator, a first approximation to the RPA propagators is calculated from the Dyson–Schwinger equation in the second line of Fig. 2.11. Using again the modified Hartree propagator and the just found RPA propagators, the rhs. of the first line of Fig. 2.11 can be calculated to find an improved solution for the quark propagator. From this point on we calculate the Dyson–Schwinger equations of Fig. 2.11 consecutively until the results for the propagators converge. In the calculations we keep the chemical potential of the system fixed. The effective quark mass and the density are free to change in every iteration.

The speed of convergence depends on several factors like the choice of the initialization (i.e., quark width and effective mass) and the structure of the self-consistent result. Usually, full convergence is achieved after $5-10$ iterations. In the vicinity of the chiral phase transition, where the gap equation may have several solutions, more iterations can be necessary. We will discuss this aspect later in more detail.

To demonstrate the effect of the iterative procedure, we show in Figs. 5.1 and 5.2 how the quark width converges to the self-consistent result in two representative calculations. We have chosen a chemical potential below and a chemical potential right above the chiral phase transition ($\mu \approx 327\,\mathrm{MeV}$) where the effective quark mass m^* and the density ρ jump discontinuously (cf. Fig. 5.10). In both cases, the

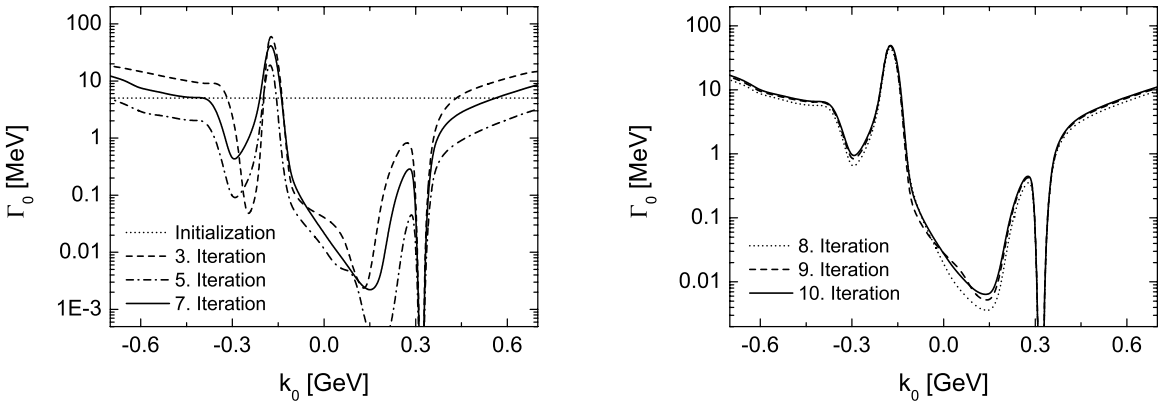

Figure 5.1: The quark width in an iterative calculation at a chemical potential of $\mu = 323\,\mathrm{MeV}$ (chirally broken phase, $\rho = 0.5\rho_0$), using parameter set I from Table 5.1. The calculation has been initialized with a constant width of $\Gamma_0 = 5\,\mathrm{MeV}$, $\Gamma_{s,v} = 0$ and $m^* = 325\,\mathrm{MeV}$.

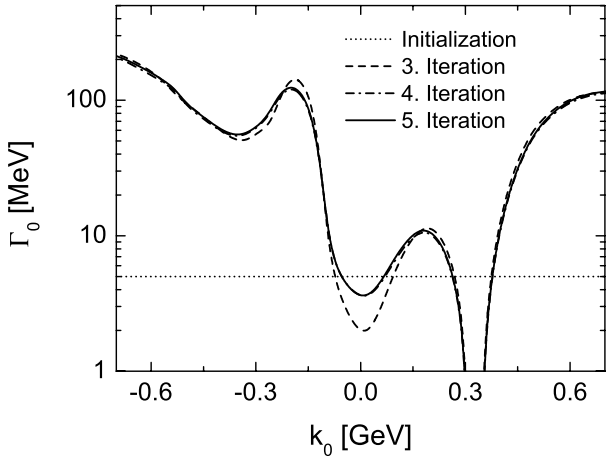

Figure 5.2: The quark width in an iterative calculation at a chemical potential of $\mu = 328\,\mathrm{MeV}$ (chirally restored phase, $\rho = 4\rho_0$), using parameter set I from Table 5.1. The calculation has been initialized with a constant width of $\Gamma_0 = 5\,\mathrm{MeV}$, $\Gamma_{s,v} = 0$ and $m^* = 143\,\mathrm{MeV}$.

calculations were initialized with a constant width of $\Gamma_0 = 5\,\mathrm{MeV}$ ($\Gamma_{s,v} = 0$) and an effective mass close to the final result.

The system is in the chirally broken phase in the calculation that is shown in Fig. 5.1. As we can see in the left panel, it takes a couple of iterations for the collisional width – i.e., the short-range correlations – to build up. The appropriate shape is assumed rather quickly, however, the magnitude of the width changes from

Table 5.2: The fluctuation of the effective quark mass m^* in the iterative calculation shown in Fig. 5.1 ($\mu = 323\,\mathrm{MeV}$, chirally broken phase). The mass and the density of each iteration are obtained from a calculation where the mass from the previous iteration enters.

Iteration #	m^* [MeV]	ρ [ρ_0]
0	325	—
1	433	0.0002
2	282	0.0012
3	318	0.16
4	327	0.15
5	316	0.29
6	310	0.38
7	308	0.43
8	306	0.48
9	304	0.49
10	304	0.5

iteration to iteration. Those fluctuations are directly related to the fluctuating results for the effective quark mass in the iterations. In Table 5.2, we show how m^* and the quark density ρ change in the iterative calculation. Recalling the quasiparticle relation $\rho \sim (\mu^2 - m^{*2})^{3/2}$, cf. (3.10), we can see that small changes of m^* have significant impact on the density when m^* and μ are of comparable size. On the other hand, we have found in Section 4.3 that the quark width is strongly density dependent (and likewise the real part of the self-energy that is calculated dispersively from the width). After $7-8$ iterations, the results stabilize. The right panel of Fig. 5.1 confirms that self-consistency is reached after 10 iterations.

Fig. 5.2 shows the results of a calculation in the chirally restored phase. The self-consistent result is found much faster in this case, $4-5$ iterations are sufficient. In the chirally restored phase, the effective quark mass is significantly smaller than the chemical potential. Consequently, the fluctuations of m^* have much less influence on the quark density and the short-range correlations can stabilize much faster than in the chirally broken phase.

We have to calculate the real and imaginary parts of the quark self-energy and the RPA polarizations to solve the Dyson–Schwinger equations. The analytical analysis of the real parts of Σ^{ret} and Π^{ret} in Sections 3.6 and 3.8 has been rather involved. The integrals for the quark and meson widths (3.16,3.22), on the other hand, were derived directly from the Feynman rules (Appendix C) and did not require much analytical effort. Considering the numerical efforts, it is the other way around. The calculation of the dispersion integrals and the energy independent shifts that are

given in Eqs. (3.39,3.53,3.61,3.62) is a straightforward exercise. The integrands of the multidimensional width integrals, however, consist of products of two spectral functions with pronounced on-shell peaks and thus have a complicated structure. The numerical solution of these integrals is technically challenging and the most time consuming part of the iterative calculation. We use the package CUBPACK [CH03] for this task since it is able to solve the integrals reliably. For a detailed discussion of the numerical implementation of the integrals we refer to Appendix H.

5.1.3 Numerical grid

The quark self-energy and the meson polarizations depend separately on the energy and the modulus of the three-momentum. Hence, it is necessary to solve the Dyson–Schwinger equations on numerical grids in energy and momentum space. For the quarks we cover a range of $|k_0| \leq 3.5\,\mathrm{GeV}$, $|\vec{k}\,| \leq \Lambda$ and for the mesons a range of $|k_0| \leq 3\,\mathrm{GeV}$, $|\vec{k}\,| \leq 2\Lambda$. Using grids with 300×100 mesh points for the quarks and 300×200 mesh points for the mesons we achieve a resolution of $dk_0 \approx 20\,\mathrm{MeV}$ and $d|\vec{k}\,| \approx 6\,\mathrm{MeV}$ in both cases. This choice is justified by the results – the energy and momentum dependence of the self-energy and the RPA polarizations (real parts and widths) is smooth with respect to the mesh size. As we will see later, the grid resolution is on the order of the on-shell quark width. Thus, the spectral functions cannot be discretized on the grid – in contrast to the self-energy and the polarizations. The on-shell peaks of the quark spectral function would be lost. In the width integrals, the spectral functions are always calculated from Eqs. (2.40,2.48) – using interpolated grid data for self-energy and polarizations.

Note that the upper limits for the three-momenta of the quarks and mesons on the grid are fixed by the cutoff scheme that we use in our approach, see Section 2.4 for details. In comparison to these limits, the energy limits are chosen rather high. This is necessary since we want to calculate the real parts of Σ^{ret} and Π^{ret} from the dispersion integrals in (3.24). The limits of those integrals are located at infinitely high energies. Hence, we must make sure that the quark and meson widths $\Gamma_{s,\mu}$ and $\Gamma_{\sigma,\pi}$ vanish at the borders of the grids. In Chapter 4 we have determined the cutoff induced thresholds above which the quark and antiquark widths must vanish in the Hartree+RPA approximation. We must go beyond this threshold here, since the finite width of the quarks generates small but finite contributions above the threshold.

It is important to note that the quark spectral function at such high energies will not sizably influence the integrals for the quark and meson widths (3.16,3.22). At higher energies, the on-shell peaks are located at three-momenta above the cutoff Λ. Only the – much smaller – off-shell contributions at momenta below the cutoff enter the integrals.

5.1.4 Quarks, antiquarks and effective masses

As discussed in Chapter 4, we identify the quark states $k = (k_0, \vec{k})$ at negative energies k_0 with antiquark states $\bar{k} = (-k_0, \vec{k}) = (\bar{k}_0, \vec{k})$ that have a positive energy $\bar{k}_0$. Populated antiquark states correspond to holes in the Dirac sea. Note that, strictly speaking, the border between quarks and antiquarks is not located at $k_0 = 0$ in our approach. The real part of $\Sigma_0^{\rm ret}(k)$ – that is not necessarily zero at $k_0 = 0$ – induces a shift of the energy scale. Thus, the border is located closer to $\mathrm{Re}\tilde{k}_0 = k_0 - \mathrm{Re}\,\Sigma_0^{\rm ret}(k_0, \vec{k}) = 0$ (see Fig. E.1). More details and the exact definition of the border can be found in Appendix E.

The momentum dependent shift of the border between the quarks and antiquarks is smaller than 5 MeV in the chirally broken and smaller than 50 MeV in the chirally restored phase. In the numerical calculations we use the appropriate border, i.e., $k_0 = \mathrm{Re}\,\Sigma_0^{\rm ret}(k)$. This is important when determining the quark density and the momentum distribution. In the discussion of the results, however, we will just refer to positive and negative energy states to denote quarks and antiquarks, respectively.

For the discussion of the results (not for the numerics) we introduce an effective quark mass m^* that is easier to handle than the complex $\tilde{m}^{\rm ret,av}(k)$ of Eq. (2.34). Like in [DBM93, DM94], we define the real and constant mass m^* in terms of the real part of the on-shell self-energy $\Sigma_{s,\rm os}^{\rm ret}(\vec{k})$, cf. Eqs. (2.51) and (2.39), for a quark at rest:

$$m^* = m_0 + \mathrm{Re}\,\Sigma_{s,\rm os}^{\rm ret}(\vec{k} = 0) = \mathrm{Re}\tilde{m}^{\rm ret,av}(k_0^{\rm os}(0), 0)\,. \tag{5.1}$$

The numerical results show that the momentum dependence of $\mathrm{Re}\tilde{m}(k)$ ranges below 5% for the on-shell states. Hence, m^* yields a good classification for the states in the vicinity of the on-shell peak at all momenta.

5.2 Collisional broadening

5.2.1 General structure

To give a qualitative overview of the short-range effects in quark matter, the quark spectral function $\mathcal{A}_0$, the corresponding width Γ_0, and the real part of the self-energy $\mathrm{Re}\,\Sigma_0^{\rm ret}$ are shown in Fig. 5.3 as cuts at a constant three-momentum. We have selected the γ_0-components for closer inspection here since they show all relevant features and correspond to the non-relativistic limits of spectral function and self-energy. In addition, Γ_0 yields the largest contribution to the width of the spectral function and the quark density is determined by an integral over $\mathcal{A}_0$, cf. Eq. (3.9).

Fig. 5.3 shows results of calculations in the chirally broken ($\rho \approx 0.17\,\mathrm{fm}^{-3} = \rho_0$) and restored phases ($\rho \approx 0.765\,\mathrm{fm}^{-3} = 4.5\rho_0$), using the parameter sets 0 and I from Table 5.1. Note that we use $\rho_0 = 0.17\,\mathrm{fm}^{-3}$ to normalize the quark density. The numerical value of ρ_0 corresponds to the nucleon density in normal nuclear matter $\rho_{\rm nm}$. Nonetheless, ρ is here a quark density and not a nucleon density. Assuming that

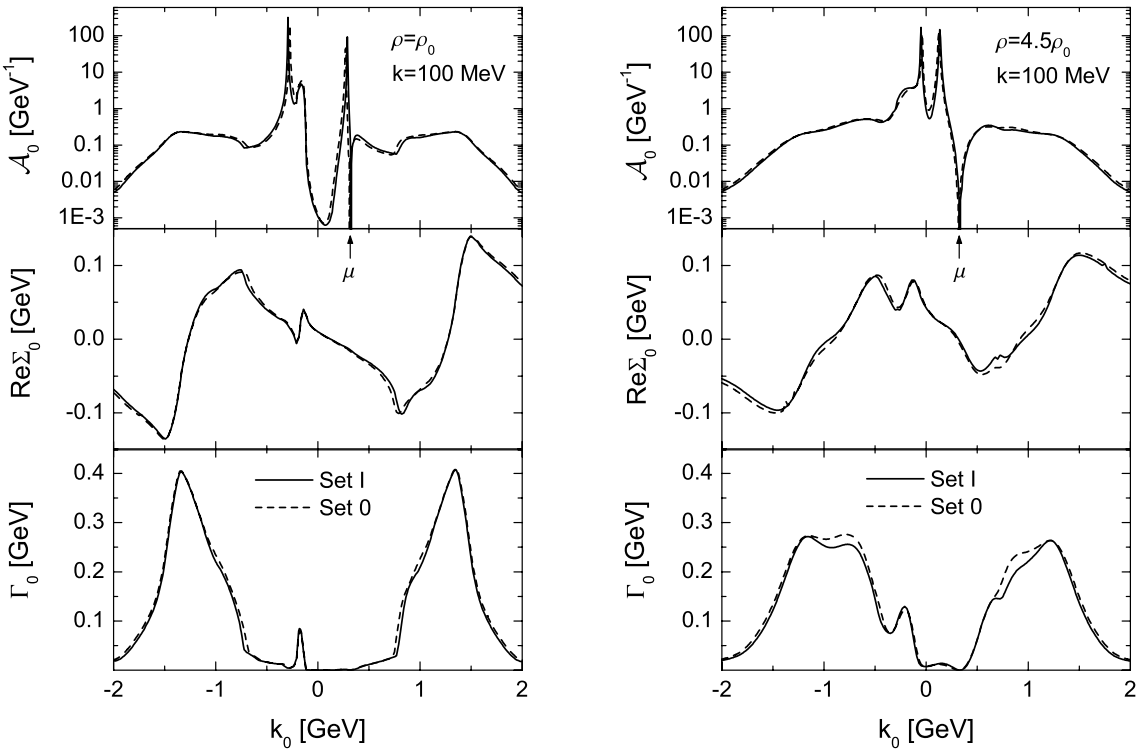

Figure 5.3: Cuts of the quark spectral function $\mathcal{A}_0$, the real part $\mathrm{Re}\,\Sigma_0^{\mathrm{ret}}$, and the width Γ_0 at a constant three-momentum in the chirally broken (left) and restored (right) phases. The two parameter sets of Table 5.1 have been used. The results on the left correspond to a quark density of $\rho = \rho_0$ ($\mu = 308.5\,\mathrm{MeV}$ for parameter set 0, $\mu = 325\,\mathrm{MeV}$ for set I), the results on the right to $\rho = 4.5\rho_0$ ($\mu = 318\,\mathrm{MeV}$ for parameter set 0, $\mu = 332\,\mathrm{MeV}$ for set I). Since the quark mass drops in the chirally restored phase, the on-shell peaks are located at lower energies $|k_0|$ in the right panel.

each nucleon consists of three constituent quarks, quark matter with a density of ρ_0 should be compared to nuclear matter at $\rho_{\mathrm{nm}}/3$.

The spectral functions in Fig. 5.3 are dominated by the on-shell peaks. In the upper left panel of Fig. 5.3, we find the antiquark peak at $k_0 \approx -290\,\mathrm{MeV}$ and the quark peak at $k_0 \approx 290\,\mathrm{MeV}$, cf. (2.39). In the right panel, the peaks are located at lower energies since the mass of the quarks drops significantly in the chirally restored phase. The peak-like structure right next to the antiquark peak ($k_0 \approx -180\,\mathrm{MeV}$) in the left panel (it turns into the shoulder of the antiquark peak in the right panel) is generated by a pronounced contribution to the quark width – see the lower panel. In contrast to the on-shell peaks, it does not correspond to a pole of the quark propagator. We will come back to this structure in Section 5.2.2.

The peaks sit on a broad underground of off-shell states. Most of the strength

of the spectral functions, however, is still located close to the on-shell peaks. Note the log scale for $\mathcal{A}_0$ in Fig. 5.3. Both, $\mathcal{A}_0$ and Γ_0 vanish at $k_0 = \mu$. As we have already seen in Section 3.3, the quarks at the Fermi energy are stable quasiparticles for $T = 0$. The quark peak is located close to the chemical potential in the left panel of Fig. 5.3. Thus, the spectral function drops to zero very sharply. This zero should not be confused with the off-shell region between the quark and the antiquark peak where the spectral function becomes very small.

The influence of the width on the structure of the spectral function and the real part of the self-energy is clearly visible. The width is strongly energy dependent and becomes as large as 400 MeV in certain energy ranges. Those regions are far off-shell, hence this result should not be overestimated. When we later discuss the on-shell width we will find that much smaller values are relevant for the properties of the medium. Concerning the density dependence of the width, it should be noted that the width becomes larger at low $|k_0|$ while it becomes smaller at large $|k_0|$ when the density increases. As we will see in the next section, this is in agreement with the estimates from Section 4.3.

The impact of the cutoff at large $|k_0|$ can also be observed in Fig. 5.3. As expected, Γ_0 and $\mathcal{A}_0$ become rapidly smaller at high energies and will eventually vanish. The real part of the self-energy approaches the value of $\Sigma^{\mathrm{F}}_{\mathrm{eff},0}$, as we have already seen in Section 3.8, cf. Fig. 3.5. The influence of the cutoff on the results is not entirely unphysical. Originally, we have introduced the cutoff for technical reasons. Since the NJL coupling constant G is really constant it has been necessary to regularize the divergent self-energy and polarization integrals. The combination of a constant coupling G with a momentum cutoff Λ roughly resembles the running coupling constant of QCD [PS95]. Quarks with large momenta are free and do not participate in the interactions that generate the self-energy. Hence, the cutoff can be understood as a crude approximation of asymptotic freedom. In the results of Fig. 5.3, the quark width breaks down and the off-shell states of the spectral function vanish for the asymptotically free states at large $|k_0|$.

In vacuum, $\mathcal{A}_0$ and Γ_0 would be symmetric in k_0 while $\mathrm{Re}\,\Sigma^{\mathrm{ret}}_0$ would be antisymmetric. This symmetry is induced by the invariance of the vacuum ground state under charge conjugation, see Appendix E in [Pos04] for details. We can observe in Fig. 5.3 that the existence of a medium with finite density breaks the symmetry between the quark and antiquark states. In the case of the lower density ($\rho = \rho_0$) the symmetry still holds approximately. Only the structure at small negative energies breaks it. For the higher density of $4.5\rho_0$ the symmetry is lost – in particular for energies $|k_0|$ on the order of the cutoff Λ and below. Only at higher energies, the symmetry is partially recovered.

The differences between the results for the parameter sets 0 and I are rather small. This is not surprising in the chirally broken phase. The couplings G as well as the cutoffs Λ are of similar size in both sets. The different values for the current quark mass should be negligible when the constituent quark mass is large. In the chirally restored phase, the differences between the results are slightly larger since the effective

quark masses differ significantly there: The quarks become massless when parameter set 0 is used. The finite current quark mass m_0 of parameter set I, on the other hand, breaks chiral symmetry explicitly. At a density of $4.5\rho_0$, the quarks still have an effective mass of $m^* = 100\,\mathrm{MeV}$ (see also Fig. 5.10 below).

In Figs. 5.4 and 5.5 we show $\mathcal{A}_0$ and Γ_0 in more detail for the energy range $|k_0| < E_\Lambda = k_0^{\mathrm{os}}(\Lambda) \approx \sqrt{\Lambda^2 + m^{*2}}$. This is the region where the on-shell peak is not suppressed by the cutoff in the integrands of the width integrals (3.16,3.22) – recall our discussion of the regularization scheme in Section 2.4.2. Several cuts for different three-momenta are shown, again at the densities of ρ_0 and $4.5\rho_0$ for both parameter sets of Table 5.1.

Significant differences between the results for the different parameter sets can be observed only in Fig. 5.5 (chirally restored phase) for the cuts of $\mathcal{A}_0$ at low momenta. The locations of the on-shell peaks differ due to the different effective masses. The position of the peaks is determined approximately by $k_0^2 = \vec{k}^2 - m^{*2}$ (Hartree approximation) – the exact relation is given by $\mathcal{P}(k) = 0$, cf. (2.39). Since we compare the results at the same density – and not at the same chemical potential – the zero at $k_0 = \mu$ is also slightly shifted. Recall that the (quasiparticle) density is proportional to $(\mu^2 - m^{*2})^{3/2}$, cf. (3.10). Since the effective quark masses differ in both cases, this leads to smaller chemical potentials for parameter set 0 than for parameter set I.

Figs. 5.4 and 5.5 show very clearly that even a small quark density breaks the symmetry between the quarks and antiquarks. The antiquark width has no zeros and on average increases with $-k_0$ ($\bar{k}_0$), phase space opens for the relevant scattering and decay processes shown in Figs. 4.1 and 4.3 (we will discuss these processes in detail in the next section). Thus, the antiquark peak of the spectral function broadens with increasing momentum. At the lower density (Fig. 5.4), the on-shell width of the peak rises up to $20 - 30\,\mathrm{MeV}$. At the higher density, the correlations have increased and the on-shell width rises even up to $100 - 200\,\mathrm{MeV}$. In the quark sector, we see a very different picture. At energies below the chemical potential the width stays small. Thus, the on-shell peaks that correspond to the populated states of the medium remain narrow. Above the Fermi energy, where the width increases again, the peaks become broader.

5.2.2 Correspondence to scattering and decay processes

We have seen that the position of the on-shell peaks can be easily understood. To explain the full (off-shell) structure of $\mathcal{A}_0$ in Figs. 5.3, 5.4, and 5.5 we have to investigate the structure of the width that is reflected in the spectral function. Therefore, we have to recall our discussion of the scattering and decay processes that contribute to the total collision rates and self-energies $\Sigma^{\gtrless}$ from Chapter 4. All processes that contribute to the quark width are shown in Figs. 4.1 and 4.3. We will refer to these processes as 4.1(a), 4.3(a), etc. in the following. As discussed in Chapter 4, we interpret the outgoing meson lines in Fig. 4.1 as bound $q\bar{q}$ states (on-shell peaks) while the intermediate mesons in Fig. 4.3 may be off-shell.

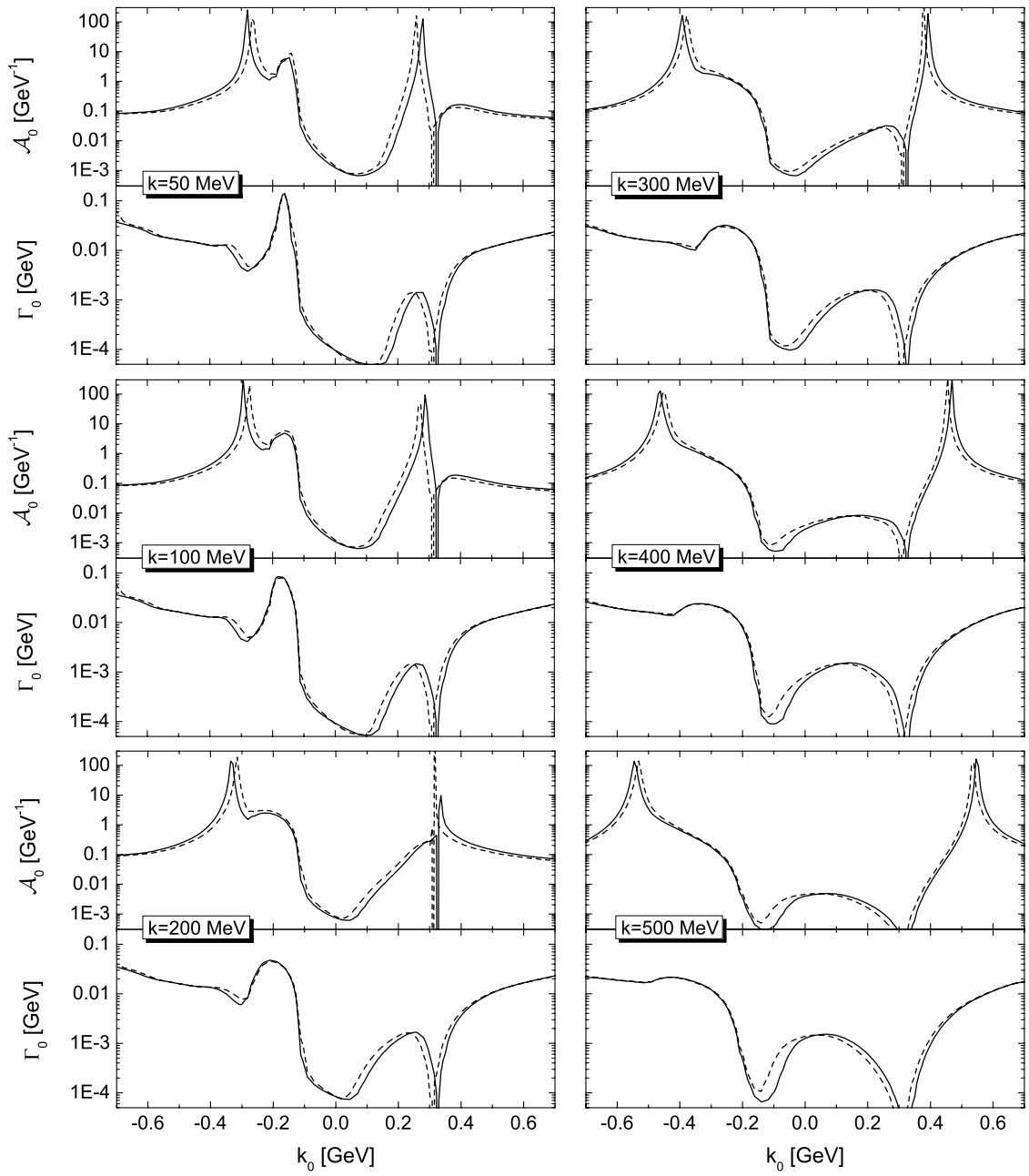

Figure 5.4: Cuts of the quark spectral function $\mathcal{A}_0$ and the width Γ_0 in the chirally broken phase ($\rho = \rho_0$) at several constant three-momenta, using parameter sets 0 (dashed lines, $\mu = 308.5\,\mathrm{MeV}$, $m^* = 263\,\mathrm{MeV}$, $k_F = 188\,\mathrm{MeV}$) and I (solid lines, $\mu = 325\,\mathrm{MeV}$, $m^* = 284\,\mathrm{MeV}$, $k_F = 186\,\mathrm{MeV}$). Note the different scale in k_0 as compared to Fig. 5.3.

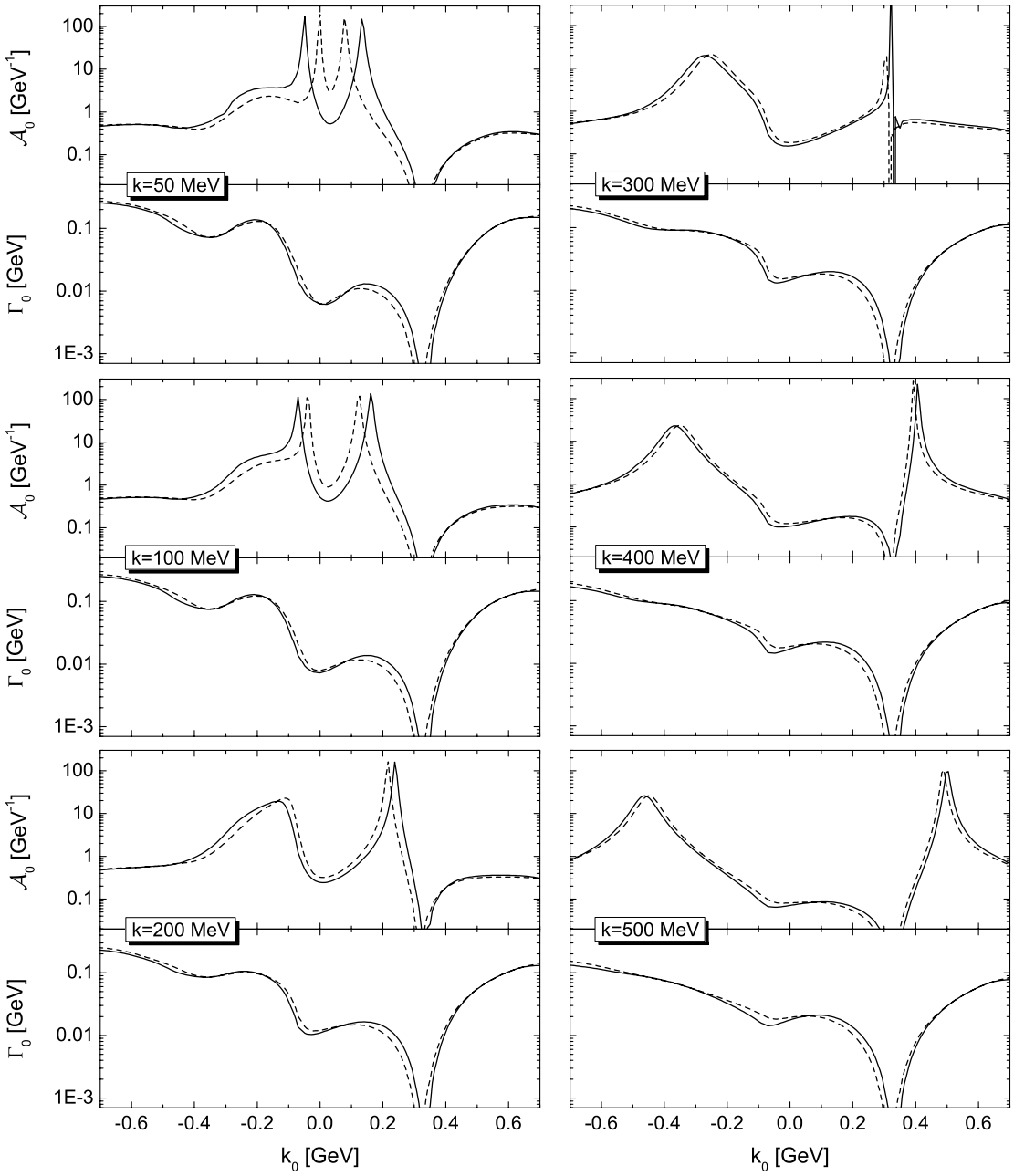

Figure 5.5: Cuts of the quark spectral function $\mathcal{A}_0$ and the width Γ_0 in the chirally restored phase ($\rho = 4.5\rho_0$) at several constant three-momenta, using parameter sets 0 (dashed lines, $\mu = 318\,\mathrm{MeV}$, $m^* = 0$, $k_F = 312\,\mathrm{MeV}$) and I (solid lines, $\mu = 332\,\mathrm{MeV}$, $m^* = 100\,\mathrm{MeV}$, $k_F = 315\,\mathrm{MeV}$).

Table 5.3: The energy thresholds of Tables 4.1 and 4.2, adjusted to the results for $|\vec{k}\,| = 100\,\mathrm{MeV}$ and parameter set I that are shown in Figs. 5.3 and 5.4, 5.5. The quark and meson masses from the $\mathcal{O}(1/N_c)$ calculations have been inserted into the analytical (Hartree+RPA) expressions, ignoring shifts due to the collisional self-energies. The left column corresponds to $\mu = 325\,\mathrm{MeV}$ ($m^* = 284\,\mathrm{MeV}$, $m_\pi = 444\,\mathrm{MeV}$), the right column to $\mu = 332\,\mathrm{MeV}$ ($m^* = 100\,\mathrm{MeV}$, $m_\pi = 416\,\mathrm{MeV}$).

Process		Thresholds [MeV]								
		ch. broken phase					ch. restored phase			
Fig. 4.1	(a)	769	$<$	k_0	$<$	1547	748	$<$	k_0	$<$ 1480
	(b),(c)	127	$<$	$\bar{k}_0$	$<$	189	136	$<$	$\bar{k}_0$	$<$ 331
	(d)	735	$<$	$\bar{k}_0$	$<$	1547	526	$<$	$\bar{k}_0$	$<$ 1480
Fig. 4.3	(a)	325	$<$	k_0	$<$	1100	332	$<$	k_0	$<$ 1178
	(b)	934	$<$	k_0	$<$	2076	764	$<$	k_0	$<$ 1917
	(c),(d)	99	$<$	k_0	$<$	325	-73	$<$	k_0	$<$ 332
	(e),(f)	284	$<$	$\bar{k}_0$	$<$	1100	100	$<$	$\bar{k}_0$	$<$ 1178
	(g)	893	$<$	$\bar{k}_0$	$<$	2076	532	$<$	$\bar{k}_0$	$<$ 1917

The upper and lower energy thresholds for each of the processes are given in terms of the effective quark and RPA pion masses in Tables 4.1 and 4.2. In Table 5.3 we list numerical values that are found by inserting the masses of the present approach. The real parts of $\Sigma_\mu^{\mathrm{ret}}$ have not been taken into account. Hence, the thresholds should be slightly shifted with respect to the numerical results. The thresholds are strict limits in the Hartree+RPA approximation. In the full $\mathcal{O}(1/N_c)$ approach, the limits are softened since we deal with quarks that have a finite width. Nonetheless, the thresholds of Table 5.3 allow us to fully understand the structure of the quark width in Figs. 5.3, 5.4, and 5.5.

A noticeable feature that can be found in both, the width and the spectral function, are the zeros at $k_0 = \mu$ for all three-momenta. Due to Pauli blocking it is not possible to scatter into or out of the states at the Fermi energy. The states are stable for $T = 0$. As we have already observed in Section 3.3, the integral for the quark width (3.17) vanishes for $k_0 = \mu$ at zero temperature – none of the processes in Figs. 4.1 and 4.3 yields finite contributions to the width. It follows directly from the definitions (2.37,2.40) that the spectral function has to vanish then, too. When the on-shell peak of $\mathcal{A}_0$ comes close to the chemical potential, it turns almost into a sharp quasiparticle peak – see the $|\vec{k}\,| = 200\,\mathrm{MeV}$ cut of Fig. 5.4 ($k_F = 188\,\mathrm{MeV}$) and the $|\vec{k}\,| = 300\,\mathrm{MeV}$ cut of Fig. 5.5 ($k_F = 312\,\mathrm{MeV}$). This underlines the stability of the states in this region. At finite temperatures, the width at the Fermi energy would become finite.

Then, the states could participate in scattering processes.

The quark and antiquark decay processes 4.3(b) and 4.3(g) are responsible for the huge bumps that dominate the structure of Γ_0 at large $|k_0|$ in Fig. 5.3. Such decays can occur at zero density since no partner from the medium is required. The outgoing quarks of the decays are subject to Pauli blocking. Thus, the bumps decrease in the chirally restored phase where the density is large.

The smaller bump at low negative energies ($k_0 \approx -180\,\mathrm{MeV}$ in the chirally broken phase) is generated by process 4.1(c). Since the RPA pion is rather heavy in our approach, the common k_0 limits for 4.1(b,c) are negative. Hence, the quark scattering process 4.1(b) is suppressed in the results. The bump that is generated by process 4.1(c) has significant influence on the spectral function. In the chirally restored phase it contributes to the collisional broadening of the antiquark peak at moderate momenta. In the chirally broken phase it generates a structure at low momenta that almost looks like a second on-shell peak in the antiquark sector. This is clearly an artifact of the too large RPA pion mass in the chirally broken phase. For a more reasonable pion mass, the bump would be located at small positive energies – then generated by process 4.1(b), cf. Section 4.2. Note that there exists no process comparable to 4.1(c) in the quark sector (i.e., $k\bar{q} \to \pi$). Such a process would require an incoming antiquark from the medium. Thus, the spectral function at positive energies is free from similar artifacts.

In the chirally broken phase, we can identify the contributions to the width Γ_0 from the processes 4.1(a) and 4.1(d) as the shoulders on the inner slopes of the big bumps in Fig. 5.3. Process 4.1(a) remains visible in the chirally restored phase while process 4.1(d) is hidden beneath the increased contributions from the processes 4.3(e,f). As we have already discussed in Section 4.3, those processes – like 4.3(a) and 4.3(c,d) – rely on incoming quarks from the medium as scattering partners. Hence, their contributions to the width remain comparably small in the chirally broken phase where the quark density is low. The contributions from processes 4.3(e,f) are found between the large and the small bump in the antiquark sector, the contributions from 4.3(a) and 4.3(c,d) right above and below the Fermi energy, respectively. In the chirally restored phase, where much more quarks become available as scattering partners, the importance of the processes increases. The contributions of 4.3(e,f) reach almost the same size as those of the antiquark decay 4.3(g), the contributions of 4.3(a) at least half the size of the quark decay 4.3(b). We will come back to the density dependence of the width later on a more quantitative level.

Recall that the quarks of the medium occupy all states at positive energies below the chemical potential. The Fermi momentum k_F is determined by $\mathcal{P}(\mu, k_F) = 0$, cf. (2.36,2.39). In Fig. 5.4, the cuts for $|\vec{k}\,| \leq 100\,\mathrm{MeV}$ and in Fig. 5.5 the cuts for $|\vec{k}\,| \leq 300\,\mathrm{MeV}$ correspond to momenta below the Fermi momentum. Thus, the quark on-shell peaks are located below the chemical potential, in the region of the populated states. In the cuts at momenta above k_F, the spectral functions do not entirely vanish in the energy range $0 < k_0 < \mu$. Off-shell states exist due to the

width that is generated by process 4.3(c). Those states are populated by quarks and generate a so-called high-momentum tail in the momentum distribution of the medium. Later, when we investigate the momentum distribution in more detail, we will use the high-momentum tail as a measure for the short-range correlations. In the case of quasiparticles, the momentum distribution would drop to zero at k_F where the on-shell states cross the Fermi energy.

We close the discussion on the structure of the quark width with an important observation: Most of the processes that involve bound $q\bar{q}$ states (Fig. 4.1) have no influence on the width in the energy range $|k_0| < E_\Lambda\,(\approx 630 - 700\,\mathrm{MeV})$ that is shown in Figs. 5.4 and 5.5. Process 4.1(b) is completely forbidden and the thresholds for the processes 4.1(a,d) are located at very large $|k_0|$. Only process 4.1(c) yields a considerable contribution to the width in the antiquark sector. Most of the quark and antiquark width is generated – as expected from our quasiparticle considerations of Chapter 4 – by the processes of Fig. 4.3. It is interesting to note that the contributions of the collisional processes to the overall width in the chirally broken phase are small in comparison to the huge off-shell contributions from decays. This can be readily explained by the strong density dependence of the collisions with partners from the medium. In addition, we have found in Section 4.4.2 that the contributions from the t-channel processes of Fig. 4.3 depend – in contrast to the decays – on the RPA pion mass. Thus, we may underestimate these processes below the chiral phase transition.

We have already discussed the influence of process 4.1(c) on the antiquark width. We note here that this process generates a structure that is located close to – but not within – the on-shell region of the antiquark spectral function in the chirally broken phase, cf. Fig. 5.4. Thus, the influence of process 4.1(c) does not become too large in this phase. As we can see in Fig. 5.5, the process has considerable influence on the on-shell width in the chirally restored phase. There, however, the Hartree+RPA pions aquire a considerable mass, too. Thus, the contributions of process 4.1(c) should be located approximately in the right position.

5.2.3 Comparison to the loop-expansion

In Fig. 5.6 we compare the results of the present work to our earlier approach in [FLM03b]. In the loop-expansion of [FLM03b] we have used the Born diagrams that are shown in Fig. 2.2(c) and (d) to calculate the collisional quark width. We did not perform a $1/N_c$ expansion with dynamically generated RPA mesons there. In both calculations, the system is in the chirally restored phase at densities of $3\rho_0$ and $9\rho_0$, using a parameter set for the chiral limit. Since the quark widths that were found in [FLM03b] have been rather small, it was justified to use the Hartree parameter set 0 of Table 2.1 there. For the calculations with the present model, we have used the comparable parameter set 0 from Table 5.1. Recall that the couplings G differ by a total factor of 0.78. We have chosen a density of $3\rho_0$ in [FLM03b] since the system should then be comparable to nuclear matter at normal density (three quarks per nucleon). As we will see later, quark matter at $3\rho_0$ corresponds to a stable solution

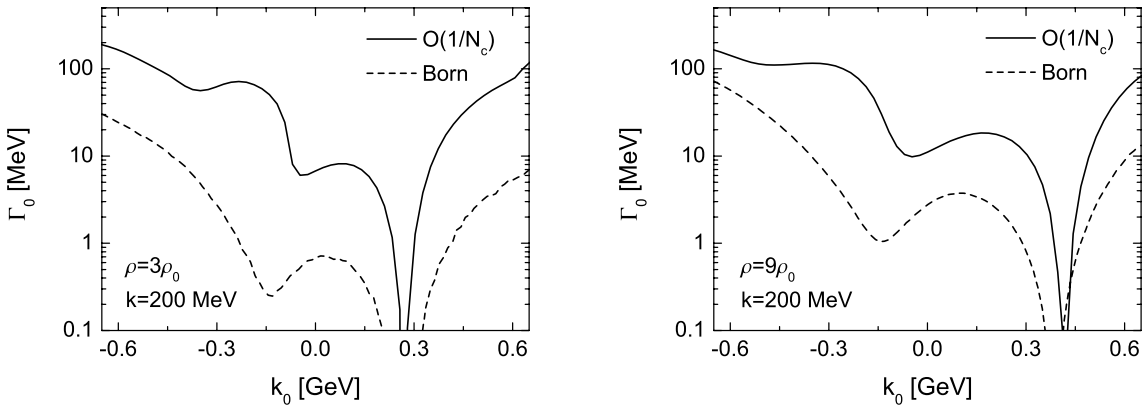

Figure 5.6: Cuts of the quark width Γ_0 in the chirally restored phase at constant three-momentum. The solid lines show the results of a full $\mathcal{O}(1/N_c)$ calculation using parameter set 0 from Table 5.1, the dashed lines show the corresponding results from [FLM03b] using parameter set 0 (Hartree) from Table 2.1.

of the Dyson–Schwinger equations in Fig. 2.11 for $m^* = 0$. However, it might not be realized in nature since an energetically favored solution exists in the chirally broken phase – for the same chemical potential and a lower density.

The density of $3\rho_0$ is reached in both approaches at a chemical potential of $\mu \approx 270\,\mathrm{MeV}$. The chemical potentials that correspond to $9\rho_0$ differ significantly. Values of $\mu = 415\,\mathrm{MeV}$ and $\mu = 387\,\mathrm{MeV}$ are found for the $\mathcal{O}(1/N_c)$ and the Born approach, respectively. The difference is induced by the γ_0-component of $\mathrm{Re}\,\Sigma^{\mathrm{ret}}$ that shifts the energy scale. The real part of the quark self-energy has been neglected in [FLM03b]. In the $\mathcal{O}(1/N_c)$ calculation, however, $\mathrm{Re}\,\Sigma_0^{\mathrm{ret}}$ is included and becomes larger when the density increases.

Qualitatively, there is some agreement between the results in Fig. 5.6. The curves have a similar shape. Since we did not introduce RPA mesons in [FLM03b], the processes of Fig. 4.1 – involving bound $q\bar{q}$ states – did not contribute to the width there. Hence, the bump that is generated by process 4.1(c) is only found in the $\mathcal{O}(1/N_c)$ results. Quantitatively, the results differ by one order of magnitude. The simple expansion in terms of the coupling constant clearly misses large contributions to the short-range correlations by ignoring the terms that also are of next-to-leading order in the number of colors but of higher orders in the coupling.

5.3 RPA mesons in the $\mathcal{O}(1/N_c)$ approach

We have discussed earlier that the RPA mesons must not be identified with the physical sigma and pion, see Section 2.5 for details. The corrections to the RPA polarizations that are needed to find the Goldstone modes, i.e. the physical pion, are

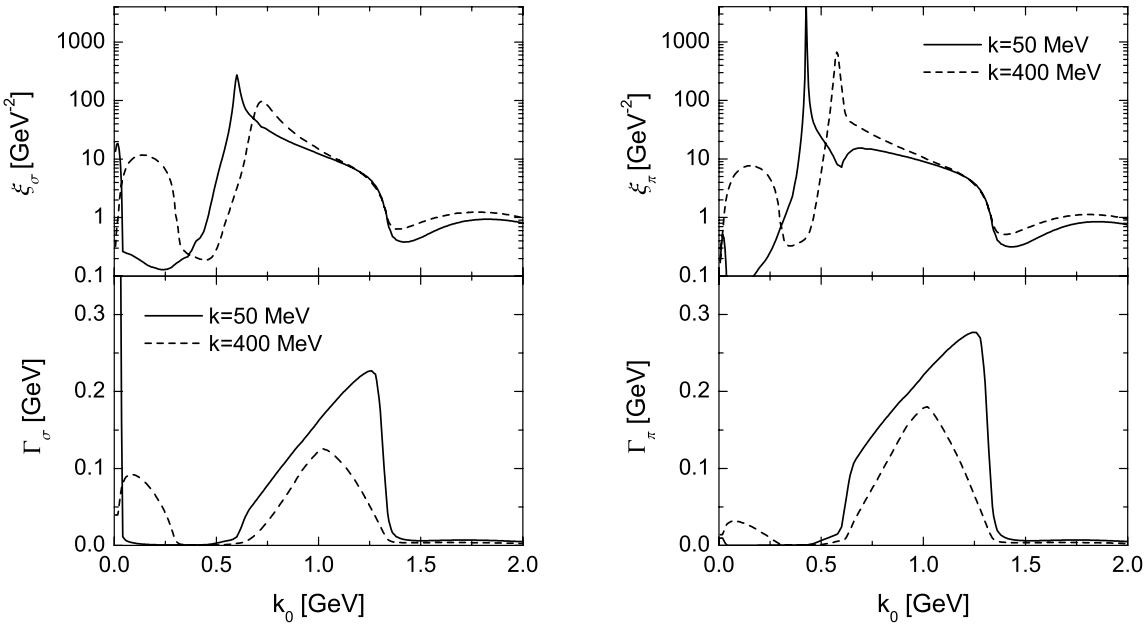

Figure 5.7: Cuts of the RPA meson spectral functions and widths at two constant three-momenta. The left panel shows the results for the RPA sigma, the right panel the results for the RPA pion. The calculation was performed below the chiral phase transition at a chemical potential of $\mu = 308.5\,\mathrm{MeV}$ ($\rho = \rho_0$, $m^* = 263\,\mathrm{MeV}$), using parameter set 0 from Table 5.1 (chiral limit).

presently not calculated. Nonetheless, we briefly discuss the properties of the RPA mesons before we investigate the quarks in more detail.

5.3.1 Structure of width and spectral function

The spectral functions and widths of the RPA sigma and pion are shown in Fig. 5.7. The results have been obtained from a calculation with parameter set 0 from Table 5.1 in the chirally broken phase. Since the parameter set does not include a finite current quark mass, the physical pion should be massless. In the $\mathcal{O}(1/N_c)$ calculation, however, we find masses of 603 MeV for the RPA sigma and 424 MeV for the RPA pion at the given density. As expected, the RPA pion is not a Goldstone boson.

The meson widths are generated by the processes that we have discussed in Section 4.5. The structure is dominated by the $q\bar{q}$ continuum that is generated by unbound $q\bar{q}$ states from decay processes. In other words: the RPA mesons decay into $q\bar{q}$ pairs when the energy is high enough. In the Hartree+RPA approach, the lower threshold for $q\bar{q}$ decays is located at $k_0 = \mu + m^*$. For energies above $k_0 = 2E_\Lambda = 2\sqrt{\Lambda^2 + m^{*2}}$, the decays are suppressed by the cutoff. As for the quark width, those limits are not strict in the full $\mathcal{O}(1/N_c)$ calculation. Small but finite

meson widths are found below the lower and above the upper threshold. We can also see in Fig. 5.7 that the $q\bar{q}$ continuum shrinks in magnitude for larger three-momenta. Here, the cutoff provides a sharp limit. At least one of the quark propagators in the integral of (3.18) must have a momentum above the cutoff for $|\vec{k}\,| > 2\Lambda$. Consequently, the integral becomes zero and the $q\bar{q}$ continuum vanishes at this point.

At spacelike four-momenta – i.e., $k_0 < 50,400\,\mathrm{MeV}$ for the given cuts – Landau damping [KG06] generates another structure in Fig. 5.7: The scattering processes $q\pi \to q$, $q\sigma \to q$ (cf. Fig. 4.6(b)) that are only allowed when the four-momentum of the mesons is spacelike yield considerable contributions to the widths in this region. Since the widths are defined as $\Gamma_{\sigma,\pi}(k) = -\mathrm{Im}\,\Pi^{\mathrm{ret}}_{\sigma,\pi}(k)/k_0$ (2.54), they can become rather large at small k_0 – in particular for the lower three-momentum. However, the widths do not diverge for $k_0 \to 0$.

The features of the widths can also be identified in the spectral functions. In addition to the continuum effects, we see the on-shell peaks from the bound $q\bar{q}$ states. Their positions are determined by the zeros of $1+2\mathrm{GRe}\,\Pi^{\mathrm{ret}}_{\sigma,\pi}$, cf. Section 3.7. The RPA pion peak is located – due to the large mass – close to but still below the threshold of the $q\bar{q}$ continuum where the width is small. Thus the peak is rather sharp. The RPA sigma peak, however, sits on top of the continuum and is very broad.

5.3.2 Comparison to mean-field results and chiral properties

In Fig. 5.8 we show a direct comparison of the polarizations in the $\mathcal{O}(1/N_c)$ approach at low densities and the Hartree+RPA approximation in vacuum, using parameter sets I from Tables 2.1 and 5.1. The results for the widths are in good agreement. The $q\bar{q}$ continuum is located at the same position and is of similar size in the $\mathcal{O}(1/N_c)$ and the mean-field approach – the observable shifts are due to the slightly different effective masses of the quarks. Landau damping is suppressed at the lower density and in the vacuum because it depends on quarks from the medium. We can conclude that the $q\bar{q}$ continuum parts of the RPA spectral functions generate reasonable contributions to the quark width when the diagrams of Fig. 3.1 are calculated (see also Fig. 4.4).

The results for the real parts of the polarizations are at least in qualitative agreement. The sharp spike at $k_0 = 2E_\Lambda$ in the Hartree result becomes smeared out in the $\mathcal{O}(1/N_c)$ calculation where the $q\bar{q}$ continuum does not drop to zero but remains finite above the threshold.

In spite of the seemingly good agreement of the results at moderate energies, the real part of Π^{ret}_{π} generates a much larger pion mass in the $\mathcal{O}(1/N_c)$ approach. In Fig. 5.9 we take a closer look at the zeros of $1 + 2\mathrm{GRe}\,\Pi^{\mathrm{ret}}_{\sigma,\pi}$ in the $\mathcal{O}(1/N_c)$ approach and the Hartree+RPA approximation at low energies. At small k_0, the $\mathcal{O}(1/N_c)$ pion curves are shifted by ≈ 0.2 to higher values in comparison to the Hartree+RPA result. This is in agreement with the estimate from Section 3.7. About 50% of this shift can be attributed to the Fock self-energy, cf. Eq. (B.8). The dispersive contributions to $\mathrm{Re}\,\Pi^{\mathrm{ret}}$ that exist only beyond the mean-field approximation, see Section 3.7, are

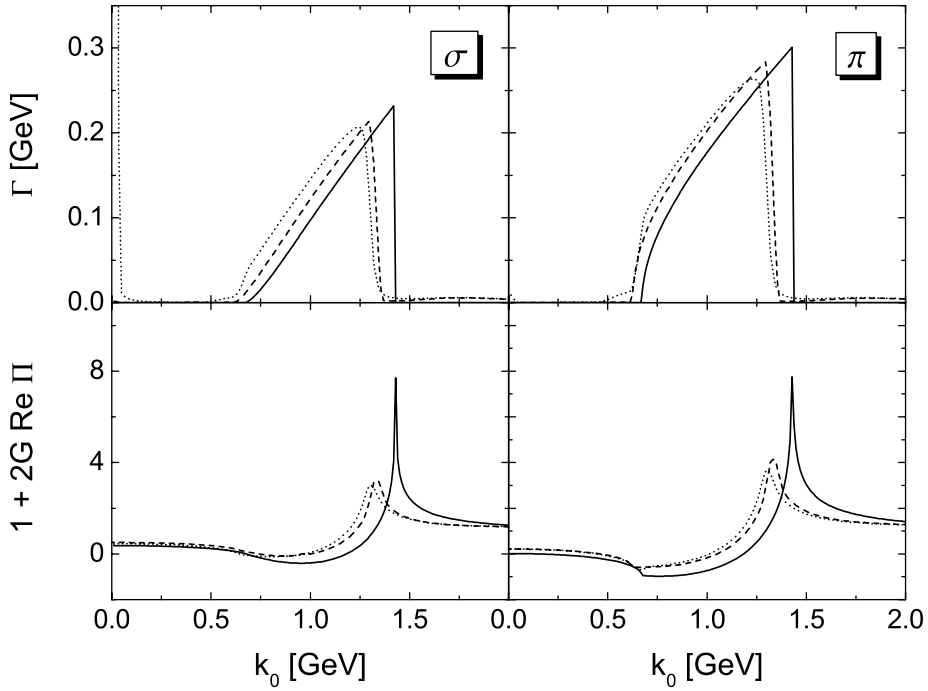

Figure 5.8: The RPA meson widths and the real parts of the RPA polarizations in the chirally broken phase at a three-momentum of 50 MeV. The solid line corresponds to the Hartree+RPA result at zero density, the dashed and the dotted lines correspond to results from full $\mathcal{O}(1/N_c)$ calculations at densities of $\rho = 0.05\rho_0$ and $\rho = \rho_0$, respectively. In the calculations, the parameter sets I from Tables 2.1 and 5.1 have been used.

responsible for the remaining 50% of the shift. The mass of the RPA pion increases from 142 MeV (Hartree+RPA) to 460 MeV ($\rho = 0.05\rho_0$) in the $\mathcal{O}(1/N_c)$ calculation. The small shift that is barely visible in Fig. 5.8 has large consequences.

It should be noted that the RPA pion is not only heavier than the physical pion but also broader. Due to the higher mass, the on-shell peak is shifted closer to the $q\bar{q}$ continuum, where the width becomes larger. In the case of the RPA sigma, the shift of the real parts is smaller. Furthermore, the zero is located in a region where the shift has – due to the slope of the curve – less influence on the mass, cf. Fig. 5.9, left panel. The effect is on the order of 10%. We can see in Fig. 5.9 that the density dependence of the RPA sigma mass is stronger than that of the RPA pion. It drops from 731 to 667 MeV between the two shown densities.

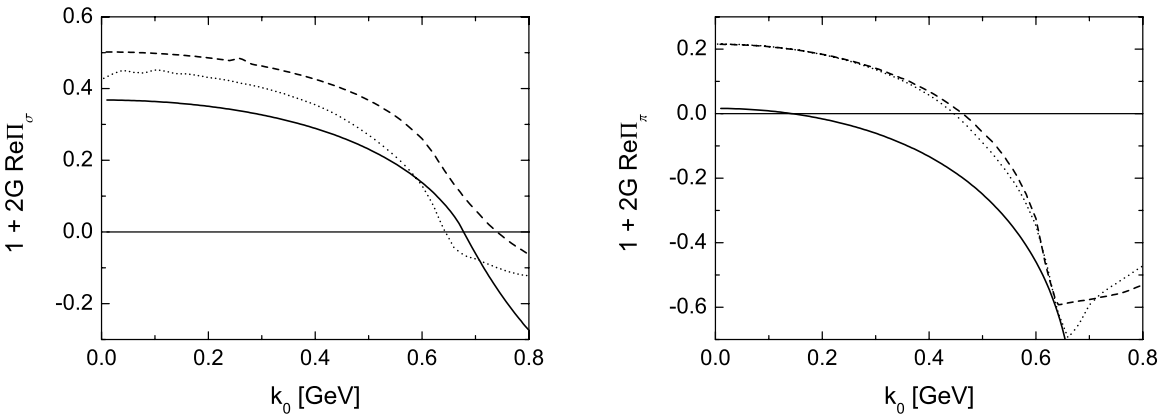

Figure 5.9: The real parts of the denominators of the retarded RPA meson propagators at a constant three-momentum of 50 MeV in the chirally broken phase. The RPA meson masses are determined by the zeros of $1 + 2\mathrm{ReG}\,\Pi^{\mathrm{ret}}$. See Fig. 5.8 for more details.

5.4 Chiral phase transition

5.4.1 The Hartree+RPA approximation

To examine the influence of the short-range correlations on the chiral phase transition, we have to investigate the effective quark mass m^* (5.1) as a function of the chemical potential μ. Before we discuss the results of the $\mathcal{O}(1/N_c)$ calculation, we first take a closer look at the results for the Hartree(–Fock) gap equation (2.11) that are shown in Fig. 1.3 (solid line) and Fig. 2.8 and the schematic plot of the thermodynamical potential (free energy) from Fig. 1.4.

In the quasiparticle calculation, a chiral phase transition of first order is found. At small μ and at large μ, the gap equation has only one solution $m^*(\mu)$ for each value of μ – the mass m^* is large at small μ (chirally broken phase) and small at large μ (chirally restored phase). The solutions correspond to minima of the thermodynamical potential [SKP99, Kle92] and thus are stable. As we can see in Fig. 1.4, lines (a) and (e), the thermodynamical potential has only one minimum in those regions.

In the region that has been shaded in Fig. 1.3, the gap equation has three solutions $m^*(\mu)$ for a given value of μ. This behavior is characteristic for a first-order phase transition [PB94]. The upper and the lower solution of the gap equation correspond again to minima of the thermodynamical potential. The intermediate solution, on the other hand, corresponds to a maximum of the potential, see line (c) of Fig. 1.4. Hence, this solution is only metastable.

The energetically favored solution of the gap equation – that is realized in nature at a certain chemical potential – is given by the absolute minimum of the thermodynamical potential. We can see in Fig. 1.4 that this minimum corresponds either to the upper (line (b)) or to the lower solution (line (d)) of the gap equation, depend-

ing on the value of μ. The chiral phase transition is located where the two minima of the thermodynamical potential have the same value, cf. line (c) of Fig. 1.4. At this point, the quark mass m^* drops discontinuously from a large to a small value. Consequently, the quark density, cf. (3.10), increases significantly. The intermediate range of (metastable) masses and densities is not realized. It should be noted that the quark density $\rho = 3\rho_0$ – corresponding to nuclear matter at normal density – lies within this gap in Fig. 1.3. This is a known shortcoming of the NJL model on the quasiparticle level [Kle92].

In Fig. 1.3, the quark mass remains finite in the chirally restored phase since chiral symmetry is explicitly broken by a small current quark mass (parameter set I from Table 2.1). In the chiral limit, m^* would drop to zero at the chiral phase transition. The (inverted) "S" shape of Fig. 1.3 would then turn into a '2' shape. Note that the solution $m^* = 0$ of the gap equation exists for all chemical potentials in the chiral limit.

The dashed line in Fig. 1.3 shows an alternative scenario to a first-order phase transition: It is possible that short-range correlations modify the system so that only one unique solution of the gap equation exists for all values of μ. For the thermodynamical potential this means that only one minimum exists at all chemical potentials. The phase transition is then turned into a smooth crossover where the system moves continuously from a large to a small quark mass. In Fig. 1.3 we have simulated this effect by adding a constant width of $\Gamma_0 = 28\,\mathrm{MeV}$ to the Hartree–Fock propagator. This is, of course, a rather crude approximation – in particular, since neither the energy nor the density dependence of the correlations are taken into account. It is not clear in advance if the $\mathcal{O}(1/N_c)$ approach will generate short-range effects that are large enough to modify the phase transition in the same way.

5.4.2 Phase transition in the $\mathcal{O}(1/N_c)$ approach

Fig. 5.10 shows the effective masses of quarks and RPA mesons and the corresponding quark density that were found in the $\mathcal{O}(1/N_c)$ calculation using parameter set I from Table 5.1. The corresponding result for the quark condensate $\langle\bar{u}u\rangle$ can be found in Fig. 5.12. It will be discussed later when the results from different parameter sets are compared. The phase transition is still of first order. Note that we have, in principle, access to all solutions of the gap equation (2.13) in the full $\mathcal{O}(1/N_c)$ calculation. However, the iterative calculations will not converge for the metastable intermediate solutions that exist in the vicinity of a first-order phase transition. Only the stable solutions for large or small m^* can be found numerically. Thus, the "S" shape in Fig. 5.10 is interrupted.

The gap between the upper and the lower solutions of the gap equation has decreased in the $\mathcal{O}(1/N_c)$ calculation – the phase transition has moved towards a crossover (compare Fig. 2.8 with Fig. 5.10). The region of chemical potentials μ for which several solutions to the gap equation exist is only 2 MeV wide. In the Hartree–Fock approximation, this region has a size of $\Delta\mu = 4\,\mathrm{MeV}$. We will not

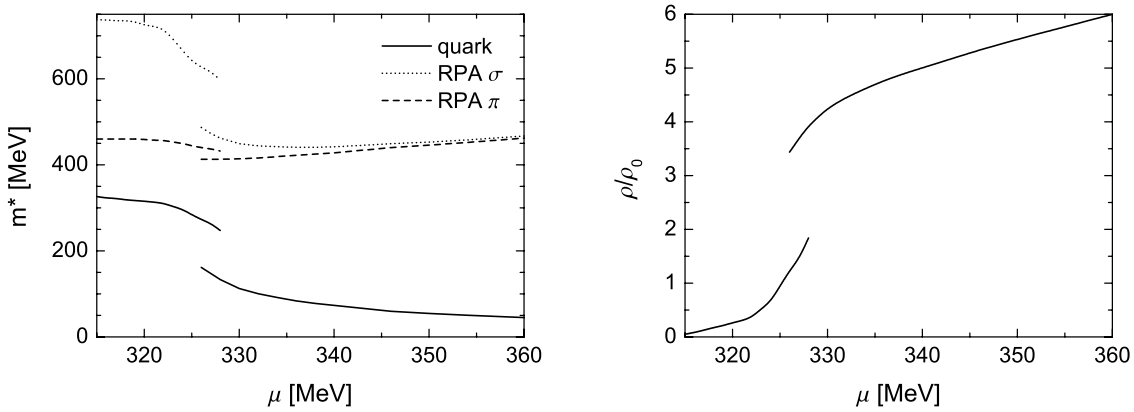

Figure 5.10: The effective quark mass and the masses of the RPA sigma and pion as functions of the chemical potential are shown in the left plot. The right plot shows the corresponding quark density in units of $\rho_0 = 0.17\text{fm}^{-3}$. In the range $326\,\text{MeV} < \mu < 328\,\text{MeV}$ the chiral phase transition occurs. The calculation was performed with parameter set I from Table 5.1.

Table 5.4: Solutions to the gap equation in the vicinity of the chiral phase transition. See Fig. 5.10 and text for details.

	upper solution		lower solution	
μ [MeV]	m^* [MeV]	ρ [ρ_0]	m^* [MeV]	ρ [ρ_0]
326	273	1.2	162	3.4
327	264	1.5	147	3.7
328	248	1.8	134	3.9

calculate the thermodynamical potential here to determine the exact location of the phase transition. To investigate the impact of the short-range correlations on the phase transition it is sufficient to check the differences between the upper and the lower solutions of the gap equation at fixed μ. In Table 5.4 we have summarized the results for the quark mass and density in the region of the phase transition. We find the mass and density gaps $\Delta m^* = 111 - 116\,\text{MeV}$ and $\Delta\rho = 2.1 - 2.2\,\rho_0$, respectively, in the $\mathcal{O}(1/N_c)$ approach. The Hartree–Fock approximation, on the other hand, yields the gaps $\Delta m^* = 188\,\text{MeV}$ and $\Delta\rho = 4.4\rho_0$ [Kle92].

We can conclude that the short-range correlations are not strong enough to change the type of the phase transition at zero temperature. However, the mass and density gaps at the phase transition have decreased significantly by 40% (Δm^*) and 50% ($\Delta\rho$), respectively. The quark density of $3\rho_0$ is still located within the gap. Recall that we consider a conservative estimate of the short-range effects below the phase

transition here, cf. Section 4.4.2. A calculation with a more realistic pion mass in the chirally broken phase should yield even smaller gaps or turn the phase transition into a crossover. We will come back to this point in Section 5.6.3.

Note that the position of the phase transition is shifted to a lower chemical potential in the $\mathcal{O}(1/N_c)$ calculation. This can be explained by the fact that the rescaled coupling generates smaller effective masses ($m^* = 320\,\mathrm{MeV}$ in vacuum) than the Hartree–Fock coupling ($m^* = 336\,\mathrm{MeV}$). An additional shift of the energy scale is induced by the γ_0-component of the effective Fock self-energy, $\Sigma^{\mathrm{F}}_{\mathrm{eff},0}$, cf. Eqs. (3.61,3.62), that is larger than the mean-field Fock self-energy Σ^{F}_0.

Fig. 5.10 shows that the quark density depends strongly on the chemical potential. Its behavior is linked to the effective mass m^*. Recall the quasiparticle relation for the density (3.10), $\rho \sim k_F^3 = (\mu^2 - m^{*2})^{3/2}$. Since m^* is a function of the chemical potential, the explicit cubic μ dependence of ρ is enhanced where the quark mass changes rapidly, i.e., in the region of the chiral phase transition. The short-range effects are strongly density dependent since they are generated by interactions with the medium. At low densities, the correlations remain weak. Consequently, they have little influence on the gap equation. Only when the chemical potential – and thus the density – increases, the short-range effects become relevant and deviations from the mean-field models can be observed in Fig. 5.10.

The density dependence of the short-range effects also explains the difference between the $\mathcal{O}(1/N_c)$ approach and the naive calculation with a constant width in Fig. 1.3. There, a value of $\Gamma_0 = 28\,\mathrm{MeV}$ has been chosen since that is just large enough to turn the first-order phase transition into a crossover. As we will see later in Section 5.6, a width of 28 MeV might be realistic for quarks in the chirally restored phase. In the chirally broken phase, however, the same width overestimates the effects of the short-range correlations. Thus, only the low mass solutions of the gap equation change strongly enough in the present approach. The large mass solutions stay closer to the quasiparticle result so that we do not find a crossover.

The relations between the quark mass, the density and the short-range correlations have considerable influence on the iterative calculations. When a calculation at $\mu = 329 - 330\,\mathrm{MeV}$ – that ends up in the chirally restored phase eventually – is initialized with a large quark mass of $250 - 330\,\mathrm{MeV}$ and a small width, the system will stay in the chirally broken phase for a few iterations. For quasiparticles a stable solution is nearby. This solution does not exist for quarks with a finite width. Nonetheless, the thermodynamical potential will be rather flat when the width is small – the system still "feels" the quasiparticle solution. Hence, the mass will drop only slowly in the first iterations and the width does not grow very fast. Only when the effective mass has dropped below 200 MeV after a couple of iterations, the calculation will quickly converge on the solution in the chirally restored phase that is shown in Fig. 5.10. Note that the existence of several solutions will also slow down the convergence of the iterative approach. The thermodynamical potential may become almost constant in the region of the intermediate solution. When the numerical calculation is initialized

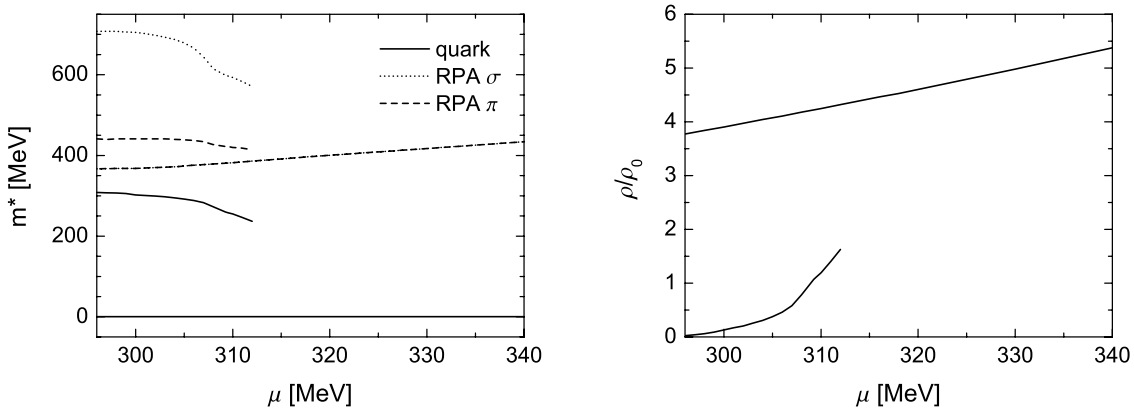

Figure 5.11: The effective quark mass and the masses of the RPA sigma and pion as functions of the chemical potential are shown in the left plot. The right plot shows the corresponding quark density in units of $\rho_0 = 0.17\text{fm}^{-3}$. Note that the results for the RPA sigma and pion lie on top of each other in the chirally restored phase. The calculation was performed with parameter set 0 from Table 5.1.

in this region, the system is driven only slowly towards one of the stable solutions.

Fig. 5.10 shows not only the quark masses but also the masses of the RPA mesons. In the Hartree+RPA approximation [Kle92] that is shown in Fig. 2.8, the RPA mesons have masses of $m_\pi \approx 140\,\text{MeV}$ and $m_\sigma \approx 600 - 700\,\text{MeV}$, respectively, in the chirally broken phase. The sigma mass jumps to $\approx 300\,\text{MeV}$ while the pion mass rises to $\approx 200\,\text{MeV}$ at the chiral phase transition. At higher μ, the two meson masses increase and converge (chiral partners). Technically, this effect can be easily explained by the fact that the difference between the Hartree+RPA sigma and pion is determined by the effective quark mass, cf. Eqs. (B.6,B.11), which decreases with increasing μ.

The RPA pion of the $\mathcal{O}(1/N_c)$ approach has a considerable mass in the chirally broken phase. The mass of the RPA sigma is rather close to the Hartree+RPA result. It shows a stronger density dependence than the pion mass. At the chiral phase transition, the sigma mass does not drop as far as in the mean-field calculation. The pion mass drops instead of increasing, thus moving towards the mean-field result. At higher μ, the results resemble the Hartree+RPA result qualitatively and quantitatively. The RPA pion and sigma masses come close to each other, and reach a value of $\approx 460\,\text{MeV}$ at a chemical potential of $\mu = 360\,\text{MeV}$ which is 30 MeV above the phase transition.

Fig. 5.11 shows the results for quark and meson masses and the density that are found in the chiral limit ($m_0 = 0$) with parameter set 0 from Table 5.1. Again, a first-order phase transition is found. The results for the chirally broken phase are rather close to the results that are found using parameter set I – the value of m_0 becomes almost irrelevant when the constituent quark mass is large. Working in the

chiral limit has little influence on the large RPA pion mass in the chirally broken phase. It is of similar size as in Fig. 5.10. In the Hartree+RPA approximation, the RPA pion would be massless in the chiral limit. The small differences in the results for the parameter sets 0 and I can be explained by the different values for the coupling G and the cutoff Λ. The position of the phase transition is shifted to lower μ since the two parameter sets generate different effective quark masses, cf. Table 5.1.

Huge differences between the calculations with parameters sets 0 and I exist, of course, in the chirally restored phase. Chiral symmetry is not explicitly broken by a finite current quark mass in the results of Fig 5.11. Thus, the symmetry is fully restored above the phase transition. The Lorentz scalar component of the self-energy and thus the effective quark mass drop to zero, $\Sigma_s^{\mathrm{ret}} = \tilde{m} = 0$. Like in the mean-field models (2.11), the solution $\tilde{m} = 0$ for the gap equation exists at all chemical potentials. This is an important result of the present work. Restored chiral symmetry is still a good symmetry in the $\mathcal{O}(1/N_c)$ approach.

The masses of the RPA sigma and pion are equal in the chirally restored phase. In the chiral limit, the differences between the RPA polarizations are determined solely by the Lorentz scalar component of the quark self-energy that vanishes in the chirally restored phase, cf. Eqs. (3.51,3.52). Note that the Lorentz components $\Sigma_{0,v}^{\mathrm{ret}}$ remain finite when chiral symmetry is restored. This means, in particular, that the collisional width of the quarks remains finite. At higher μ, when the effective quark mass becomes very small in Fig. 5.10, the results for the parameter sets 0 and I are comparable again. The quark density as well as the RPA meson masses have similar values. Partly, the different values of G and Λ are again responsible for the differences in the results.

At the end of this section, we take a look at the results for the quark condensate $\langle \bar{u}u \rangle$ that are shown in Fig. 5.12. The behavior of the quark condensate resembles that of the effective mass m^*. It has a considerable size at low densities (see Table 5.1 for the vacuum results) and decreases when the density grows. As we can see, the results in the chirally broken phase are almost equal for both parameter sets. When parameter set 0 (chiral limit) is used, the quark condensate drops to zero above the phase transition. The condensate remains finite, when chiral symmetry is explicitly broken. At a quark density of $8\rho_0$ it is still on the order of $-100\,\mathrm{MeV}$.

5.5 On-shell self-energy

In Section 5.2 we have investigated the collisional broadening of the quark spectral function qualitatively. In this section we will analyze the short-range correlations of the quarks on a more quantitative level. The next-to-leading order effects enter the quark spectral function via the collisional part of the retarded self-energy, i.e., $\Sigma^{\mathrm{ret}}(k) - \Sigma^{\mathrm{H}}$. For a quantitative investigation of the collisional self-energy we will restrict ourselves to the on-shell states (2.39). As we have seen in Fig. 5.3, strength is shifted away from the quasiparticle peaks of the spectral function due to the collisional

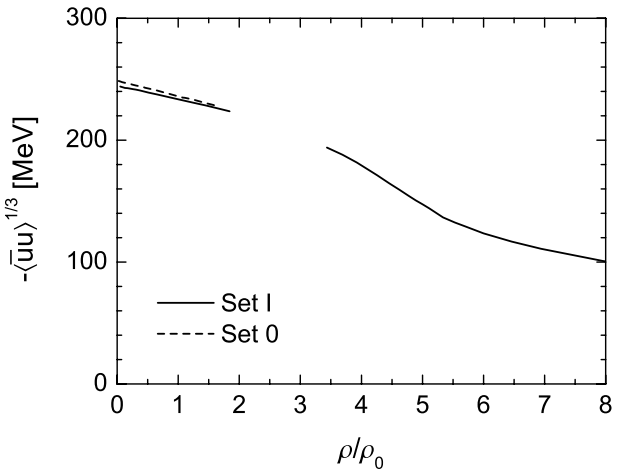

Figure 5.12: The quark condensate $\langle \bar{u}u \rangle^{1/3}$ as a function of the quark density for both parameter sets of Table 5.1. The gap in the curves corresponds to the intermediate range of densities that is skipped at the chiral phase transition, cf. Fig. 5.10.

broadening. Most of this strength, however, remains in the vicinity of the peaks. While the self-energy has an interesting structure far off-shell, the influence on the properties of the medium is limited.

5.5.1 Real part of Σ_s^{ret}

Fig. 5.13 shows $\text{Re}\tilde{m}_{\text{os}}$, the real part of the effective mass $\tilde{m}^{\text{ret}}(k)$ (2.34) on the mass shell, at five different densities, two below and three above the chiral phase transition. The curves begin at the on-shell energies that correspond to a quark at rest, $k_0^{\text{os}}(0)$, for each given density. Since we do not consider quarks with momenta above the cutoff, the curves end at the on-shell energies $k_0^{\text{os}}(\Lambda)$ that corresponds to $\vec{k} = \Lambda$. The results for the antiquark states are not shown explicitly in Fig. 5.13. They are very close to the results for the quark states.

The energy and momentum dependence of the on-shell mass is obviously weak. The curves have a simple structure, the mass just increases slightly towards higher energies and momenta. For all shown densities, the effective mass of a quark at rest differs by only $4-5\%$ from the mass of a quark with $|\vec{k}\,| = \Lambda$. The weak energy dependence of $\text{Re}\tilde{m}_{\text{os}}$ is due to the large constant contribution from the Hartree self-energy. The values of $m_0 + \Sigma^{\text{H}}$ are indicated in Fig. 5.13 by the thin lines. These contributions account for $76-84\%$ of the total effective masses. The Fock self-energy Σ_s^{F} that is included in the meson exchange diagram provides another constant contribution to $\tilde{m}^{\text{ret}}(k)$. It is related to the Hartree self-energy by $\Sigma_s^{\text{F}} = \frac{1}{2N_f N_c}\Sigma^{\text{H}} \approx 0.1\,\Sigma^{\text{H}}$, cf. Eq. (3.7). Adding up $m_0 + \Sigma^{\text{mf}} + \Sigma^{\text{F}}$, we find that $80-90\%$ of $\text{Re}\tilde{m}_{\text{os}}$ are determined

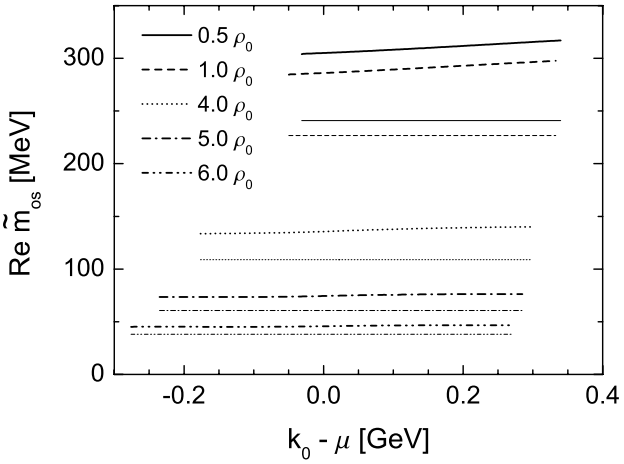

Figure 5.13: The on-shell real part of the effective quark mass $\tilde{m}^{\rm ret}$ (thick lines), i.e. $\mathrm{Re}\tilde{m}^{\rm ret}(k_0, |\vec{k}_{\rm os}(k_0)|)$, shown for the quark states at five different densities in the chirally broken $(0.5\rho_0, \rho_0)$ and restored phase $(4\rho_0, 5\rho_0, 6\rho_0)$. Parameter set I from Table 5.1 was used in the calculations. The thin lines indicate the constant contributions from $m_0 + \Sigma^{\rm H}$.

by constant contributions on the mean-field level (to be more precise: $82 - 86\%$ in the chirally broken phase and $83 - 90\%$ in the chirally restored phase).

The remaining $10 - 20\%$ of the total on-shell mass are generated by short-range correlations. Recall that the $\mathcal{O}(1/N_c)$ coupling – and thus the Hartree self-energy – has been lowered by 22% in comparison to the Hartree coupling. Hence, we can conclude that the collisional self-energy $\mathrm{Re}\,\Sigma_s^{\rm ret}$ just replaces the missing mean-field contributions without generating new effects.

5.5.2 Real part of $\Sigma_0^{\rm ret}$

The γ_μ-components of $\mathrm{Re}\,\Sigma_{\rm os}^{\rm ret}$ readjust the position of the on-shell peaks in the spectral function, cf. Eq. (2.36). We will not discuss $\mathrm{Re}\,\Sigma_{v,\rm os}^{\rm ret}$ explicitly here since it remains small in comparison to the other components and to $\vec{k}$ ($\mathrm{Re}\,\Sigma_{v,\rm os}^{\rm ret}/|\vec{k}\,| < 0.03$ for quarks and < 0.07 for antiquarks at all densities). $\mathrm{Re}\,\Sigma_{0,\rm os}^{\rm ret}$ is shown in Fig. 5.14 for the quark and antiquark states. In the chirally broken phase, $\mathrm{Re}\,\Sigma_{0,\rm os}^{\rm ret}$ is almost density independent. The energy dependence of $\mathrm{Re}\,\Sigma_{0,\rm os}^{\rm ret}$ is moderate. It is approximately antisymmetric in k_0 – up to a small positive shift[1] – and has opposite signs for the quark and antiquark states. Thus, it cannot be absorbed into a redefined chemical potential like the constant $\mathrm{Re}\,\Sigma_0^{\rm ret} = \Sigma_0^{\rm F}$ of the Hartree–Fock approach. The overall influence of $\mathrm{Re}\,\Sigma_{0,\rm os}^{\rm ret}$ on the spectral function remains limited in the chirally broken

[1] $\Sigma_0^{\rm F}$ and $\Sigma_{\rm eff,0}^{\rm F}$ vanish in the vacuum and remain small at low μ as discussed in Sections 3.1 and 3.8.

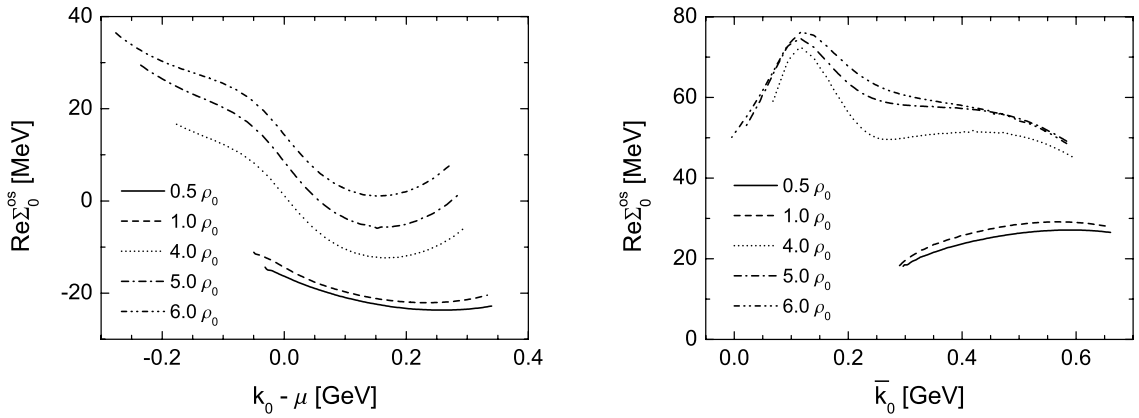

Figure 5.14: On-shell real parts of Σ_0^{ret} for the quark and antiquark states. See Fig. 5.13 for details.

phase. It is one order of magnitude smaller than the effective mass. In addition, we find $|\mathrm{Re}\,\Sigma^{\mathrm{ret}}_{0,\mathrm{os}}/k_0| < 0.07$.

In contrast to the decreasing effective mass, $\mathrm{Re}\,\Sigma^{\mathrm{ret}}_{0,\mathrm{os}}$ becomes larger in the chirally restored phase. When parameter set I is used, $\mathrm{Re}\,\Sigma^{\mathrm{ret}}_{0,\mathrm{os}}$ will be on the order of $\mathrm{Re}\tilde{m}_{\mathrm{os}}$. The overall energy dependence increases and the approximate antisymmetry is completely lost. Note that the density dependence has enhanced for the quark states but is still moderate in the antiquark sector. $\Sigma^{\mathrm{F}}_{\mathrm{eff},0}$, the non-dispersive contribution to $\mathrm{Re}\,\Sigma^{\mathrm{ret}}_{0,\mathrm{os}}$ is on the order of $10 - 25\,\mathrm{MeV}$. At low energies, $\mathrm{Re}\,\Sigma^{\mathrm{ret}}_{0,\mathrm{os}}$ is of similar size and has the same sign for quarks and antiquarks. Thus, both peaks of the spectral functions are shifted to higher energies. This shift can be clearly observed in the cuts for small three-momenta in Fig. 5.5.

The bump in the antiquark sector at $\bar{k}_0 \approx 120\,\mathrm{MeV}$ (right panel of Fig. 5.14) is generated by the contributions to the self-energy from process 4.1(c), i.e., the generation of a bound $q\bar{q}$ state. In the chirally restored phase, this process moves into the region of the on-shell peak of the antiquarks. Due to the higher quark mass, this was not the case in the chirally broken phase. As we have already observed in Section 5.2.2, the processes involving bound $q\bar{q}$ states (see Fig. 4.1) have no influence on the on-shell self-energy in the quark sector (this also holds for the width, cf. Fig. 5.15). The results for the on-shell self-energy of the quarks are independent of the RPA pion mass.

The considerable size and the strong energy dependence of $\mathrm{Re}\,\Sigma^{\mathrm{ret}}_{0,\mathrm{os}}$ in the quark sector lead to the conclusion that the properties of the medium are modified in comparison to the Hartree and Hartree–Fock+RPA approximations. There, $\mathrm{Re}\,\Sigma^{\mathrm{ret}}_{0,\mathrm{os}}$ is zero or has a constant value. Shifting the quark on-shell peaks with respect to the (fixed) chemical potential μ has influence on the quark mass and density. Consequently, the properties of the chiral phase transition are modified. Since $\mathrm{Re}\,\Sigma^{\mathrm{ret}}_{0,\mathrm{os}}$ has larger values and a stronger energy dependence at high densities, the impact on the solutions of the gap equation is stronger in the chirally restored phase. In other

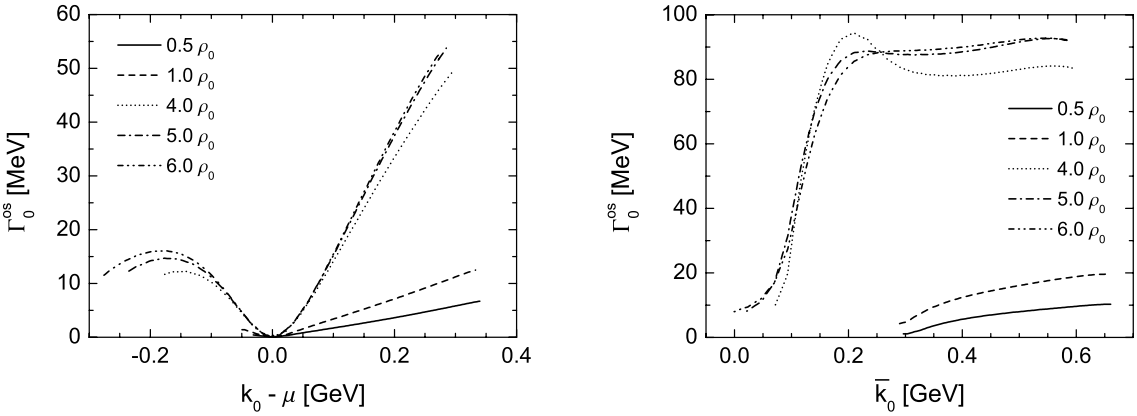

Figure 5.15: On-shell width Γ_0 of the quark and antiquark states. See Fig. 5.13 for details.

words, the changes of the lower part of the (inverted) "S" shaped curve in Fig. 1.3 are larger than those of the upper part. This is agreement with our observations in Section 5.4.

5.5.3 On-shell width

We turn now to the imaginary part of the self-energy. To check how much strength is shifted away from the quasiparticle peaks in the spectral function, we have to investigate the on-shell width of the quarks. We restrict ourselves here to Γ_0 since it is much larger than the two other Lorentz components of the width. In Fig. 5.15, the on-shell width Γ_0^{os} is shown for the same five densities as the real parts of the self-energy in Figs. 5.13 and 5.14.

Like in the cuts for constant three-momenta, the width vanishes at $k_0 = \mu$. Phase space opens for scattering processes above and below the chemical potential – in the vicinity of μ we find an approximately quadratic energy dependence. The width of the populated quark states can be found below $k_0 = \mu$. It is generated by process 4.3(c). Below the chiral phase transition – at low densities – the few populated states are close to the Fermi energy. Consequently, the width of those states does not become much larger than 1 MeV. The states above the Fermi energy as well as the antiquark states can acquire much larger width of $10 - 20$ MeV. We find an approximately linear density dependence of the width for those states. This is not surprising since the relevant processes 4.3(a) and 4.3(e) both involve one quark from the medium as scattering partner.

Above the chiral phase transition, i.e. for the densities $\geq 4\rho_0$ in Fig. 5.15, the region of populated states is much larger than below the phase transition. The width of those states increases up to $10 - 20$ MeV. It drops at low k_0 since the lower threshold for process 4.3(c) is approached, cf. Chapter 4. Like in the chirally broken phase, the

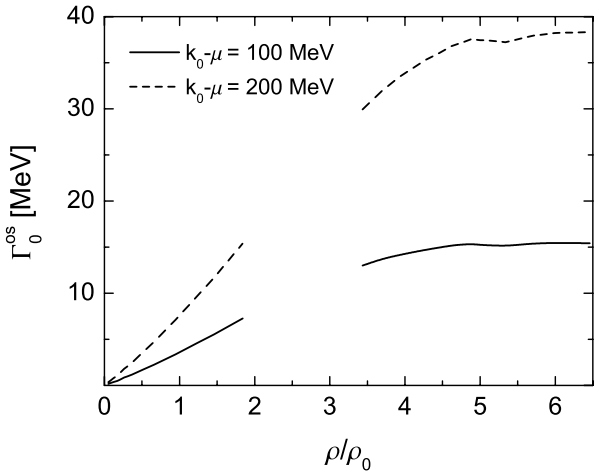

Figure 5.16: The density dependence of the on-shell quark width Γ_0 at two fixed energies $k_0 - \mu$ above the chemical potential.

width of the free quark states and the antiquark states is even larger.

The density dependence of the width becomes rather weak in the chirally restored phase. The curves for $5\rho_0$ and $6\rho_0$ are almost identical in the proximity of the chemical potential. We can interpret that as a saturation of the short-range effects at high densities. This is agreement with our estimates for the density dependence of the scattering diagrams in Section 4.3. At higher densities, the effects of Pauli blocking and the cutoff become more important. We can observe the same effect for nucleons in nuclear matter at *nucleon* densities of a few times ρ_0, see Figs. 6.16 and 6.18 in Chapter 6. There, we will also discuss calculations without Pauli blocking to verify its connection to the saturation. As Fig. 6.20 shows, the correlations in nuclear matter do not saturate when Pauli blocking is switched off in the calculations.

At low densities, the density dependence of the quark–quark collision process 4.1(a) should be given by the relation $\Gamma = \rho\sigma v$, where σ is the total cross section and v is the relative velocity of the two scattering partners. As we have seen in Section 4.4, the on-shell width above the chemical potential is solely determined by process 4.1(a). Thus, we can use the on-shell width at energies above the chemical potential for a check up to which densities this approximation is valid. In Fig. 5.16, we show the density dependence of the on-sell width at two fixed energies (relative to the chemical potential). In agreement with the results from Fig. 5.15, we observe an approximately linear density dependence of the width in the chirally broken phase and a saturation of the width above the phase transition for both energies. This leads to the conclusion that the approximation $\Gamma = \rho\sigma v$ works well for densities up to (at least) $2\rho_0$.

It is difficult to relate the velocity dependence of the on-shell width to the approximation $\Gamma = \rho\sigma v$. This has two reasons. First, the quark width drops to zero at the chemical potential where the quarks have a finite velocity k_F/μ. Second, the

cross-section is velocity dependent (recall that the scattering amplitude of process 4.1(a) corresponds to the four-momentum dependent $|\,\Delta_l^{\mathrm{ret}}\,|^2$). Thus, we find – even at low densities – only very small regions where the width shows a linear velocity dependence. To get a feeling for the typical strength of the quark–quark interactions, we can determine average values for σv from the slope of the curves in Fig. 5.16. For $k_0 - \mu = 100\,\mathrm{MeV}$, we obtain a value of $\langle \sigma v \rangle = 1.2\,\mathrm{mb}$ and for $k_0 - \mu = 200\,\mathrm{MeV}$ a value of $\langle \sigma v \rangle = 2.5\,\mathrm{mb}$. Those values appear reasonable for processes governed by the strong interaction.

5.6 Average quark width

For a better understanding of the density dependence of the width, we will now investigate the average width of the populated quark states $\langle \Gamma_0^{\mathrm{pop}} \rangle$ and the average width of all quark states $\langle \Gamma_0^{\mathrm{all}} \rangle$ (excluding antiquarks, see Appendix E.2.1). We define the average width of the populated states as

$$\langle \Gamma_0^{\mathrm{pop}} \rangle = \frac{\int_0^\Lambda dk k^2 \int_{\mathrm{Re}\tilde{k}_0=0}^\infty dk_0 \Gamma_0(k) \mathcal{A}_0(k) \mathrm{n_F}(k_0)}{\int_0^\Lambda dk k^2 \int_{\mathrm{Re}\tilde{k}_0=0}^\infty dk_0 \mathcal{A}_0(k) \mathrm{n_F}(k_0)} \,. \tag{5.2}$$

In the numerator we weight the width with the spectral function and integrate over all populated states. The result is normalized by the quark density (3.9) in the denominator. As usual, the three-momentum is regularized by the cutoff Λ. The average width of all quark states is found by removing the distribution functions from the integrands in (5.2),

$$\langle \Gamma_0^{\mathrm{all}} \rangle = \frac{\int_0^\Lambda dk k^2 \int_{\mathrm{Re}\tilde{k}_0=0}^\infty dk_0 \Gamma_0(k) \mathcal{A}_0(k)}{\int_0^\Lambda dk k^2 \int_{\mathrm{Re}\tilde{k}_0=0}^\infty dk_0 \mathcal{A}_0(k)} \,. \tag{5.3}$$

Due to the weighting with the spectral function, the contributions from the on-shell width will dominate the integrals in the numerators of (5.2,5.3). Nonetheless, the off-shell states are also taken into account. If the width becomes large in an off-shell region – recall the huge bumps in Fig. 5.3 – this has also influence on the average width.

5.6.1 Average width of the populated states

In Fig. 5.17 the average widths $\langle \Gamma_0^{\mathrm{pop}} \rangle$ and $\langle \Gamma_0^{\mathrm{all}} \rangle$ from calculations with both parameter sets of Table 5.1 are shown. The gap at $\rho \approx 2 - 4\rho_0$ corresponds to the chiral phase transition where the quark mass drops and the density increases discontinuously. The intermediate solutions of the gap equation are numerically not accessible in our approach since the iterative procedure does not converge on those solutions, cf. Section 5.4.

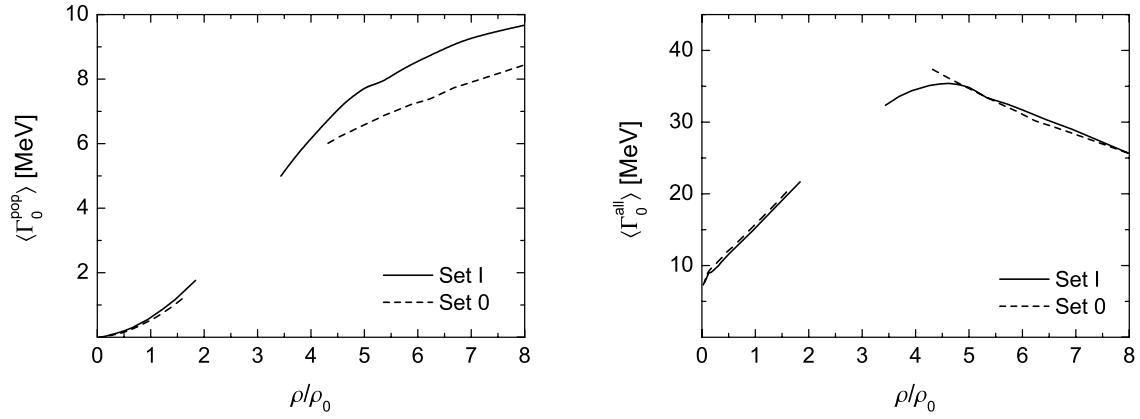

Figure 5.17: The average width of the populated quark states (left panel) and of all quark states (right panel). The solid lines show the results for parameter set I, the dashed lines the results for parameter set 0 from Table 5.1.

We find that $\langle\Gamma_0^{\rm pop}\rangle$ remains smaller than 2 MeV in the chirally restored phase. The results for the two parameter sets do not differ significantly. In the present approach, the width in the region $0 < k_0 < \mu$ is generated solely by the scattering process 4.3(c), see Sections 4.4 and 5.2 for details. This process depends on two scattering partners from the medium. Each incoming quark from the medium introduces a linear density dependence into the total collision rate. As we have already estimated in Section 4.3, we find an approximately quadratic density dependence of $\langle\Gamma_0^{\rm pop}\rangle$ below the phase transition. In this region the quark density is low and the damping effect of Pauli blocking remains weak. At zero density the average width vanishes due to the lack of scattering partners.

At the chiral phase transition, both, the density and the average width increase by a factor of $2-3$. The density dependence of $\langle\Gamma_0^{\rm pop}\rangle$ weakens significantly in the chirally broken phase, it is not even linear at high densities. The average width does not exceed 10 MeV at a density of $8\rho_0$. This is just the saturation effect that we have expected from the results for the on-shell width in Fig. 5.15.

The weakened density dependence of $\langle\Gamma_0^{\rm pop}\rangle$ in the chirally restored phase is the consequence of Pauli blocking and the cutoff. We have discussed in Section 4.3 that – in the Hartree approximation – the cutoff becomes relevant for process 4.3(c) only above the chiral phase transition, where $\mu > E_\Lambda/2$. Using parameter set I in the present approach, we find a value of $E_\Lambda \approx 653\,\text{MeV}$ in the chirally broken phase ($\rho = 1.5\rho_0$) and a value of $E_\Lambda \approx 628\,\text{MeV}$ in the chirally restored phase ($\rho = 3.7\rho_0$) at a chemical potential of 327 MeV. Note that $E_\Lambda = k_0^{\rm os}(\Lambda)$ has been determined numerically from (2.39), not using the simple expression $\sqrt{\Lambda^2 + m^{*2}}$ but including also the shifts from the real parts $\mathrm{Re}\,\Sigma_\mu^{\rm ret}$. As we can see, the chemical potential crosses the threshold $\mu = E_\Lambda/2$ at the phase transition. The results for the chirally restored phase differ in size and shape for the two parameter sets. The differences

can be attributed to the effective quark masses in this phase. While the quarks are massless in the chiral limit (parameter set 0), they still have mass of a few tens of MeV when parameter set I is used.

5.6.2 Average width of all quark states

When we calculate the average width of all states $\langle\Gamma_0^{\text{all}}\rangle$, we find significantly larger values than for $\langle\Gamma_0^{\text{pop}}\rangle$. The contributing processes are 4.3(a) and 4.3(c) in the region of the on-shell states below E_Λ and 4.1(a), 4.3(b) at higher energies close to and above E_Λ, cf. Chapter 4. Due to the (off-shell) decay processes 4.3(b) and 4.1(a), the average width $\langle\Gamma_0^{\text{all}}\rangle$ does not vanish at zero density. These processes require no scattering partners from the medium. They provide a constant contribution to the width as long as the density is low and Pauli blocking not too important. The main contributions to $\langle\Gamma_0^{\text{all}}\rangle$ are generated by the width of the on-shell states that are favored in the integral (5.3). In the chirally broken phase there exist substantially more free than populated on-shell states. Thus, process 4.3(a) will yield the largest contributions to $\langle\Gamma_0^{\text{all}}\rangle$. This process involves only one scattering partner from the medium. Consequently, we find an approximately linear density dependence of $\langle\Gamma_0^{\text{all}}\rangle$ for the chirally broken phase in Fig. 5.17. The width grows up to 20 MeV.

In the chirally restored phase, $\langle\Gamma_0^{\text{all}}\rangle$ shows a very interesting behavior. This can best been seen in the result for parameter set I. Right above the phase transition, the linear increase of $\langle\Gamma_0^{\text{all}}\rangle$ turns smoothly into a decrease. We cannot see the turnover region for parameter set 0. Due to the larger and less smooth change of the quark mass at the phase transition, it has most likely the shape of a sharp bend. As we have suspected in Section 4.3, the effects of Pauli blocking and the cutoff in the scattering process 4.3(a) yield a decrease of the collision rate. The almost instant change of the density dependence can be attributed to the dropping of E_Λ at the phase transition.

At first glance, the behavior of $\langle\Gamma_0^{\text{all}}\rangle$ seems to contradict the results from Fig. 5.15. However, this is not the case. To understand the decrease, we have to recall the definition of the average width. The factor k^2 in the integrals of Eq. (5.2) gives the width at large three-momenta a higher weight than at low momenta. The density of states increases with $\vec{k}^2$ and not with $|\vec{k}\,|$. When the chemical potential – and thus the Fermi momentum – rises, the range of free states ($k_F < |\vec{k}\,| < \Lambda$) decreases. This is, however, the region where the width has the largest values. To illustrate this effect, we show $k^2\Gamma_0(k)$ as a function of the three-momentum in Fig. 5.18. The curve for $5\rho_0$ clearly provides larger contributions to the average width $\langle\Gamma_0^{\text{all}}\rangle$ than the curves for $6\rho_0$ and $8\rho_0$. The width may become larger than the $5\rho_0$ result at higher momenta beyond the cutoff. However, this region is not covered by the integrals in (5.3). It is of little importance here that the on-shell width in the region below k_F is larger at higher densities.

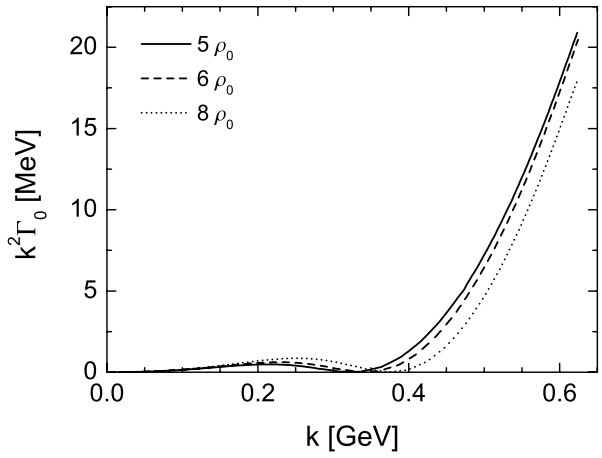

Figure 5.18: On-shell width Γ_0 of the quark states multiplied with k^2 at three different densities above the chiral phase transition. The curves end at the three-momentum cutoff Λ. Parameter set I from Table 5.1 was used in the calculations.

5.6.3 Further remarks

The results for the average width appear rather small in comparison to Figs. 5.4, 5.5, and 5.15. They are, however, not too different from the nuclear matter results in Chapter 6. At zero temperature and normal nuclear matter density, we find an average width of the populated nucleon states of 6 MeV, cf. Fig. 6.18. For a three times higher density, a width of 16 MeV is found. Of course, nucleon and quark widths should not be compared directly – in particular since the masses differ significantly. The quantitative agreement, however, indicates, that the short-range correlations are of similar importance for quarks in quark matter as they are for nucleons in nuclear matter.

At this point, we come back to the results of Section 5.4. We have found there that the chiral phase transition does not turn into a smooth crossover like in the naive Hartree–Fock calculation with a finite width that is shown in Fig. 1.3. In the simple extension of the mean-field model, we have used a constant width of $\Gamma_0 = 28\,\mathrm{MeV}$. That is the minimum value to turn the first-order phase transition into a crossover in this approach. As we see in Fig. 5.17, the realistic value for $\langle \Gamma_0^{\mathrm{pop}} \rangle$ is more than one order of magnitude smaller in the chirally broken phase near the phase transition. Hence, it is not very surprising that we do not find a crossover but only a first-order phase transition with a gap that is smaller than in a pure mean-field calculation.

In Section 4.4.2, we have found that the on-shell quark width in the chirally broken phase is suppressed by the too large pion mass of our approach. We have estimated that the upper limit for this suppression is one order of magnitude. However, the real suppression should be smaller. We can conclude that a calculation with a more

realistic pion mass could still yield a first-order phase transition, however, with a very small mass gap.

We note that the average width is strongly temperature dependent in nuclear matter, see Fig. 6.17 in Chapter 6. A similar behavior can be expected for quark matter. This should lead to a stronger influence of the short-range correlations on the chiral phase transition at finite temperatures. Such a study is, however, beyond the scope of the present work.

5.7 Momentum distribution

The short-range correlations manifest themselves in the spectral functions by the broadening of the on-shell peaks and the existence of off-shell states even far away from the peaks. Those states can be easily identified in the cuts of the spectral function in Figs. 5.4 and 5.5. To estimate the importance of the off-shell states, we will investigate the momentum distribution of the quarks in the medium. The momentum distribution $n(|\vec{k}\,|)$ is closely related to the density (3.9). It is found by integrating the quark spectral function over the region of the populated states at fixed three-momentum,

$$n(|\vec{k}\,|) = \frac{1}{\pi} \int\limits_{\mathrm{Re}\tilde{k}_0=0}^{\infty} dk_0 \mathcal{A}_0(k) \mathrm{n_F}(k_0)\,. \tag{5.4}$$

The factor $1/\pi$ has been chosen to normalize the momentum distribution, cf. (D.6). Note that the above definition is – like the definition of the density (3.9) – only an approximation that is introduced for numerical reasons. We show in Appendix E that the exact definition (E.15) yields strong numerical fluctuations, in particular above the Fermi momentum (see Figs. E.3 and E.4).

In a mean-field approach, the spectral function is determined by sharp quasiparticle peaks (4.1). The momentum distribution corresponds then to that of a free Fermi gas, $n(|\vec{k}\,|) = \mathrm{n_F}(|\vec{k}\,|)$: At zero temperature, the (quasiparticle) momentum distribution is given by a step function $\Theta(k_F - |\vec{k}\,|)$ that drops from 1 to 0 at the Fermi momentum.

The finite width of the quarks modifies the simple mean-field picture. At momenta below the Fermi momentum k_F, the off-shell states shift some strength of the – normalized – spectral function away from the peaks to energies above the chemical potential. This leads to a depletion of the momentum distribution below k_F since the off-shell states above the chemical potential are not populated. Above the Fermi momentum, on the other hand, the off-shell states shift some strength back into the region below the chemical potential. Those states are populated and yield – even at zero temperature – finite contributions to the momentum distribution above k_F, the so-called high-momentum tail. The depletion below k_F and the high-momentum tail can be interpreted as a universal measure for the short-range correlations in the medium. We can use them not only to estimate the importance of the short-range

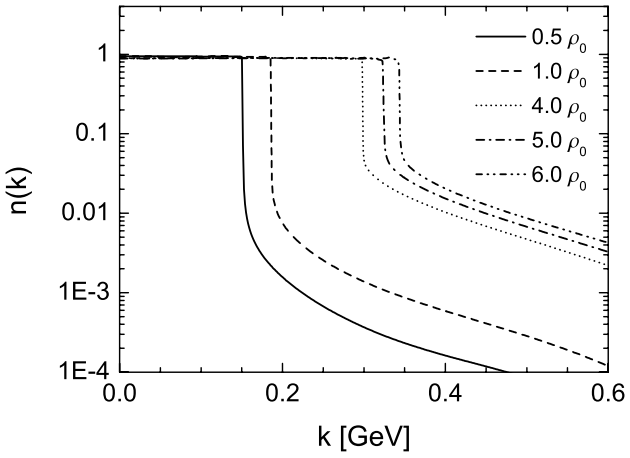

Figure 5.19: The momentum distribution of quarks in quark matter, using parameter set I from Table 5.1. The solid and the dashed line correspond to quark matter at densities below the chiral phase transition, the other lines to quark matter above the phase transition.

effects in quark matter at different densities, but also to compare the short-range effects in quark matter to those in nuclear matter.

In Fig. 5.19 we show the momentum distribution in quark matter at two densities below and three densities above the chiral phase transition. As expected for an infinite system at zero temperature, we find a sharp step at the Fermi momentum[2] [DVN05]. The density dependent high-momentum tail is located at momenta above k_F. Recall that the quark width in the range $0 < k_0 < \mu$ is generated by process (c) of Fig. 4.3. As we have already discussed before, the density dependence of this process is quadratic in the chirally broken phase and weakens above the phase transition due to Pauli blocking, cf. Fig. 5.17. This behavior is reflected in the density dependence of the momentum distribution. While the high-momentum tails at the two lower densities differ significantly in size, the results for the higher densities in the chirally restored phase are very close to each other.

At low momenta, the momentum distribution has values of approximately 0.94 below and 0.89 above the chiral phase transition. The values do not differ significantly for the individual densities in both phases. The discontinuity at the Fermi momentum, $n(k_F^-) - n(k_F^+)$, has a value of $0.82-0.85$ for the two lower densities and a value of $0.72-0.75$ for the three higher densities. These results can be readily compared to the well established values for nucleons in nuclear matter [DVN05]. At zero temperature and normal nuclear matter density, the depletion of the nucleon momentum distribution is on the order of $15-18\%$, see e.g. [VDPR93, BBG$^+$92, CdAS96]. The discontinuity

[2]The quarks are quasiparticles at the Fermi energy, cf. Figs. 5.4 and 5.5. Since the on-shell peak of the spectral function has no width there, the full strength of the peak crosses the Fermi energy at k_F instantaneously.

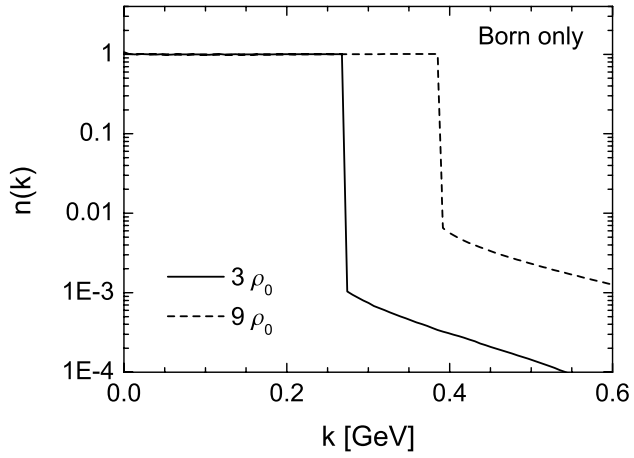

Figure 5.20: Momentum distribution for calculations at two different densities above the chiral phase transition. Results from [FLM03b], using the parameter set 0 from Table 2.1 (mean-field parametrization) and restoring chiral symmetry by hand.

at the Fermi momentum has a size of approximately $0.7-0.75$ [Bȯz02, BFF92, DB04]. We can conclude that the short-range effects in quark matter in the chirally restored phase are of similar size as in normal nuclear matter. In the chirally broken phase, where the quarks reach the same particle number density ρ_0 as the nucleons at normal density, the correlations are slightly smaller for the quarks.

It is also interesting to compare the results of the present $\mathcal{O}(1/N_c)$ approach to our previous calculations [FLM03b] using only the Born diagrams in the calculation of the self-energies. Fig. 5.20 shows the momentum distributions from [FLM03b] for massless quarks at two different densities. The high-momentum tails are significantly smaller than in the $\mathcal{O}(1/N_c)$ approach. The $3\rho_0$ result of Fig. 5.20 is more than one order of magnitude smaller than the $4\rho_0$ result in Fig. 5.19. This finding is in agreement with the observations that we have made for the quark width in Section 5.2. A density of $9\rho_0$ in the Born approach is needed to generate short-range effects on the same level as in the $\mathcal{O}(1/N_c)$ approach at the much lower densities of $0.5\rho_0-1\rho_0$. This confirms again that the Born approximation, an expansion in terms of the coupling, is not well suited for calculations with the NJL model. In comparison to a consistent expansion in the number of colors, we have missed significant contributions to the collisional self-energies in [FLM03b].

6 Nuclear matter at high densities and finite temperatures

An interesting but only partially explored problem of nuclear many-body theory are the contributions from short-range correlations to the binding properties of nuclear matter and finite nuclei. The long-range correlations that determine the bulk properties – like the binding energies – of nucleons in nuclei and nuclear matter, are usually treated on the mean-field level. The nucleon–nucleon interaction, generated by meson exchange, is attractive at long ranges. At short distances, however, the interaction becomes strongly repulsive and may induce effects that can not be described in the framework of a mean-field model.

Short-range effects in finite nuclei can be observed experimentally, for example, in nucleon knockout reactions (see, e.g., [DdWH90, CdAPS91]). To illustrate the role of the short-range correlations, we show the excitation energy spectrum of the reaction $^{12}\mathrm{C}(e,e'p)^{11}\mathrm{Be}$ in Fig. 6.1 [dWH90]. The three peaks at the lowest energies correspond to proton knockouts from the $1p$ shell of $^{12}\mathrm{C}$. This is in agreement with the (mean-field) shell model that predicts that those states are populated. The additional peaks that can be found at higher energies ($E_X > 6\,\mathrm{MeV}$) correspond to the knockout of protons populating $2s_{1/2}$ ($1/2^+$) and $2d$ ($5/2^+$, $3/2^+$) states in the residual $^{11}\mathrm{Be}$

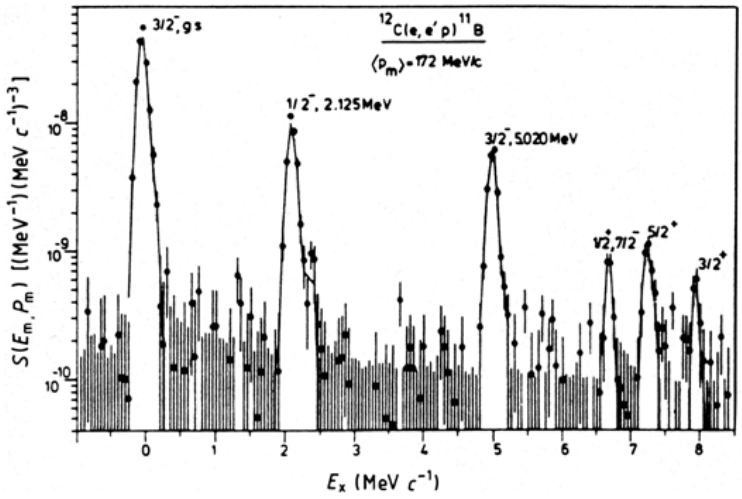

Figure 6.1: The spectral function found in the $^{12}\mathrm{C}(e,e'p)^{11}\mathrm{Be}$ nucleon knockout reaction as function of the excitation energy. (Figure taken from [dWH90].)

nucleus. According to the single-particle shell model, these shells are not populated in ^{12}C, cf. [DdWH90]. The observation of the spectral lines in the experiment is thus a clear sign of short-range effects that go beyond the mean-field picture of the shell model.

Of particular interest for various regions of nuclear physics ranging from heavy ion collisions to astrophysical processes is the density and temperature dependence of the short-range correlations in nuclear matter. In heavy ion collisions like those planned at the Compressed Baryonic Matter facility at GSI [GGHM01], temperatures of several tens of MeV and densities of several times the nuclear matter saturation density ρ_0 are reached. Very similar conditions are encountered in the formation of neutron stars in supernova explosions, where nucleon correlations may have considerable influence on the emitted neutrino spectra [Saw95, RPLP99]. So far, there has been no consistent investigation of the properties of the nucleon spectral function that covers the full temperature and density range of those scenarios. Only a few studies exist for densities from half to twice ρ_0 and temperatures up to 20 MeV [ARFdCO96, Bȯz99].

Below, we will extend the approach to short-range correlations in nuclear matter presented initially in [LEL$^+$00, LLLM02] to the more general cases of arbitrary temperatures and densities. The self-consistent calculation of Lehr et al. is based on the two-particle–one-hole ($2p1h$) and one-particle–two-hole ($1p2h$) sunset diagrams. The short-range part of the NN interactions is approximated by an averaged matrix element. The previously obtained results at zero temperature and saturation density have turned out to be in surprisingly good agreement with much more sophisticated and numerically extremely involved, "state-of-the-art" calculations utilizing the full machinery of modern nuclear many-body theory [BFF92, BBG$^+$92].

Different from [LEL$^+$00, LLLM02], we require a reliable description of the static mean-field self-energy, i.e. the long-range correlations, in our approach. This is essential to obtain consistent results at all T and ρ. Calculations for the equation of state for dense matter and finite temperatures have been made using microscopic Hamiltonians, see e.g. [Wir88, FP81]. In our model, however, we incorporate the static properties of the mean-field by an empirical, Skyrme-type energy density functional [Sky59, BFvGQ75, VB72].

It is important to point out that our approach becomes unphysical at higher temperatures and densities. In the scattering processes that generate the nucleon width, we consider only nucleons in the incoming and outgoing channels. We do not take into account that it becomes possible to excite nucleon resonances at higher temperatures. Such resonances, however, may reach final states that are Pauli blocked for nucleons when the density is large – and thus enhance the width. We will come back to this point at the end of the chapter. There, we will show that the influence of resonance does not become too large in the temperature and density range that we cover in this work.

In the following, we will present our approach to the short-range correlations in hot and dense nuclear matter. After introducing the self-consistent calculation scheme and discussing the structure of the employed short-range interaction, we will show how

the mean-field self-energy is introduced into our model. We will also comment on the short-range behavior of realistic NN potentials (at zero temperature) in comparison to our averaged matrix element. The results of our numerical calculations will show that the short-range correlations have an interesting temperature and density dependence that can be explained – to a large extent – by Pauli blocking. Note that a shorter version of this chapter can be found in [FLM03a].

6.1 The model

6.1.1 Self-consistent approach

The basis of our approach to short-range correlations in hot and dense nuclear matter are the direct relations between the nucleon self-energies and the full in-medium propagators that can be used for a self-consistent, i.e. iterative, calculation. We use – like in the quark case – the real-time formalism [Dan84, BM90, Das97] in our calculations. Hence, the nucleon propagators $(\mathrm{S}^{\mathrm{c}}, \mathrm{S}^{\mathrm{ret}}, \mathrm{S}^{\gtrless}, \ldots)$ and self-energies $(\Sigma^{\mathrm{c}}, \Sigma^{\mathrm{ret}}, \Sigma^{\gtrless}, \ldots)$ have formally the same structure (in terms of the fields) and are related in the same ways as the quark propagators and self-energies introduced in Sections 2.6 and 2.8, respectively. Because they are of equal validity for fermions, we can reinterpret the quark relations of those sections as nucleon relations here. Below, we will also come back to the results of Chapter 4, where the correspondence of the collisional quark self-energies to collision and decay rates is investigated on the quasiparticle level. Some of the thresholds that were determined in Section 4.2.2 can be readily mapped to the nucleon self-energies.

The much larger mass of the nucleons in comparison to the quarks allows us to perform the investigation of nuclear matter in a non-relativistic scheme. This simplifies the calculations considerably: The nucleon spectral function and self-energy become scalar functions of energy and momentum without a complicated Lorentz structure (in the non-relativistic limit, the expressions in Eqs. (2.23,2.52) reduce to their γ_0-components). Antiparticles do not contribute. Note that we consider only symmetric nuclear matter in thermodynamical equilibrium here and work in the rest frame of the medium.

We will now discuss the individual components of our approach – in the same order as they occur in the calculations. Let us begin with the non-relativistic, retarded nucleon propagator (2.18). The full in-medium propagator is explicitly given by, cf. (2.33),

$$\mathrm{S}^{\mathrm{ret}}(\omega, k) = \frac{1}{\omega - \frac{k^2}{2m} - \Sigma^{\mathrm{ret}}(\omega, k)} \,. \tag{6.1}$$

Using this propagator, we find for the single-particle spectral function (2.26)

$$\mathcal{A}(\omega, k) = -2\mathrm{Im}\, \mathrm{S}^{\mathrm{ret}}(\omega, k) = \frac{\Gamma(\omega, k)}{(\omega - \frac{k^2}{2m} - \mathrm{Re}\, \Sigma^{\mathrm{ret}}(\omega, k))^2 + \frac{1}{4}\Gamma^2(\omega, k)} \,, \tag{6.2}$$

where $\Gamma(\omega, k) = -2\mathrm{Im}\,\Sigma^{\mathrm{ret}}(\omega, k)$ is the width of the spectral function. As shown in Appendix D, the spectral function is normalized, see Eq. (D.6) for $\mathcal{A}_0$ (non-relativistic limit). The correlation functions $\mathrm{S}^{>}$ and $\mathrm{S}^{<}$, cf. (2.17), are closely related to the spectral function. They are essential components of our approach since they enter into the collisional self-energies. Introducing the fermionic phase space distribution function $\mathrm{n_F}(\omega, k)$, we find the relations

$$\begin{aligned} \mathrm{S}^{<}(\omega, k) &= i\mathcal{A}(\omega, k)\mathrm{n_F}(\omega, k)\,, \\ \mathrm{S}^{>}(\omega, k) &= -i\mathcal{A}(\omega, k)[1 - \mathrm{n_F}(\omega, k)]\,. \end{aligned} \tag{6.3}$$

Recall that we have identified $-i\,\mathrm{S}^{<}(\omega, k)$ and $i\,\mathrm{S}^{>}(\omega, k)$ with the density of occupied (particle) and free (hole) states at a given energy and momentum in Section 2.6.3.

In thermal equilibrium, $\mathrm{n_F}$ will not depend on the momentum but only on the energy, the temperature, and – through the chemical potential ω_F – on the density of the system,

$$\mathrm{n_F}(\omega) = \frac{1}{e^{(\omega-\omega_F)/T} + 1}\,. \tag{6.4}$$

The previous calculations in [LEL$^+$00, LLLM02] were – like our approach to quark matter, cf. (3.17,3.23) – greatly simplified by the fact that the Fermi distribution reduces to a step function at zero temperature (2.29). This is, of course, not the case in the present approach. Here, we have to take into account that the distribution function does not drop discontinuously at the chemical potential but turns into a smooth transition for finite temperatures. This affects mainly the numerical calculations. They become more involved because the limits of integrals over the propagators $\mathrm{S}^{\gtrless}$ (6.3) cannot be shifted from $+\infty$ of $-\infty$ to ω_F.

We turn now to the self-energy that enters the propagator in Eq. (6.1) and the spectral function in (6.2). It follows from the considerations in Section 2.8.1 that the nucleon self-energy can be split up into a time-local mean-field part $\Sigma^{\mathrm{mf}}(1,2) \sim \Sigma(1)\delta(t_1 - t_2)$ and a collisional part that is generated by the (non-time ordered) self-energies $\Sigma^{\gtrless}$,

$$\Sigma^{\mathrm{ret}}(1,2) = \Sigma^{\mathrm{mf}}(1,2) + \Theta(t_1 - t_2)\,[\Sigma^{>}(1,2) - \Sigma^{<}(1,2)]\,.$$

The purely real Σ^{mf} contains the contributions to the self-energy arising from ground state tadpole diagrams which describe mainly the static Hartree–Fock mean-field. In a perturbative expansion, the leading order contributions are the Hartree and the Fock diagram that are shown in the first line of Fig. 6.2.

The short-range correlations – in which we are mainly interested here – are generated by the collisional self-energies $\Sigma^{\gtrless}$ that yield non-hermitian contributions to Σ^{ret}. In leading order, i.e. on the two-particle–one-hole ($2p1h$) and one-particle–two-hole ($1p2h$) level, the collisional self-energies $\Sigma^{\gtrless}$ correspond the Born diagrams shown in the second line of Fig. 6.2. Like in [LEL$^+$00, LLLM02], we will determine the

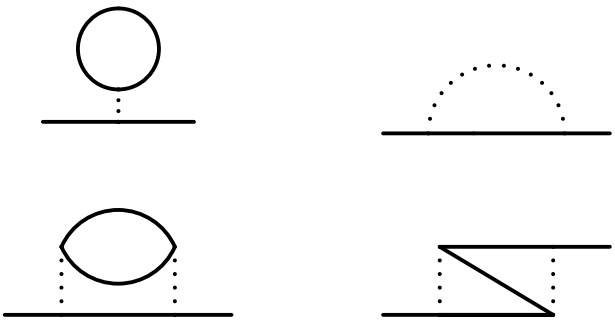

Figure 6.2: First and second order contributions to the nucleon self-energy. The time-local Hartree and Fock self-energy diagrams in the first line are the leading order contributions to the mean-field self-energy. The direct and the exchange Born diagram in the second line yield complex contributions to the self-energy and generate the short-range correlations in our approach.

short-range effects from those diagrams – using full in-medium propagators – in our approach.

For the calculation of the collisional self-energies, a direction has to be assigned to each of the nucleon lines in the Born diagrams. This has been shown in Fig. 4.2 for the quark self-energies (4.17). Using the Feynman rules of the real-time formalism (see Appendix C), we find

$$\Sigma^{\gtrless}(\omega,k) = g\int \frac{d^3p d\omega_p}{(2\pi)^4}\frac{d^3q d\omega_q}{(2\pi)^4}\frac{d^3r d\omega_r}{(2\pi)^4}(2\pi)^4\delta^4(k+p-q-r) \times \overline{|\mathcal{M}|^2}\; \mathrm{S}^{\lessgtr}(\omega_p,p)\,\mathrm{S}^{\gtrless}(\omega_q,q)\,\mathrm{S}^{\gtrless}(\omega_r,r)\,, \tag{6.5}$$

with the short-hand notation

$$\delta^4(k+p-q-r) = \delta(\omega+\omega_p-\omega_q-\omega_r)\delta^3(\vec{k}+\vec{p}-\vec{q}-\vec{r})$$

for energy and momentum conservation. $g = 4$ is the nucleonic spin-isospin degeneracy factor. $\overline{|\mathcal{M}|^2}$ denotes the square of the nucleon–nucleon scattering amplitude averaged over spin and isospin of the incoming and summed over spin and isospin of the outgoing nucleons (see [Leh03, KLM05] for details). $\overline{|\mathcal{M}|^2}$ combines the contributions from the direct and the exchange diagram in the second line of Fig. 6.2. Note that the self-energies and propagators in Eq. (6.5) depend only on the modulus of the three-momenta and not on their direction since an infinite medium in thermal equilibrium is considered.

From the collisional self-energies we obtain immediately, cf. (2.50), the imaginary part of the retarded self-energy and the width that enters the spectral function (6.2),

$$\Gamma(\omega,k) = -2\mathrm{Im}\,\Sigma^{\mathrm{ret}}(\omega,k) = i\left[\Sigma^{>}(\omega,k) - \Sigma^{<}(\omega,k)\right]\,. \tag{6.6}$$

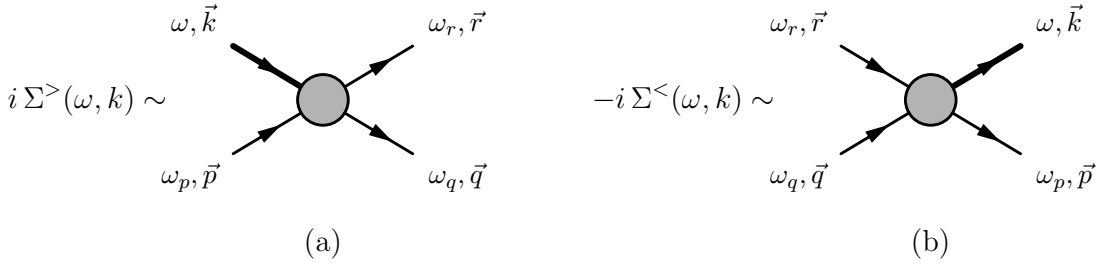

Figure 6.3: Scattering processes corresponding to the collisional self-energies $i\,\Sigma^{>}$ (loss rate) and $-i\,\Sigma^{<}$ (gain rate). Total collision rates are found by integrating over the energies $\omega_p, \omega_q, \omega_r$ and momenta $\vec{p}, \vec{q}, \vec{r}$, cf. Eq. (6.5).

Let us briefly comment on the structure of the nucleon width before we continue to present our approach. As we have discussed in Section 4.2, the self-energies $i\,\Sigma^{>}(\omega,k)$ and $-i\,\Sigma^{<}(\omega,k)$ can be identified with total collision rates for scattering out of (loss rate) and into (gain rate) the configuration (ω,k), respectively. The scattering processes that contribute to the collision rates are shown in Fig. 6.3, where each incoming line corresponds to a propagator $\mathrm{S}^{<}$ (density of particles) and each outgoing line to a propagator $\mathrm{S}^{>}$ (density of holes) in Eq. (6.5). Note that the expressions in (6.5) resemble those for the quark self-energies in Eq. (4.17) when $\overline{|\mathcal{M}|^2}$ is replaced by $\Delta^{\mathrm{ret}}\,\Delta^{\mathrm{av}}$. Particle–hole excitations take over the role of the quark–antiquark excitations, cf. Fig. 4.2, in the present, non-relativistic approach.

At zero temperature, it follows from simple kinematical considerations (each incoming nucleon from the medium must have an energy lower than ω_F and each outgoing nucleon must have an energy higher than ω_F) that the phase space for both processes of Fig. 6.3 closes at the chemical potential ω_F. Process (a) may only contribute to $\Sigma^{>}$ for energies above ω_F and process (b) only to $\Sigma^{<}$ for energies below ω_F – this is a sufficient and necessary condition for a stable ground state. In other words, it is not possible to scatter into or out of the states at the Fermi energy. Thus, the width drops to zero and the nucleons at the chemical potential are stable quasiparticles in cold nuclear matter. (At finite temperatures, the kinematical constraints are less strict. The width will then be finite at ω_F.)

We return now to the presentation of our approach. The real part of the retarded self-energy and the nucleon width are related by a dispersion relation, cf. (3.24),

$$\mathrm{Re}\,\Sigma^{\mathrm{ret}}(\omega,k) = \Sigma^{\mathrm{mf}}(k) + \mathcal{P}\int_{-\infty}^{+\infty} \frac{d\omega'}{2\pi}\,\frac{\Gamma(\omega',k)}{\omega-\omega'} + \mathrm{const.} \tag{6.7}$$

As we have discussed in Section 3.5, the dispersive calculation of $\mathrm{Re}\,\Sigma^{\mathrm{ret}}$ should be favored over the direct calculation from the Feynman diagrams since it ensures that analyticity is preserved. The energy independent mean-field self-energy cannot be found dispersively and must be added explicitly. Note that the width will – due

to our choice of the short-range interaction – not vanish at large energies. This interferes with the convergence of the dispersion integral in (6.7). Thus, we will drop the dispersive part of $\mathrm{Re}\,\Sigma^{\mathrm{ret}}$, but not Σ^{mf}, in Section 6.1.2 to simplify the calculations.

Following the approach of Lehr et al. [LEL$^+$00], we will use a constant scattering amplitude in the integrals of Eq. (6.5). The details will be discussed in Section 6.1.2. While a (repulsive) constant coupling is a sensible approximation to the short-range part of the NN interaction, it cannot be used to describe the (attractive) long-range interactions. This means that the diagrams in the first line of Fig. 6.2 cannot be calculated using the same (simple) interaction as those in the second line. In [LEL$^+$00, LLLM02], this problem could be mostly ignored since calculations were performed only at $T = 0$ and $\rho = \rho_0$. Σ^{mf} was set to a constant value and absorbed into a redefined chemical potential. Here, however, we want to determine the temperature and density dependence of the short-range correlations to which long-range correlations contribute. To obtain consistent results at all T and ρ, we need a reliable description of the temperature, density, and momentum dependence of the mean-field.

A fully self-consistent (microscopic) approach that deals with the long-range and the short-range interactions in nuclear matter simultaneously requires the use of a more realistic – and more complicated – interaction model in the self-consistent calculation, see e.g. [Bȯz02, FM03]. This would, however, spoil the simple structure of our approach – which is its most appealing feature. On the other hand, the properties of nuclear matter have been investigated on the mean-field level in a variety of effective models that were adjusted to experimental and empirical data. The results of such an approach can be readily incorporated into our model.

The above considerations lead to the following two-step procedure: We determine $\Sigma^{\mathrm{mf}}(k, \rho, T)$ from a Skyrme-type energy-density functional (see [SR07] for a recent review) in the first step. This corresponds to a self-consistent calculation on the Hartree–Fock level. The details will be discussed below in Section 6.1.3. The short-range correlations are determined self-consistently in the second step, using a constant matrix element for the short-range interactions. The mean-field self-energy Σ^{mf} – that has been adjusted to experimental data – is kept fixed in this part of the calculation and is not be modified by short-range effects.

Our approach can be summarized by the two Dyson–Schwinger equations that are shown in Fig. 6.4: The equation in the first line generates the self-consistent (Hartree–Fock) mean-field propagator using a Skyrme-type interaction. In the second equation, this propagator is used as starting point to determine the full in-medium propagator – including the short-range correlations – from the Born diagrams. Note that we do not have to solve the first Dyson–Schwinger equation explicitly. This has already been done in the derivation of the Skyrme-type energy-density functional. The functional provides us with an effective mass $m^*(\rho)$ and an effective potential $U_{\mathrm{eff}}(\rho, T)$ that can be inserted into the full in-medium propagator (see Section 6.1.3).

The actual self-consistency problem, i.e. the second Dyson–Schwinger equation in Fig. 6.4, is given by the relations in Eqs. (6.2)–(6.7). Like in the quark case, this problem cannot be solved directly. Iterative procedures are the appropriate methods

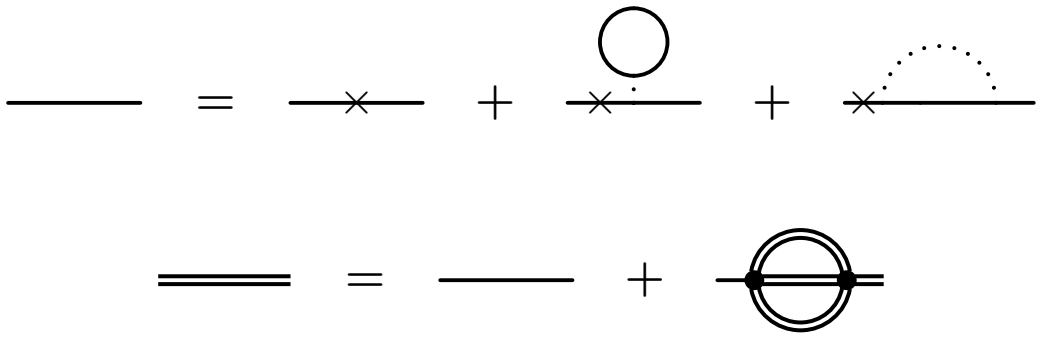

Figure 6.4: The Dyson–Schwinger equations corresponding to our approach. Free nucleons are denoted by lines marked with ×. Plain single lines denote the (Hartree–Fock) mean-field propagators, double lines denote the full in-medium propagators including the short-range effects. The dotted lines represent an effective long-range NN interaction while the solid dots stand for the constant scattering amplitude that is used to generate the short-range effects. Note that the sunset diagram in the second line combines the direct and the exchange Born diagram.

of solution. Hence, the spectral function is obtained by the following procedure: Starting with an initial guess for the width in the spectral function $\mathcal{A}(\omega, k)$, the integrals of Eq. (6.5) are solved (numerically) to find an improved approximation for the width Γ. Inserting this $\Gamma(\omega, k)$ into Eq. (6.2) yields an improved expression for the spectral function that is inserted into (6.5) again. This procedure can be repeated until convergence is achieved. In the language of Feynman diagrams, the solution of this self-consistency problem corresponds to the non-perturbative summation of a whole class of diagrams by reinserting the full in-medium Green's functions into the self-energies in the second line of Fig. 6.2. We conclude the presentation of the self-consistent procedure by illustrating this effect. Fig. 6.5 shows some examples of diagrams that are automatically resummed by our approach.

6.1.2 Short-range interactions

For a complete definition of our approach, we have to specify the scattering amplitude $\mathcal{M}$ in the collision integrals (6.5). Taking into account the observation of Lehr et al. [LEL$^+$00, LLLM02] that the short-range correlations primarily depend on global properties of the interactions on ranges of the (repulsive) vector meson masses and the available phase space, we will also use a constant matrix element in our calculations, corresponding to an effective zero-range contact interaction.

The value of $\mathcal{M}$ will be chosen independent of temperature and density of the system. It is noteworthy that until now a description of short-range correlations – including a fully self-consistent description of the interactions – is still pending, although first attempts in that direction have been made. In such calculations, e.g. by

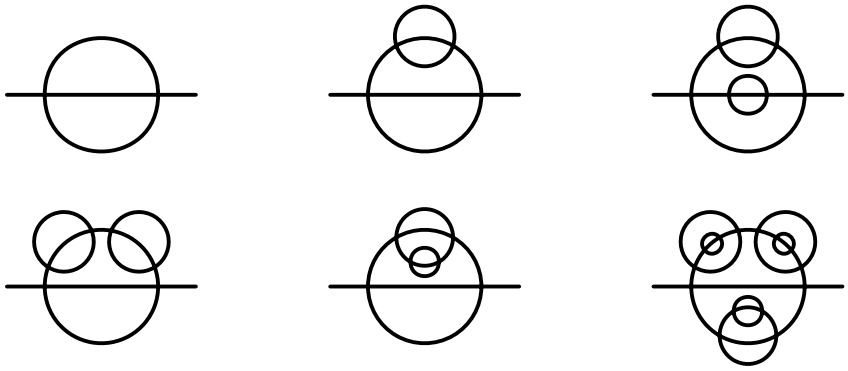

Figure 6.5: Some examples of diagrams that we sum up in our self-consistent calculation. This is neither a systematic not a complete compilation. The lines correspond to propagators that are dressed with the static mean-field self-energy only (cf. Fig. 6.4). When full in-medium propagators are used to calculate the elementary sunset diagram (left diagram in the first line), the other diagrams are resummed automatically.

the Rostock group [ARS+96] or, more recently, by Bożek [Bòz99, Bòz02] significant variations of the interactions with temperature are not obtained.

When a constant coupling is used, the integrals in (6.5) essentially sum up the phase space that is available for the collisions shown in Fig. 6.3. In Section 4.2.2, we have analyzed in detail where phase space opens and closes for the corresponding quark processes. The results of this analysis, that are summarized in Table 4.2, can be readily transfered to the present case. While process (b), corresponding to the quark process in Fig. 4.3(c), is – on the quasiparticle level at zero temperature – restricted to a finite energy range[1], there is no upper threshold for process (a), corresponding to the quark process in Fig. 4.3(a) (the threshold in Table 4.2 refers to the NJL cutoff that is not relevant here). This means that the nucleon width will not vanish at large energies but – due to the increasing phase space volume that becomes available for scattering – grows when the energy rises.

By physical reasons [Mac89] and in order to enforce the convergence of integrations involving $\mathcal{M}$ and extending over the space of $2p1h$ and $1p2h$ configurations, we will introduce a form factor into the collision integrals in Eq. (6.5). Lehr et al. had introduced a form factor in [LLLM02] that acts on the total energies and momenta of the collisions corresponding to Eq. (6.5),

$$F_{\mathrm{tot}}(\omega_{\mathrm{tot}}, \vec{k}_{\mathrm{tot}}) = \frac{\Lambda^4}{\Lambda^4 + \left(\omega_{\mathrm{tot}} + \frac{k_{\mathrm{tot}}^2}{4m_N}\right)^4}\,, \tag{6.8}$$

with $\omega_{\mathrm{tot}} = \omega + \omega_p$ and $\vec{k}_{\mathrm{tot}} = \vec{k} + \vec{p}$. Setting the value of Λ to the free nucleon mass

[1] The non-relativistic limit of the lower threshold for the process in Fig. 4.3(c) is given by $2\omega_F - (2k_F + k)^2/(2m) < \omega$.

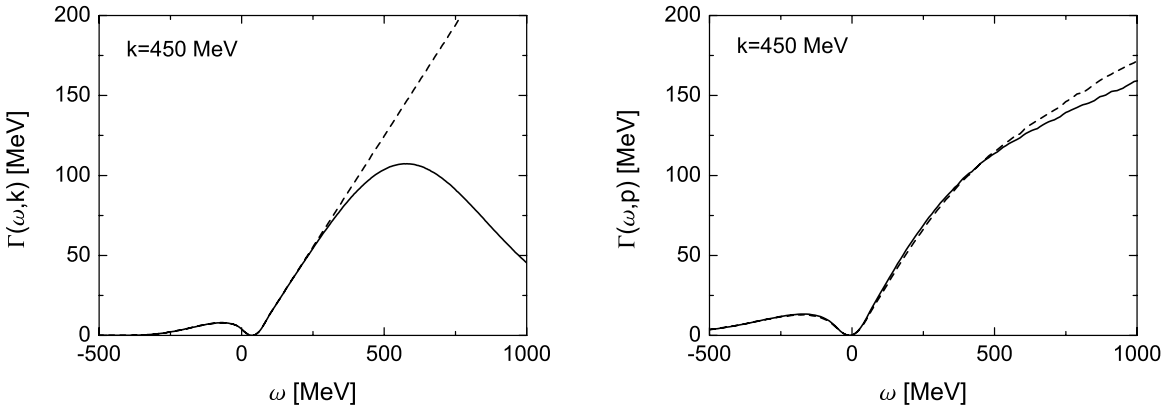

Figure 6.6: The influence of form factors on the nucleon width at $T = 0$ and $\rho = \rho_0$. The left panel shows results of Lehr et al. [LLLM02] for the nucleon width, calculated with (solid line) and without (dashed line) the form factor of Eq. (6.8), using $\Lambda = m_N = 938\,\mathrm{MeV}$. The right panel shows results of our calculations with (solid line) and without (dashed line) the t-channel form factor of Eq. (6.9), using $\Lambda = 1.2\,\mathrm{GeV}$, $m_\mu = 600\,\mathrm{MeV}$, and the constant scattering amplitude $(\overline{|\mathcal{M}|^2})^{1/2} = 309\,\mathrm{MeV\,fm}^3$. In all calculations, the dispersive real part of the retarded self-energy has been neglected.

m_N, this form factor did only affect the results for the nucleon width at energies considerably above the chemical potential (at $T = 0$ and $\rho = \rho_0$). For the occupied states below ω_F, the results remained unchanged in comparison to [LEL$^+$00] where no form factor was used.

The effect of the form factor F_{tot} on the results in [LLLM02] is shown in the left panel of Fig. 6.6. At large energies, the form factor (6.8) stops the increase of the width and turns it into a decrease. Due to the strong density dependence of the chemical potential (see Fig. 6.8), however, this form factor is not a sensible choice for our calculations. Let us briefly outline the problem (for $T = 0$): The chemical potential sets the lower energy limit for the (free) outgoing states that may contribute to collisions. The form factor F_{tot}, on the other hand, sets an upper energy limit. This limit is determined – independent of the chemical potential – by the choice of Λ. When raising the chemical potential in our calculations, the number of outgoing states (i.e., phase space) would shrink due to the (fixed) form factor. Consequently, we would observe a density dependent decrease of the short-range correlations. Note that we have investigated a similar effect for the quark width – induced by the cutoff of the NJL model[2] – in Section 4.3.1. Since such a density dependence is rather

[2]In the NJL model, the fixed cutoff also induces the chiral phase transition at higher densities. Such an effect is, however, out of question here. The form factor affects only the short-range correlations and not the long-range correlations that determine the bulk properties – like the effective mass – of the nucleons in the medium.

artificial, we must not use the form factor F_{tot} here.

Different to [LLLM02], we follow the common approach and use a form factor that acts in the t-channel and suppresses processes with large energy and momentum transfers:

$$F_{\mathrm{t}}(\omega_{\mathrm{t}}, \vec{k}_{\mathrm{t}}) = \frac{\Lambda^4}{\Lambda^4 + \left(m_\mu^2 - \omega_{\mathrm{t}}^2 + k_{\mathrm{t}}^2\right)^2}\,, \tag{6.9}$$

where $\omega_{\mathrm{t}} = \omega - \omega_q$ and $\vec{k}_{\mathrm{t}} = \vec{k} - \vec{q}$. The mass $m_\mu \sim \mathcal{O}(m_\rho)$ corresponds to the typical mass of a vector meson exchange in nucleon scattering processes and Λ defines the scale of the cutoff. F_{t} has been adapted from one of the form factors that have been introduced for K-matrix calculations in [FM98]. Note that this form factor has no poles on the real axis. Unlike the form factor in (6.8), F_{t} will not lead to a breakdown of the width at higher energies. It only stops the unlimited growth of $\Gamma(\omega, k)$. This effect is shown in the right panel[3] of Fig. 6.6.

The behavior of the form factor has consequences for the calculation of the dispersive real part of the self-energy $\mathrm{Re}\,\Sigma^{\mathrm{ret}}_{\mathrm{disp}} = \mathrm{Re}\,\Sigma^{\mathrm{ret}} - \Sigma^{\mathrm{mf}}$. The integral in (6.7) can only be solved numerically when Γ vanishes at large energies. The convergence of the dispersion integral may be improved in a subtracted dispersion relation [BD65]. We are presently not interested in contributions of the dispersive real part to the on-shell condition, i.e., the position of the on-shell peak should not be shifted by the collisional self-energies. Hence, it is possible to use a subtracted dispersion relation,

$$\begin{aligned}\mathrm{Re}\,\Sigma^{\mathrm{ret}}(\omega, k) &= \Sigma^{\mathrm{mf}}(k) \\ &+ \left(\frac{k^2}{2m} + \Sigma^{\mathrm{mf}}(k) - \omega\right)\ \mathcal{P}\int_{-\infty}^{+\infty} \frac{d\omega'}{2\pi} \frac{\Gamma(\omega', k)}{(\omega - \omega')(\frac{k^2}{2m} + \Sigma^{\mathrm{mf}}(k) - \omega')}\,,\end{aligned} \tag{6.10}$$

with the on-shell energy $k^2/2m + \Sigma^{\mathrm{mf}}$ as subtraction point.

Due to the additional factor $\sim 1/\omega'$, the integral on the rhs. of (6.10) has an improved convergence behavior. Checks have shown, however, that it would still be necessary to calculate the width up to very high energies – in comparison to the relevant contributions to the collisional self-energies in (6.5) – to obtain a stable result from the subtracted dispersion relation. In [LLLM02], the importance of the dispersive contributions was investigated by performing calculations with and without $\mathrm{Re}\,\Sigma^{\mathrm{ret}}_{\mathrm{disp}}$. Although analyticity is not conserved when $\mathrm{Re}\,\Sigma^{\mathrm{ret}}_{\mathrm{disp}}$ is neglected [LEL$^+$00], it was found that overall the results for the spectral functions did not change significantly. Taking advantage of this finding, we will ignore the dispersive part for the present investigations, thus simplifying the calculations considerably. For a full treatment of $\mathrm{Re}\,\Sigma^{\mathrm{ret}}_{\mathrm{disp}}$ we refer to [LLLM02] and [Leh03].

[3] Note that our results are not exactly equal to the results of Lehr et al., even when no form factor is used. For example, the width rises more slowly at large energies in our calculations. In contrast to the approach in [LEL$^+$00, LLLM02], we take the momentum dependence of the static mean-field into account by replacing the vacuum nucleon mass m with an effective mass m^* in the spectral function (6.2), see Eq. (6.11) and Fig. 6.8. This leads to the observed discrepancies.

6.1.3 Mean-field self-energy

In this section we will show how the static mean-field is obtained from a Skyrme-type energy-density functional. We begin our discussion by rewriting the first term in the denominator of the spectral function (6.2). Expanding the temperature, density, and momentum dependent mean-field self-energy up to $\mathcal{O}(k^2)$ yields

$$\Sigma^{\mathrm{mf}}(k,\rho,T) \approx \Sigma^{\mathrm{mf}}(k_F,\rho,T) + (k^2-k_F^2)\Sigma^{\mathrm{mf}\prime}(k_F,\rho,T) + \dots\,,$$

where k_F is the Fermi momentum. The momentum dependent part of Σ^{mf} can then be absorbed into the kinetic energy term in the denominator of (6.2) by introducing a density dependent effective mass $\frac{1}{m^*} = \frac{1}{m}(1+2m\Sigma^{\mathrm{mf}\prime})$, as successfully used, e.g., in Skyrme density functionals [SCM76, BFvGQ75, VB72]. We get

$$\frac{k^2}{2m} + \Sigma^{\mathrm{mf}}(k,\rho,T) + \mathrm{Re}\,\Sigma^{\mathrm{ret}}_{\mathrm{disp}}(\omega,k) \;\cong\; \frac{k^2}{2m^*} + U_{\mathrm{eff}}(\rho,T) + \mathrm{Re}\,\Sigma^{\mathrm{ret}}_{\mathrm{disp}}(\omega,k)\,, \qquad (6.11)$$

where the effective potential U_{eff} is the momentum independent part of Σ^{mf} and $\mathrm{Re}\,\Sigma^{\mathrm{ret}}_{\mathrm{disp}}$ denotes the dispersive real part of the retarded self-energy that can be obtained from the integral on the rhs. of Eq. (6.10).

The net effect of the potential U_{eff} is a temperature and density dependent energy shift of the pole structure of the single-particle propagator and hence the spectral function. The on-shell energy of the nucleons in the medium is determined by the rhs. of (6.11), cf. (6.2). When a subtracted dispersion relation (6.10) is used or the dispersive real part is neglected, as discussed in Section 6.1.2, we find

$$\omega_{\mathrm{os}}(k) = \frac{k^2}{2m^*} + U_{\mathrm{eff}}(\rho,T)\,, \qquad (6.12)$$

even when short-range correlations are present. For the single-particle spectral function on the quasiparticle level, Eq. (6.11) yields

$$\mathcal{A}_{\mathrm{qp}}(\omega,k) = 2\pi\delta\left(\omega - \frac{k^2}{2m^*} - U_{\mathrm{eff}}(\rho,T)\right)\,. \qquad (6.13)$$

The temperature and density dependence of the single-particle potential in nuclear matter has been studied before microscopically, ranging from self-consistent Brueckner and Brueckner Hartree–Fock approaches e.g. in [ARS+96, dJL97] to the variational calculations with 2- and 3-body forces by the Urbana group [Wir88, FP81]. In a different context, the density and momentum dependence of the variational mean-field was studied in [Wir88]. A reanalysis of these rather involved mean-field results by a second order polynomial in $k^2-k_F^2$ leads to an almost perfect description of the momentum dependence with an effective mass of $m^*/m = 0.69$. This confirms the effective mass approach utilized in Eq. (6.11). These findings also confirm the use of a schematic description of the mean-field part, in particular so because the static

parts of the self-energy are canceled to a large extent in dynamical quantities like propagators. Hence, we have decided to describe the mean-field in a Skyrme model [Sky59, VB72, BFvGQ75] for the sake of a most transparent and simple approach. By this choice thermodynamical consistency is ensured by fulfilling the Hugenholtz-van Hove theorem [HvH58] at mean-field level.

Effective Skyrme-type interactions are typically used for the investigation of nuclei in self-consistent Hartree–Fock calculations. The interactions are constructed from central, non-local, density dependent and spin–orbit terms that incorporate a set of $6-10$ free parameters [CBH$^+$97]. When infinite (isospin) symmetric nuclear matter is considered, the spin and isospin dependent parts as well as the non-local parts of the interaction can be dropped. Thus, we find for the Skyrme energy-density functional in standard notation [VB72, BFvGQ75]:

$$\mathcal{H}(\rho,\tau) = \frac{\tau}{2m} + \frac{3}{8}t_0\rho^2 + \frac{1}{16}(3t_1+5t_2)\rho\tau + \frac{1}{16}t_3\rho^3\,, \tag{6.14}$$

where t_0, t_1, t_2, and t_3 are parameters of the Skyrme interaction. ρ and τ are the (quasiparticle) nucleon density and the kinetic energy density, respectively. At finite temperatures they are given by

$$\begin{aligned}\rho(\omega_F,T) &= g\int\limits_{-\infty}^{+\infty}\frac{d\omega d^3k}{(2\pi)^4}\mathcal{A}(\omega,k)\mathrm{n_F}(\omega,T)\,,\\ \tau(\omega_F,T) &= g\int\limits_{-\infty}^{+\infty}\frac{d\omega d^3k}{(2\pi)^4}k^2\mathcal{A}(\omega,k)\mathrm{n_F}(\omega,T)\,.\end{aligned}$$

Inserting the quasiparticle spectral function from Eq. (6.13) yields

$$\begin{aligned}\rho(\omega_F,T) &= \frac{g}{2\pi^2}\int\limits_0^\infty dk k^2\ \frac{1}{e^{(k^2-k_F^2)/2m^*T}+1} \quad \left(\xrightarrow{T=0}\frac{2}{3\pi^2}k_F^3\right)\,,\\ \tau(\omega_F,T) &= \frac{g}{2\pi^2}\int\limits_0^\infty dk k^2\ \frac{k^2}{e^{(k^2-k_F^2)/2m^*T}+1} \quad \left(\xrightarrow{T=0}\frac{2}{5\pi^2}k_F^5\right)\,,\end{aligned} \tag{6.15}$$

with the Fermi momentum $k_F^2 = 2m^*(\omega_F - U_{\text{eff}})$. Note that we do not consider a temperature dependence of the Skyrme parameters [SCM76]. Thus, $\mathcal{H}$ is not explicitly temperature dependent. An indirect temperature dependence is, however, introduced by the densities ρ and τ.

From the energy-density functional $\mathcal{H}$ in (6.14), we readily obtain the effective potential and the effective nucleon mass in infinite symmetric nuclear matter [SCM76],

$$\begin{aligned}U_{\text{eff}}(\rho,T) &= \frac{\partial\mathcal{H}}{\partial\rho} = \frac{3}{4}t_0\rho + \frac{1}{16}(3t_1+5t_2)\tau + \frac{3}{16}t_3\rho^2\,,\\ \frac{1}{2m^*(\rho)} &= \frac{\partial\mathcal{H}}{\partial\tau} = \frac{1}{2m} + \frac{1}{16}(3t_1+5t_2)\rho\,.\end{aligned} \tag{6.16}$$

Table 6.1: The parameters of the Skyrme force SIII' [SCM76, BFvGQ75] used in the calculations. For completeness this table also contains the spin-interaction parameter x_0 and the spin-orbit parameter W_0.

t_0 [MeV fm^3]	t_1 [MeV fm^5]	t_2 [MeV fm^5]	t_3 [MeV fm^6]	x_0	W_0 [MeV fm^5]
-1133.4	395	-95	14000	0.49	120

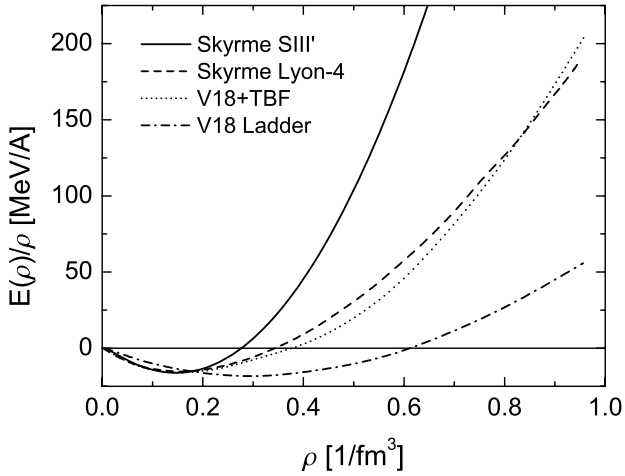

Figure 6.7: The nuclear equation of state for cold ($T = 0$) symmetric matter as a function of the total density, based on the set of parameters given in Table 6.1 (solid line). Results obtained with the Lyon-4 Skyrme energy-density functional [CBH$^+$98] and the variational many-body approach of Akmal et al. [APR98] are compared.

The effective mass m^* depends only on ρ and not on τ. Thus, m^* is temperature independent when the density is fixed. Furthermore, we find for the energy per nucleon

$$\frac{E}{A} = \frac{\mathcal{H}}{\rho} = \frac{1}{2m}\frac{\tau}{\rho} + \frac{3}{8}t_0\rho + \frac{1}{16}t_3\rho^2 + \frac{1}{16}(3t_1 + 5t_2)\tau\,. \tag{6.17}$$

In our calculations, we will use the parameter set SIII' from [SCM76, BFvGQ75]. The parameters are listed Table 6.1. The resulting equation of state for cold symmetric nuclear matter is displayed in Fig. 6.7. For comparison, we also show the Lyon-4 parametrization [CBH$^+$98] and variational calculations of the Urbana group [APR98].

From Fig. 6.7 it is seen that nuclear matter ceases to be bound beyond a critical density $\rho_c(T) > \rho_0$ where the repulsive kinetic energy term overrules the nuclear

attraction. For the processes in heavy ion collisions and supernova explosions this is, however, not a crucial problem. The core collapse of a supernova is not driven by nuclear, but by gravitational forces. Eventually, the repulsive nuclear potential even stops the collapse when several times nuclear matter density is reached.

At the end of this section, we take a brief look at the last term of the Skyrme energy-density functional $\mathcal{H}$ in Eq. (6.14). This term corresponds to a density dependent interaction $\sim t_3\rho\delta(\vec{r}-\vec{r}')$ and provides saturation [SR07]. In other words, this term represents a repulsive short-range interaction. Thus, it is interesting to compare the scattering amplitude of our approach to the scattering amplitude that is generated by this interaction. Calculating $\partial^2\mathcal{H}/\partial\rho^2$ and multiplying with 1/4 (our scattering amplitude has been averaged over spin and isospin, cf. [KLM05]) yields $\mathcal{M} = \frac{3t_3}{32}\rho$. For a density of ρ_0, we obtain the numerical value $\mathcal{M} = 223\,\mathrm{MeV\,fm^3}$. This result supports the choice of the scattering amplitude in our calculation: By comparison to other calculations, we will obtain a – density independent – value of $309\,\mathrm{MeV\,fm^3}$ that differs by less than 30% from the Skyrme result.

6.2 Numerical Details and Results

6.2.1 Details of the calculation

We have investigated the nucleon spectral function in nuclear matter at temperatures from 0 to 70 MeV and at densities from the saturation density ρ_0 up to $3\rho_0$ ($\rho_0 = 0.16\,\mathrm{fm^{-3}}$) in our self-consistent approach. The numerical calculations have been performed on a grid in energy and momentum space, where we store the results for the nucleon width. This grid covers an energy range of $-0.5\,\mathrm{GeV} < \omega - \omega_F < 0.5\,\mathrm{GeV}$ and a momentum range of $|\vec{k}| < 1.25\,\mathrm{GeV}$. With 130×120 grid points we achieve a resolution of $d\omega = 8\,\mathrm{MeV}$ and $dk = 10.5\,\mathrm{MeV}$ for energy and momentum, respectively. A variation of the grid borders and the mesh size has shown that the chosen setup of the grid has no influence on the results at energies in the vicinity of the chemical potential and below (i.e., the populated states). The convergence of the iterative calculations – that are initialized with a constant width of 10 MeV – can be compared to that of the quark calculations that is shown in Fig. 5.2. Self-consistency is typically reached after 4-5 iterations.

We have used the Skyrme force SIII' [SCM76, BFvGQ75] to generate a mean-field potential U_{eff} and an effective mass m^*, cf. (6.11,6.16). The corresponding set of parameters is given in Table 6.1. In infinite nuclear matter at zero temperature, we find for this choice of parameters a binding energy of $-16.1\,\mathrm{MeV}$ and a mass ratio of $m^*/m = 0.76$ at a Fermi momentum of $k_F = 254\,\mathrm{MeV}$ ($\rho = \rho_0$). For the mean-field potential, a value of $U_{\mathrm{eff}} = -61.6\,\mathrm{MeV}$ is found. Compared to the variational results of Wiringa [Wir88], the saturation properties are slightly different with an equilibrium point shifted to a somewhat lower density. The larger effective mass indicates a weaker momentum dependence of the SIII' interaction.

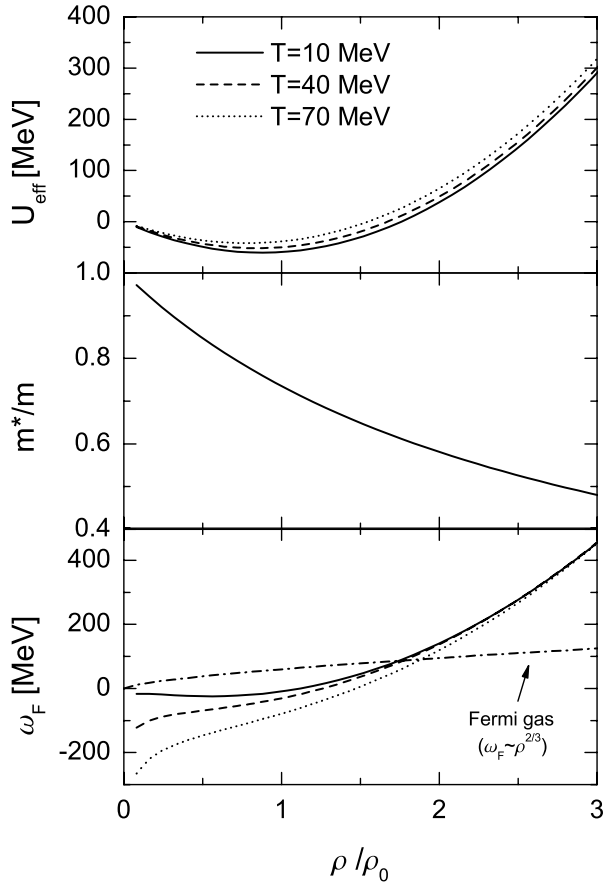

Figure 6.8: The effective potential U_{eff}, the mass ratio m^*/m, and the chemical potential ω_F as functions of the (quasiparticle) density at several temperatures. The Skyrme SIII' interaction, cf. Table 6.1, has been used in the calculation. For comparison, we also show the chemical potential of a free Fermi gas at zero temperature in the lowest panel (for a constant mass of 600 MeV).

In Fig. 6.8, we show the temperatures and density dependence of U_{eff}, m^*/m, and the chemical potential ω_F. The effective mass is not temperature dependent since it depends only on ρ but not on τ, cf. (6.16). The temperature dependence of U_{eff} remains weak in comparison to the density dependence. This reflects the fact that the temperature does not enter the Skyrme energy-density functional explicitly. U_{eff} vanishes – as expected – at zero density while the effective mass approaches the vacuum nucleon mass. The chemical potential drops significantly at low densities when the temperature becomes larger. This behavior is connected to the fact that an increasing number of states above ω_F is populated when the temperature rises. Consequently, at higher temperatures the same nucleon density is reached at lower chemical potentials. We note that the Skyrme mean-field strongly modifies the density

dependence of the chemical potential in comparison to a free Fermi gas ($U_{\text{eff}} = 0$, $m^* = \text{const.}$), where $\rho \sim k_F^3$ and thus $\omega_F \sim \rho^{2/3}$ (for $T = 0$, cf. Eqs. (6.15,6.12)).

For technical reasons, we keep the chemical potential (and U_{eff},m^*) and not the density fixed in our calculations[4]. Off-shell contributions will shift strength away from the on-shell peaks of the (normalized) spectral function. In part, this strength will be shifted across the chemical potential. Thus, it is likely that the quasiparticle density (6.15) and the density that is calculated from the full in-medium spectral function of our approach,

$$\rho(\omega_F, T) = g \int_{-\infty}^{+\infty} \frac{d\omega d^3k}{(2\pi)^4} \mathcal{A}(\omega, k) \mathrm{n_F}(\omega) \,, \tag{6.18}$$

are not exactly equal for the same chemical potential. Our numerical results show, however, that the discrepancies do not become too large. The densities differ by less than 15% at low T and by less than 3% at higher temperatures. Thus, we determine $U_{\text{eff}}(\rho, T)$, $m^*(\rho)$ and $\omega_F(\rho, T)$ such that the desired density is obtained on the quasiparticle level (6.15). We do not readjust them to correct the density in the full calculation.

The averaged scattering amplitude in Eq. (6.5) has been adjusted to a value of $(\overline{|\mathcal{M}|^2})^{1/2} = 309\,\text{MeV}\,\text{fm}^3$, so that the results of the many-body calculations of Benhar et al. [BFF89, BFF92] and Baldo et al. [BBG$^+$92] for $T = 0$ are reproduced. Note that this value differs from the one used in [LEL$^+$00, LLLM02] – where no effective mass was introduced – by a factor $m/m^* \approx 1.4$. The cutoff parameter Λ of the form factor (6.9) was set to 1.2 GeV and the mass m_μ to 600 MeV.

To verify that our choice for the parameters is reasonable, we compare the on-shell width

$$\Gamma_{\text{os}}(\omega) = \Gamma(\omega, k_{\text{os}}(\omega)) \,, \tag{6.19}$$

where $k_{\text{os}}(\omega) = [2m^*(\omega - U_{\text{eff}}(k_{\text{os}}))]^{1/2}$, and the momentum distribution

$$n(k, T) = \int_{-\infty}^{+\infty} \frac{d\omega}{2\pi} \mathcal{A}(\omega, k) \mathrm{n_F}(\omega) \tag{6.20}$$

from our calculation to the results of Benhar et al. and Baldo et al. In Fig. 6.9, the on-shell widths and momentum distributions are shown for normal nuclear matter density and $T = 0$. As we can see, our result for the on-shell width is in good agreement with the result of Baldo and in qualitative agreement with the sophisticated many-body calculation of Benhar. Our result for the momentum distribution[5] is

[4] The numerical calculations are more stable and converge faster when the chemical potential does not change during the iterations.

[5] The high-momentum tail that sums up the off-shell strength of the spectral function above the Fermi momentum can be interpreted as a universal measure for the short-range correlations, recall the discussion in Section 5.7

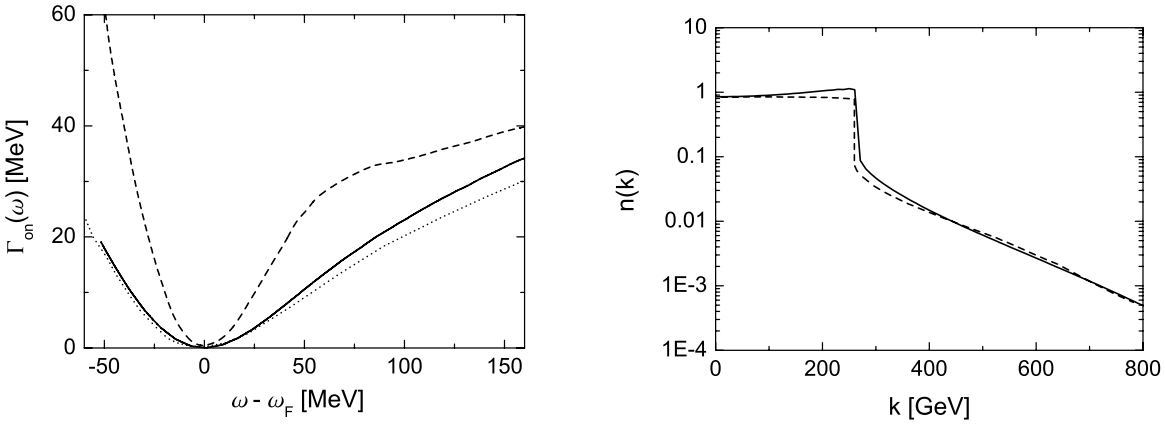

Figure 6.9: The on-shell width $\Gamma_{\rm os}(\omega)$ as a function of $\omega - \omega_F$ (left panel) and the momentum distribution in nuclear matter (right panel). Both panels show results for $T = 0$ and normal nuclear matter density. Solid lines show the results of our calculation, dashed lines the results of Benhar et al. [BFF89, BFF92]. The dotted line shows the result for the on-shell width of Baldo et al. [BBG$^+$92].

even in quantitative agreement with the Benhar result. Note that the considerable discrepancies between the results of Baldo and Benhar have been explained in [BFF89, BFF92] by the differences in the Argonne and the Urbana NN interactions that are employed in the calculations (the Argonne v14 potential has a much stronger tensor force).

6.2.2 Comparison to phenomenological NN potentials at T = 0

Before we discuss the results of our calculations at finite temperatures and high densities, let us briefly comment on the quality of phenomenological NN potentials at short interaction ranges in comparison to an averaged matrix element. The many-body results in Fig. 6.9 indicate that the use of a (so-called) realistic NN potential does not automatically lead to an unambiguous result for the short-range correlations. Phenomenological potentials have recently been used in fully microscopic approaches to nuclear matter, where they generate both, the long- and the short-range correlations. Fig. 6.10 shows cuts of the nucleon width at constant momenta that have been obtained by Bożek and collaborators [Bòz02, BC03, BDM06] using several realistic potentials in self-consistent T-matrix approaches. The results of our approach are shown for comparison.

As expected at zero temperature (see the comment below Eq. (6.6)), the curves in Fig. 6.10 drop to zero at the Fermi energy ($\omega_F \approx 0$). This is a kinematical constraint that must be satisfied in all calculations. We can see that the NN potentials lead to results that are in qualitative agreement at energies below and slightly above the chemical potential. At higher energies, the results differ qualitatively. While the

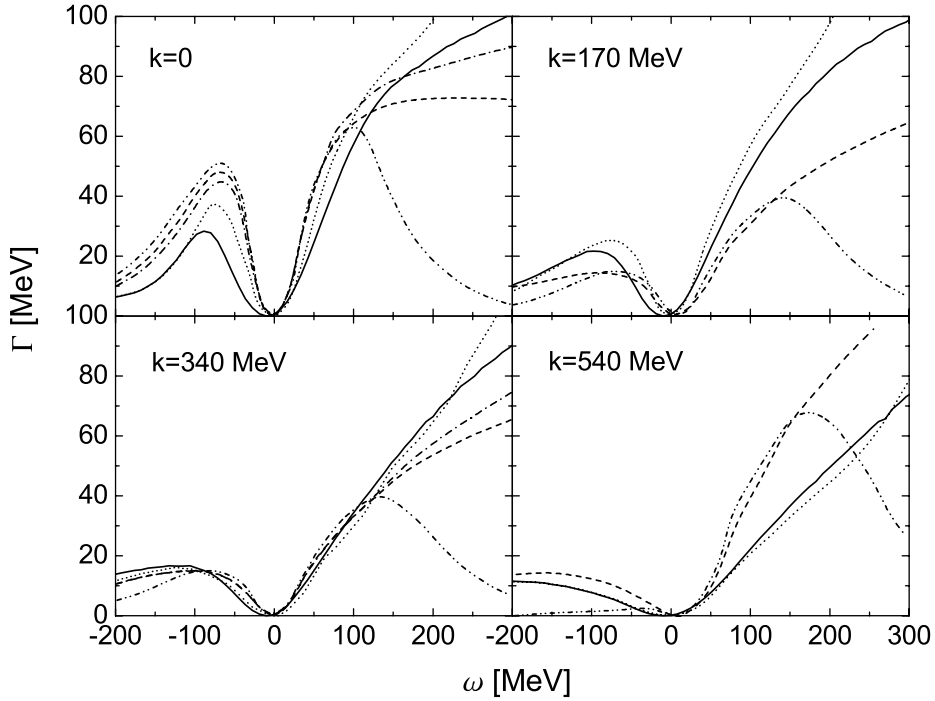

Figure 6.10: Results for the nucleon width at $T = 0$ and $\rho = \rho_0$, using different NN potentials in the calculation. The solid lines indicate the results of our approach that is described in the text. The other lines show results of the fully self-consistent T-matrix approaches found in [Bòz02, BC03, BDM06], using the Paris (dotted lines), the CD-Bonn (dashed lines), the Nijmegen (dash-dotted lines, not in all panels), and a $V_{\text{low k}}$ potential [BKS03] (dash-dot-dotted lines).

width drops for the $V_{\text{low k}}$ potential at all momenta and seems at least to saturate for the CD-Bonn potential at the lowest momentum, it grows for the other potentials when the energy rises. The quantitative differences that can be observed are of considerable size at all energies. It should also be noted that the discrepancies between the potentials are momentum dependent. For example, the CD-Bonn potential yields a smaller width than the Paris potential for $k = 170\,\text{MeV}$ but a larger width for $k = 540\,\text{MeV}$.

The reason for the deviations of the results in Fig. 6.10 is readily found. The empirical nucleon–nucleon interactions are adjusted to experimental NN data. This ensures that they agree in their predictions of on-shell quantities, as e.g. free space NN scattering phase shifts. Due to the lack of experimental data, however, the interactions may differ in the off-shell regions that are relevant for the short-range correlations.

The fact that the short-range components of phenomenological nucleon–nucleon interactions are poorly constrained has also been observed in a completely different

context: In [FJDR05], the possibility of bound deuteron-like states of nucleons and heavy flavor hyperons – like the recently discovered Ξ_{cc} [M$^+$02, O$^+$05] – has been explored. For that purpose, several NN potentials were rescaled on the quark level (using their representation in terms of spin and isospin operators that have well defined expectation values in the quark model), so that only the light flavor quarks participate in the interaction of the two-baryon system. Due to the larger mass, the double charm hyperons in a deuteron-like state come much closer to each other than nucleons in the deuteron. Thus, the calculations in [FJDR05] did mainly probe the short-range part of the NN interactions. It was found that the results are only of qualitative value. The large variations in the short-range interactions led to a considerable scattering of the obtained binding energies.

Fig. 6.10 shows that the results of our simple approach (constant matrix element with form factor on the $2p1h$ and $1p2h$ level plus effective Skyrme-type mean-field) are qualitatively in good agreement with the other results at all energies and momenta. In particular, the Paris potential yields a very similar nucleon width. This agreement confirms the observation in [LEL$^+$00, LLLM02] that the short-range correlations in nuclear matter are mainly determined by the overall strength of the interaction and the collisional phase space. Most of the fluctuations in the off-shell structure of the width in Fig. 6.10 should disappear when integrated quantities – like the momentum distribution or the averaged width (6.21) that we will consider below – are investigated. For a qualitative study of the temperature and density dependence of the short-range correlations, it is thus perfectly justified to approximate the short-range interactions by an averaged (constant) matrix element as long as the static mean-field is taken into account separately.

6.2.3 Spectral function and width

In the following, we will show the results of our calculations and investigate the density and temperature dependence of the short-range correlations. First, we present cuts of the nucleon spectral function and the corresponding width at constant momenta. This illustrates the general role of temperature and density. Fig. 6.11 shows the spectral function for temperatures of 0, 10 and 50 MeV at normal nuclear matter density. The broadened quasiparticle peak is the most prominent feature of the spectral function. At the lower momentum it is located below and at the higher momentum above the chemical potential. We can also see that the width becomes very large at high energies due to the opening of phase space that has been discussed in Section 6.1.2.

The spectral function as well as the width drop to zero at the chemical potential when the temperature is zero. The states at the Fermi energy are stable in cold nuclear matter since it is – due to kinematical constraints – not possible to scatter into or out of those states. The effect of rising the temperature is clearly visible. The gap at the Fermi energy gets smeared out for $T = 10$ MeV and has almost vanished at $T = 50$ MeV. This phenomenon is directly related to the fact that for non-vanishing T – in contrast to a system at zero temperature – states at energies above

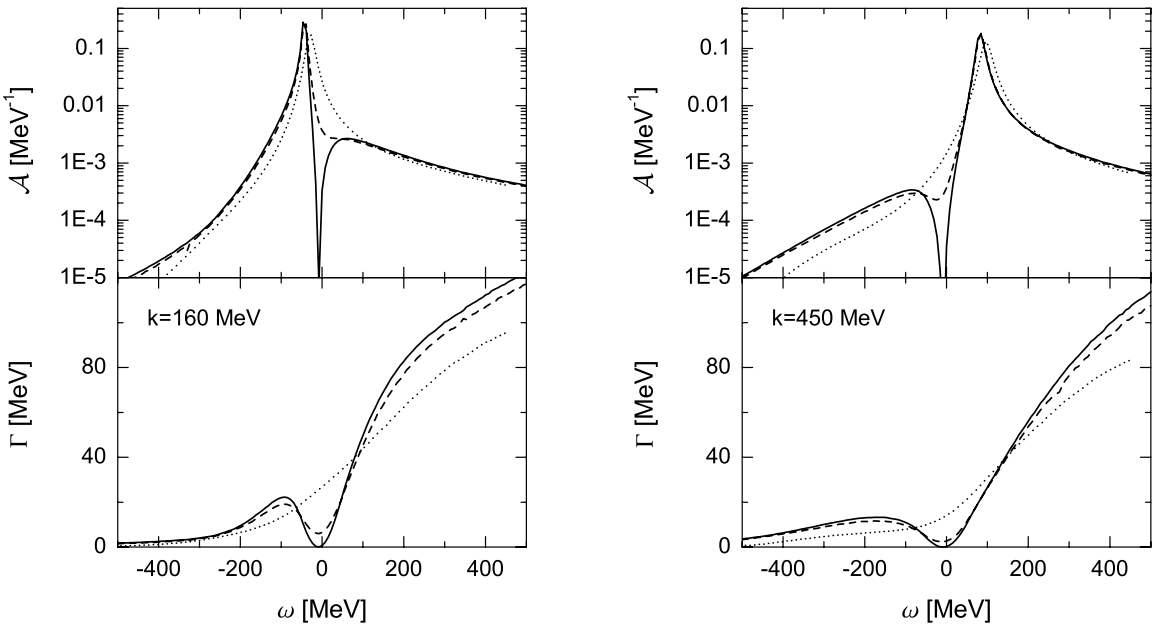

Figure 6.11: The nucleon spectral function at $T = 0\,\mathrm{MeV}$ (solid line), $T = 10\,\mathrm{MeV}$ (dashed line) and $T = 50\,\mathrm{MeV}$ (dotted line) for normal nuclear matter density. All cuts were made at constant momenta.

ω_F are populated. The states at the Fermi surface cease to be stable quasiparticles. Concerning the temperature dependence of the width we note that Γ rises only in the vicinity of the Fermi energy while it drops in the other regions at higher temperatures.

In Fig. 6.12, the spectral function and the width are shown for three different densities at a constant temperature of 10 MeV. Since the chemical potential and the effective mass depend on the density (cf. Fig. 6.8), the three curves are shifted along the energy axis. One should not get confused by the observation that the on-shell peak at the highest density is broader than the peaks at the lower densities in the left panel and narrower than those peaks in the right panel. We can understand this effect from the width that is shown in the lower panels of Fig. 6.12: At the higher momentum, the on-shell peak lies closer to the Fermi energy for the highest density. This induces a stronger suppression of the on-shell peak than in the other cases. We note that the overall result suggests that the width is strongly density dependent and rises at higher densities.

6.2.4 On-shell width

Figs. 6.11 and 6.12 give a first impression of the spectral functions and the collisional widths. To investigate the temperature and density dependence of the short-range correlations on a qualitative level, however, we use the better suited on-shell width

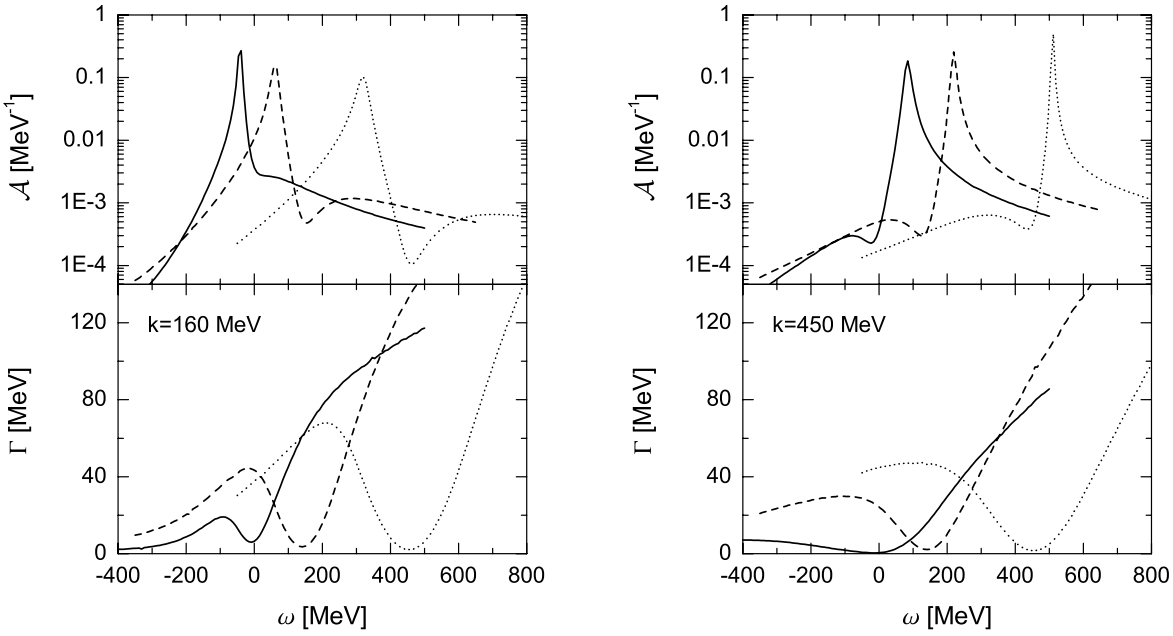

Figure 6.12: The nucleon spectral function for normal nuclear matter density (solid line), a two times higher density (dashed line), and a three times higher density (dotted line) at $T = 10\,\mathrm{MeV}$. All cuts were made at constant momenta. (The curves end at the border of the numerical grid that has been used in the calculation.)

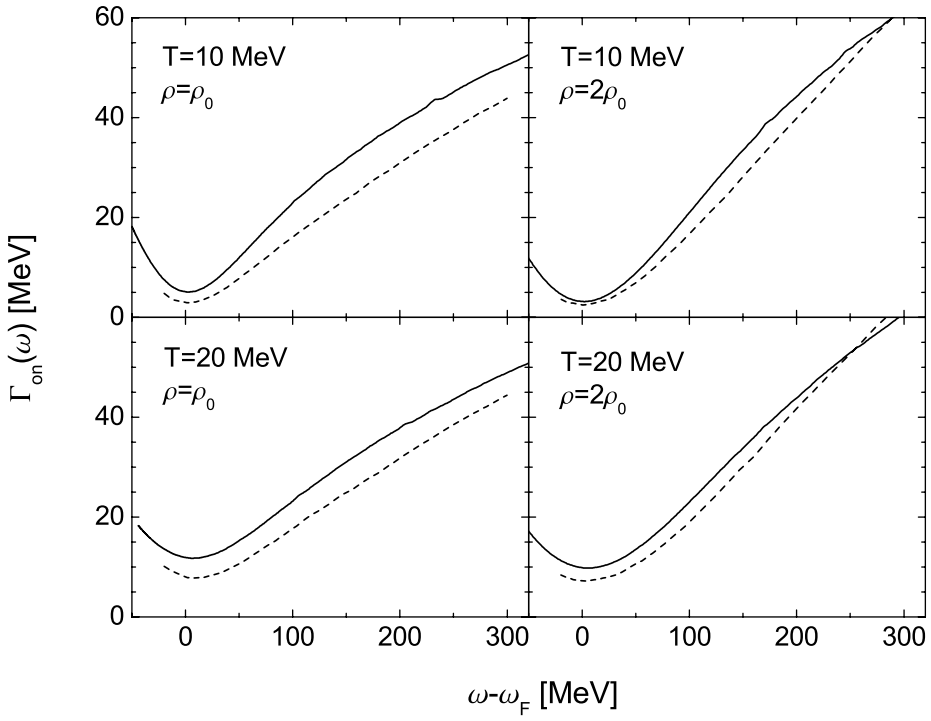

Figure 6.13: The on-shell width $\Gamma_{\rm os}(\omega)$ as a function of $\omega - \omega_F$ for two temperatures and densities. The solid lines show the results of our calculations, the dashed lines show the results of Alvarez-Ruso et al. [ARFdCO96].

of the spectral function, $\Gamma_{\rm os}(\omega)$, that has been introduced in Eq. (6.19). This allows us also to compare our results to other calculations that have been performed at temperatures up to 20 MeV and densities up to $2\rho_0$ [ARFdCO96, Bȯz99].

In Fig. 6.13 we show our results for $\Gamma_{\rm os}(\omega)$ at temperatures of 10 and 20 MeV and densities of ρ_0 and $2\,\rho_0$. Also shown are results of Alvarez-Ruso et al. [ARFdCO96]. In their "semi-phenomenological" approach they have – similar to our model – evaluated second order diagrams, taking the magnitude of the NN interaction from experiment. However, they did not perform their calculations self-consistently and did not consider long-range contributions from the mean-field. As we have already seen in Figs. 6.11 and 6.12, the width of the states at the Fermi surface does not drop to zero for finite temperatures. Increasing the temperature leads to larger values of $\Gamma_{\rm os}$ in the vicinity of the Fermi surface while the size and the shape of $\Gamma_{\rm os}$ do not change significantly at higher energies. Increasing the density shows the opposite effect. $\Gamma_{\rm os}$ is left unchanged in the vicinity of the Fermi surface while the slope at high energies increases.

Compared to [ARFdCO96], our results seem to be shifted by a few MeV to higher values of $\Gamma_{\rm os}$. The shift can be explained by the differences in the NN interactions that were used in both calculations[6]. The shape of the curves is in good agreement

[6]Using the low-density approximation $\Gamma = \rho\sigma v$, Alvarez-Ruso et al. have related their scattering

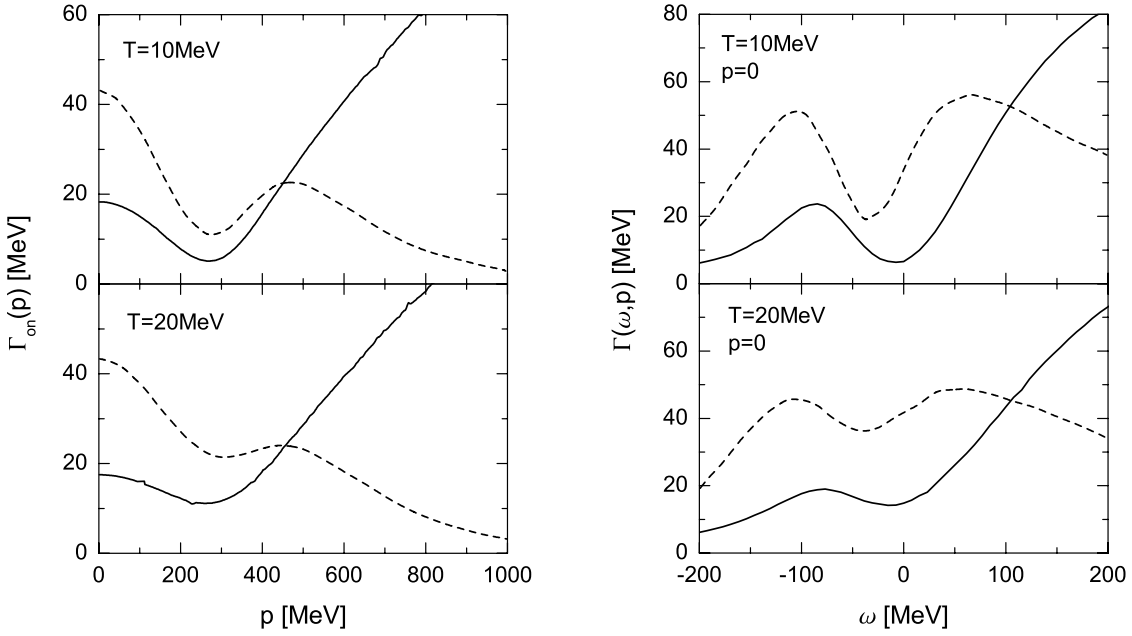

Figure 6.14: On-shell (left panel) and off-shell (right panel) results for the nucleon width at saturation density ρ_0 in the fully self-consistent T-matrix approach of Bożek [Bòz99] (dashed lines) in comparison to the results of our approach (solid lines).

for $\omega - \omega_F < 150\,\mathrm{MeV}$. At higher energies the form factor that was used in our calculations affects the shape of Γ_{os}, e.g. leading to the observed curvature in our results.

In Fig. 6.14, we compare our results for the nucleon width at $T = 10, 20\,\mathrm{MeV}$ and $\rho = \rho_0$ to the results of Bożek in [Bòz99]. Qualitatively, our results are similar to those obtained in the self-consistent T-matrix approach (using a first-rank Yamaguchi potential [Yam54]) below and not too far above the chemical potential where the populated states are located. The curves differ mainly by factor of 2 in this region. At higher energies, however, significant differences are found. The deviations range within the uncertainties introduced by using different nucleon-nucleon interactions in fully microscopic calculations that we have discussed in Section 6.1.2. Similar observations can be found in [Bòz02] where results of different approaches – including [LEL$^+$00] and [Bòz99] – are compared.

amplitude to the elastic NN cross-section σ_{NN}, i.e. $|\mathcal{M}|^2 = 4\pi\sigma_{\mathrm{NN}}/m^2$. Inserting the empirical value $\sigma_{\mathrm{NN}} = 20\,\mathrm{mb}$ [CMV81, Eff99] and $m = 938\,\mathrm{MeV}$ yields $|\mathcal{M}| = 207\,\mathrm{MeV\,fm^3}$. This value is close to the one used in [LEL$^+$00], where – like in [ARFdCO96] – no effective mass has been introduced. Replacing the vacuum nucleon mass m by the effective nucleon mass m^* of our approach, we obtain $|\mathcal{M}| \approx 270\,\mathrm{MeV\,fm^3}$ at a density of ρ_0, i.e. a scattering amplitude that is 10% smaller than the one in our calculation. Since m^* drops, the difference becomes smaller at higher densities.

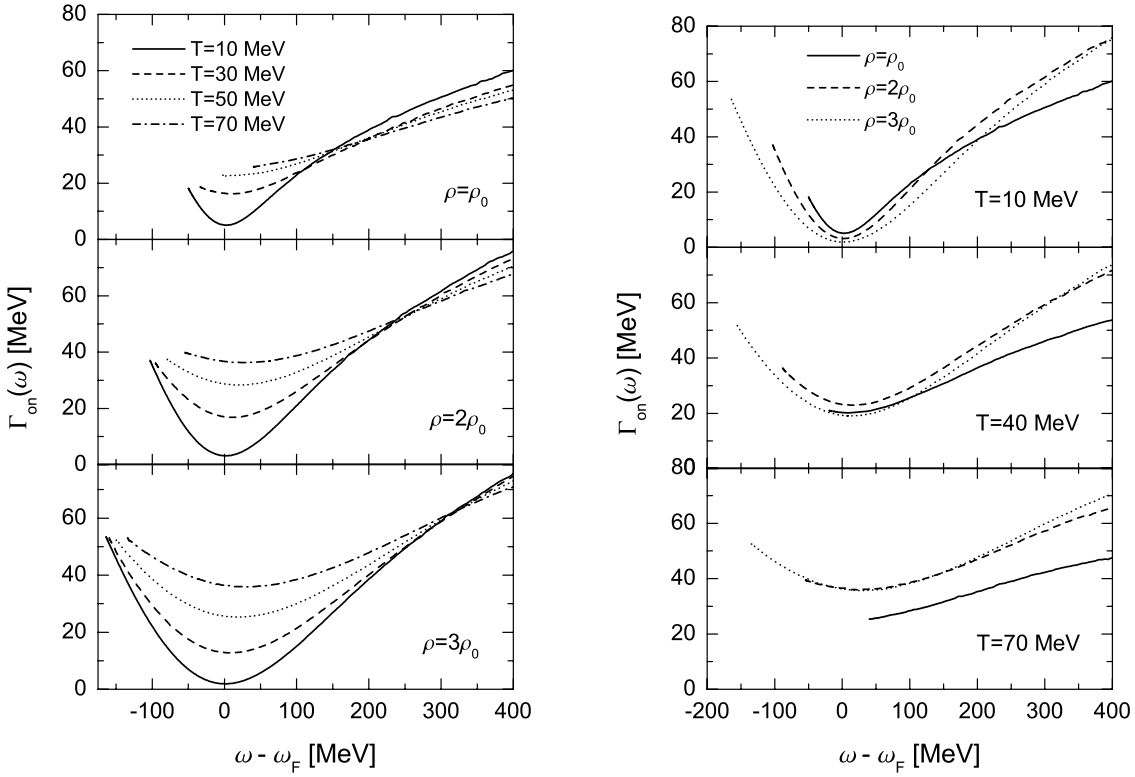

Figure 6.15: The on-shell width $\Gamma_{\rm os}(\omega)$ as a function of $\omega - \omega_F$ for different temperatures and densities.

We can conclude from the comparison to the results of Alvarez-Ruso et al. and Bożek that our calculations yield a reasonable temperature and density dependence of the nucleon width and thus the short-range correlations at moderate T and ρ. This should still be the case at higher temperatures and densities. The quantitative deviations observed in Figs. 6.13 and 6.14 (and in Fig. 6.10) show that an investigation of the density and temperature dependence of the short-range correlations must be performed consistently within a single approach. The combination of the results from different approaches (at different temperature and densities) will not necessarily lead to meaningful results.

In Fig. 6.15, we illustrate the temperature and the density dependence of the on-shell width in our approach. The shown results cover the full T and ρ range of our calculations[7] . The most significant effect that can be observed in the left panel of Fig. 6.15 is the filling of the gap at the Fermi energy when the temperature rises. Since most of the populated states are located in the vicinity of the chemical potential (we will come back to that point below), this effect suggests a strong temperature

[7]For the lowest density at the highest temperature, $U_{\rm eff}$ exceeds ω_F. Hence, all on-shell states are located above the chemical potential (recall the discussion in Section 6.2.1).

dependence of the short-range correlations in nuclear matter.

The magnitude of the on-shell width at very low energies does not change too much at higher temperatures. At the highest energies that are shown, the temperature induced changes are also moderate. We observe a leveling off in the energy dependence of $\Gamma_{\mathrm{os}}(\omega)$ at the highest temperatures indicating the gradual changes in the available phase space in a heated system. This is the same effect that we have observed earlier, when discussing the cuts of the width at constant momenta in Fig. 6.11.

The right panel of Fig. 6.15 allows us to investigate the density dependence of $\Gamma_{\mathrm{os}}(\omega)$. Let us note first that the parabola shaped structures become larger at higher densities since an increasing amount of states below the chemical potential is populated. Naively, one could expect a linear density dependence for the state above the chemical potential. The simple low-density approximation $\Gamma \sim \rho\sigma v$ does, however, not hold anymore at densities of ρ_0 and higher where Pauli blocking becomes increasingly important. We can see that the density dependence in the vicinity of the Fermi energy is strongly temperature dependent. While the lowest density yields the largest result for Γ_{os} in this region at $T = 10\,\mathrm{MeV}$, it yields the smallest result at $T = 70\,\mathrm{MeV}$. For very high energies, the results for $2\rho_0$ and $3\rho_0$ do not differ too much (at all T) while we find considerably smaller values for ρ_0.

The most interesting observation in the right panel of Fig. 6.15 can be made for the density dependence of Γ_{os} at the highest temperature. At $T = 70\,\mathrm{MeV}$, the results for $\rho = 2\rho_0$ and $\rho = 3\rho_0$ are almost exactly equal in a wide region around the chemical potential. Noting again that this is the region where most of the populated states are located, we can conclude that a saturation of the short-range correlations occurs at high temperatures and densities.

The T and ρ dependent behavior seen in Fig. 6.15 deserves a closer inspection. Before doing so, we should recall that the chemical potential ω_F depends strongly on the nucleon density, as was shown in Fig. 6.12. Thus, one has to be careful at which energy ω or momentum $k(\omega)$ the widths for different temperatures and densities are compared. Clearly, a comparison of the on-shell widths at the chemical potential will lead to results that differ not only quantitatively but also qualitatively from a comparison at zero momentum (the lowest energies shown in Fig. 6.15). We will solve this problem in the next section by averaging the width over the populated states.

6.2.5 Average width

To determine the temperature and density dependence of the short-range correlations, it would be convenient to have a single quantity that determines the magnitude of the correlations at each value of T and ρ. For that purpose, we introduce the average width of the populated states,

$$\langle \Gamma_{\mathrm{pop}} \rangle (\rho, T) = \frac{\int_0^\infty dk k^2 \int_{-\infty}^{+\infty} d\omega \Gamma(\omega, k) \mathcal{A}(\omega, k) \mathrm{n_F}(\omega)}{\int_0^\infty dk k^2 \int_{-\infty}^{+\infty} d\omega \mathcal{A}(\omega, k) \mathrm{n_F}(\omega)}\,, \tag{6.21}$$

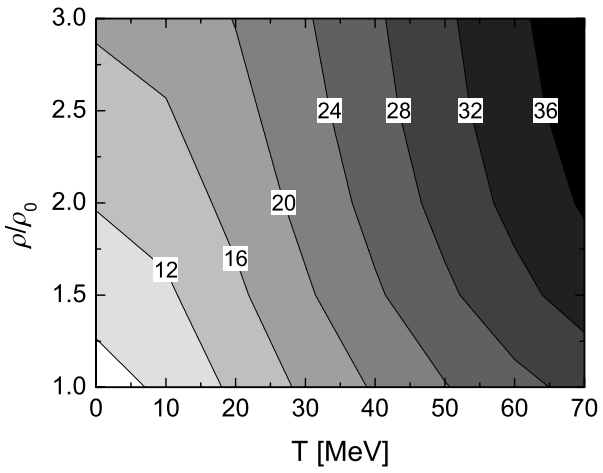

Figure 6.16: The average width of the populated states $\langle\Gamma_{\rm pop}\rangle$ in the (T, ρ)-plane (Γ in MeV).

that is not energy or momentum dependent. This definition is equivalent to the one in Eq. (5.2) that has been used to investigate the density dependence of the quark width in Section 5.6. In the integral in the numerator, the nucleon width is weighted with the spectral function. When the on-shell peak of the spectral function is rather sharp, we will mainly average over the on-shell states. When the peak is broad, however, the off-shell states will also contribute to the average width. The integral in the denominator is just the nucleon density that normalizes the result. At low temperatures, the average width $\langle\Gamma_{\rm pop}\rangle$ will be – due to the factor $k^2 {\rm n_F}$ – most sensitive to the on-shell states right below the chemical potential. At higher temperatures, where the distribution $\rm n_F$ softens, the influence of on-shell states above the chemical potential will become increasingly important. We will come back to this aspect below (see Fig. 6.19).

The contour plot in Fig. 6.16 shows the overall behavior of $\langle\Gamma_{\rm pop}\rangle$ for the full temperature and density range that was covered in our calculations. We can see that the average width ranges from $6 - 8\,{\rm MeV}$ at low T and ρ up to $40\,{\rm MeV}$ at high temperatures and densities. Note that one gets a very similar picture when the averaged on-shell width of the populated states or the on-shell width at the average momentum of the populated states is displayed instead. The general features of this figure are thus universal.

More details on the T and ρ dependence of $\langle\Gamma_{\rm pop}\rangle$ can be found in Figs. 6.17 and 6.18, where cuts at fixed densities and temperatures, respectively, are shown. Fig. 6.17 shows that $\langle\Gamma_{\rm pop}\rangle$ rises approximately quadratically at temperatures below $20\,{\rm MeV}$. At higher temperatures, the T dependence becomes linearly – at least for medium and high densities. At normal nuclear matter density, the T dependence weakens above $40 - 50\,{\rm MeV}$. The main observation that can be made in Fig. 6.17 is the linear

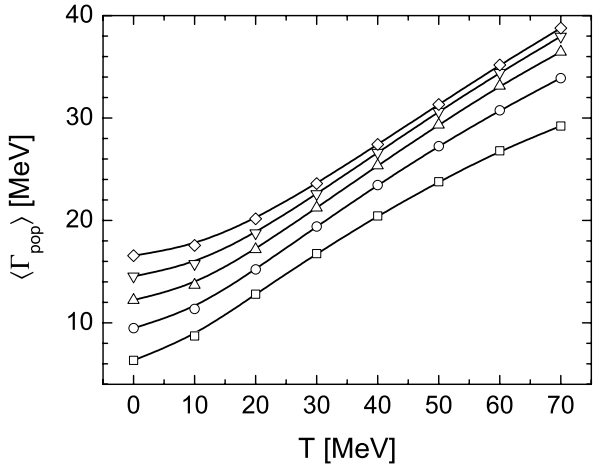

Figure 6.17: The average width of the populated states $\langle\Gamma_{\mathrm{pop}}\rangle$ as a function of the temperature for various densities ($\square = \rho_0$, $\bigcirc = 1.5\rho_0$, $\triangle = 2\rho_0$, $\triangledown = 2.5\rho_0$, $\diamond = 3\rho_0$).

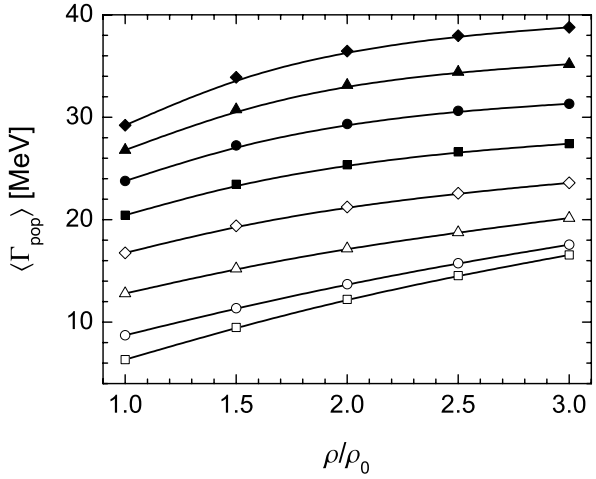

Figure 6.18: The average width of the populated states $\langle\Gamma_{\mathrm{pop}}\rangle$ as function a function of the density for various temperatures ($\square = 0\,\mathrm{MeV}$, $\bigcirc = 10\,\mathrm{MeV}$, $\triangle = 20\,\mathrm{MeV}$, $\diamond = 30\,\mathrm{MeV}$, $\blacksquare = 40\,\mathrm{MeV}$, $\bullet = 50\,\mathrm{MeV}$, $\blacktriangle = 60\,\mathrm{MeV}$, $\blacklozenge = 70\,\mathrm{MeV}$).

T dependence of the short-range correlation over a wide range of temperatures and densities. We will come back to this result below.

The density dependence of the average width that can be derived from Fig. 6.18 has also a rather simple structure. At low ρ, $\langle\Gamma_{\mathrm{pop}}\rangle$ increases with the density just as one would expect naively. At higher densities, however, we can observe a saturation of the average width and thus of the short-range correlations. This effect – that becomes relevant approximately above $2\rho_0$ – is weak at low T and strongly increases when the temperature rises.

The observations that we have made here, confirm the estimates from Section 6.2.4. For a qualitative understanding of the behavior of $\langle\Gamma_{\mathrm{pop}}\rangle$, we have to determine how the two scattering processes shown in Fig. 6.3 contribute to the average width. Let us first discuss the density dependence of these processes (see also Section 4.3): At low densities, the ρ dependence should be determined by the incoming nucleons from the medium. Since process (a) of Fig. 6.3 involves one incoming nucleon (not counting the nucleon that carries the external energy and momentum since we do not integrate over ω and k), a linear density dependence is expected. For process (b) with two incoming nucleons from the medium, we expect a quadratic density dependence. Note that this estimate has been confirmed in the quark calculations. In can be nicely observed in Fig. 5.17 (left panel for process (b), right panel for process (a) of 6.3) for the densities below the chiral phase transition.

The density dependence of the processes has to change at higher densities. In fact, we do not observe a quadratic ρ dependence in our results for $\rho \geq \rho_0$. Pauli blocking suppresses nucleon collisions (the source of the correlations) with final states below the Fermi surface. Since the chemical potential depends strongly on the nucleon density, more (kinematically allowed) final states are blocked at higher ρ. The contributions from process (b) to the width may still rise at higher densities: There are two initial states from the medium but only one final state that is subject to Pauli blocking. Process (a), on the other hand, involves only one initial state from the medium but two final states. Thus, the effect of increased Pauli blocking is more important than the gain of collision partners in that case.

We come now to the relevance of the individual processes for the average width of the populated states. At zero temperature, where the Fermi distribution is a sharp step function, all populated states are located below the chemical potential. The width of those states is solely generated by process (b) for $T = 0$. When the distributions in (6.5) soften at finite temperatures, the contributions of process (a) and (b) will mix. Process (a) will, however, remain the dominant process at energies above ω_F while process (b) remains dominant below ω_F.

Even more important than this mixing, populated states will be located at energies above the Fermi energy. Since the number of states increases with k^2, most of the populated states will be found in the vicinity of the Fermi momentum (note that the width is weighted with a factor $k^2 \mathrm{n_F}(\omega, k)$ in the numerator of Eq. (6.21)). At high temperatures, where the Fermi distribution drops only slowly, most of the states may even be located above the Fermi momentum. We illustrate this effect in

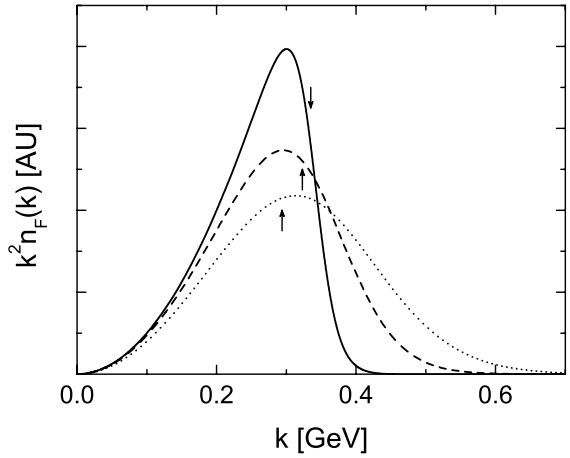

Figure 6.19: The density of the populated on-shell states, given by $k^2 \mathrm{n_F}(k)$, as a function of momentum at a density of $2\rho_0$. The solid, dashed, and dotted lines correspond to temperatures of 10 MeV ($k_F = 335\,\mathrm{MeV}$), 30 MeV ($k_F = 323\,\mathrm{MeV}$), and 50 MeV ($k_F = 294\,\mathrm{MeV}$), respectively. The small arrows denote the position of the Fermi momentum at each of the temperatures.

Fig. 6.19 for the on-shell states: While the Fermi momentum drops at higher temperatures, the maximum of the function $k^2 \mathrm{n_F}(k)$ moves to higher momenta. For the highest temperature that is shown, the maximum of the curve is located above the corresponding Fermi momentum. Thus, we can conclude that process (a) becomes increasingly important for the properties of the average width while the influence of process (b) drops when T rises.

The above considerations allow us to understand the density dependence of $\langle \Gamma_{\mathrm{pop}} \rangle$: At low temperatures, the width of the populated states is mainly determined by process (b). The Pauli blocking in one final state damps the quadratic density dependence of the incoming states. However, we still observe an almost linear density dependence at $0 - 10\,\mathrm{MeV}$ in Fig. 6.18. At higher temperatures, most of the populated states are located in the vicinity of the chemical potential and above. Hence, the influence of process (a) becomes visible. This process is much stronger affected by Pauli blocking. Consequently, we observe a saturation of the average width.

The fact that most of the populated states are located near the chemical potential explains also the temperature dependence of $\langle \Gamma_{\mathrm{pop}} \rangle$. When we determine the average width, we are most sensitive to those states. At low temperatures, where all populated states are located below the chemical potential and Pauli blocking is a strict condition, the width is very small (zero at $T = 0$) in the vicinity of the chemical potential. When the temperature rises and both scattering processes (a) and (b) are allowed in this region, the gap closes and the average width rises. As we can directly see in the left panel of Fig. 6.15, the filling of the gap at ω_F is a strongly T dependent effect.

We are sensitive to two effects here: First, the population of states above the

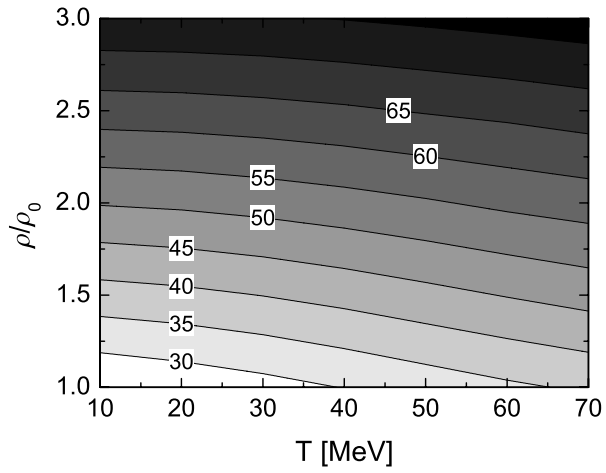

Figure 6.20: The average width of the populated states $\langle \Gamma_{\rm pop} \rangle$ in the (T, ρ)-plane (Γ in MeV) when Pauli blocking is switched off in the calculations.

Fermi energy allow allows scattering into states with higher energies and momenta that are not Pauli blocked. Second, the softening of Pauli blocking allows scattering into states below the chemical potential. An analytical understanding of the exact temperature dependence of the two scattering processes – that are mixed here – is complicated, even though it is striking that we observe a linear rise over a wide region of temperatures. We note that the linear dependence can most likely not be extrapolated to much higher temperatures. The behavior of the width at higher energies in Fig. 6.15 indicates that the width levels off at very large T. This is supported by the fact that the value of the on-shell width at the lowest energies ($k = 0$) is almost T independent.

To verify that Pauli blocking is in fact the explanation for the saturation of the short-range correlations at large densities, we have performed additional calculations in which Pauli blocking was artificially switched off. Therefore, all factors $(1 - \mathrm{n_F})$ were removed from the integrands in (6.5). The result is shown in Fig. 6.20. It can be clearly seen that $\langle \Gamma_{\rm pop} \rangle$ depends now linearly on both, temperature and density, over the full range covered by our calculations when Pauli blocking is disabled. This is exactly the picture we would naively expect (for process (a) of Fig. 6.3) when Pauli blocking is not taken into account. Thus Pauli blocking is in fact the correct explanation for the saturation of the short-range correlations at high densities.

6.2.6 Influence of nucleon resonances

In our calculations, we have worked with a model that considers only nucleons as degrees of freedom. Thus, Pauli blocking plays an important role in the scattering processes of Fig. 6.3 and we have observed saturation effects at higher densities. At

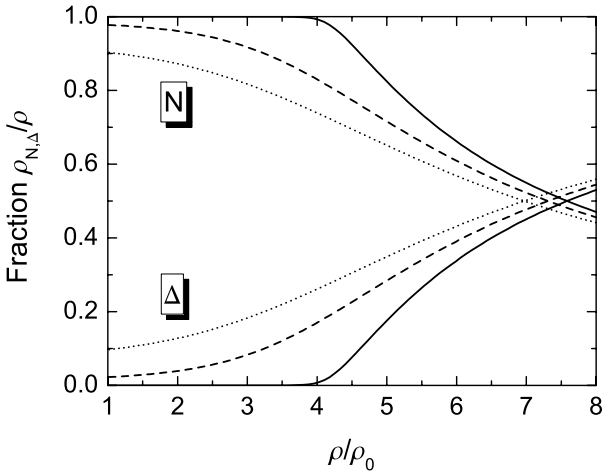

Figure 6.21: The density of nucleons and Δ resonances in thermal equilibrium as fractions of the total density. The solid, dashed, and dotted lines correspond to temperatures of 10 MeV, 50 MeV, and 70 MeV, respectively. The curves have been obtained in a calculation that demands equal chemical potentials for nucleons and Δ resonances [KL07].

higher temperatures, our results represent an idealization of the physical situation since it should become possible to excite nucleon resonances. Provided that there are only few resonances in the thermally equilibrated medium, the possibility to excite resonances in the outgoing states will weaken the effects of Pauli blocking and thus the saturation of the width that we have discussed above.

Reinterpreting the outgoing nucleons as resonances, we can use our calculation without Pauli blocking to illustrate the upper limit of the possible effects. The results in Fig. 6.20 indicate that the width does not saturate but rises linearly with the density at high temperatures. While the width does not change to much at $T = 70\,\mathrm{MeV}$ and $\rho = \rho_0$, it doubles at $\rho = 3\rho_0$ in comparison to Fig. 6.16. However, Fig. 6.20 represents an unrealistic scenario: Outgoing states are never Pauli blocked. This means that we excite resonances in *all* collisions (concerning process (a) of Fig. 6.3 even two resonances per collision). On the other hand, we do not consider that some resonances exist in the thermally equilibrated medium. Thus, we neglect the (weak) effects of Pauli blocking for resonances. Finally, the different masses of the nucleons and the resonances (the Δ resonance is 300 MeV heavier than a nucleon) are ignored in this calculation.

Let us consider a more realistic estimate. In Fig. 6.21, we show the density fractions of nucleons and Δ resonances in a medium that is in thermodynamical equilibrium. We can see immediately that there are no resonances in the medium at a temperature of 10 MeV and densities below $3\rho_0$. At $T = 50\,\mathrm{MeV}$, we find that $2 - 9\%$ of the populated states are resonances in the density range covered by our calculations. At

the highest temperature that we consider in this work, i.e. $T = 70\,\mathrm{MeV}$, the fraction of resonances rises from 10% at ρ_0 to 18% at $3\rho_0$.

We can identify these fractions with the probability to excite a resonance in a collision. Hence, we will never generate a resonance at low temperatures and our results of Fig. 6.16 remain unchanged. The chance to excite a resonance is still low at $T = 50\,\mathrm{MeV}$ and can be ignored at $\rho = \rho_0$. At higher densities, resonances are excited in 10% of the collisions. Using the estimate that such a collision yields – at most – a two times larger contribution to the width at $\rho = 3\rho_0$ (cf. Figs. 6.16 and 6.20), the total width may rise by 10% in comparison to our result in Fig. 6.16. Likewise, we can expect an increase of the width by 20% at $T = 70\,\mathrm{MeV}$ and $\rho = 3\rho_0$. We do not expect a significant increase at ρ_0 since the calculations with and without Pauli blocking yield very similar results in this region.

Our estimate shows that the possibility to excite nucleon resonances in the collisions will not change the results of our calculations too much. In the temperature and density range that we cover in the present work, observable changes are only expected at the highest temperatures *and* densities. The $10 - 20\%$ effects may weaken the – Pauli blocking incuded – saturation of the width, cf. Fig. 6.17. However, the saturation effects will not vanish entirely, even at higher temperatures. Recall that the present estimate is – like our regular calculation – an idealization. It does not take into account the increasing number of populated resonance states in the medium at higher temperatures and densities, cf. Fig. 6.21. When a considerable number of resonance states is populated, the resonances that are excited in collisions will also be subject to Pauli blocking. Thus, we will again observe a saturation effect (a combination of the saturation effects for nucleons and for the resonances) at higher densities.

We conclude this section by pointing out the large conceptual similarities between the present approach and our quark approach that has been discussed in the previous chapters. In both cases, a constant matrix element has been used and the short-range correlations (in the on-shell regions for the quarks) have been calculated from self-energy diagrams that have the structure of Born diagrams, cf. Figs. 4.2 and 6.2. Hence, we can expect that the temperature dependence of the short-range correlations in quark matter – that has not been investigated so far – will be similar to the temperature dependence in nuclear matter that has been studied here. This states an interesting, scale independent universality of dynamical correlations in fermionic systems of any kind.

7 Summary and Outlook

In the first part of this work we have explored the possibility of short-range correlations in cold and dense quark matter within the framework of the SU(2) NJL model. Employing a next-to-leading order expansion in $1/N_c$ for the quark self-energy, we have constructed a fully self-consistent model that is based on the relations between spectral functions and self-energies. In calculations at finite chemical potentials and zero temperature we have investigated the (off-shell) structure of the collisional quark width, the size of the short-range correlations, and their influence on the chiral phase transition. The results have been compared to the loop-expansion approach of [Frö01, FLM03b] and the results from nuclear matter calculations.

Our approach is based on techniques that have proven to be very successful in the investigation of nuclear matter. Self-consistent calculations have shown that pointlike interactions are well suited to explore the short-range correlations in nuclear matter. The overall strength of the interactions is more important than the detailed structure in this case. Assuming that this also holds for the short-range correlations in quark matter, we have used the NJL interaction as the starting point for our approach.

The NJL model in its SU(2) version has been introduced in Chapter 2. It is based on a pointlike interaction that resembles all relevant symmetries of QCD. Due to the large coupling of the QCD inspired theory, the validity of a loop-expansion in terms of the coupling constant is unclear in this model. We have discussed the concept of an expansion in the inverse number of colors and demonstrated the difference to the loop expansion. The classification of self-energy diagrams in terms of their order in $1/N_c$ has led us to the concept of dynamically generated mesons. Quark–antiquark scattering processes are summed up in a random phase approximation to construct effective meson propagators. The RPA mesons consist of bound $q\bar{q}$ states – the actual mesons – and a continuum of unbound $q\bar{q}$ states. As we have seen, the dynamically generated mesons can be used to merge the next-to-leading order contributions to the quark self-energy – like the Fock diagram and the direct Born diagram – in a single meson exchange diagram of order $\mathcal{O}(1/N_c)$.

When such a diagram is included in the Dyson–Schwinger equation for the quark self-energy, this leads to a feedback of the RPA meson properties into the properties of the quarks. Such a connection is not present in the standard leading-order approach to the NJL model, namely the Hartree+RPA approximation. In the coupled set of Dyson–Schwinger equations that we have constructed in Chapter 2, all quark propagators in the quark self-energy and RPA polarization diagrams are full in-medium propagators. Due to the non-local structure of the meson exchange diagram, the propagators acquire a finite width. We take this consistently into account

in our approach. In contrast to the Hartree+RPA approach that is briefly reviewed in Appendix B, we do not work with quasiparticles. Thus, the self-consistent solution of the Dyson–Schwinger equations can only be found numerically in an iterative procedure.

It has turned out that the RPA pions of our $\mathcal{O}(1/N_c)$ approach cannot be identified with the Goldstone bosons of the theory. The bound $q\bar{q}$ states have a considerable mass. This is a problem that arises already on the mean-field level for the Hartree–Fock+RPA approximation. The fulfillment of the chiral theorems in a diagrammatic expansion depends on delicate cancellation effects. A careful choice of the diagrams is necessary to leave the chiral theorems intact. Our approach has been constructed from a consistent next-to-leading order expansion of the quark self-energy. Due the self-consistent nature, however, it automatically generates higher order contributions to the RPA polarizations. Those contributions are only part of the complete sets of diagrams that are needed to restore the chiral properties in higher orders.

In Section 2.5 we have discussed a chirally invariant $1/N_c$ extension to the Hartree+RPA approximation on the quasiparticle level. This approach is based on a set of next-to-leading order polarization diagrams that have the character of vertex corrections for the quark–meson interaction. The diagrams are not calculated during the self-consistent calculation, but only afterwards – using the self-consistently obtained quark propagator and the (massive) RPA propagators – to determine a $1/N_c$ improved pion propagator. The correctional diagrams could, in principle, also be used to fix the chiral theorems in next-to-leading order in our approach. Calculating the polarization corrections *after* solving our Dyson–Schwinger equations would have no influence on the quarks. Their properties were still determined by a calculation with massive RPA pions. Hence, such an approach is of little use for us since we are primarily interested in the quark properties. On the other hand, including the vertex corrections in our self-consistent approach would also yield corrections for the quark self-energies. Such an approach is, however, technically very challenging. Since the $q\bar{q}$ continuum states are not affected by the cancellation problems, we postpone the vertex corrections to future studies.

Finding expressions from which the quark and RPA meson widths can be calculated is a straightforward exercise. As we have shown in Chapter 3, the integrals for the collisional self-energy and polarizations can be readily expressed in terms of spectral functions and fermionic and bosonic distribution functions. The numerical evaluation of the integrals is, however, technically challenging. We have discussed the main issues in Appendix H. To preserve analyticity, the real parts of the self-energy and the polarizations are calculated from dispersion relations in our approach. This has required a careful inspection of the analytical expressions to identify all energy independent terms that are not included in the actual dispersion integrals. We have shown that the RPA polarizations in terms of full in-medium propagators can be decomposed in a similar way as in the Hartree+RPA approximation. After identifying the term that leads to the violation of the Goldstone theorem we have estimated the size of the RPA pion mass. At the inspection of the quark self-energy we have found

a non-dispersive term that resembles the Fock self-energy – only the constant NJL coupling has been replaced by the $k_0^2 \to \infty$ limit of the RPA propagators. This is not surprising since the Fock self-energy has been part of the meson exchange self-energy diagram.

To gain a better understanding of the structure of the quark width, we have identified the decay and scattering processes that contribute to the collisional self-energies in Chapter 4. In the decomposition of the collision rates, the contributions from the bound $q\bar{q}$ states and the off-shell states of the RPA propagators have been treated separately. Using quasiparticle approximations and simple phase space arguments, we have determined the energy thresholds for which phase space opens and closes for each of the processes. Furthermore, we have estimated the density dependence of each process and investigated which processes yield contributions to the on-shell width of the quarks and antiquarks. It follows from theses considerations that the quark width has a complex structure and a non-uniform density dependence which can be understood in terms of the various processes shown in Figs. 4.1 and 4.3.

The analysis of the on-shell width has shown that the large RPA pion mass of our approach has some influence on the properties of the occupied quark states in the chirally broken phase. When the RPA pions have a finite mass – no matter if it is 100 MeV or 400 MeV – processes involving the bound $q\bar{q}$ state component of the RPA pion propagator do not generate contributions to the quark width in this region. However, the spacelike off-shell components of the RPA propagators, that are most important for the generation of the on-shell quark width, also depend on the RPA pion mass. We have found that the large mass in the chirally broken phase suppresses the contributions to the on-shell width by less than one order of magnitude. Thus, our results below the chiral phase transition represent a conservative estimate of the short-range effects in quark matter. The analysis has also shown that the bound $q\bar{q}$ states will contribute to the width of the occupied quark states when the pions are really massless (chiral limit). This may lead to considerably different results for the quark width between calculations with massless pions and calculations with pions that have a mass – close to the physical pion mass or heavier – in the chirally broken phase.

In our numerical calculations we have investigated quark matter at zero temperature. The results have been presented in Chapter 5. We have solved the coupled set of Dyson–Schwinger equations of our approach in an iterative procedure for a wide range of chemical potentials. Due to the influence of the short-range effects, we had to readjust the mean-field parameter sets of the NJL model. We have found that a reduction of the (Hartree) coupling constant by 22% is sufficient to obtain a reasonable result for the quark condensate.

The quark width can become very large at high energies but remains small at moderate energies – its qualitative structure is in good agreement with the quasiparticle considerations of Chapter 4. The on-shell peaks of the quark spectral function show clear signs of collisional broadening. In the off-shell regions, the structure of the width is reflected. Due to the presence of a medium with a finite chemical potential, the

symmetry between the quark and the antiquark states is broken. A comparison to the calculations in the loop-expansion has shown that the consistent $\mathcal{O}(1/N_c)$ expansion generates quark widths that are similar in shape but one order of magnitude larger. The $q\bar{q}$ continuum components of the RPA width and the spectral function are of similar shape and size as in the mean-field results. A small shift in the real part of the RPA polarizations leads to the predicted large mass of the bound $q\bar{q}$ state in the RPA pion spectral function – even when an NJL parameter set in the chiral limit is used. The shift has not so much influence on the mass of the RPA sigma that becomes only slightly heavier.

Our investigation of the chiral phase transition in the $\mathcal{O}(1/N_c)$ approach has shown that the short-range correlations are not strong enough to turn the first-order phase transition of the mean-field approximations into a smooth crossover at zero temperature. Nonetheless, the mass and density gaps at the chiral phase transition have dropped by $40 - 50\%$. Below the chiral phase transition, the quark density depends strongly on the chemical potential. Due to the density dependence of the short-range correlations, the quantitative differences between the $\mathcal{O}(1/N_c)$ approach and the mean-field models increase at higher chemical potentials. Qualitatively, the quark and the RPA sigma mass show the same behavior as in the Hartree+RPA approach. In the chirally restored phase this holds also for the RPA pion. When a parameter set in the chiral limit ($m_0 = 0$) is used in the calculations, the Lorentz scalar component of the quark self-energy vanishes above the phase transition. Chiral symmetry is fully restored and the quarks become massless. In contrast to the chiral properties of the pions, this behavior is not disturbed by the next-to-leading-order approach.

A closer inspection of the on-shell self-energy has provided some interesting insights. The effective quark mass keeps a very simple structure and remains almost energy and momentum independent in the $\mathcal{O}(1/N_c)$ approach. The real part of the collisional self-energy merely replaces the contributions from the mean-field self-energy that have been lost by reducing the coupling. The γ_0-component of the real part of the self-energy has a considerable size in the chirally restored phase. It shifts the on-shell peaks of the spectral function with respect to the chemical potential.

The on-shell width shows a strong density dependence in the chirally broken phase and seems to saturate in the chirally restored phase. For a better understanding of the density dependence of the width, we have investigated the average width of the populated and the average width of all quark states. Below the chiral phase transition, the average widths show a density dependence that is closely related to the density of the scattering partners from the medium. Above the phase transition, however, the average width of the populated states saturates and the width of all quarks even starts to decrease. These effects are due to Pauli blocking and due to the cutoff in the scattering processes that contribute to the quark width. The same effect is observed in the nuclear matter calculations of Chapter 6. We have also found that the results for the average width of the populated states are numerically very close to the results for nucleons in nuclear matter. However, such a comparison should be taken with care.

Finally, we have determined the momentum distribution of the quarks to investigate the role of the states that are far off-shell. We have found a depletion of the momentum distribution below the Fermi momentum that is on the order of 10%. Off-shell states above the Fermi momentum generate a high-momentum tail in the momentum distribution. The size of the effects in the chirally restored phase is comparable to nuclear matter. The short-range effects are one order of magnitude larger than in the loop-expansion.

We can conclude that our initial calculation in the loop-approximation [Frö01, FLM03b] has clearly missed important contributions to the quark self-energy and thus generated only very small short-range correlations. The larger results of the present work are more reasonable since they are the product of a consistent expansion in the inverse number of colors. Apart from the problem of the RPA pion mass – that also has influence on the short-range effects – our $\mathcal{O}(1/N_c)$ approach is a natural extension of the standard Hartree+RPA approximation. The comparison of the quark matter results to nuclear matter calculations shows that the short-range correlations are of similar magnitude in both systems. In nuclear matter, the short-range effects play a very important role. A complete description of nuclear systems is only possible when those effects are taken into account. Therefore, the effects of short-range correlations on the properties of the quarks (and the dynamically generated mesons) should also not be ignored.

Let us consider the QCD phase diagram to stress this point: It is not feasible to investigate the chiral phase transition at arbitrary temperatures and densities within (Lattice) QCD. Therefore, phenomenological models are used to determine the properties of the phase transition. Many of these models suggest that the chiral phase transition turns from a first-order phase transition into a crossover at a critical point, see Fig. 1.2. As we have seen in this work, short-range correlations change the properties of the chiral phase transition with respect to the results of quasiparticle calculations. Nuclear matter calculations suggest that the short-range correlations will be even larger at finite temperatures, see Fig. 6.17. This suggests that mean-field models will most likely predict a wrong position for the critical point (at a too large temperature). We note that calculations with a more realistic pion mass should differ even more from the quasiparticle approaches.

The present $\mathcal{O}(1/N_c)$ approach can be improved in many ways. Most of them have already been discussed before in more or less detail. We will review the improvements here and discuss the possible consequences of including them in the model.

So far, we have only considered one regularization scheme. A different type of regularization might have some influence on the properties of the quarks and RPA mesons. It is, however, unlikely that the resulting changes will be too large. As we have discussed above, it is even possible to implement the three-momentum cutoff in different ways. Our version (regularizing the quark propagators) differs only from a regularization of the integration variables when the integrand contains two or more quark propagators. This is only the case for the RPA polarization integrals in our approach. The implementations are equivalent for the quark self-energy integrals.

Consequently, the differences between the resulting quark masses and widths should be limited.

The most interesting but also most complicated extension of our model would be to fix the chiral properties of the RPA pions. A first step into that direction would be to include the next-to-leading order corrections to the RPA polarization in the self-consistent calculation. Technically, that corresponds to the transition from one-loop to two- and three-loop integrals. This yields not only a significant complication of the numerical calculations. As the $1/N_c$ enhanced quasiparticle approaches [DSTL95, NBC$^+$96, OBW00] have shown, it requires also considerable analytical efforts to incorporate these diagrams into the model.

Such an approach would improve the chiral properties of the RPA pions only in next-to-leading order but not in the higher orders. Nonetheless, it would be very interesting to take a closer look at dynamically generated pions with more reasonable masses and the chiral theorems in the presence of short-range correlations. As our investigations from Chapter 4 indicate, the on-shell width of the quarks could even be much larger than determined here. It would also be interesting to investigate a system in the chiral limit with such an approach. If the pions become really massless in the chirally broken phase, the thresholds of some decay processes that involve bound $q\bar{q}$ states move very close to the on-shell regions of the quark spectral function. It is possible that this has noticeable influence on the properties of the quarks.

In nuclear matter, the short-range correlations are strongly temperature dependent. Since the nuclear matter calculations of Chapter 6 are technically rather similar to the present approach, it is likely that the short-range correlations in quark matter will also increase when the temperature rises. This should be checked in an explicit calculation. We have already discussed that this may have serious consequences for the structure of the chiral phase transition. The temperature at which the first-order phase transition turns into a crossover presumably will be lower than in the mean-field approximations. Performing calculations at finite temperatures should not be too complicated. The formalism that has been presented here was already derived in a form that allows for finite temperatures. Hence, it is mainly the numerical implementation that has to be modified.

In the present approach, we have completely ignored the phenomenon of color superconductivity [RW02, Bub05]. This should have little influence on the results in the chirally broken phase. The existence of a diquark condensate above the chiral phase transition, however, may have influence on the short-range effects in the chirally restored phase [CD99]. It is also likely that the short-range effects have some influence on the diquark condensate. Note that diquark states can be dynamically generated in our approach in the same fashion as the RPA mesons. Hence, the inclusion of color superconductivity should not complicate the present formalism too much.

For the investigation of systems like neutron stars and hypernuclear matter, it would also be interesting to extend our model to asymmetric quark matter and flavor SU(3). Similar approaches exist already for nuclear matter. See, e.g., [KLM05] for a calculation in flavor asymmetric nuclear matter. In such an approach, the quarks

of different flavor – and the three pions $\pi^{0,\pm}$ – must be treated separately. In an SU(3) approach, we would also encounter additional dynamically generated mesons, i.e., kaons and η, η' [Kle92]. In principle, however, the extension of our framework to such systems is straightforward.

In the second part of this work, we have presented an approach to short-range correlations in nuclear matter at finite temperatures and high densities. As an extension of the work of Lehr et al. [LEL$^+$00, LLLM02] we have constructed a simple but self-consistent model in Section 6. The interactions between the nucleons were described by a constant matrix element in combination with a form factor that limits the energy and momentum transfer in the collisions. In [LEL$^+$00, LLLM02] the averaged coupling constant has led to excellent results for a system at zero temperature. We have calculated the mean-field contributions by a Skyrme-type interaction model in order to assure a realistic thermodynamical behavior of the chemical potential.

We have calculated the spectral function of nucleons in symmetric nuclear matter at temperatures from 0 to 70 MeV and densities from ρ_0 to $3\rho_0$. This is just the region that is expected to be relevant in supernova explosions and heavy ion collisions like those planned at the CBM facility at GSI. For the first time, such a large range of temperatures and densities has been investigated consistently within the same model. Our results are in good agreement with other calculations at temperatures up to 20 MeV and densities up to $2\,\rho_0$ – outside this range, data for comparison are not available. The averaged on-shell width of the spectral function was used to determine the temperature and energy dependence of the short-range correlations. We have found that the correlations scale approximately linear with temperature. At densities above $2\rho_0$, however, the correlations saturate. This behavior is not expected in a naive picture, however, it can be easily explained by Pauli blocking which is a genuine quantum mechanical effect.

The model we have presented here is open for further improvements. First of all, it should be investigated whether the choice of Skyrme parametrization has influence on the short-range correlations. It may be also possible to calculate the real part dispersively when a suitable approximation scheme for the nucleon width at high energies is introduced. In [KLM05], the same approach has been extended to cold isospin asymmetric nuclear matter. A combination with our approach should be straightforward – we would have to consider separate spectral functions for protons and neutrons and to introduce an isospin dependent coupling. Such an extension would be desirable, in particular, for the investigation of short-range correlations in astrophysical scenarios. The typical result of a supernova explosion (hot) and the following core collapse (dense) – i.e., a neutron star – is clearly not an isospin symmetric object.

A Notation and conventions

The notation and the conventions in this work correspond mainly to those in the book of Peskin and Schroeder [PS95] (field theory and relativity), the review of Danielewicz [Dan84] (real-time formalism), and the article of Rehberg (NJL model) [Reh98]. Below, we briefly review the most important aspects.

Units

We work in natural units, i.e.,

$$\hbar = c = 1\,.$$

This yields the relations

$$[\text{length}] = [\text{time}] = [\text{energy}]^{-1} = [\text{mass}]^{-1}\,.$$

The only unit conversion that will be needed throughout this work is given by

$$197.327\,\text{MeV} = 1\,\text{fm}^{-1}\,.$$

Metric tensor and four-vectors

We use the metric tensor in the "west coast" form,

$$g_{\mu\nu} = g^{\mu\nu} = \begin{pmatrix} 1 & 0 & 0 & 0 \\ 0 & -1 & 0 & 0 \\ 0 & 0 & -1 & 0 \\ 0 & 0 & 0 & -1 \end{pmatrix}\,.$$

Four-vectors are denoted by italic letters (x), three-vectors are marked by arrows ($\vec{x}$). Unit vectors that point into the same direction as a vector $\vec{x}$ are denoted by $\vec{e}_x$.

Greek indices denote the components of a four-vector and run from 0 to 3 (where the zeroth component is the time or energy component of the four-vector). Latin indices denote the three-vector components only. They run from 1 to 3. Following the Einstein summation convention, we sum over all indices that appear twice in a term.

We distinguish between four-vectors with upper (contravariant) and lower (covariant) indices,

$$\begin{aligned} x^\mu &= (x^0, \vec{x}) && \text{(contravariant)}\,, \\ x_\mu &= g_{\mu\nu} x^\nu = (x^0, -\vec{x}) && \text{(covariant)}\,. \end{aligned}$$

The scalar product of two four-vectors is defined by

$$x \cdot p = x_\mu x^\mu = g_{\mu\nu} x^\mu p^\nu = x^0 p^0 - \vec{x} \cdot \vec{p}.$$

Fourier transforms

In Fourier transformations, we attribute the usual factors 2π fully to the momentum integrals. Hence, the transformation integrals in four dimensions are given by

$$f(x) = \int \frac{d^4k}{(2\pi)^4} e^{-ik\cdot x} \tilde{f}(k)\,,$$
$$\tilde{f}(k) = \int d^4x e^{ik\cdot x} f(x)\,.$$

The tilde that is used here to denote functions in momentum space will be omitted throughout this work. It will always be clear from the arguments of a function whether its coordinate space or the momentum space form is meant.

Traces

Unless indicated otherwise, we use the following convention for traces: "tr" denotes a trace in spinor space only while the symbol "Tr" is used for a full trace in color, flavor, and spinor space,

$$\mathrm{tr}(1) = 4\,, \qquad \mathrm{Tr}(1) = 4N_f N_c\,.$$

Pauli matrices

The (iso-)spin Pauli matrices are given by

$$\tau^1 = \begin{pmatrix} 0 & 1 \\ 1 & 0 \end{pmatrix}, \qquad \tau^2 = \begin{pmatrix} 0 & -i \\ i & 0 \end{pmatrix}, \qquad \tau^3 = \begin{pmatrix} 1 & 0 \\ 0 & -1 \end{pmatrix}.$$

The Pauli matrices obey the (anti-)commutation relations

$$\{\tau_i, \tau_j\} = 2\delta_{ij} \qquad \text{and} \qquad [\tau_i, \tau_j] = 2i\epsilon_{ijk}\tau_k\,,$$

where δ_{ij} is the Kronecker delta and ϵ_{ijk} is the totally antisymmetric tensor (Levi-Civita symbol) in three dimensions. From the (anti-)commutation relations follows the helpful relation

$$\tau^i \tau^j = \delta^{ij} + i\epsilon^{ijk}\tau^k\,.$$

For further reference, we introduce the matrices $\tau^\pm = (\tau^1 \pm i\tau^2)/\sqrt{2}$:

$$\tau^+ = \begin{pmatrix} 0 & 1 \\ 0 & 0 \end{pmatrix}, \qquad \tau^- = \begin{pmatrix} 0 & 0 \\ 1 & 0 \end{pmatrix}.$$

Dirac matrices

The Dirac matrices (or γ matrices) satisfy – independently of the chosen representation – the anticommutation relations

$$\{\gamma^\mu, \gamma^\nu\} = 2g^{\mu\nu}\,.$$

Products of γ matrices and four-vectors are denoted in the Feynman slash notation,

$$p \cdot \gamma = p_\mu \gamma^\mu = \not{p}\,.$$

Two frequently occurring combinations of the Dirac matrices are

$$\gamma^5 = i\gamma^0\gamma^1\gamma^2\gamma^3\,,$$
$$\sigma^{\mu\nu} = \frac{i}{2}[\gamma_\mu, \gamma_\nu]\,.$$

By construction, the matrix γ^5 has the following properties,

$$(\gamma^5)^2 = \mathbb{1}_{4\times4}\,, \qquad (\gamma^5)^\dagger = \gamma^5\,, \qquad \{\gamma^5, \gamma^\mu\} = 0\,.$$

There exist several explicit representations of the Dirac matrices. We will use the so-called chiral (or Weyl) representation that can be constructed from the Pauli matrices in a 2×2 block form:

$$\gamma^0 = \begin{pmatrix} 0 & \mathbb{1}_{2\times2} \\ \mathbb{1}_{2\times2} & 0 \end{pmatrix}, \qquad \gamma^i = \begin{pmatrix} 0 & \tau^i \\ -\tau^i & 0 \end{pmatrix}, \qquad \gamma^5 = \begin{pmatrix} -\mathbb{1}_{2\times2} & 0 \\ 0 & \mathbb{1}_{2\times2} \end{pmatrix}.$$

Traces of γ matrices

In this work we will frequently encounter traces of γ matrices. For further reference, we list some helpful relations below:

$$\begin{aligned}
\mathrm{tr}(\mathbb{1}_{4\times4}) &= 4 \\
\mathrm{tr}(\gamma^\mu\gamma^\nu) &= 4g^{\mu\nu} \\
\mathrm{tr}(\gamma^\mu\gamma^\nu\gamma^\rho\gamma^\sigma) &= 4(g^{\mu\nu}g^{\rho\sigma} - g^{\mu\rho}g^{\nu\sigma} + g^{\mu\sigma}g^{\nu\rho}) \\
\mathrm{tr}(\gamma^5) &= 0 \\
\mathrm{tr}(\gamma^\mu\gamma^\nu\gamma^5) &= 0 \\
\mathrm{tr}(\gamma^\mu\gamma^\nu\gamma^\rho\gamma^\sigma\gamma^5) &= -4i\epsilon^{\mu\nu\rho\sigma}.
\end{aligned}$$

Note that the trace of an odd number of γ matrices is always zero. From the trace in the second line follows immediately

$$\mathrm{tr}(\not{p}\not{k}) = p_\mu k_\nu\,\mathrm{tr}(\gamma^\mu\gamma^\nu) = 4p_\mu k^\mu\,.$$

Real and imaginary parts of Dirac matrices

We use the hermitian conjugate $\gamma_0 F^\dagger \gamma_0$ to define the real and the imaginary part of functions that have a matrix structure in spinor space (Lorentz structure) [BD65, FLM03b],

$$\begin{aligned} \mathrm{Re}F &= \frac{1}{2}(F + \gamma_0 F^\dagger \gamma_0)\,, \\ \mathrm{Im}F &= \frac{1}{2i}(F - \gamma_0 F^\dagger \gamma_0)\,. \end{aligned}$$

For Lorentz scalar functions there is no difference to the normal definition. Note that [BD65]

$$\gamma^0 (\gamma^\mu)^\dagger \gamma^0 = \gamma^\mu\,,$$

and thus $\gamma_\mu = \mathrm{Re}\gamma_\mu$ in this formalism. In other words, the γ matrices are treated – independently of the explicit representation – as real quantities. This ensures that, cf. (2.23),

$$\begin{aligned} \mathrm{Re}\,\mathrm{S} &= (\mathrm{Re}\,\mathrm{S}_s)\,\mathbb{1}_{4\times4} + (\mathrm{Re}\,\mathrm{S}_\mu)\,\gamma^\mu\,, \\ \mathrm{Im}\,\mathrm{S} &= (\mathrm{Im}\,\mathrm{S}_s)\,\mathbb{1}_{4\times4} + (\mathrm{Im}\,\mathrm{S}_\mu)\,\gamma^\mu\,, \end{aligned}$$

and likewise for the quark self-energy.

B RPA on the Hartree(–Fock) level

For the understanding of the RPA in the full $\mathcal{O}(1/N_c)$ approach it is helpful to investigate the RPA on the quasiparticle level, i.e., in the Hartree+RPA and in the Hartree–Fock+RPA approximation, first. An investigation at $T = \mu = 0$ is sufficient to provide insights about the Goldstone boson character of the RPA pions and the proper use of dispersion integrals. The results of [Kle92] are summarized in this section. Special attention is paid to the aspects that are relevant for the transition to the $\mathcal{O}(1/N_c)$ approach. In particular, it will become clear that the RPA pions in the Hartree–Fock+RPA approximation that we have introduced in Section 2.3.2 – a precursor to the full $\mathcal{O}(1/N_c)$ approach – do not have the properties of Goldstone bosons.

For $\mu = 0$ the (time-ordered) quark propagator in the mean-field approximation is given by

$$\mathrm{S}^{\mathrm{c}}(k) = \frac{\not{k} + m^*}{k^2 - m^{*2}} \,,$$

with the effective mass m^* that is constant and real. In the Hartree approximation we have $m^* = m_0 + \Sigma^{\mathrm{H}}$ and in the Hartree–Fock approximation $m^* = m_0 + \Sigma^{\mathrm{H}} + \Sigma_s^{\mathrm{F}}$. Inserting $\mathrm{S}^{\mathrm{c}}(k)$ into the time-ordered RPA meson polarizations yields

$$-i\,\Pi_l^{\mathrm{c}}(k^2) = -\int \frac{d^4p}{(2\pi)^4}\,\mathrm{Tr}\left[\tilde{\Gamma}_l\,\mathrm{S}^{\mathrm{c}}(p+\tfrac{1}{2}k)\Gamma_l\,\mathrm{S}^{\mathrm{c}}(p-\tfrac{1}{2}k)\right] .$$

The isospin matrices in Γ_l and $\tilde{\Gamma}_l$ (2.3) commute with the quark propagator in flavor symmetric matter or vacuum. Thus we find the same result for all pions ($\pi^{0,\pm}$) when working out the trace,

$$-i\,\Pi_{\sigma,\pi}^{\mathrm{c}}(k^2) = 4N_f N_c \int \frac{d^4p}{(2\pi)^4} \frac{\frac{1}{4}k^2 - p^2 \mp m^{*2}}{[(p+\frac{1}{2}k)^2 - m^{*2}][(p-\frac{1}{2}k)^2 - m^{*2}]} \,, \tag{B.1}$$

where the upper sign of $\mp m^{*2}$ refers to the σ and the lower sign to the π polarization, respectively.

The numerator of the integrand in (B.1) can be written as $-(p^2 + \frac{1}{4}k^2 - m^{*2}) + (\frac{1}{2}k^2 - m^{*2} \mp m^{*2})$. Partial fractions are used to decompose the denominator,

$$\frac{p^2 + \frac{1}{4}k^2 - m^{*2}}{[(p+\frac{1}{2}k)^2 - m^{*2}][(p-\frac{1}{2}k)^2 - m^{*2}]} = \frac{1}{2}\left[\frac{1}{(p+\frac{1}{2}k)^2 - m^{*2}} + \frac{1}{(p-\frac{1}{2}k)^2 - m^{*2}}\right] .$$

Inserting the rewritten numerator and denominator into (B.1) we find

$$-i\,\Pi^{\mathrm{c}}_{\sigma,\pi}(k^2) = -2N_fN_c\int\frac{d^4p}{(2\pi)^4}\left[\frac{1}{(p+\frac{1}{2}k)^2-m^{*2}}+\frac{1}{(p-\frac{1}{2}k)^2-m^{*2}}\right] + 2N_fN_c\int\frac{d^4p}{(2\pi)^4}\frac{k^2-2(m^{*2}\pm m^{*2})}{[(p+\frac{1}{2}k)^2-m^{*2}][(p-\frac{1}{2}k)^2-m^{*2}]}\,. \tag{B.2}$$

The two terms in the first integral can be merged by shifting the integration variables, $p+\frac{1}{2}k\to p$ for the first term and $p-\frac{1}{2}k\to p$ for the second term, respectively. We do not consider the influence of the momentum cutoff at this point. After introducing the abbreviation

$$\mathrm{I}(k^2) = \int\frac{d^4p}{(2\pi)^4}\frac{1}{[(p+\frac{1}{2}k)^2-m^{*2}][(p-\frac{1}{2}k)^2-m^{*2}]}\,, \tag{B.3}$$

the polarizations become

$$\begin{aligned} -i\,\Pi^{\mathrm{c}}_{\pi}(k^2) &= -4N_fN_c\int\frac{d^4p}{(2\pi)^4}\frac{1}{p^2-m^{*2}} + 2N_fN_ck^2\mathrm{I}(k^2)\,,\\ -i\,\Pi^{\mathrm{c}}_{\sigma}(k^2) &= -4N_fN_c\int\frac{d^4p}{(2\pi)^4}\frac{1}{p^2-m^{*2}} + 2N_fN_c(k^2-4m^{*2})\mathrm{I}(k^2)\,. \end{aligned} \tag{B.4}$$

Note that the *imaginary* part of I corresponds to the *real* part of Π^{c}.

The first term resembles the Hartree self-energy,

$$\Sigma^{\mathrm{H}} = 2i\mathrm{G}N_fN_c\int\frac{d^4p}{(2\pi)^4}\,\mathrm{tr}\,S(p) = 8i\mathrm{G}N_fN_cm^*\int\frac{d^4p}{(2\pi)^4}\frac{1}{p^2-m^{*2}}\,.$$

We can use this to eliminate the integral and to simplify the expressions. For the RPA pion polarization we get

$$-i\,\Pi^{\mathrm{c}}_{\pi}(k^2) = -\frac{1}{2i\mathrm{G}}\frac{\Sigma^{\mathrm{H}}}{m^*} + 2N_fN_ck^2\mathrm{I}(k^2)\,. \tag{B.5}$$

To investigate the chiral behavior of the RPA pions, the poles of the propagator have to be found. The denominator of the RPA pion propagator is given by

$$1+2\mathrm{G}\,\Pi^{\mathrm{c}}_{\pi}(k^2) = \frac{m^*-\Sigma^{\mathrm{H}}}{m^*} + 4i\mathrm{G}N_fN_ck^2\mathrm{I}(k^2)\,. \tag{B.6}$$

If the pions are Goldstone modes, their mass should be small for finite m_0 and vanish in the absence of a current quark mass (chiral limit) when chiral symmetry is spontaneously broken. The propagator should then have a pole at $k^2=0$, i.e., $1+2\mathrm{G}\,\Pi^{\mathrm{c}}_{\pi}(0)=0$. The second term on the rhs. of (B.6) is surely zero for

$k^2 = 0$. The first term needs closer inspection. In the Hartree approximation we have $m^* = m_0 + \Sigma^{\mathrm{H}}$,

$$\frac{m^* - \Sigma^{\mathrm{H}}}{m^*} = \frac{m_0}{m_0 + \Sigma^{\mathrm{H}}} \,. \tag{B.7}$$

This expression will be zero in the chiral limit. For finite m_0 we have $m_0 \ll \Sigma^{\mathrm{H}}$ and thus $m_0/(m_0 + \Sigma^{\mathrm{H}}) \ll 1$ below the chiral phase transition ($m_0/\,\Sigma^{\mathrm{H}} \approx 0.02$). This means that the RPA pions show the behavior of Goldstone bosons.

Let us turn now to the Hartree–Fock+RPA approximation that we have introduced in Section 2.3.2. This scheme does not represent a clean expansion of the quark self-energy in $1/N_c$. However, we can use it to estimate what effects might occur in our $\mathcal{O}(1/N_c)$ approach. The effective mass on the Hartree–Fock level is given by $m^* = m_0 + \Sigma^{\mathrm{H}} + \Sigma_s^{\mathrm{F}}$. Below the chiral phase transition, where $m_0 \ll \Sigma_s^{\mathrm{F}} < \Sigma^{\mathrm{H}}$, the first term of (B.6) becomes

$$\frac{m^* - \Sigma^{\mathrm{H}}}{m^*} = \frac{m_0 + \Sigma_s^{\mathrm{F}}}{m_0 + \Sigma^{\mathrm{H}} + \Sigma_s^{\mathrm{F}}} \approx \frac{\Sigma_s^{\mathrm{F}}}{\Sigma^{\mathrm{H}} + \Sigma_s^{\mathrm{F}}} = \frac{1}{2N_f N_c + 1}, \tag{B.8}$$

using $\Sigma^{\mathrm{H}} = 2N_f N_c\, \Sigma_s^{\mathrm{F}}$. As we can see, this term is not zero but on the order 0.1. This is significantly larger than $m_0/\,\Sigma^{\mathrm{H}}$. Thus the RPA pions in the Hartree–Fock+RPA approximation of Fig. 2.9 – in contrast to the Hartree+RPA approximation of Fig. 2.6 – will not behave like Goldstone bosons. They will have a finite mass, even in the chiral limit where the current quark mass is zero.

A regular random phase approximation on the Hartree–Fock level [RS80, BR86, DVN05] should actually yield the Goldstone modes – provided that the mean-field part of the interaction and the residual part that generates the RPA mesons are treated in a consistent way. The reason for the breakdown of the chiral properties of the pions in our Hartree–Fock+RPA approximation are discussed in detail in Section 2.5: In a $1/N_c$ expansion, the generation of massless pions (in the chiral limit) depends on a delicate balance [DSTL95] – in each order of $1/N_c$, the contributions from different diagrams must cancel each other. The Hartree–Fock propagator is – in contrast to the Hartree propagator – not purely $\mathcal{O}(1)$ (since the $\mathcal{O}(1/N_c)$ Fock diagram is iterated self-consistently, the propagator contributes in all orders of $1/N_c$). When it is inserted into the RPA polarization loops, it automatically generates higher order contributions to the polarizations in an incomplete way. Since some of the diagrams that would be needed for the cancellation effect are missing, the RPA pions become massive.

It is interesting to note that we could fix the chiral properties of the pions by adjusting the mean-field interaction of the quarks and the residual interaction that generates the RPA mesons separately (instead of using the NJL coupling G in both cases). Introducing a residual interaction $\mathcal{G}$ in the second line of Fig. 2.9 – while keeping the NJL coupling G for the mean-field in the first line – has no influence on

the result for the polarization in Eq. (B.5). However, the denominator of the RPA pion propagator at $k^2 = 0$ is then given by

$$1 + 2\mathcal{G}\,\Pi_\pi^{\mathrm{c}}(k^2 = 0) = \frac{m^* - \frac{\mathcal{G}}{\mathrm{G}}\,\Sigma^{\mathrm{H}}}{m^*}\,. \tag{B.9}$$

Demanding that the rhs. of (B.9) vanishes in the chiral limit yields the condition $m^* = \Sigma^{\mathrm{H}} + \Sigma_s^{\mathrm{F}} = \frac{\mathcal{G}}{\mathrm{G}}\,\Sigma^{\mathrm{H}}$. Hence, massless pions (Goldstone bosons) would be obtained for

$$\mathcal{G} = \frac{\Sigma^{\mathrm{H}} + \Sigma_s^{\mathrm{F}}}{\Sigma^{\mathrm{H}}} = \frac{2N_f N_c + 1}{2N_f N_c}\,\mathrm{G}\,, \tag{B.10}$$

where we have again used $\Sigma^{\mathrm{H}} = 2N_f N_c\,\Sigma_s^{\mathrm{F}}$, cf. (3.7). Not too surprising, the correction $\Sigma^{\mathrm{F}}\,/\,\Sigma^{\mathrm{H}}$ is on the order of $\mathcal{O}(1/N_c)$.

We will not pursue the idea of a readjusted residual interaction any further. In the present work, we use the Hartree–Fock+RPA approximation of Fig. 2.9 as a simple framework to illustrate higher order effects that are relevant for our $\mathcal{O}(1/N_c)$ approach (the construction of a fully self-consistent $1/N_c$ extension that yields massless pions is still an unsolved problem, see Section 2.5 for details). The finite term in (B.8) – that violates the Goldstone theorem and should not be present in a regular random phase approximation – is exactly such an effect. Fig. 2.15 shows $1 + 2\mathrm{G}\mathrm{Re}\,\Pi_l^{\mathrm{ret}}$ from a Hartree+RPA and a Hartree–Fock+RPA calculation. The shift of the Hartree–Fock+RPA curve raises the RPA pion mass by 150 MeV. The full $\mathcal{O}(1/N_c)$ approach includes the Fock self-energy and further contributions to the effective mass that arise from the collisional self-energy. If no cancellation effect occurs it should be expected that the RPA pions behave even less like Goldstone bosons in that case.

So far, we have not considered the dynamically generated sigma. The denominator of the RPA sigma propagator is found in the same way as (B.6),

$$1 + 2\mathrm{G}\,\Pi_\sigma^{\mathrm{c}}(k^2) = \frac{m^* - \Sigma^{\mathrm{H}}}{m^*} + 4i\mathrm{G}N_f N_c\left(k^2 - 4m^{*2}\right)\mathrm{I}(k^2)\,. \tag{B.11}$$

The first term is only of minor importance here. As long as it is small, the pole of the propagator should be approximately determined by the zero of the second term at $k^2 = 4m^{*2}$. The mass of the RPA sigma is then on the order of $2m^*$.

In the full $\mathcal{O}(1/N_c)$ approach it is necessary to calculate the real parts of the retarded quark self-energy and the retarded RPA polarizations from dispersion integrals. Constant terms that occur in an explicit calculation of the real part must be identified and added to the dispersion integral, cf. Appendix F. We can use the Hartree(–Fock)+RPA approximation as a guideline to study how such constant terms arise.

At $T = 0$ the retarded and the time-ordered self-energies are related in a simple way, $\mathrm{Re}\,\Pi_l^{\mathrm{ret}}(k^2) = \mathrm{Re}\,\Pi_l^{\mathrm{c}}(k^2)$ and $\mathrm{Im}\,\Pi_l^{\mathrm{ret}}(k_0, \vec{k}\,) = \mathrm{Im}\,\Pi_l^{\mathrm{c}}(k_0, \vec{k}\,)\,\mathrm{sgn}(k_0)$, cf. (3.25).

Inserting the explicit imaginary parts of the time-ordered polarizations (B.4) yields

$$\begin{aligned}\mathrm{Im}\,\Pi_{\pi}^{\mathrm{ret}}(k_0,\vec{k}\,) &= 2N_f N_c k^2 \mathrm{ReI}(k^2)\,\mathrm{sgn}(k_0)\,,\\ \mathrm{Im}\,\Pi_{\sigma}^{\mathrm{ret}}(k_0,\vec{k}\,) &= 2N_f N_c (k^2-4m^{*2})\mathrm{ReI}(k^2)\,\mathrm{sgn}(k_0)\,.\end{aligned}$$

The real and the imaginary part of the integral $\mathrm{I}(k^2)$ (B.3) can be calculated explicitly using either the residue theorem or Cutkosky rules [PS95] when a three-momentum cutoff Λ is used to regularize the integrals. We find

$$\mathrm{ReI}(k^2) = \begin{cases} -\frac{1}{16\pi}\sqrt{1-\frac{4m^{*2}}{k^2}} & \text{for} \quad 4m^{*2} < k^2 < 4(\Lambda^2+m^{*2}) \\ \\ 0 & \text{for} \quad k^2 < 4m^{*2} \text{ or } k^2 > 4(\Lambda^2+m^{*2}) \end{cases} \tag{B.12}$$

and

$$\mathrm{ImI}(k^2) = \frac{1}{16\pi^2} \int\limits_{m^{*2}}^{\Lambda^2+m^{*2}} dE_k^2 \frac{\sqrt{1-m^{*2}/E_k^2}}{E_k^2-\frac{1}{4}k^2}\,. \tag{B.13}$$

Note that ReI – and thus $\mathrm{Im}\,\Pi^{\mathrm{ret}}$ – becomes finite for four-momenta $\sqrt{k^2} > 2m^*$. In vacuum, this is the threshold for the decay of a RPA meson into a quark and an antiquark. At $k^2 = 4(\Lambda^2+m^{*2})$ the decay width breaks down again since the cutoff limits the momenta of the outgoing quark and antiquark.

The result (B.12,B.13) suggests that $\mathrm{ReI}(k^2)\,\mathrm{sgn}(k_0)$ – the main contribution to $\mathrm{Im}\,\Pi_{\sigma,\pi}^{\mathrm{ret}}$ – and $\mathrm{ImI}(k^2)$ are related by a dispersion integral without the need for additional constant terms. We will use the abbreviation $\mathrm{ReI}^{\mathrm{ret}}(k_0,\vec{k}\,) = \mathrm{ReI}(k^2)\,\mathrm{sgn}(k_0)$ in the following ($\mathrm{ImI}^{\mathrm{ret}}(k^2) = \mathrm{ImI}(k^2)$). $\mathrm{ReI}^{\mathrm{ret}}(k_0,\vec{k}\,)$ is surely antisymmetric in k_0. Thus the dispersion relation for $\mathrm{ImI}^{(\mathrm{ret})}$ and $\mathrm{ReI}^{\mathrm{ret}}$ is in general given by

$$\mathrm{ImI}(k_0,\vec{k}\,) = -\frac{1}{\pi}\,\mathcal{P}\int\limits_0^\infty dq_0^2 \frac{\mathrm{ReI}^{\mathrm{ret}}(q_0,\vec{k}\,)}{q_0^2-k_0^2} + \mathrm{const.} \tag{B.14}$$

Inserting $0 = \vec{k}^2 - \vec{k}^2$ in the denominator of the integrand and introducing $E_k^2 = \frac{1}{4}(q_0^2-\vec{k}^2)$ yields

$$\mathrm{ImI}(k_0,\vec{k}\,) = -\frac{1}{\pi}\,\mathcal{P}\int\limits_{-\frac{1}{4}\vec{k}^2}^\infty dE_k^2 \frac{\mathrm{ReI}^{\mathrm{ret}}(\sqrt{4E_k^2+\vec{k}^2},\vec{k}\,)}{E_k^2-\frac{1}{4}k^2} + \mathrm{const.}$$

Note that the arguments of $\mathrm{ReI}^{\mathrm{ret}}$ correspond to a four-momentum with the square value $4E_k^2$. Due to the limits of the integration, the energy argument of $\mathrm{ReI}^{\mathrm{ret}}$ will

always be positive. Thus $\mathrm{ReI}^{\mathrm{ret}}((4E_k^2+\vec{k}^2)^{1/2},\vec{k}\,)$ is equivalent to $\mathrm{ReI}(4E_k^2)$ in the integrand. Inserting the analytical result for ReI from Eq. (B.12) we get

$$\mathrm{ImI}(k_0,\vec{k}\,)=\frac{1}{16\pi^2}\int\limits_{m^{*2}}^{\Lambda^2+m^{*2}}dE_k^2\frac{\sqrt{1-m^*/E_p^2}}{E_p^2-\frac{1}{4}k^2}+\text{const.}$$

This result from the dispersion relation is identical to the result of the analytical calculation (B.13) for const. $=0$.

When the real part of the polarization $\Pi^{\mathrm{ret}}_{\sigma,\pi}(k^2)$ shall be calculated from a dispersion integral it must be taken into account that the k_0 dependence of $\mathrm{Im}\,\Pi^{\mathrm{ret}}_{\sigma}$ and $\mathrm{Im}\,\Pi^{\mathrm{ret}}_{\pi}$ is not given by $\mathrm{ReI}^{\mathrm{ret}}$ alone but by the products $(k^2-4m^{*2})\mathrm{ReI}^{\mathrm{ret}}(k_0,\vec{k}^2)$ and $k^2\mathrm{ReI}^{\mathrm{ret}}(k_0,\vec{k}^2)$, respectively. Calculating the dispersion integral over $\mathrm{ReI}^{\mathrm{ret}}$ and multiplying the result with a factor k^2 – i.e., inserting the dispersive result for ImI into $\mathrm{Re}\,\Pi^{\mathrm{ret}}_{\sigma,\pi}$ – is not equivalent to calculating a dispersion integral over $k^2\mathrm{ReI}^{\mathrm{ret}}\sim\mathrm{Im}\,\Pi^{\mathrm{ret}}_{\sigma,\pi}$. The difference of both calculations is a k_0 independent term,

$$\begin{aligned}k^2\mathrm{ImI}(k_0,\vec{k}\,)&=-\frac{1}{\pi}k^2\,\mathcal{P}\int\limits_0^\infty dq_0^2\frac{\mathrm{ReI}^{\mathrm{ret}}(q_0,\vec{k}\,)}{q_0^2-k_0^2}\\&=\frac{1}{\pi}\int\limits_0^\infty dq_0^2\mathrm{ReI}^{\mathrm{ret}}(q_0,\vec{k}\,)-\frac{1}{\pi}\,\mathcal{P}\int\limits_0^\infty dq_0^2\frac{(q_0^2-\vec{k}^2)\mathrm{ReI}^{\mathrm{ret}}(q_0,\vec{k}\,)}{q_0^2-k_0^2}\\&=\underbrace{\frac{1}{\pi}\int\limits_0^\infty dq_0^2\mathrm{ReI}^{\mathrm{ret}}(q_0,\vec{k}\,)}_{\text{const. in }k_0}-\frac{1}{2N_fN_c\pi}\,\mathcal{P}\int\limits_0^\infty dq_0^2\frac{\mathrm{Im}\,\Pi^{\mathrm{ret}}_{\pi}(q_0,\vec{k}\,)}{q_0^2-k_0^2}\,,\end{aligned}\tag{B.15}$$

and likewise for the σ case. We have shown that the first approach, using the dispersion integral over $\mathrm{ReI}^{\mathrm{ret}}$ and multiplying with k^2 afterwards, is equivalent to the direct calculation of $\mathrm{Re}\,\Pi^{\mathrm{ret}}_{\sigma,\pi}$. This means that the constant term in the last line of Eq. (B.15) must be calculated explicitly when $\mathrm{Re}\,\Pi^{\mathrm{ret}}_{\sigma,\pi}$ is calculated from a dispersion integral over $\mathrm{Im}\,\Pi^{\mathrm{ret}}_{\sigma,\pi}$,

$$\begin{aligned}\mathrm{Re}\,\Pi^{\mathrm{ret}}_{\sigma,\pi}(k)&=\frac{1}{\pi}\,\mathcal{P}\int\limits_0^\infty dq_0^2\frac{\mathrm{Im}\,\Pi^{\mathrm{ret}}_{\sigma,\pi}(q_0,\vec{k}\,)}{q_0^2-k_0^2}\\&\quad-\frac{1}{2\mathrm{G}}\frac{\Sigma^{\mathrm{H}}}{m^*}-\frac{2N_fN_c}{\pi}\int\limits_0^\infty dq_0^2\mathrm{ReI}^{\mathrm{ret}}(q_0,\vec{k}\,)\,.\end{aligned}\tag{B.16}$$

The first term of the expression on the rhs. is the regular dispersion integral. The two other terms are k_0 independent terms that cannot be calculated dispersively from

$\mathrm{Im}\,\Pi^{\mathrm{ret}}_{\sigma,\pi}$. They are important and must not be neglected. For example, the second term on the rhs. of (B.16) is relevant for the chiral behavior of the RPA pion, as discussed earlier.

A decomposition similar to (B.16) is found for the full $\mathcal{O}(1/N_c)$ approach, see Section 3.6 for details. Note that Π_{n} in Eq. (3.54) corresponds to the second term of (B.16) and $\Pi^{\mathrm{ret}}_{\mathrm{d}}$ in (3.54) corresponds to the sum of the first and the third term of (B.16).

Finally we note that $\mathrm{Re}\,\Pi^{\mathrm{ret}}_{\sigma,\pi}(k)$ does not reduce to $-\frac{1}{2\mathrm{G}}\frac{\Sigma^{\mathrm{H}}}{m^*}$ in the limit $k^2 \to \infty$. Instead, we find using (B.12,B.14):

$$\mathrm{Re}\,\Pi^{\mathrm{ret}}_{\sigma,\pi}(k) \quad \xrightarrow{k^2\to\infty} \quad -\frac{1}{2\mathrm{G}}\frac{\Sigma^{\mathrm{H}}}{m^*} + \frac{N_f N_c}{2\pi^2}\int\limits_{m^{*2}}^{\Lambda^2+m^{*2}} dE_k^2 \sqrt{1-m^{*2}/E_k^2}\,. \tag{B.17}$$

C Feynman rules of the real-time formalism

We use the real-time formalism (see Section 2.6 and [Dan84, BM90, Das97]) for the calculation of self-energies and polarizations at finite quark densities. In this formalism, the time arguments of operators are placed on the closed time-path shown in Fig. C.1 and the time ordering along the real time axis is replaced by a path ordering along the contour. The path-ordered (quark) Green's function $\mathrm{S}^{\mathrm{P}}(1,2)$ is given by

$$\begin{aligned}\mathrm{S}^{\mathrm{P}}(1,2) &= -i\left\langle \mathrm{P}[\psi(1)\bar{\psi}(2)]\right\rangle \\ &= \Theta_C(t_1,t_2)\,\mathrm{S}^{>}(1,2) - \Theta_C(t_2,t_1)\,\mathrm{S}^{<}(1,2)\end{aligned}$$

where $\mathrm{S}^{\gtrless}$ are the usual non-ordered propagators, cf. (2.17), and Θ_C is the generalized step function on the time-path (2.16). This scheme allows the derivation of Feynman rules for systems with finite chemical potentials and temperatures [Dan84]. The main difference of these rules to the Feynman rules of standard (ground state) perturbation theory is that all time integrals are replaced by integrals along the contour C.

In the following, we will first introduce the Feynman rules for the evaluation of path-ordered self-energies and polarizations. Then, we will turn to their time-ordered and non-ordered counterparts. For those quantities – that are more relevant for the present work – a simplified set of Feynman rules in coordinate space and momentum space will be presented.

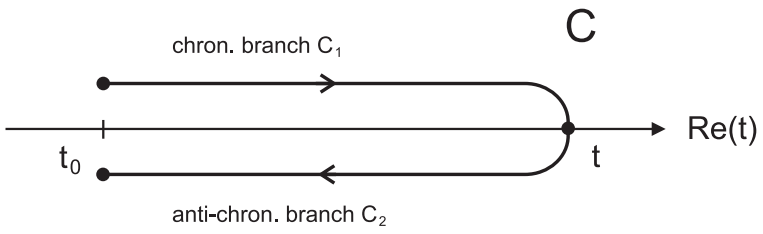

Figure C.1: The closed time-path of the real-time formalism in the complex plane. Points on the upper branch are always considered to be earlier than points on the lower branch.

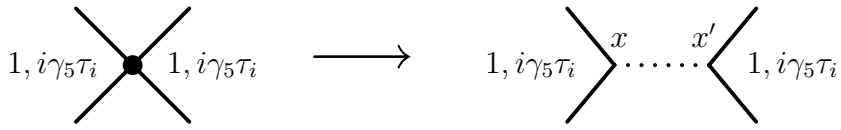

Figure C.2: The four-point vertices of the NJL Lagrangian (2.1) must be replaced by finite interaction lines $\sim \delta^4(x - x')$ so that all topologically distinct diagrams can be found, cf. Fig.2.2.

C.1 Feynman rules on a closed time-path

The Feynman rules that can be found in [Dan84] have been derived for a non-relativistic system of particles (fermions or bosons) that interact via a potential $V(\vec{x}\,)$. Those rules can be adopted to the NJL interaction that is given in Eq. (2.1) and in Eq. (2.4) as a quark–quark and a quark–meson interaction, respectively. Note that the Feynman rules for a relativistic fermion–meson interaction that is very similar to (2.4) can be found in [Gre92].

C.1.1 Rules for the quark–quark interaction

Before we introduce the Feynman rules, it is important to note that all topologically distinct diagrams must be found. This is difficult when the four-point vertices of the local interaction in Eq. (2.1) are represented by the simple dots shown in Fig. 2.1(a). Hence, we will replace the pointlike vertices – like in Fig. 2.2 – by finite interaction lines. This is illustrated in Fig. C.2. To avoid confusion, we will not refer to the points, where two quark lines and an interaction line meet, as vertices. Instead, we will call these points endpoints of an interaction line. A full (NJL) vertex is given by the interaction line *and* the two corresponding endpoints.

The following (coordinate space) Feynman rules for the evaluation of the path-ordered self-energy $-i\,\Sigma^{\mathrm{P}}(1,2)$ are obtained for the quark–quark interaction given by the NJL Lagrangian in Eq. (2.1), cf. [Dan84]:

1. Draw all directed diagrams that are topologically distinct and connected, using the vertices of Fig. C.2 (right side).

2. A quark line that runs from $(\vec{x}', t')$ to $(\vec{x}, t)$ stands for a non-interacting Green's function $i\,\mathrm{S}_0^{\mathrm{P}}(1,1')$. When the two arguments are equal, the line is interpreted as $i\,\mathrm{S}_0^{<}(1,1)$.

3. Each interaction line represents a factor

$$2i\mathrm{G} \times \delta_C(t,t')\delta^3(\vec{x} - \vec{x}')\,,$$

where δ_C is the generalized δ-function on the contour,

$$\delta_C(t,t') \begin{cases} +\delta(t-t') & \text{for } t,t' \in C_1, \\ -\delta(t-t') & \text{for } t,t' \in C_2, \\ 0 & \text{for } t \in C_1, t' \in C_2 \text{ or } t \in C_2, t' \in C_1. \end{cases}$$

4. A spin- and isospin factor $\mathbb{1}_{4\times4}\mathbb{1}_{2\times2}$ or $i\gamma^5\tau_i$ is assigned to each endpoint of an interaction line (identical factors at both ends).

5. Each closed fermion loop generates a factor (-1).

6. Integrate all internal variables over space and – along the contour C – over time from t_0 to t_0.

Note that the time integrals along C_1 and C_2 run into opposite directions. This is compensated by the different signs of $\delta_C(t,t')$ on C_1 and C_2.

C.1.2 Rules for the quark–meson interaction

Let us now consider the Feynman rules for the quark–meson interaction in Eq. (2.4). The corresponding $q\bar{q}-\sigma$ and $q\bar{q}-\pi$ vertices are shown in Fig. 2.1(b). Note that the vertices at the ends of a π^+ line are not given by two π^+ vertices but by a π^+ and a π^- vertex (and likewise for a π^- line), cf. Eq. (2.41). This should be clear from the construction of the RPA propagators, see Eqs. (2.2,2.7) and Fig. 2.3. To avoid confusion, factors $\Gamma_-(\Gamma_+)$ at the end of a $\pi_+(\pi_-)$ line will be relabeled as $\tilde{\Gamma}_+(\tilde{\Gamma}_-)$ below, cf. (2.3).

Taking the above considerations into account, we find the following Feynman rules for the evaluation of path-ordered self-energies $-i\,\Sigma^{\mathrm{P}}(1,2)$ and polarizations $-i\,\Pi_l^{\mathrm{P}}(1,2)$ (see also [Gre92]):

1. Draw all directed diagrams that are topologically distinct and connected, using the vertices in Fig. 2.1(b).

2. A quark line that runs from $(\vec{x}',t')$ to $(\vec{x},t)$ stands for a non-interacting Green's function $i\,\mathrm{S}_0^{\mathrm{P}}(1,1')$. When the two arguments are equal, the line is interpreted as $i\,\mathrm{S}_0^{<}(1,1)$.

3. A meson line that runs from $(\vec{x}',t')$ to $(\vec{x},t)$ stands for one of the non-interacting Green's functions $i\,\Delta_{0,l}^{\mathrm{P}}(1,1')$ with $l=\sigma,0,\pm$.

4. A spin- and isospin factor $-i\Gamma_l$ or $-i\tilde{\Gamma}_l$ is assigned to each vertex.

5. Each closed fermion loop generates a factor (-1).

6. Integrate all internal variables over the full space and – along the contour C – over time from t_0 to t_0.

As suggested by Eq. (2.7), the dynamically generated mesons can be understood as a generalization of the (local) interaction line shown in Fig. C.2. The Feynman rules for the quark–quark interaction and the quark–meson interaction differ only in rules 3 and 4 – the interaction line is replaced by a meson propagator and the (iso-)spin factors are rearranged like in the transition from (2.1) to (2.2).

C.2 Feynman rules on the divided contour

As shown in Section 2.6, the propagators $\mathrm{S}^{\mathrm{c,a,}\gtrless}$ correspond to special cases of S^{P}, where each time argument is located on a fixed branch of the contour,

$$\begin{aligned}
\mathrm{S}^{\mathrm{c}}(1,2) &= -i\left\langle \mathrm{T}[\psi(1)\bar{\psi}(2)]\right\rangle && \text{for } t_1, t_2 \in C_1\,,\\
\mathrm{S}^{\mathrm{a}}(1,2) &= -i\left\langle \bar{\mathrm{T}}[\psi(1)\bar{\psi}(2)]\right\rangle && \text{for } t_1, t_2 \in C_2\,,\\
\mathrm{S}^{>}(1,2) &= -i\left\langle \psi(1)\bar{\psi}(2)\right\rangle && \text{for } t_1 \in C_2, t_2 \in C_1\,,\\
\mathrm{S}^{<}(1,2) &= i\left\langle \bar{\psi}(2)\psi(1)\right\rangle && \text{for } t_1 \in C_1, t_2 \in C_2\,.
\end{aligned} \tag{C.1}$$

The time arguments of the self-energies $\Sigma^{\mathrm{c,a,}\gtrless}$ (and the polarizations $\Sigma_l^{\mathrm{c,a,}\gtrless}$) have the same structure. This allows us to use a simplified version of the Feynman rules: When the location of the time arguments on the branches is known, it is possible to split up the contour into its branches in the calculations [Dan84]. Thus, the integral along the full time-path contour can be avoided and it becomes possible to introduce Feynman rules in momentum space.

We will discuss the coordinate space Feynman rules only for the quark–quark interaction (2.1) here. This should be sufficient to understand the changes that arise when the contour is separated into its branches. In our actual calculations, we use the Feynman rules in momentum space. These rules will be discussed for both interactions (2.1,2.4).

C.2.1 Coordinate space rules for the quark–quark interaction

The Feynman rules for the evaluation of a self-energy $-i\,\Sigma^{\mathrm{c,a,}\gtrless}(1,2)$, using the quark–quark interaction of Eq. (2.1), are given by (see [Dan84]):

1. Split up the drawing plane into two parts with a vertical line. Each part corresponds to a branch of the contour (chronological or anti-chronological). For each function argument, place a point on the appropriate side of the line that divides the branches. The positions for a specific type of function are given in (C.1).

2. Draw all diagrams that are topologically distinct and connected, using the vertices of Fig. C.2 (right side). Assign a direction to each quark line. Diagrams that are cut differently by the vertical line are distinct. Interaction lines may not cross the division line.

3. Depending on the location of the start- and endpoints with respect to the division line, cf. (C.1), a quark line stands for a non-interacting Green's function $i\,\mathrm{S}_0^>$, $i\,\mathrm{S}_0^<$, $i\,\mathrm{S}_0^\mathrm{c}$, or $i\,\mathrm{S}_0^\mathrm{a}$. When the two arguments are equal, the line is interpreted as $i\,\mathrm{S}_0^<$.

4. An interaction line represents a factor $2i\mathrm{G} \times \delta^4(x - x')$.

5. An additional factor (-1) corresponds to each interaction line on the anti-chronological branch.

6. A spin- and isospin factor $\mathbb{1}_{4\times4}\mathbb{1}_{2\times2}$ or $i\gamma^5\tau_i$ is assigned to each endpoint of an interaction line (identical factors at both ends).

7. Each closed fermion loop generates a factor (-1).

8. Integrate all internal variables over space and time (from t_0 to the largest time argument of the evaluated function).

9. Every time integral on the anti-chronological branch generates a factor (-1).

The rules 4 and 5 replace rule 3 of Section C.1.1 – the generalized δ-function on the contour is split up into a regular δ-function and a factor (-1) on the anti-chronological branch. Likewise, the rules 8 and 9 replace rule 6 of Section C.1.1. The factor (-1) of rule 9 arises since the time integrals along C_1 and C_2 run into opposite directions (this is not taken into account by rule 8). Note that the combination of rules 5 and 9 yields an overall factor (-1) for each internal NJL vertex (interaction line and endpoints) on the anti-chronological branch.

C.2.2 Momentum space rules for the quark–quark interaction

We come now to the Feynman rules in momentum space. These are the rules that are most suitable to work out the diagrams in the Dyson–Schwinger equations in Fig. 2.11 since our whole approach is based on momentum space calculations. For the quark–quark interaction (2.1), we find the following rules for the evaluation of $-i\,\Sigma^{\mathrm{c,a,}\gtrless}(k)$ [Dan84]:

1. Draw all diagrams as described by the coordinate space rules 1 and 2 of Section C.2.1.

2. Assign a four-momentum variable to each quark line and each interaction line.

3. Impose energy and momentum conservation at the endpoints of each interaction line.

4. A quark line on the chronological branch stands for $i\,\mathrm{S}_0^{\mathrm{c}}$, a quark line on the anti-chronological branch stands for $i\,\mathrm{S}_0^{\mathrm{a}}$. Quark lines that cross the division line stand for $i\,\mathrm{S}_0^{\gtrless}$.

5. An interaction line represents a factor $2i\mathrm{G}$.

6. An additional factor (-1) corresponds to each interaction line on the anti-chronological branch.

7. A spin- and isospin factor $\mathbb{1}_{4\times4}\mathbb{1}_{2\times2}$ or $i\gamma^5\tau_i$ is assigned to each endpoint of an interaction line (identical factors at both ends).

8. An additional factor (-1) corresponds to each internal endpoint of an interaction line on the anti-chronological branch.

9. Each closed fermion loop generates a factor (-1).

10. Integrate over all internal energies and momenta.

Like in coordinate space, the combination of rules 6 and 8 yields an overall factor (-1) for each internal NJL vertex (interaction line and endpoints) on the anti-chronological branch.

C.2.3 Momentum space rules for the quark–meson interaction

Finally, we present the momentum space Feynman rules for the evaluation of the self-energies $-i\,\Sigma^{\mathrm{c,a},\gtrless}(k)$ and the polarizations $-i\,\Pi_l^{\mathrm{c,a},\gtrless}(k)$. Using the interaction in Eq. (2.4), we find:

1. Draw all diagrams as described by the coordinate space rules 1 and 2 of Section C.2.1, using the vertices in Fig. 2.1(b).

2. Assign a four-momentum variable to each quark line and each meson line.

3. Impose energy and momentum conservation at each vertex.

4. A quark line on the chronological branch stands for $i\,\mathrm{S}_0^{\mathrm{c}}$, a quark line on the anti-chronological branch stands for $i\,\mathrm{S}_0^{\mathrm{a}}$. Quark lines that cross the division line stand for $i\,\mathrm{S}_0^{\gtrless}$.

5. A meson line on the chronological branch stands for $i\,\Delta_{0,l}^{\mathrm{c}}$, a meson line on the anti-chronological branch stands for $i\,\Delta_{0,l}^{\mathrm{a}}$. Meson lines that cross the division line stand for $i\,\Delta_{0,l}^{\gtrless}$. $(l = \sigma, 0, \pm)$

6. A spin- and isospin factor $-i\Gamma_l$ or $-i\tilde{\Gamma}_l$ is assigned to each vertex.

7. An additional factor (-1) corresponds to each internal vertex on the anti-chronological branch.

8. Each closed fermion loop generates a factor (-1).

9. Integrate over all internal energies and momenta.

Note that meson lines – in contrast to the (local) interaction line of the quark–quark interaction – may cross the division line. There is no rule that assigns a factor (-1) to meson lines on the anti-chronological branch (like rule 6 of Section C.2.2). Such factors are implicitly in rule 5 – different meson propagators are used according to the position of their endpoints on the contour.

C.3 Concluding remarks

In the previous sections, we have not derived Feynman rules for the evaluation of retarded or advanced quantities. This has a simple reason: The position of the time arguments on the two branches of the time-path contour are not well defined. We can see that in the definition of the retarded quark propagator (2.18), where the contributions from $\mathrm{S}^{\mathrm{c}}(1,2)$ with $t_1, t_2 \in C_1$ and $\mathrm{S}^{<}(1,2)$ with $t_1 \in C_1, t_2$ mix. As we have discussed at the end of Section 3.5, this is not a crucial problem. For example, the retarded self-energy can be constructed from time-ordered self-energies – for $T = 0$ they differ only in the sign of the imaginary part, cf. (3.25).

The Feynman rules that are presented here, identify particle lines with free, non-interacting propagators – this is the basic idea of a perturbative approach. In the (self-consistent) Dyson–Schwinger equations of Fig. 2.11, however, the lines correspond to full in-medium propagators. Thus, we use the Feynman rules (of Sections C.2.2 and C.2.3) to obtain analytic expression from the self-energy diagrams in the Dyson–Schwinger equations. But instead of inserting free propagators, we use full propagators in these expressions. If this is done, one has to exclude two-particle reducible diagrams[1] to avoid double counting.

[1] These are diagrams which contain more than one propagator with the same momentum.

D Energy integral over the retarded quark propagator

The two poles of the retarded quark propagator $\mathrm{S}^{\mathrm{ret}}(p)$ are located in the same complex energy half plane. Thus the contour integral along the real p_0 axis that is closed in the upper half plane as shown in Fig. D.1 is zero,

$$\oint dp_0\, \mathrm{S}^{\mathrm{ret}}(p) = \int_{-\infty}^{+\infty} dp_0\, \mathrm{S}^{\mathrm{ret}}(p) + \int_{\cap} dp_0\, \mathrm{S}^{\mathrm{ret}}(p) = 0\,. \tag{D.1}$$

The integral $\int_{-\infty}^{+\infty} dp_0\, \mathrm{S}^{\mathrm{ret}}(p)$ occurs frequently in the present work. Because of Eq. (D.1) one might suspect that this integral is zero. It will turn out, however, that the integral along the real p_0 axis and the integral along the semicircle at large p_0^2 are finite and cancel each other in (D.1).

We can calculate the integral along the semicircle rather easily. At infinitely high energies it is safe to assume that no interactions occur. Thus the full propagator can be replaced by the free one,

$$\mathrm{S}^{\mathrm{ret}}_{\mathrm{fr.}}(p) = \frac{\not{p} + m}{p^2 - m^2} = \frac{p_0\gamma_0 - \vec{p}\cdot\vec{\gamma} + m}{p^2 - m^2} \quad \xrightarrow{p_0^2\to\infty} \quad \frac{p_0\gamma_0 - \vec{p}\cdot\vec{\gamma} + m}{p_0^2}\,.$$

Along the semicircle we have $p_0^2 \gg \vec{p}^{\,2}$ and $p_0^2 \gg m^2$. Therefore $\vec{p}^{\,2}$ and m are negligible in the denominator. Parametrizing the complex p_0 along the semicircle,

$$p_0 = Pe^{i\phi}\,, \quad \frac{dp_0}{d\phi} = iPe^{i\phi} = ip_0\,,$$

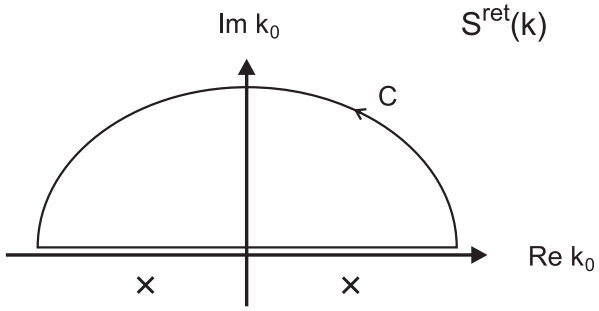

Figure D.1: The poles of the retarded quark propagator $\mathrm{S}^{\mathrm{ret}}$ are both located in the lower complex half plane. The integral along the shown contour C vanishes.

we get

$$\int_{\cap} dp_0\, \mathrm{S}^{\mathrm{ret}}(p) = \int_0^{\pi} d\phi i p_0 \frac{p_0\gamma_0 - \vec{p}\cdot\vec{\gamma} + m}{p_0^2}\bigg|_{p_0=Pe^{i\phi}} \tag{D.2}$$
$$= i\gamma_0 \int_0^{\pi} d\phi + i(-\vec{p}\cdot\vec{\gamma} + m)\int d\phi \underbrace{\frac{e^{-i\phi}}{P}}_{=0\,(P\to\infty)} = i\pi\gamma_0\,.$$

For the real p_0 integral it follows immediately from (D.1):

$$\int_{-\infty}^{+\infty} dp_0\, \mathrm{S}^{\mathrm{ret}}(p) = -i\pi\gamma_0\,. \tag{D.3}$$

The integral has the same Lorentz structure as the propagator (2.23). The scalar and the $\vec{\gamma}$-component are zero while the γ_0-component has a finite value,

$$\int_{-\infty}^{+\infty} dp_0 \mathrm{Im}\, \mathrm{S}_0^{\mathrm{ret}}(p) = -\pi\,, \quad \int_{-\infty}^{+\infty} dp_0 \mathrm{Re}\, \mathrm{S}_0^{\mathrm{ret}}(p) = 0\,. \tag{D.4}$$

Note that the integral over the trace of the retarded propagator vanishes since $\mathrm{tr}\,\gamma_0 = 0$,

$$\int_{-\infty}^{+\infty} dp_0\, \mathrm{tr}\, \mathrm{S}^{\mathrm{ret}}(p) = 0\,. \tag{D.5}$$

Finally it should be noted that the normalization of the Lorentz components of the quark spectral function defined in (2.26) can be directly read off from Eq. (D.3),

$$\int_{-\infty}^{+\infty} \frac{dp_0}{2\pi}\mathcal{A}_0(p) = 1\,, \quad \int_{-\infty}^{+\infty} \frac{dp_0}{2\pi}\mathcal{A}_s(p) = 0\,, \quad \int_{-\infty}^{+\infty} \frac{dp_0}{2\pi}\mathcal{A}_v(p) = 0\,. \tag{D.6}$$

The explicit expression for the RPA meson polarizations $\Pi_l^{\mathrm{c}}(k)$ in Eq. (3.27) includes another interesting integral that might be zero,

$$\int_{-\infty}^{+\infty} dp_0\, \mathrm{Tr}\left[\tilde{\Gamma}_l\, \mathrm{S}^{\mathrm{ret}}(p)\Gamma_l\, \mathrm{S}^{\mathrm{ret}}(p-k)\right]$$
$$\sim \int_{-\infty}^{+\infty} dp_0\, \left[\mathrm{S}_0^{\mathrm{ret}}(p)\, \mathrm{S}_0^{\mathrm{ret}}(p-k) \pm \mathrm{S}_\mu^{\mathrm{ret}}(p)\, \mathrm{S}_{\mathrm{ret}}^{\mu}(p-k)\right]\,,$$

where the upper sign refers to $l = s$ and the lower sign to $l = 0, \pm$. All the poles of both propagators – and thus of their Lorentz components – are located in the same complex half plane. So the contour integral along the closed path C from Fig. D.1 is again zero. The integral along the semicircle in the upper half plane can be calculated in analogy to (D.2). Using

$$\mathrm{S}^{\mathrm{ret}}_{\mathrm{fr.}}(p-k) \quad \xrightarrow{p_0^2 \to \infty} \quad \frac{(p-k)_\mu \gamma^\mu + m}{p_0^2}$$

we get

$$\begin{aligned}
&\int_{\cap} dp_0 \left[\mathrm{S}^{\mathrm{ret}}_0(p)\, \mathrm{S}^{\mathrm{ret}}_0(p-k) \pm \mathrm{S}^{\mathrm{ret}}_\mu(p)\, \mathrm{S}^{\mu}_{\mathrm{ret}}(p-k) \right] \\
&\quad = \pm \int_0^\pi d\phi i p_0 \left[\frac{p_0^2 - p_0 k_0}{p_0^4} - \frac{\vec{p}^{\,2} - \vec{p}\cdot\vec{k} \pm m^2}{p_0^4} \right] \Bigg|_{p_0 = P e^{i\phi}} \overset{P\to\infty}{=} 0\,.
\end{aligned}$$

Since the integral along the closed contour is zero, too, it follows that the integral along the real p_0 axis must vanish,

$$\begin{aligned}
&\int_{-\infty}^{+\infty} dp_0 \left[\mathrm{S}^{\mathrm{ret}}_0(p)\, \mathrm{S}^{\mathrm{ret}}_0(p-k) \pm \mathrm{S}^{\mathrm{ret}}_\mu(p)\, \mathrm{S}^{\mu}_{\mathrm{ret}}(p-k) \right] \\
&\quad = \int_{-\infty}^{+\infty} dp_0\, \mathrm{Tr}\left[\tilde{\Gamma}_l\, \mathrm{S}^{\mathrm{ret}}(p) \Gamma_l\, \mathrm{S}^{\mathrm{ret}}(p-k) \right] = 0\,. \qquad \text{(D.7)}
\end{aligned}$$

E Quarks and antiquarks, density and momentum distribution

The quark spectral function $\mathcal{A}(k)$ consists of states at positive and negative energies (see the schematic plot in Fig. 2.17). For the interpretation of our results – not for the actual calculations – it is helpful to split up the spectral function into a quark and an antiquark part. This means that we reinterpret the quark states below a certain energy threshold as antiquark states. Since an antiquark corresponds to a hole in the Fermi sea, we also have to invert the occupation probability of these states. A populated quark state is equivalent to a free antiquark state. In this appendix we will discuss how to disentangle the quarks and the antiquarks in our $\mathcal{O}(1/N_c)$ approach where the spectral function contains a broad range of off-shell states.

In the vacuum it is easy to identify the antiquark region of the spectral function. The occupation probability of a *quark* state at the energy k_0 is given by the Fermi distribution function $\mathrm{n_F}(k_0)$. At zero temperature and chemical potential, all states at negative energies are populated by quarks (Fermi sea) and all states at positive energies are free. Since there are no quarks and no antiquarks in the vacuum, we can identify all (populated quark) states at negative energies with (free) antiquark states. Note that the border between the quark and the antiquark states ($q\bar{q}$ border) is not necessarily located at $k_0 = 0$ for finite chemical potentials. The self-energy may induce (momentum dependent) shifts.

The density and the momentum distribution of the quarks in the medium are closely related to the distinction of quarks and antiquarks. Both quantities are determined by integrals over $\mathcal{A}(k)\mathrm{n_F}(k_0)$. In those integrals, contributions from the populated quark states that are reinterpreted as *free* antiquark states should not be considered. Below, we will see that the density and the momentum distribution do not only depend on the $q\bar{q}$ border but can also be used to determine its location.

E.1 Mean-field approaches

Before we discuss the $\mathcal{O}(1/N_c)$ case in more detail, let us first have a brief look at the Hartree and the Hartree–Fock approximations. On the quasiparticle level it is a straightforward exercise to distinguish between quark and antiquark states. The full strength of the spectral function is concentrated in the on-shell peaks, off-shell states do not exist. In the Hartree approximation, the Lorentz components of the spectral

function are (anti-)symmetric in k_0, cf. Section 4.1.1,

$$\mathcal{A}(k) = 2\pi(\not{k} + m^*)\frac{1}{2E_k}[\delta(k_0 - E_k) - \delta(k_0 + E_k)]\,, \tag{E.1}$$

where $E_k = [\vec{k}^2 + (m_0 + \Sigma^{\mathrm{H}})]^{1/2}$. Σ^{H} is the Lorentz scalar Hartree self-energy (3.2). We can identify the on-shell peak at positive energies with a quark peak and the on-shell peak at negative energies with an antiquark peak. Due to the (anti-)symmetry of $\mathcal{A}(k)$, the border between quarks and antiquarks can be drawn at $k_0 = 0$ (where the two peaks meet for $\vec{k} = 0$ when the quarks are massless).

We know from (D.6) that the γ_0-component of the spectral function is normalized. In the Hartree approximation we find in addition

$$\int\limits_{-\infty}^{0} \frac{dk_0}{2\pi}\mathcal{A}_0(k) = \frac{1}{2}\,, \qquad \int\limits_{0}^{+\infty} \frac{dk_0}{2\pi}\mathcal{A}_0(k) = \frac{1}{2}\,. \tag{E.2}$$

I.e., the quark and the antiquark states are normalized to 1/2 separately.

In the Hartree–Fock approximation, the on-shell peaks are shifted by the γ_0-component of the Fock self-energy,

$$\mathcal{A}(k) \;\sim [\delta(k_0 - \Sigma_0^{\mathrm{F}} - E_k) - \delta(k_0 - \Sigma_0^{\mathrm{F}} + E_k)]\,, \tag{E.3}$$

where $E_k = [\vec{k}^2 + (m_0 + \Sigma^{\mathrm{H}} + \Sigma_s^{\mathrm{F}})]^{1/2}$. Recall that the $\vec{\gamma}$-component of Σ^{F} is zero, cf. Section 3.1.2. The Lorentz components of the Hartree–Fock spectral function are (anti-)symmetric in the effective energy $\tilde{k}_0 = k_0 - \Sigma_0^{\mathrm{F}}$. Thus, the border between the quark and the antiquark states is located at $\tilde{k}_0 = 0$, i.e., $k_0 = \Sigma_0^{\mathrm{F}}$. For the normalization of the spectral function we find in analogy to (E.2)

$$\int\limits_{-\infty}^{\Sigma_0^{\mathrm{F}}} \frac{dk_0}{2\pi}\mathcal{A}_0(k) = \frac{1}{2}\,, \qquad \int\limits_{\Sigma_0^{\mathrm{F}}}^{+\infty} \frac{dk_0}{2\pi}\mathcal{A}_0(k) = \frac{1}{2}\,. \tag{E.4}$$

Note that, in practice, one will not introduce an effective energy in the Hartree–Fock approximation but absorb the constant Σ_0^{F} into a redefined chemical potential [Kle92].

E.2 $\mathcal{O}(1/N_c)$ approach

E.2.1 Quarks and antiquarks

The spectral function of our $\mathcal{O}(1/N_c)$ approach has a more complicated structure than the quasiparticle spectral functions in (E.1,E.3). The energy and momentum dependent, complex self-energy Σ^{ret} shifts the on-shell peaks in a non-uniform way and generates a broad continuum of off-shell states. These off-shell states blur the

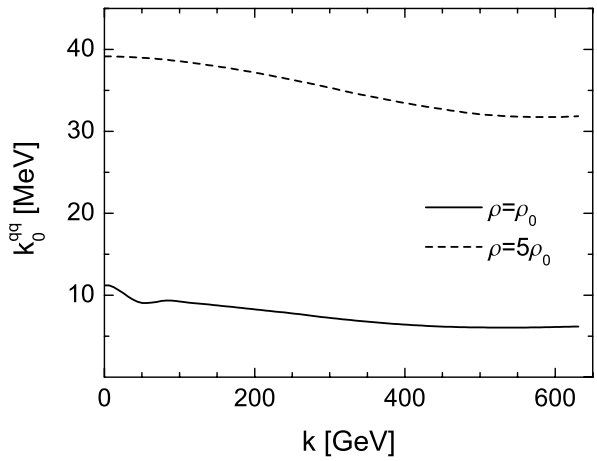

Figure E.1: The border between the quark and antiquark states $k_0^{q\bar{q}}(|\vec{k}\,|)$ of scheme I as defined in (E.5). Parameter set I has been used in the $\mathcal{O}(1/N_c)$ calculations at densities below and above the chiral phase transition.

distinction between quarks and antiquarks. Since the spectral function does not vanish between the on-shell peaks, the $q\bar{q}$ border must be drawn in a region where the spectral function is finite.

The mean-field approaches suggest two ways to define the $q\bar{q}$ border. First, we could draw the border – like in the Hartree–Fock approximation – where the real part of the effective energy $\mathrm{Re}\tilde{k}_0$, cf. (2.34), changes its sign. States at positive effective energies are then identified with quarks and states with negative effective energies as antiquarks. The energy $k_0^{q\bar{q}}(|\vec{k}\,|)$ that determines the position of the border is found by solving

$$\mathrm{Re}\tilde{k}_0\left(k_0^{q\bar{q}}(|\vec{k}\,|),|\vec{k}\,|\right)=0\,. \tag{E.5}$$

Second, we could demand that the quark and the antiquark part of the spectral function are separately normalized to 1/2, cf. (E.2,E.4). The location of the $q\bar{q}$ border is then determined by the integrals

$$\int\limits_{k_0^{q\bar{q}}(|\vec{k}\,|)}^{+\infty}\frac{dk_0}{2\pi}\mathcal{A}_0(k)=\frac{1}{2}\,,\qquad \int\limits_{-\infty}^{k_0^{q\bar{q}}(|\vec{k}\,|)}\frac{dk_0}{2\pi}\mathcal{A}_0(k)=\frac{1}{2}\,. \tag{E.6}$$

In the following, we will refer to the two definitions in Eqs. (E.5) and (E.6) as scheme I and scheme II, respectively.

To illustrate the density and momentum dependence of the $q\bar{q}$ border, we show some results for $k_0^{q\bar{q}}$ – calculated using scheme I – in Fig. E.1. At the lower density, i.e. in the chirally broken phase, $k_0^{q\bar{q}}$ remains very small with respect to the effective

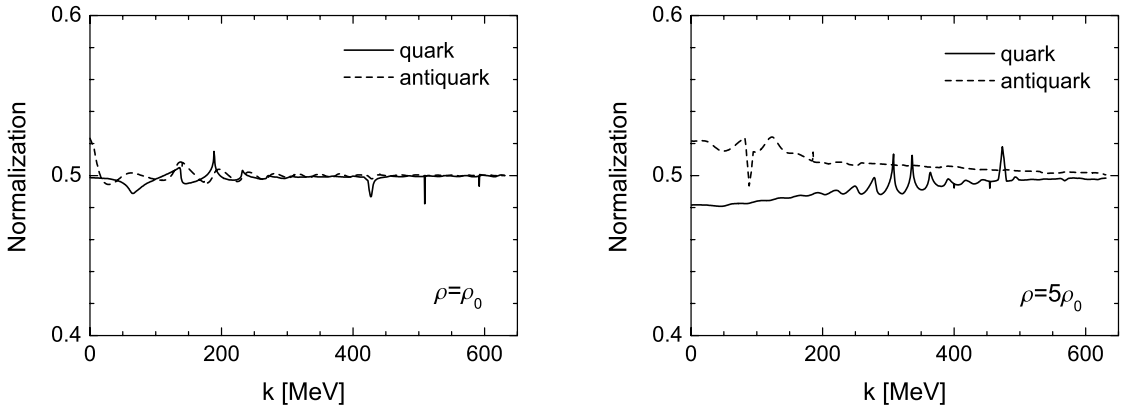

Figure E.2: The normalizations N_q and $N_{\bar{q}}$ of the quark and the antiquark part of the spectral function $\mathcal{A}_0$,respectively, as defined in Eq. (E.7) for scheme I. Note that $N_{\bar{q}}(|\vec{k}\,|) + N_q(|\vec{k}\,|) = 1$, cf. (2.28). See Fig. E.1 for more details.

quark mass. Since the short-range correlations are strongly density dependent, $k_0^{q\bar{q}}$ becomes larger in the chirally restored phase. The size of $k_0^{q\bar{q}}$ is comparable to the effective mass at the higher density. Nonetheless, $k_0^{q\bar{q}}$ remains small with respect to the cutoff.

A numerical check shows that scheme I and scheme II are not completely equivalent in the $\mathcal{O}(1/N_c)$ approach: Let us consider the normalizations of the quark and the antiquark states of the spectral function. When scheme I is used, the normalizations are given by

$$N_q(|\vec{k}\,|) = \int\limits_{\mathrm{Re}\tilde{k}_0=0}^{+\infty} \frac{dk_0}{2\pi}\mathcal{A}_0(k)\,, \qquad N_{\bar{q}}(|\vec{k}\,|) = \int\limits_{-\infty}^{\mathrm{Re}\tilde{k}_0=0} \frac{dk_0}{2\pi}\mathcal{A}_0(k)\,. \tag{E.7}$$

Numerical results for N_q and $N_{\bar{q}}$ can be found in Fig. E.2. The spikes on the curves are small numerical fluctuations (note the scale), we will come back to them below. In the chirally broken phase ($\rho = \rho_0$), no deviations of N_q and $N_{\bar{q}}$ from 1/2, i.e. from scheme II, are visible – within the numerical precision. In the chirally restored phase ($\rho = 5\rho_0$), however, we find deviations on the order of 5% at low momenta.

The discrepancies can be readily understood. The energy dependent quark width is not symmetric in $\mathrm{Re}\tilde{k}_0$ at finite chemical potential. Consequently, the off-shell states of the spectral function are also not symmetric, cf. Figs. 5.3-5.5. These states shift spectral strength across the border defined by $\mathrm{Re}\tilde{k}_0 = 0$. This is an effect that is not taken into account by scheme I. At higher densities, the width becomes larger and less symmetric in $\mathrm{Re}\tilde{k}_0$. Hence, the deviations of N_q and $N_{\bar{q}}$ from 1/2 are larger in the right panel of Fig. E.2. Note that the relations of (2.28), in particular $N_{\bar{q}}(|\vec{p}|) + N_q(|\vec{p}|) = 1$, still hold. No spectral strength is lost by the shifts across the $q\bar{q}$ border.

The results of Section 5.6 show that the short-range correlations saturate above the chiral phase transition. Hence, the deviations of N_q and $N_{\bar{q}}$ from 1/2 – and thus the discrepancies between scheme I and II – do not become much larger at densities above $5\rho_0$. We note that the position of the on-shell peaks is well defined with respect to the $q\bar{q}$ border in both schemes (the on-shell peaks of massless quarks and antiquarks meet at $\mathrm{Re}\tilde{k}_0 = 0$ for $\vec{k} = 0$).

To determine which of the two schemes is a more reasonable choice for our approach, we will turn to the quark density and the momentum distribution in the next section. A closer inspection of these quantities will show that the $q\bar{q}$ border that is defined by scheme II is analytically favorable. Numerically, however, the $q\bar{q}$ border of scheme I is easier to handle. This will lead to a compromise for the definition of the $q\bar{q}$ border, the density and the momentum distribution that is discussed at the end of Section E.2.2.

E.2.2 Density and momentum distribution

The number of quarks in the medium with a given four-momentum k is determined by $-i\,\mathrm{Tr}\,\gamma_0\,\mathrm{S}^<(k)$, cf. (2.25). We can find the quark density ρ by integrating the number of particles over energy and momentum. Using $\mathrm{S}^<(k) = i\mathcal{A}(k)\mathrm{n_F}(k_0)$, cf. (2.31), and $\mathrm{Tr}\,\gamma_0\mathcal{A} = 4N_fN_c\mathcal{A}_0$ yields

$$\mathrm{I}(\mu,T) = 4N_fN_c\int_\Lambda \frac{d^3k}{(2\pi)^3}\int_{-\infty}^{+\infty}\frac{dk_0}{2\pi}\mathrm{n_F}(k_0)\mathcal{A}_0(k)\,. \tag{E.8}$$

This is not yet the density. The integral sums up the populated quark states at all energies – including the states at negative energies which we interpret as free antiquark states. To find the actual quark density of the medium, the contributions from these states must be removed. We can easily do that by subtracting the result for I in the vacuum,

$$\rho(\mu,T) = \mathrm{I}(\mu,T) - \mathrm{I}(\mu=0)\,. \tag{E.9}$$

This definition of the density ensures that ρ vanishes for $\mu = 0$. As we will see below, the value of $\mathrm{I}(\mu=0)$ is independent of T.

It is possible to calculate $\mathrm{I}(\mu=0)$ analytically. Consider the energy integral

$$\mathrm{J}(|\vec{k}\,|,\mu,T) = \int_{-\infty}^{+\infty}\frac{dk_0}{2\pi}\mathcal{A}_0(k)\mathrm{n_F}(k_0) \tag{E.10}$$

that is part of (E.8). It can be split up into

$$\mathrm{J}(|\vec{k}\,|,\mu,T) = \underbrace{\int\frac{dk_0}{2\pi}\mathcal{A}_0(k)\left[\mathrm{n_F}(k_0)-\frac{1}{2}\right]}_{=0\quad(\mu=0)} + \frac{1}{2}\underbrace{\int\frac{dk_0}{2\pi}\mathcal{A}_0(k)}_{=1}\,. \tag{E.11}$$

Due to the structure of the integrand, the first term vanishes for $\mu = 0$: $\mathcal{A}_0(k)$ is symmetric in k_0 for $\mu = 0$ – recall the discussion in Section 5.2.1. $\mathrm{n_F}(k_0) - 1/2$, on the other hand, is antisymmetric,

$$\mathrm{n_F}(k_0) - \frac{1}{2} \overset{\mu=0}{=} \frac{1}{2} \cdot \frac{1 - e^{k_0/T}}{e^{k_0/T} + 1} = \frac{1}{2} \cdot \frac{e^{-k_0/T} - 1}{1 + e^{-k_0/T}} = \frac{1}{2} - \mathrm{n_F}(-k_0)\,. \tag{E.12}$$

The second term on the rhs. of (E.11) corresponds to the normalization of the spectral function (D.6). Like in the quasiparticle approaches (E.2,E.4), the antiquark states yield half of the strength of the spectral function. We find the – temperature independent – result

$$\mathrm{I}(\mu = 0) = 2N_f N_c \int_\Lambda \frac{d^3k}{(2\pi)^3} = \frac{N_f N_c \Lambda^3}{3\pi^2}\,, \tag{E.13}$$

and thus,

$$\rho(\mu, T) = 4N_f N_c \int_\Lambda \frac{d^3k}{(2\pi)^3} \int_{-\infty}^{+\infty} \frac{dk_0}{2\pi} \mathrm{n_F}(k_0) \mathcal{A}_0(k) - \frac{N_f N_c \Lambda^3}{3\pi^2}\,. \tag{E.14}$$

The momentum distribution of the quarks is found by integrating the number of particles over the energy at fixed three-momentum. Thus, it corresponds to the integral J in (E.10). Like for the density, the vacuum contributions must be subtracted. Using (E.11,E.12) yields

$$n(|\vec{k}\,|, \mu, T) = 2\mathrm{J}(|\vec{k}\,|, \mu, T) - 2\mathrm{J}(|\vec{k}\,|, \mu = 0) = \frac{1}{\pi} \int_{-\infty}^{+\infty} dk_0 \mathcal{A}_0(k) \mathrm{n_F}(k_0) - 1\,, \tag{E.15}$$

where the factors have been chosen such that the momentum distribution is normalized to 1 for quasiparticles below the Fermi momentum.

Eqs. (E.14) and (E.15) allow us to calculate ρ and n without explicit knowledge of the $q\bar{q}$ border at finite chemical potentials. However, there is a price to pay for this convenience: Instead of calculating the density and the momentum distribution from an integral over the quark states above the $q\bar{q}$ border only[1], the integrals in (E.14) and (E.15) involve the states of the spectral function at *all* energies. The numerical results for these integrals are "corrected" by subtracting the analytical vacuum results. This approach makes the calculations sensitive to numerical fluctuations in the antiquark sector.

The problem is illustrated in Fig. E.3. The left panel shows numerical results for the integral J (E.10) at two densities and zero temperature. We can see that the

[1] At finite temperatures, a few quark states at negative energies are not populated due to thermal excitations. The corresponding populated antiquark states yield small contributions to ρ and n, see (E.19,E.20) below.

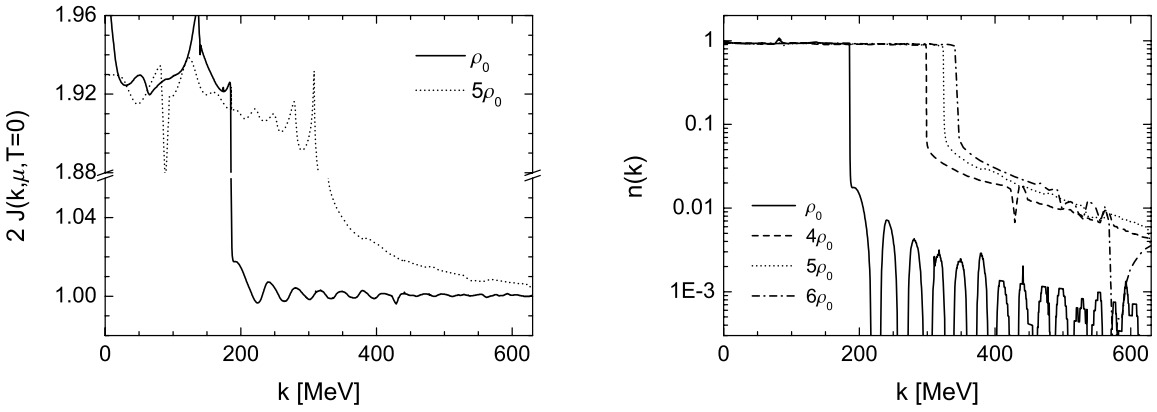

Figure E.3: Numerical results for $\mathrm{J}(|\vec{k}\,|,\mu,T)$ of Eq. (E.10) and the momentum distribution $n(|\vec{k}\,|,\mu,T)$ of the quarks in the medium, calculated using Eq. (E.15) at several densities and $T = 0$. Note the break in the vertical scale of the left panel. The uncertainties that arise from integrating over the antiquark states numerically and subtracting the analytical result have large influence on the high-momentum tail of the momentum distribution.

numerical uncertainties are on the order of 2% (note the scale). Above the Fermi momentum, the quark on-shell peak is located above the chemical potential. Hence, the results – and the (absolute) size of the numerical fluctuations – are dominated by the integration over the antiquark on-shell peak. The contributions from the off-shell quark states are much smaller.

When we subtract the (constant) vacuum contributions $\mathrm{J}(\mu = 0)$ from $\mathrm{J}(|\vec{k}\,|,\mu)$, cf. (E.15), the numerical fluctuations of J transfer directly to the momentum distribution shown in the right panel of Fig. E.3. We can see that the numerical uncertainties of J are of the same order of magnitude as the high-momentum tail of the momentum distribution (or even larger) below the chiral phase transition ($\rho = \rho_0$). Only in the chirally restored phase, the contributions from the quark states become larger than the fluctuations. Nonetheless, the curves have still an irregular structure.

Note that the momentum distribution below the Fermi momentum is – due to the contributions from the on-shell quark states – much larger than the fluctuations. The numerical error stays below 4% in this region. The largest contributions to the quark density arise also from the states below k_F. Thus, the numerical error of the density should be of similar size.

The search for a better way to calculate the momentum distribution (and the density) brings us back to the introduction of a $q\bar{q}$ border. Introducing the antiquark distribution function $\bar{\mathrm{n}}_\mathrm{F}(k_0)$,

$$\bar{\mathrm{n}}_\mathrm{F}(k_0) = 1 - \mathrm{n}_\mathrm{F}(k_0) = \frac{e^{(k_0-\mu)/T}+1}{e^{(k_0-\mu)/T}+1} - \frac{1}{e^{(k_0-\mu)/T}+1} = \frac{1}{e^{(-k_0+\mu)/T}+1}\,, \qquad \text{(E.16)}$$

the integral on the rhs. of (E.15) can be split up into three parts,

$$\mathrm{J}(|\vec{k}\,|,\mu,T) = \int\limits_{k_0^{q\bar{q}}}^{+\infty} \frac{dk_0}{2\pi}\mathcal{A}_0(k)\mathrm{n_F}(k_0) + \int\limits_{-\infty}^{k_0^{q\bar{q}}} \frac{dk_0}{2\pi}\mathcal{A}_0(k) - \int\limits_{-\infty}^{k_0^{q\bar{q}}} \frac{dk_0}{2\pi}\mathcal{A}_0(k)\bar{\mathrm{n}}_\mathrm{F}(k_0)\,. \tag{E.17}$$

The meaning of the three terms can be easily understood. The first term is an integral over the populated quark states above the $q\bar{q}$ border. This integral should be sufficient to calculate the momentum distribution (and the density) of the quarks at zero temperature. The second term is an integral over the antiquark states, not weighted with a distribution function. This term should just cancel against the vacuum contribution $\mathrm{J}(\mu = 0)$ in (E.15) – and likewise against $\mathrm{I}(\mu = 0)$ in (E.14).

The third term is a correction to the first two terms. When the Fermi distribution softens at finite temperatures, some quark states below the $q\bar{q}$ border will be free due to thermal excitations. Hence, some antiquark states are populated (occupation probability $\bar{\mathrm{n}}_\mathrm{F} = 1 - \mathrm{n_F}$). The contributions of those states (third term) must be subtracted from the contributions of the quark states (first term) to find the momentum distribution and the density of the medium. Note that this term vanishes for $T = 0$ since $\bar{\mathrm{n}}_\mathrm{F}$ turns into a step function, $\bar{\mathrm{n}}_\mathrm{F}(k_0) \to \Theta(k_0 - \mu)$, and $k_0^{q\bar{q}}$ must always be smaller than μ.

When the rhs. of (E.17) is inserted into the definition of the momentum distribution (E.15), the second term will only cancel against $\mathrm{J}(\mu = 0)$ when the condition

$$\int\limits_{-\infty}^{k_0^{q\bar{q}}} \frac{dk_0}{2\pi}\mathcal{A}_0(k) = \frac{1}{2} \tag{E.18}$$

is satisfied, cf. (E.11). This condition is nothing but our definition of the $q\bar{q}$ border in scheme II, see Eq. (E.6). As shown in the right panel of Fig. E.2, scheme I does not satisfy the condition at higher densities. This leads to the conclusion that scheme II is – at least formally – a more reasonable choice for the $q\bar{q}$ border in our approach.

Using Eqs. (E.17) and (E.18), we can rewrite the definitions of the momentum distribution (E.15),

$$n(|\vec{k}\,|,\mu,T) = \frac{1}{\pi}\int\limits_{k_0^{q\bar{q}}}^{\infty} dk_0\mathcal{A}_0(k)\mathrm{n_F}(k_0) - \frac{1}{\pi}\int\limits_{-\infty}^{k_0^{q\bar{q}}} dk_0\mathcal{A}_0(k)\bar{\mathrm{n}}_\mathrm{F}(k_0)\,, \tag{E.19}$$

and of the quark density (E.14),

$$\rho(\mu,T) = 4N_fN_c\int_\Lambda \frac{d^3k}{(2\pi)^3}\int\limits_{k_0^{q\bar{q}}}^{\infty}\frac{dk_0}{2\pi}\mathcal{A}_0(k)\mathrm{n_F}(k_0)$$
$$- 4N_fN_c\int_\Lambda \frac{d^3k}{(2\pi)^3}\int\limits_{-\infty}^{k_0^{q\bar{q}}}\frac{dk_0}{2\pi}\mathcal{A}_0(k)\bar{\mathrm{n}}_\mathrm{F}(k_0)\,. \tag{E.20}$$

In contrast to the original definitions, these expressions do not include integrals over the antiquark states. However, these integrals have not vanished, but were only shifted into the definition of $k_0^{q\bar{q}}$ in (E.6).

To find $k_0^{q\bar{q}}$, at least one of the integrals in (E.6) must be calculated numerically. The numerical fluctuations will be comparable to those of the normalizations in Fig. E.2 (scheme I). Since the spectral function is not very large near the $q\bar{q}$ border, small fluctuations of the normalizations will generate considerable shifts of $k_0^{q\bar{q}}$ in (E.6). Consequently, the results for the momentum distribution calculated from (E.19) will be of the same quality as those in the right panel of Fig. E.3.

Fig. E.1 shows that the $q\bar{q}$ border that is defined by scheme I, i.e. $\mathrm{Re}\tilde{k}_0 = 0$, can be determined numerically with very high precision. This leads to the following compromise that we employ throughout this work: We use the expressions in (E.19) and (E.20) to calculate the momentum distribution and the quark density. However, the $q\bar{q}$ border of scheme II (E.6) is replaced by the border of scheme I (E.5). At zero temperature, this yields

$$n(|\vec{k}\,|,\mu) \approx \frac{1}{\pi}\int\limits_{\mathrm{Re}\tilde{k}_0=0}^{\infty} dk_0\mathcal{A}_0(k)\mathrm{n_F}(k_0)\,, \tag{E.21}$$

$$\rho(\mu) \approx 4N_fN_c\int_\Lambda \frac{d^3k}{(2\pi)^3}\int\limits_{\mathrm{Re}\tilde{k}_0=0}^{\infty}\frac{dk_0}{2\pi}\mathcal{A}_0(k)\mathrm{n_F}(k_0)\,. \tag{E.22}$$

As we have seen in Fig. E.2, the $q\bar{q}$ border of scheme I will not satisfy the condition (E.18) at high densities. Hence, the expressions in (E.21) and (E.22) are not exact relations. They will, however, allow us to find numerically stable solutions – in particular for the high-momentum tail of the momentum distribution. We show some numerical results for the momentum distribution in Fig. E.4. When the $q\bar{q}$ border of scheme I is used, cf. Eq. (E.21), the results are free of numerical fluctuations at both densities.

The systematical error that we make by using (E.21,E.22) is given by the deviations of $N_q(|\vec{k}\,|)$, cf. (E.5), from 1/2. In the left panel of Fig. E.2, such deviations are not visible. Hence, Eqs. (E.21) and (E.22) yield exact results – within the numerical precision – at moderate densities (chirally broken phase).

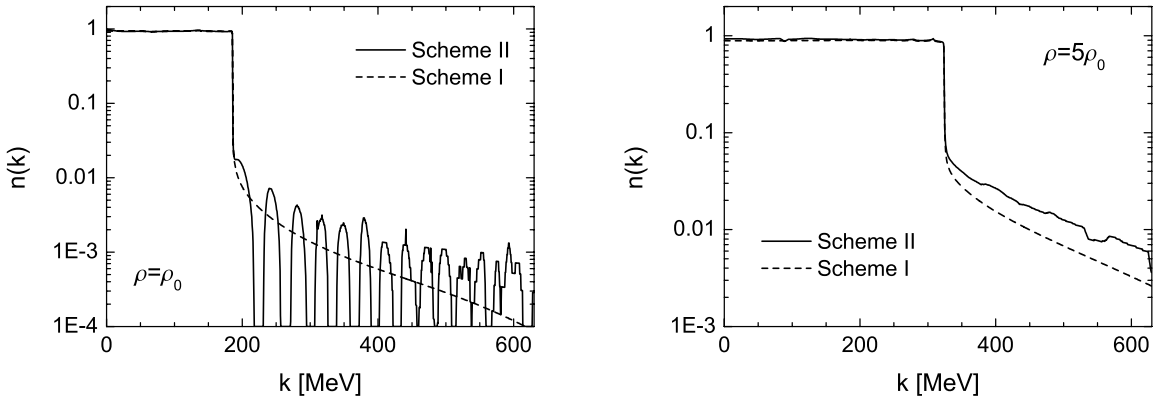

Figure E.4: The momentum distribution of the quarks in the medium, calculated from the exact relation (E.19) (scheme II) and the approximation (E.21) (scheme I). See the text for details. Note the different scales in the two panels.

The deviations of N_q from 1/2 become more relevant in the chirally restored phase, see the right panel of Fig. E.2. Below the Fermi momentum ($k_F = 322\,\mathrm{MeV}$), we expect effects on the order of 5% for the momentum distribution. This is confirmed by the results in the right panel of Fig. E.4. The influence of the deviations on the quark density – that is found by integrating over the momentum distribution – will be of the same size. Above k_F, we find $1 - 2N_q \leq 0.02$ (introducing a factor 2 like in (E.15)). As we can see in the right panel of Fig. E.4, the influence of these deviations on the high-momentum tail of the momentum distribution is on the order of 40%.

The rather large impact on the high-momentum tail should not be overestimated. To compare the short-range effects in quark and nuclear matter in Section 5.7, we do not use the high-momentum tail directly but we determine the discontinuity of the momentum distribution at k_F. The size of the discontinuity is related to the size of the quark on-shell peak at the chemical potential [DVN05], far away from the $q\bar{q}$ border. Provided that the $q\bar{q}$ border is a smooth function of $|\vec{k}\,|$ that does not jump at k_F – and this is ensured by using scheme I – the explicit location should have little influence on the size of the discontinuity.

To avoid confusion, we note again that the way how the $q\bar{q}$ border is drawn has no influence on the self-consistent calculations. This border is only used to interpret the final results, i.e., to determine the momentum distribution and the density. As we have discussed before, the short-range correlations saturate above the chiral phase transition. Thus, the deviations that we have found above should not increase significantly at densities higher than $5\rho_0$. We can conclude that Eqs. (E.21) and (E.22) represent a reasonable approximation scheme. All numerical problems are fixed while the influence on the most relevant quantities, i.e. the density and the discontinuity of the momentum distribution, remains small.

F Dispersive and non-dispersive terms

In the following, a simple example [Leu06] is presented to illustrate which contributions to the real part of a complex function can be determined by a dispersion integral over the corresponding imaginary part and which contributions cannot be determined in that way. Basically, the statement is as follows: The dispersion fixes the real part up to a polynomial (in the energy). For the practical application in the main part of the present work where we study complex functions of the energy the polynomial even reduces to a simple constant. The polynomial or constant can be determined from the high-energy behavior of the real part of the studied complex function. In other words, what one needs to know is the imaginary part of the function at all energies and the real part at high energies.

To illustrate this statement we study the function

$$\Pi^{\mathrm{c}}(k_0) = -k_0^2 \left(\sqrt{1 - \frac{m^2}{k_0^2}} - 1 \right) \tag{F.1}$$

with $m > 0$ and we always use the positive square root. Obviously, $\Pi^{\mathrm{c}}(k_0)$ is purely real for $|k_0| \geq m$ and complex otherwise, i.e.,

$$\Pi^{\mathrm{c}}(k_0) = k_0^2 - ik_0^2 \sqrt{\frac{m^2}{k_0^2} - 1} \qquad \text{for } |k_0| < m. \tag{F.2}$$

We note that important features of the function introduced in (F.1) resemble the properties of the self-energies which we study in the main part of the present work: The imaginary part of $\Pi^{\mathrm{c}}(k_0)$ vanishes for high energies k_0, while the real part becomes constant. This is also true for our self-energies: The imaginary parts are caused by scattering and decay processes. At high energies the products of these processes are effectively cut down by the cutoff introduced in the NJL model. On the other hand, not all real parts are cut down by the cutoff. The simplest example is the energy independent Hartree self-energy.

The function introduced above corresponds to a Feynman self-energy. The corresponding retarded self-energy (for the vacuum case) is given by (cf. (3.25))

$$\mathrm{Re}\,\Pi^{\mathrm{ret}}(k_0) = \mathrm{Re}\,\Pi^{\mathrm{c}}(k_0) = k_0^2 + \begin{cases} 0 & \text{for} \quad |k_0| < m \\ -k_0^2 \sqrt{1 - \frac{m^2}{k_0^2}} & \text{for} \quad |k_0| \geq m \end{cases}$$

and

$$\operatorname{Im}\Pi^{\mathrm{ret}}(k_0) = \operatorname{sgn}(k_0)\operatorname{Im}\Pi^{\mathrm{c}}(k_0) = \begin{cases} -k_0\sqrt{m^2-k_0^2} & \text{for} \quad |k_0| < m \\ 0 & \text{for} \quad |k_0| \geq m \end{cases}$$

Next we define the dispersive part of $\operatorname{Re}\Pi^{\mathrm{ret}}$ as

$$\operatorname{Re}\Pi^{\mathrm{ret}}_{\mathrm{disp}}(k_0) := \frac{1}{\pi}\,\mathcal{P}\int_{-\infty}^{+\infty} dp_0\,\frac{\operatorname{Im}\Pi^{\mathrm{ret}}(p_0)}{p_0-k_0}\,.$$

A straightforward calculation yields

$$\begin{aligned}\operatorname{Re}\Pi^{\mathrm{ret}}_{\mathrm{disp}}(k_0) &= -\frac{m^2}{2} + k_0^2 + \left\{ \begin{array}{cc} 0 & \text{for} \quad |k_0| < m \\ -k_0^2\sqrt{1-\frac{m^2}{k_0^2}} & \text{for} \quad |k_0| \geq m \end{array} \right\} \\ &= -\frac{m^2}{2} + \operatorname{Re}\Pi^{\mathrm{ret}}(k_0)\,.\end{aligned}$$

However, the additional term $-m^2/2$ is just the high-energy behavior of $\operatorname{Re}\Pi^{\mathrm{ret}}(k_0) = \operatorname{Re}\Pi^{\mathrm{c}}(k_0)$. Thus we finally get

$$\operatorname{Re}\Pi^{\mathrm{ret}}(k_0) = \frac{m^2}{2} + \operatorname{Re}\Pi^{\mathrm{ret}}_{\mathrm{disp}}(k_0) = \left[\lim_{k_0\to\infty}\operatorname{Re}\Pi^{\mathrm{ret}}(k_0)\right] + \frac{1}{\pi}\,\mathcal{P}\int_{-\infty}^{+\infty} dp_0\,\frac{\operatorname{Im}\Pi^{\mathrm{ret}}(p_0)}{p_0-k_0} \quad \text{(F.3)}$$

which illustrates our statement made at beginning of this appendix. This result can easily be understood: As long as $\operatorname{Im}\Pi^{\mathrm{ret}}(p_0)$ vanishes for large $|p_0|$ the dispersion integral in (F.3) does not contribute in the limit $k_0 \to \infty$.

G Relations between Bose and Fermi distributions

When relating the time-ordered to the retarded meson polarizations in Section 3.6.1, we encounter the following relation,

$$[\mathrm{n_F}(p-k)-\mathrm{n_F}(p)][1+2\mathrm{n_B}(k)] = \mathrm{n_F}(p)+\mathrm{n_F}(p-k)-2\mathrm{n_F}(p)\mathrm{n_F}(p-k)\,. \tag{G.1}$$

This is an interesting equation since it relates a mixture of fermionic and bosonic distribution functions on the lhs. with a purely fermionic expression on the rhs. We can construct Eq. (G.1) as follows. Using $\mathrm{n_B}(k)=\frac{1}{e^{\beta k}-1}$ we start from

$$2\mathrm{n_B}(k)+1 = \frac{1+e^{\beta k}}{e^{\beta k}-1} = \frac{e^{\beta(p-k-\mu)}+e^{\beta(p-\mu)}}{e^{\beta(p-\mu)}-e^{\beta(p-k-\mu)}} \quad \left(=\coth\frac{\beta k}{2}\right). \tag{G.2}$$

Multiplying with $e^{\beta(p-\mu)}-e^{\beta(p-k-\mu)}$ yields

$$\left[e^{\beta(p-\mu)}-e^{\beta(p-k-\mu)}\right][1+2\mathrm{n_B}(k)] = e^{\beta(p-\mu)}+e^{\beta(p-k-\mu)}\,.$$

Using $\mathrm{n_F}(k)=\frac{1}{e^{\beta(k-\mu)}+1}$,

$$\left[\frac{1}{\mathrm{n_F}(p)}-\frac{1}{\mathrm{n_F}(p-k)}\right][1+2\mathrm{n_B}(k)] = \frac{1}{\mathrm{n_F}(p)}+\frac{1}{\mathrm{n_F}(p-k)}-2\,,$$

and multiplying with $\mathrm{n_F}(p)\mathrm{n_F}(p-k)$, we arrive at Eq. (G.1).

A similar relation is encountered when the retarded and the time-ordered quark self-energies are calculated, cf. Section 3.8.3,

$$2\mathrm{n_F}(p)\mathrm{n_B}(p-k)+\mathrm{n_F}(p)-\mathrm{n_B}(p-k) = -[\mathrm{n_F}(p)+\mathrm{n_B}(p-k)][1-2\mathrm{n_F}(k)]\,. \tag{G.3}$$

To construct this expression we start from $\mathrm{n_F}(k)=\frac{1}{e^{\beta(k-\mu)}+1}$,

$$2\mathrm{n_F}(k)-1 = \frac{2-\left(1+e^{\beta(k-\mu)}\right)}{1+e^{\beta(k-\mu)}} = \frac{1-e^{\beta(k-\mu)}}{1+e^{\beta(k-\mu)}} \quad \left(=\tanh\frac{\beta(k-\mu)}{2}\right). \tag{G.4}$$

Multiplying with $[1+e^{\beta(k-\mu)}]e^{\beta(p-k)}$ yields

$$\left[e^{\beta(p-k)}+e^{\beta(p-\mu)}\right][2\mathrm{n_F}(k)-1] = e^{\beta(p-k)}-e^{\beta(p-\mu)}$$

$$\left[e^{\beta(p-k)}-1+e^{\beta(p-\mu)}+1\right][2\mathrm{n_F}(k)-1] = 2+e^{\beta(p-k)}-1-e^{\beta(p-\mu)}-1\,.$$

Using $\mathrm{n_B}(p)=\frac{1}{e^{\beta p}-1}$ and $\mathrm{n_F}(p)=\frac{1}{e^{\beta(p-\mu)}+1}$ we get

$$\left[\frac{1}{\mathrm{n_B}(p-k)}+\frac{1}{\mathrm{n_F}(p)}\right][2\mathrm{n_F}(k)-1] = 2+\frac{1}{\mathrm{n_B}(p-k)}-\frac{1}{\mathrm{n_F}(p)}\,.$$

Finally, we multiply with $\mathrm{n_F}(p)\mathrm{n_B}(p-k)$ and find Eq. (G.3).

H Numerical Implementation

Finding numerical solutions for the integrals that determine the quark width $\Gamma_{s,\mu}$ (3.16) and the RPA meson widths $\Gamma_{\sigma,\pi}$ (3.22) is a rather involved procedure. The integrands of the three-dimensional integrals (after eliminating the trivial φ integral) consist of quark and RPA spectral functions. The spectral functions concentrate most of their strength in the narrow on-shell regions. Even for adaptive integration routines – that try to analyze the structure of the integrand – it is hard to localize those regions[1] when the product of two spectral functions is considered.

This problem is enhanced by two effects: First, each spectral function consists of two peaks that have to be localized – a particle and an antiparticle peak. Second, the integrands include distribution functions $\mathrm{n_F}$ and $\mathrm{n_B}$ that correspond to step functions at zero temperature. Typically, integration routines find steps in the integrands much easier than peaks. If they spend too many of their (limited) nodes to analyze the structure of these steps, they may miss the peaks.

When an integration routine overlooks the on-shell peaks in the calculation – or does not investigate them with high enough precision – the result will be useless. In this appendix we will discuss how the integrals (3.16,3.22) can be brought into a form that is most suitable for the numerical integration routine. Note that we will not consider the calculation of the nucleon width (6.5,6.6) explicitly here. However, it involves the same problems for which similar solutions can be found. We will point out the differences below.

H.1 Splitting up the integrals

The negative influence of the distribution functions on the numerical calculations can be readily compensated. In fact, the distributions can be used to stabilize the numerics at zero temperature: Instead of setting the limits of the energy integrals to the borders of the numerical grids, cf. Section 5.1.3, we can shift them to the points where the step functions drop to zero. We have already demonstrated this before,

[1] Consider the following (non-adaptive) example: When the integration routine uses 10^6 sampling points (typically, we use only $2 \cdot 10^5$ nodes) and the points are evenly distributed over all three dimensions, the integrand is discretized on a grid with $100 \times 100 \times 100$ grid points. For a constant mesh size, an energy resolution of $dp_0 = 70\,\mathrm{MeV}$ would be reached in the calculation of the quark width ($|p_0| < 3.5\,\mathrm{GeV}$). The width of the on-shell peaks of the (anti-)quarks in the chirally broken phase, however, is more than a factor of 3 smaller, cf. Fig. 5.15.

cf. Eqs. (3.17,3.23),

$$\Gamma_{s,\mu} \sim \int_{-\infty}^{+\infty} dp_0[\mathrm{n_F}(p_0) + \mathrm{n_B}(p_0 - k_0)]\cdots \quad \stackrel{T=0}{=} \quad \int_{k_0}^{\mu} dp_0 \cdots ,$$

$$\Gamma_{\sigma,\pi} \sim \int_{-\infty}^{+\infty} dp_0[\mathrm{n_F}(p_0 - k_0) - \mathrm{n_F}(p_0)]\cdots \quad \stackrel{T=0}{=} \quad \int_{\mu}^{\mu+k_0} dp_0 \cdots .$$

The shifts remove not only the unnecessary steps from the integrands, but also minimize the integration volumes. This enhances the numerical accuracy without increasing the computation time.

It is not possible to shift the integration limits in this way in our nuclear matter calculations at finite temperatures. However, when the distribution functions soften they do not distract the integration routines too much from the on-shell peaks. The calculations have shown that the influence of the distributions on the numerical stability becomes tolerable for $T \geq 10\,\mathrm{MeV}$.

Let us come back to the quark calculations, where we still have to simplify the structure of the spectral functions (particle and antiparticle peaks) in the integrands. For that purpose, we split up the energy integrals into several regions that can be calculated individually: First, we separate the quark and the antiquark peak – or the two meson peaks – of each spectral function. Additional cuts are introduced to split up the quark spectral functions at the chemical potential where they drop to zero for $T = 0$. Note that some of the regions that are found in this procedure are suppressed by the distribution functions – recall the discussion in Section 4.2.1.

For the quark width, the shift of the borders and the separation of the peaks means that we calculate the contributions from each of the processes in Fig. 4.1 individually – identifying the meson lines with the full RPA propagators, i.e. bound $q\bar{q}$ peaks and $q\bar{q}$ continuum. The energy integrals that have to be solved for a given external energy k_0 are listed in Table H.1. Correspondingly, we find one integral for each of the processes shown in Fig. 4.6 that contribute to the meson width. The integrals are listed in Table H.2. Recall that the meson width $\Gamma_{\sigma,\pi}(k)$ is antisymmetric in k_0, see the discussion below Eq. (3.22). Thus, we consider only the integrals for positive k_0 here. Since the process in Fig. 4.6(a) is not allowed for $0 < k_0 < \mu$, only one integral is found in this region.

H.2 Substitution

The on-shell peaks of the spectral functions that enter the integrals in Tables H.1 and H.2 are still narrow structures with respect to the full integration volumes. We cannot easily compensated that by further splits of the integrals. To support the numerical integration routine in finding the peaks – and sampling them with high

Table H.1: The energy integral in the definition of the quark width $\Gamma(k)$ (3.16) at zero temperature – after inserting the distribution functions explicitly, cf. (3.17), and separating the particle and antiparticle peaks of the spectral functions (drawing the $q\bar{q}$ border at $k_0 = 0$, cf. Appendix E.2.1). The allowed range for the energy $r_0 = p_0 - k_0$ is indicated. Each integral corresponds to one of the processes shown in Fig. 4.1.

$k_0 < 0$		$0 < k_0 < \mu$	$k_0 > \mu$
$\int_{k_0}^{0} dp_0 \cdots$	$+ \int_{0}^{\mu} dp_0 \cdots$	$\int_{k_0}^{\mu} dp_0 \cdots$	$- \int_{\mu}^{k_0} dp_0 \cdots$
$(r_0 > \mu)$	$(r_0 > 0)$	$(r_0 > 0)$	$(r_0 < 0)$
Fig. 4.1(d)	Fig. 4.1(c)	Fig. 4.1(b)	Fig. 4.1(a)

Table H.2: The energy integral in the definition of the meson width $\Gamma(k)$ (3.22) for positive k_0 at zero temperature – after inserting the distribution functions explicitly, cf. (3.23). The allowed range for the energy $r_0 = p_0 - k_0$ is indicated. The integrals correspond to the processes shown in Fig. 4.6.

$0 < k_0 < \mu$	$k_0 > \mu$	
$\int_{\mu}^{\mu+k_0} dp_0 \cdots$	$\int_{k_0}^{\mu+k_0} dp_0 \cdots$	$+ \int_{\mu}^{k_0} dp_0 \cdots$
$(0 < r_0 < \mu)$	$(0 < r_0 < \mu)$	$(r_0 < 0)$
Fig. 4.6(b)	Fig. 4.6(b)	Fig. 4.6(a)

enough precision – we have to "reshape" the spectral functions. As we will show in the following, this can be accomplished by a substitution in the integrals.

To illustrate the approach, let us first consider the three-momentum integral

$$\mathrm{J}(p_0) = \int\limits_{p_{\min}}^{p_{\max}} dp p^2 A(p_0, \vec{p}) = \int\limits_{p_{\min}^2}^{p_{\max}^2} dp^2 \frac{p}{2} A(p_0, \vec{p})$$

over a simplified spectral function, i.e., a Breit–Wigner distribution with a constant (scalar) width Γ:

$$A(p_0, \vec{p}) = \frac{m^2 \Gamma}{\left(p^2 - p_{\mathrm{os}}^2\right)^2 + m^2 \Gamma^2}\,,$$

where the energy dependent $p_{\mathrm{os}}(p_0) = p_0^2 - m^2$ is the on-shell three-momentum that determines the location of the on-shell peak. A substitution $p^2 \to y(p)$ that simplifies structure of the integral

$$\mathrm{J}(p_0) = \frac{1}{2} \int\limits_{p_{\min}^2}^{p_{\max}^2} dp^2 p \frac{m^2 \Gamma}{\left(p^2 - p_{\mathrm{os}}^2\right)^2 + m^2 \Gamma^2} \tag{H.1}$$

should either spread out the on-shell region in the new integration variable y or generate a factor dp^2/dy that compensates the peak structure of the spectral function. In fact, we can find a substitution that has both of these features: Inspired by the denominator of $A(p_0, \vec{p})$ and using the relation $d \arctan(x)/dx = (x^2 + 1)^{-1}$, we construct the function

$$y(p_0) = \arctan\left(\frac{p^2 - p_{\mathrm{os}}^2(p_0)}{m\Gamma}\right) / m\Gamma \tag{H.2}$$

with

$$\frac{dy}{dp^2} = \frac{1}{\left(p^2 - p_{\mathrm{os}}^2\right)^2 + m^2 \Gamma^2}\,. \tag{H.3}$$

When performing the substitution $p^2 \to y(p_0)$ on the rhs. of (H.1), the factor dp^2/dy will cancel the denominator of the (simplified) spectral function and thus entirely remove the pole structure from the integrand:

$$\mathrm{J}(p_0) = \frac{1}{2} \int\limits_{y_{\min}(p_0)}^{y_{\max}(p_0)} dy \frac{dp^2}{dy} p A(p_0, \vec{p}) = \frac{m^2 \Gamma}{2} \int\limits_{y_{\min}(p_0)}^{y_{\max}(p_0)} dy p(y)\,. \tag{H.4}$$

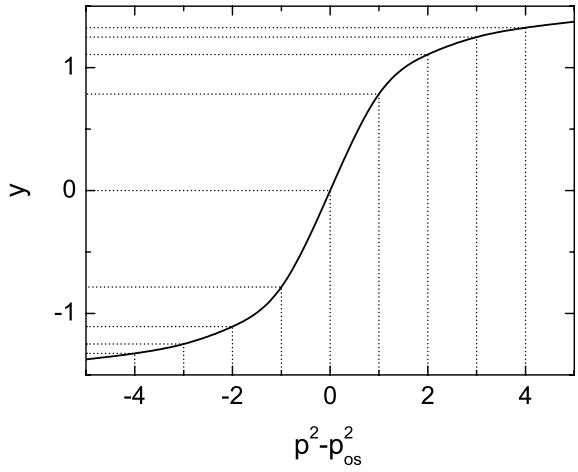

Figure H.1: Rescaling of equidistant points in the substitution $p^2 \to y$, cf. (H.2). The (on-shell) region in the vicinity of $\vec{p}^{\,2} = \vec{p}^{\,2}_{\rm os}$ is stretched out in the new coordinate y while the other (off-shell) regions are compressed. See also the upper and lower left panels of Fig. H.2.

In addition, the substitution rescales the integration variable non-linearly. This effect is of particular interest when the cancellation of dp^2/dy and A remains incomplete, e.g., because different widths are used in the definition of A and y (this cannot be avoided in the full calculation where A is replaced by $\mathcal{A}$). The slope of the function $\arctan(\vec{p}^{\,2} - \vec{p}^{\,2}_{\rm os})$ reaches its maximum for $\vec{p}^{\,2} - \vec{p}^{\,2}_{\rm os} = 0$ – i.e. at the position of the on-shell peak. Hence, the on-shell region of the spectral function is stretched out in the new coordinate y while the off-shell regions are compressed. The effect is illustrated in Fig. H.1 where we show the mapping of equidistant points in the original coordinate $\vec{p}^{\,2}$ onto points in the new coordinate y. This rescaling will spread out the residues of the on-shell peak in the full calculation. Note that the slope of y depends on the size of the width. For large Γ, the slope at $\vec{p}^{\,2} = \vec{p}^{\,2}_{\rm os}$ is smaller than for low Γ. Thus, the stretching effect of the substitution weakens for broad peaks and increases for narrow peaks. In other words, the substitution adjusts automatically to the level of difficulty of the numerical integration.

After outlining the concept, we turn now to the real substitution that we use in the numerical calculations. Our starting point is the three-momentum integral

$$\mathrm{I}(p_0) = \int\limits_{p_{\rm min}}^{p_{\rm max}} dp p^2 \mathcal{A}(p_0, p)\,. \tag{H.5}$$

that is part of the multidimensional integrals in (3.16,3.22). The integrand $p^2\mathcal{A}$ from a real calculation is shown in the upper left panel of Fig. H.2 (from $p_{\rm min} = 0$ to $p_{\rm max} = \Lambda$). We can see that the on-shell peak fills only a small part of the integration

volume. Numerically, this structure is – as part of a multidimensional integration – not favorable.

As a first step, we apply the simple substitution[2]

$$p \to \bar{p}^2(p_0) = (p - \mathrm{Re}\,\Sigma^{\mathrm{ret}}_{v,\mathrm{os}}(p_0))^2, \qquad \frac{d\bar{p}^2}{dp} = 2\bar{p}$$

to prepare the integral

$$\mathrm{I}(p_0) = \int\limits_{p_{\min}}^{p_{\max}} dp p^2 \mathcal{A}(p_0, p) = \int\limits_{\bar{p}^2_{\min}}^{\bar{p}^2_{\max}} d\bar{p}^2 \frac{p^2}{2\bar{p}} \mathcal{A}(p_0, p)\,. \tag{H.6}$$

for the main substitution. Note that the three-momentum $\bar{p}$ is similar (but not equal) to the real part of the effective momentum introduced in Eq. (2.34) since we use the momentum independent on-shell self-energy here.

Next, we have to adjust the definition of the function y from Eq. (H.2): The derivative $dy/d\bar{p}^2$ should now resemble the denominator of the full spectral function $\mathcal{A}$, cf. (2.40). Thus, we change the definition of $p_{\mathrm{os}}(p_0)$ as shown in Eq. (2.39) and replace the constant factor $m\Gamma$ with the function $\mathcal{W}_{\mathrm{os}}(p_0)$, cf. (2.37). This yields

$$\bar{p}^2(p_0) \to y(p_0) = \arctan\left(\frac{\bar{p}^2(p_0) - p^2_{\mathrm{os}}(p_0)}{\mathcal{W}_{\mathrm{os}}(p_0)}\right) / \mathcal{W}_{\mathrm{os}}(p_0)\,, \tag{H.7}$$

with

$$\frac{dy}{d\bar{p}^{\,2}} = \frac{1}{(\bar{p}^{\,2} - p^2_{\mathrm{os}})^2 + \mathcal{W}^2_{\mathrm{os}}}\,. \tag{H.8}$$

Explicit expressions for p^2_{os} and $\mathcal{W}_{\mathrm{os}}$ can be readily obtained from Eqs. (2.36) and (2.37), respectively,

$$\begin{aligned} p^2_{\mathrm{os}}(p_0) &= (p_0 - \mathrm{Re}\,\Sigma^{\mathrm{ret}}_{0,\mathrm{os}})^2 - (\mathrm{Re}\tilde{m}_{\mathrm{os}})^2 - \frac{1}{4}\left[\Gamma^{\mathrm{os}}_{\mu}\Gamma^{\mu}_{\mathrm{os}} - \Gamma^2_{s,\mathrm{os}}\right]\,, \\ \mathcal{W}_{\mathrm{os}}(p_0) &= \mathrm{Re}\tilde{p}^{\mathrm{os}}_{\mu}\Gamma^{\mu}_{\mathrm{os}} + \mathrm{Re}\tilde{m}_{\mathrm{os}}\Gamma^{\mathrm{os}}_{s}\,, \end{aligned} \tag{H.9}$$

where Γ_{os}, $\Sigma^{\mathrm{ret}}_{\mathrm{os}}$, $\tilde{p}_{\mathrm{os}}$, and $\tilde{m}_{\mathrm{os}}$ are functions of p_0. Note that it is not feasible to take the momentum dependence of $\mathcal{W}$ into account in Eq. (H.7) – it would spoil the structure of $dy/d\bar{p}^2$ and lead to further complications in the substitution. Consequently, the cancellation effect that we have observed in Eq. (H.4) will be less accurate in the off-shell regions.

[2]Note that this substitution is only well-defined for $p > \mathrm{Re}\,\Sigma^{\mathrm{ret}}_{v,\mathrm{os}}(p_0)$. This condition may be violated for some p_0 in the off-shell regions when p is very small. Our calculations take this into account by splitting up the integral at $p = \mathrm{Re}\,\Sigma^{\mathrm{ret}}_{v,\mathrm{os}}(p_0)$. We will not discuss the details here.

Before we discuss the influence of the substitution (H.7) on the structure of the integrand in more detail, we briefly note that – for purely technical reasons – a third substitution is used in the numerical calculations,

$$y \to z = \frac{y - y_{\min}}{y_{\max} - y_{\min}} \quad \Rightarrow \quad \int\limits_{y_{\min}(p_0)}^{y_{\max}(p_0)} dy \cdots = \int\limits_0^1 dz [y_{\max}(p_0) - y_{\min}(p_0)] \cdots . \tag{H.10}$$

The substitution induces just a linear rescaling of the integration variable and shifts the integration limits to 0 and 1. This allows us to call the integration routine with fixed, i.e. p_0 independent, integration limits in our computer program.

Applying the substitutions from Eqs. (H.7,H.8) and (H.10) to the rhs. of (H.6) yields for the three-momentum integral in (H.6)

$$\mathrm{I}(p_0) = \int\limits_0^1 dz [y_{\max} - y_{\min}] \frac{\left[(\bar{p}^2 - p_{\mathrm{os}}^2)^2 + \mathcal{W}_{\mathrm{os}}^2\right]}{2\bar{p}} \, p^2 \mathcal{A}(p_0, p) \, . \tag{H.11}$$

As we know, the substitutions have two effects. In Fig. H.1, we have already demonstrated the non-linear rescaling of the integration variable that stretches the on-shell region. The impact of the rescaling on the integrand of a real calculation is illustrated in the left column of Fig. H.2. The original integrand $p^2\mathcal{A}$ is shown as a function of p in the upper panel and as a function of z, cf. (H.10), in the lower panel. We can see that the broadened peak fills the whole integration volume in the lower left panel. This is clearly an improvement for the numerical integration.

The second effect of the substitutions is introduced by the factor $d\bar{p}^2/dy = [(\bar{p}^2 - p_{\mathrm{os}}^2)^2 + \mathcal{W}_{\mathrm{os}}^2]$. This factor resembles the denominator of the quark spectral function when the effective momentum $\bar{p}(p_0)$ approaches the effective on-shell momentum $p_{\mathrm{os}}(p_0)$, cf. Eqs. (2.40) and (2.36,2.37). Hence, the factor will cancel the on-shell peaks of the spectral function to a large extent. We illustrate this effect in the top panels of Fig. H.2. The left panel shows the original integrand $p^2\mathcal{A}$ of Eq. (H.5) in comparison to the full integrand of Eq. (H.11) in the right panel – both integrands are shown as functions of p. The peak structure has almost vanished in the right panel[3]. Most of the strength has been redistributed over the integration volume.

The full impact of the substitutions, i.e. the combination of the rescaling with the cancellation effect, can be seen in the lower right panel of H.2. There, we show the integrand of (H.11) as a function of the new integration variable z. The final result of our substitutions is a very smooth, almost constant function of z – the wavy structure arises from stretching out the cusp at the on-shell position (upper right panel) in the

[3]The small cusp at the on-shell position is the only remnant of the on-shell peak. Since the on-shell self-energy – and not the full energy and momentum dependent self-energy – enters the factor $d\bar{p}^2/dy$, the cancellation effect with the denominator of the spectral function is only exact at the maximum of the peak. The cusp indicates small fluctuations of the (off-shell) width at the shoulders of the peak.

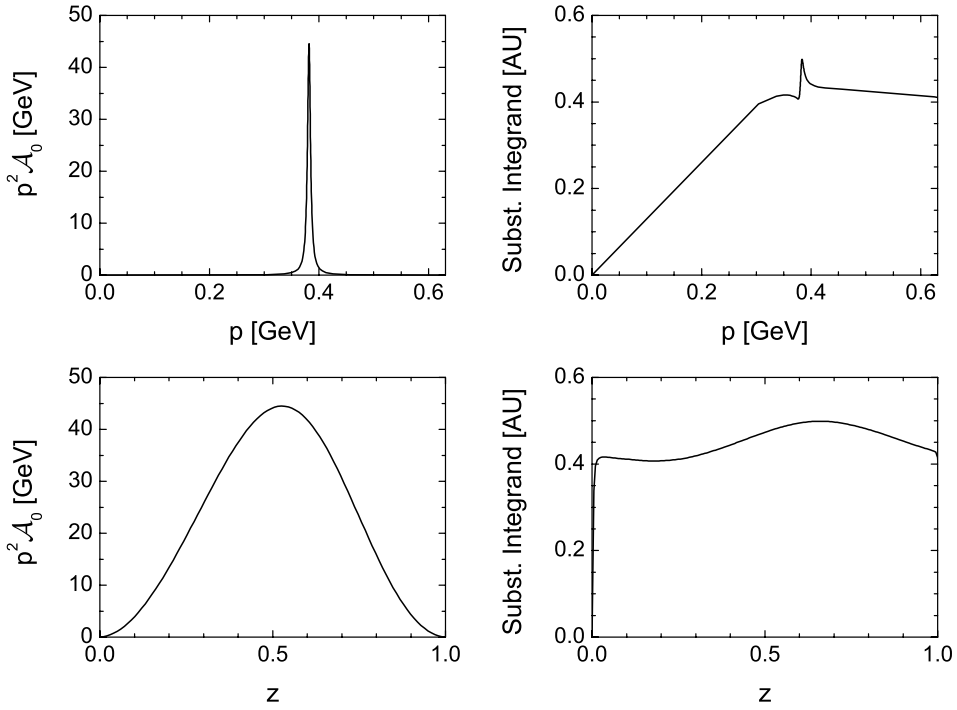

Figure H.2: The impact of the substitutions (H.7,H.10) on the quark spectral function. The upper left panel shows $p^2\mathcal{A}$, the integrand of (H.5), as a function of the three-momentum p, the lower left panel shows $p^2\mathcal{A}$ as a function of the new integration variable z. The upper right panel shows the integrand after applying the substitutions, cf. (H.11), as a function of p. The lower right panel shows the same integrand as a function of z, illustrating the full effect of the substitutions.

new coordinate z. The numerical integration of such a function is our course much simpler than the integration of the original function shown in the upper left panel of Fig. H.2.

At the end of this section, we note that the integral (3.22) that determines the meson width $\Gamma_{\sigma,\pi}$ contains two quark spectral functions,

$$\Gamma_{\sigma,\pi} \sim \int \frac{d^4p}{(2\pi)^4}\mathcal{A}(p)\mathcal{A}(p-k)\cdots .$$

So far, we have only discussed the treatment of the first spectral function $\mathcal{A}(p)$ in the integrand. Before we can simplify the structure of the second spectral function $\mathcal{A}(p-k)$ – using the substitutions that have been discussed above – we have to convert the $\cos\vartheta$ integral into an integral over the three-momentum $r = |\vec{p}-\vec{k}\,|$. The substitution

$$\cos\vartheta \to r = \sqrt{k^2+p^2-2kp\cos\vartheta}\,, \qquad \frac{dr}{d\cos\vartheta} = -\frac{kp}{r}$$

yields

$$\int_{-1}^{+1} d\cos\vartheta \mathcal{A}(p-k) \quad \rightarrow \quad \int_{|p-k|}^{p+k} \frac{drr}{kp} \mathcal{A}(p_0-k_0,r)\,.$$

The integral on the rhs. can be modified in the same way as $\mathrm{I}(p_0)$, cf. (H.5), to smear out the on-shell peaks of the spectral function $\mathcal{A}(p_0-k_0,r)$ in the integrand. The result will be very similar to (H.11).

The techniques that have been described in this section can be directly transfered to the nucleon calculations, cf. Eqs. (6.5) and (6.6). Only the explicit expressions in (H.9) have to be replaced by non-relativistic terms that can be derived from the denominator of the nucleon spectral function in Eq. (6.2). Since Σ_v^{ret} drops to zero in the non-relativistic limit, the integration variable $\bar{p}$ will be identical to the plain three-momentum p.

H.3 Performance

The integrals of the present approach (3.16,3.22) are clearly much better to handle than those of our earlier approach in [Frö01, FLM03b]. While we have to solve two three-dimensional integrals here, it was one six-dimensional integral in the old approach. For the lower number of integrals we had not only to pay with a higher number of dimensions but also with a third spectral function in the integrand. Since the computing time does not scale linearly with the dimensions but with the power of the dimensions – when the desired precision is kept fixed – the old calculations were much more time consuming (several days of computation time for one iteration on a Intel Xeon processor with 800 MHz, 200×100 grid points).

The multidimensional integration routine CUBPACK [CH03] that we use in the present approach, allows for an additional optimization. One of the features of CUBPACK is the handling of vector integrands. Hence, we can calculate all Lorentz components of the integrands in (3.16) simultaneously. This parallel integration – that in fact speeds up the calculations by a factor of three – does not lead to a loss of precision: The denominator of the quark spectral function is universal, and all Lorentz components have a very similar structure with peaks at the same positions. A single iteration needs approximately 7 hours of computation time on an AMD Opteron 248 processor with 2.2 GHz (3.5 hours for the quark width, 300×100 grid points, 3.5 hours for the meson widths, 150×200 grid points).

Note that we also have to deal with six-dimensional integrals over products of three spectral functions in the nucleon calculations that are presented in this work. This, however, is a non-relativistic approach where the spectral function is a scalar function that has only one peak. A computation time of approximately 2.5 hours is required for a single iteration (Opteron 248, 130×120 grid points).

We conclude our discussion of the numerical implementation by pointing out that the complicated multidimensional integrations of the present quark and nucleon approaches are numerically under control. Splitting up the energy integrals and using an elaborate substitution scheme in the three-momentum integrals smoothens the sharp peaks of the spectral functions and yields expressions that can be well handled in numerical calculations. There is no need for (analytical) approximations in the peak regions. The computation time that is needed to obtain self-consistent results ranges on the order of $1 - 2$ days (on computers that represent the state-of-the-art of the year 2005/06). This has allowed us to perform a variety of calculations at different densities and temperatures (in the nucleon case).

Bibliography

[APR98] A. Akmal, V. R. Pandharipande, and D. G. Ravenhall, *Equation of state of nucleon matter and neutron star structure*, Phys. Rev. **C58** (1998) 1804, nucl-th/9804027.

[ARFdCO96] L. Alvarez-Ruso, P. Fernández de Córdoba, and E. Oset, *The imaginary part of the nucleon self-energy in hot nuclear matter*, Nucl. Phys. **A606** (1996) 407, nucl-th/9610003.

[ARS+96] T. Alm, G. Röpke, A. Schnell, N. H. Kwong, and H. S. Köhler, *Nucleon spectral function at finite temperature and the onset of superfluidity in nuclear matter*, Phys. Rev. **C53** (1996) 2181, nucl-th/9511039.

[AY89] M. Asakawa and K. Yazaki, *Chiral restoration at finite density and temperature*, Nucl. Phys. **A504** (1989) 668.

[BBG+92] M. Baldo, I. Bombaci, G. Giansiracusa, U. Lombardo, C. Mahaux, and R. Sartor, *Off-the-energy-shell properties of the mass operator and spectral functions in nuclear matter*, Nucl. Phys. **A545** (1992) 741.

[BBI+95] J. P. Bondorf, A. S. Botvina, A. S. Iljinov, I. N. Mishustin, and K. Sneppen, *Statistical multifragmentation of nuclei*, Phys. Rept. **257** (1995) 133.

[BC03] P. Bożek and P. Czerski, *In medium T-matrix with realistic nuclear interactions*, Acta Phys. Polon. **B34** (2003) 2759, nucl-th/0212035.

[BCS57] J. Bardeen, L. N. Cooper, and J. R. Schrieffer, *Theory of superconductivity*, Phys. Rev. **108** (1957) 1175.

[BD65] J. D. Bjorken and S. D. Drell, *Relativistic Quantum Fields*, McGraw-Hill, New York, 1965.

[BDM06] P. Bożek, D. J. Dean, and H. Müther, *Correlations and effective interactions in nuclear matter*, Phys. Rev. **C74** (2006) 014303, nucl-th/0604003.

[BFF89] O. Benhar, A. Fabrocini, and S. Fantoni, *The nucleon spectral function in nuclear matter*, Nucl. Phys. **A505** (1989) 267.

[BFF92] O. Benhar, A. Fabrocini, and S. Fantoni, *Nuclear-matter Green functions in correlated-basis theory*, Nucl. Phys. **A550** (1992) 201.

[BFvGQ75] M. Beiner, H. Flocard, N. van Giai, and P. Quentin, *Nuclear ground-state properties and self-consistent calculations with the Skyrme interaction: (I). Spherical description*, Nucl. Phys. **A238** (1975) 29.

[BKS03] S. K. Bogner, T. T. S. Kuo, and A. Schwenk, *Model-independent low momentum nucleon interaction from phase shift equivalence*, Phys. Rept. **386** (2003) 1, nucl-th/0305035.

[BM90] W. Botermans and R. Malfliet, *Quantum transport theory of nuclear matter*, Phys. Rept. **198** (1990) 115.

[Bòz99] P. Bòzek, *Self-consistent solution of Galitskii-Feynman equations at finite temperature*, Phys. Rev. **C59** (1999) 2619, nucl-th/9811073.

[Bòz02] P. Bòzek, *One-body properties of nuclear matter with off-shell propagation*, Phys. Rev. **C65** (2002) 054306, nucl-th/0201086.

[Bòz04] P. Bòzek, *Short-range correlations in asymmetric nuclear matter*, Phys. Lett. **B586** (2004) 239, nucl-th/0311046.

[BR86] J.-P. Blaizot and G. Ripka, *Quantum Theory of Finite Systems*, The MIT Press, Cambridge, 1986.

[Bub05] M. Buballa, *NJL-model analysis of dense quark matter*, Phys. Rept. **407** (2005) 205, hep-ph/0402234.

[Buß04] O. Buß, *Low-energy pions in a Boltzmann-Uehling-Uhlenbeck transport simulation*, Diplomarbeit, Universität Gießen, 2004, http://theorie.physik.uni-giessen.de/documents/diplom/buss.pdf.

[CBH+97] E. Chabanat, P. Bonche, P. Haensel, J. Meyer, and R. Schaeffer, *A Skyrme parametrization from subnuclear to neutron star densities*, Nucl. Phys. **A627** (1997) 710.

[CBH+98] E. Chabanat, P. Bonche, P. Haensel, J. Meyer, and R. Schaeffer, *A Skyrme parametrization from subnuclear to neutron star densities Part II. Nuclei far from stablities*, Nucl. Phys. **A635** (1998) 231.

[CD99] G. W. Carter and D. Diakonov, *Light quarks in the instanton vacuum at finite baryon density*, Phys. Rev. **D60** (1999) 016004, hep-ph/9812445.

[CdAPS91] C. Ciofi degli Atti, E. Pace, and G. Salmè, *y-scaling analysis of quasielastic electron scattering and nucleon momentum distributions in few-body systems, complex nuclei, and nuclear matter*, Phys. Rev. **C43** (1991) 1155.

[CdAS96] C. Ciofi degli Atti and S. Simula, *Realistic model of the nucleon spectral function in few- and many-nucleon systems*, Phys. Rev. **C53** (1996) 1689, nucl-th/9507024.

[CH03] R. Cools and A. Haegemans, *Algorithm 824: CUBPACK: a package for automatic cubature; framework description*, ACM Trans. Math. Softw. **29** (2003) 287,
http://www.cs.kuleuven.be/~nines/software/CUBPACK/.

[CMV81] J. Cugnon, T. Mizutani, and J. Vandermeulen, *Equilibration in relativistic nuclear collisions. A Monte Carlo calculation*, Nucl. Phys. **A352** (1981) 505.

[Cre83] M. Creutz, *Quarks, Gluons and Lattices*, Cambridge University Press, Cambridge, UK, 1983.

[CSHY85] K.-C. Chou, Z.-B. Su, B.-L. Hao, and L. Yu, *Equilibrium and nonequilibrium formalisms made unified*, Phys. Rept. **118** (1985) 1.

[Dan84] P. Danielewicz, *Quantum theory of nonequilibrium processes. I*, Annals Phys. **152** (1984) 239.

[Das97] A. K. Das, *Finite Temperature Field Theory*, World Scientific, Singapore, 1997.

[DB04] W. H. Dickhoff and C. Barbieri, *Self-consistent Green's function method for nuclei and nuclear matter*, Prog. Part. Nucl. Phys. **52** (2004) 377, nucl-th/0402034.

[DBM93] P. P. Domitrovich, D. Bückers, and H. Müther, *Nambu-Jona-Lasinio models beyond the mean field approximation*, Phys. Rev. **C48** (1993) 413, nucl-th/9304001.

[DdWH90] A. E. L. Dieperink and P. K. A. de Witt Huberts, *On high resolution $(e, e'p)$ reactions*, Ann. Rev. Nucl. Part. Sci. **40** (1990) 239.

[dJL97] F. de Jong and H. Lenske, *Towards a fully self-consistent spectral function of the nucleon in nuclear matter*, Phys. Rev. **C56** (1997) 154, nucl-th/9703003.

[DM94] P. P. Domitrovich and H. Müther, *On the analytic structure of the quark self-energy in Nambu-Jona-Lasinio models*, J. Phys. **G20** (1994) 1885, nucl-th/9308019.

[DSTL95] V. Dmitrašinović, H. J. Schulze, R. Tegen, and R. H. Lemmer, *Chirally symmetric $O(1/N_c)$ corrections to the Nambu-Jona-Lasinio model*, Annals Phys. **238** (1995) 332.

[DVN05] W. H. Dickhoff and D. Van Neck, *Many-Body Theory Exposed!*, World Scientific, Singapore, 2005.

[dWH90] P. K. A. de Witt Huberts, *Proton spectral functions and momentum distributions in nuclei from high resolution $(e, e'p)$ experiments*, J. Phys. **G16** (1990) 507.

[Eff99] M. Effenberger, *Eigenschaften von Hadronen in Kernmaterie in einem vereinheitlichten Transportmodell*, Dissertation, Universität Gießen, 1999,
http://theorie.physik.uni-giessen.de/documents/dissertation/effenberger.ps.gz.

[FdCO92] P. Fernández de Córdoba and E. Oset, *Semiphenomenological approach to nucleon properties in nuclear matter*, Phys. Rev. **C46** (1992) 1697.

[FJDR05] F. Frömel, B. Juliá-Díaz, and D. O. Riska, *Bound states of heavy flavor hyperons*, Nucl. Phys. **A750** (2005) 337, nucl-th/0410034.

[FLM03a] F. Frömel, H. Lenske, and U. Mosel, *Short-range correlations in nuclear matter at finite temperatures and high densities*, Nucl. Phys. **A723** (2003) 544, nucl-th/0301038.

[FLM03b] F. Frömel, S. Leupold, and U. Mosel, *Spectral function of quarks in quark matter*, Phys. Rev. **C67** (2003) 015206, nucl-th/0111004.

[FLM03c] F. Frömel, S. Leupold, and U. Mosel, *Spectral functions of quarks in quark matter*, Eur. Phys. J. **A18** (2003) 265, nucl-th/0209033.

[FM98] T. Feuster and U. Mosel, *Unitary model for meson-nucleon scattering*, Phys. Rev. **C58** (1998) 457, nucl-th/9708051.

[FM03] T. Frick and H. Müther, *A self-consistent solution to the nuclear many-body problem at finite temperature*, Phys. Rev. **C68** (2003) 034310, nucl-th/0306009.

[FMR+05] T. Frick, H. Müther, A. Rios, A. Polls, and A. Ramos, *Correlations in hot asymmetric nuclear matter*, Phys. Rev. **C71** (2005) 014313, nucl-th/0409067.

[FP81] B. Friedman and V. R. Pandharipande, *Hot and cold, nuclear and neutron matter*, Nucl. Phys. **A361** (1981) 502.

[Frö01] F. Frömel, *Selbstkonsistente Berechnung der Quarkspektralfunktion in unendlich ausgedehnter Quarkmaterie*, Diplomarbeit, Universität Gießen, 2001,
http://geb.uni-giessen.de/geb/volltexte/2001/584/.

[GGHM01] H. H. Gutbrod, K.-D. Groß, W. F. Henning, and V. Metag, editors, *An International Accelerator Facility for Beams of Ions and Antiprotons - Conceptual Design Report*, Gesellschaft für Schwerionenforschung mbH, Darmstadt, 2001,
http://www.gsi.de/GSI-Future/cdr/.

[GL98] C. Greiner and S. Leupold, *Stochastic interpretation of Kadanoff-Baym equations and their relation to Langevin processes*, Annals Phys. **270** (1998) 328, hep-ph/9802312.

[Gre92] C. Greiner, *Gedächtniseffekte im Stoßterm in einer relativistischen Transporttheorie*, Dissertation, Universität Erlangen, 1992.

[Hen92] P. A. Henning, *Relativistic Fock diagrams at finite density*, Nucl. Phys. **A546** (1992) 653.

[HK94] T. Hatsuda and T. Kunihiro, *QCD phenomenology based on a chiral effective Lagrangian*, Phys. Rept. **247** (1994) 221, hep-ph/9401310.

[HvH58] N. M. Hugenholtz and L. van Hove, *A theorem on the single particle energy in a Fermi gas with interaction*, Physica **24** (1958) 363.

[Kar02] F. Karsch, *Lattice QCD at high temperature and density*, Lect. Notes Phys. **583** (2002) 209, hep-lat/0106019.

[Kar06] F. Karsch, *Lattice QCD at high temperature and the QGP*, AIP Conf. Proc. **842** (2006) 20, hep-lat/0601013.

[KB62] L. P. Kadanoff and G. Baym, *Quantum Statistical Mechanics*, Benjamin, New York, 1962.

[Kel64] L. V. Keldysh, *Diagram technique for nonequilibrium processes*, Zh. Eksp. Teor. Fiz. **47** (1964) 1515.

[KG06] J. I. Kapusta and C. Gale, *Finite-Temperature Field Theory: Principles and Applications*, Cambridge University Press, Cambridge, 2006.

[KL07] P. Konrad and H. Lenske, private communication, 2007.

[Kle92] S. P. Klevansky, *The Nambu-Jona-Lasinio model of quantum chromodynamics*, Rev. Mod. Phys. **64** (1992) 649.

[KLM05] P. Konrad, H. Lenske, and U. Mosel, *Short range correlations and spectral functions in asymmetric nuclear matter*, Nucl. Phys. **A756** (2005) 192, nucl-th/0501007.

[Leh03] J. Lehr, *In-Medium Eigenschaften von Nukleonen und Nukleonresonanzen in einem semiklassischen Transportmodell*, Dissertation, Universität Gießen, 2003, http://theorie.physik.uni-giessen.de/documents/dissertation/lehr.pdf.

[LEL+00] J. Lehr, M. Effenberger, H. Lenske, S. Leupold, and U. Mosel, *Transport theoretical approach to the nucleon spectral function in nuclear matter*, Phys. Lett. **B483** (2000) 324, nucl-th/0002013.

[Leu01] S. Leupold, *Life time of resonances in transport simulations*, Nucl. Phys. **A695** (2001) 377, nucl-th/0008036.

[Leu06] S. Leupold, private communication, 2006.

[Leu07] S. Leupold, *Selfconsistent approximations, symmetries and choice of representation*, Phys. Lett. **B646** (2007) 155, hep-ph/0610356.

[LLLM02] J. Lehr, H. Lenske, S. Leupold, and U. Mosel, *Nuclear matter spectral functions by transport theory*, Nucl. Phys. **A703** (2002) 393, nucl-th/0108008.

[M+02] M. Mattson et al. (SELEX), *First observation of the doubly charmed baryon* Ξ_{cc}^{+}, Phys. Rev. Lett. **89** (2002) 112001, hep-ex/0208014.

[Mac89] R. Machleidt, *The meson theory of nuclear forces and nuclear structure*, Adv. Nucl. Phys. **19** (1989) 189.

[Mat55] T. Matsubara, *A new approach to quantum-statistical mechanics*, Prog. Theor. Phys. **14** (1955) 351.

[MH94] S. Mrówczyński and U. W. Heinz, *Towards relativistic transport theory of nuclear matter*, Ann. Phys. **229** (1994) 1.

[MS59] P. C. Martin and J. S. Schwinger, *Theory of many-particle systems. I*, Phys. Rev. **115** (1959) 1342.

[NBC+96] E. N. Nikolov, W. Broniowski, C. V. Christov, G. Ripka, and K. Goeke, *Meson loops in the Nambu-Jona-Lasinio model*, Nucl. Phys. **A608** (1996) 411, hep-ph/9602274.

[NJL61a] Y. Nambu and G. Jona-Lasinio, *Dynamical model of elementary particles based on an analogy with superconductivity. I*, Phys. Rev. **122** (1961) 345.

[NJL61b] Y. Nambu and G. Jona-Lasinio, *Dynamical model of elementary particles based on an analogy with superconductivity. II*, Phys. Rev. **124** (1961) 246.

[O$^+$05] A. Ocherashvili et al. (SELEX), *Confirmation of the doubly charmed baryon $\Xi_{cc}^+(3520)$ via its decay to pD^+K^-*, Phys. Lett. **B628** (2005) 18, hep-ex/0406033.

[OBW00] M. Oertel, M. Buballa, and J. Wambach, *Meson properties in the $1/N_c$-corrected NJL model*, Nucl. Phys. **A676** (2000) 247, hep-ph/0001239.

[PB94] M. Plischke and B. Bergersen, *Equilibrium Statistical Physics*, World Scientific, Singapore, 1994.

[Pes04] A. Peshier, *Hard gluon damping in hot QCD*, Phys. Rev. **D70** (2004) 034016, hep-ph/0403225.

[PLM04] M. Post, S. Leupold, and U. Mosel, *Hadronic spectral functions in nuclear matter*, Nucl. Phys. **A741** (2004) 81, nucl-th/0309085.

[Pos04] M. Post, *Hadronic Spectral Functions in Nuclear Matter*, Dissertation, Universität Gießen, 2004, http://theorie.physik.uni-giessen.de/documents/dissertation/post.pdf.

[PS95] M. E. Peskin and D. V. Schroeder, *An Introduction to Quantum Field Theory*, Addison-Wesley, Reading, 1995.

[QK94] E. Quack and S. P. Klevansky, *Effective $1/N_c$ expansion in the Nambu-Jona-Lasinio model*, Phys. Rev. **C49** (1994) 3283.

[RDP91] A. Ramos, W. H. Dickhoff, and A. Polls, *Binding energy and momentum distribution of nuclear matter using Green's function methods*, Phys. Rev. **C43** (1991) 2239.

[Reh98] P. Rehberg, *Relativistic transport theory for systems containing bound states*, Phys. Rev. **C57** (1998) 3299, hep-ph/9803239.

[RPD89] A. Ramos, A. Polls, and W. H. Dickhoff, *Single-particle properties and short-range correlations in nuclear matter*, Nucl. Phys. **A503** (1989) 1.

[RPLP99] S. Reddy, M. Prakash, J. M. Lattimer, and J. A. Pons, *Effects of strong and electromagnetic correlations on neutrino interactions in dense matter*, Phys. Rev. **C59** (1999) 2888, astro-ph/9811294.

[RS80] P. Ring and P. Schuck, *The Nuclear Many-Body Problem*, Springer, Berlin, 1980.

[RW02] K. Rajagopal and F. Wilczek, *The condensed matter physics of QCD*, in *At the Frontier of Particle Physics: Handbook of QCD: Boris Ioffe Festschrift* (edited by M. Shifman), volume 3, 2061, World Scientific, Singapore, 2002 hep-ph/0011333.

[Saw95] R. F. Sawyer, *Reduction of weak interaction rates in the supernova core*, Phys. Rev. Lett. **75** (1995) 2260.

[Sch61] J. S. Schwinger, *Brownian motion of a quantum oscillator*, J. Math. Phys. **2** (1961) 407.

[SCM76] G. Sauer, H. Chandra, and U. Mosel, *Thermal properties of nuclei*, Nucl. Phys. **A264** (1976) 221.

[SKP99] T. M. Schwarz, S. P. Klevansky, and G. Papp, *Phase diagram and bulk thermodynamical quantities in the Nambu-Jona-Lasinio model at finite temperature and density*, Phys. Rev. **C60** (1999) 055205, nucl-th/9903048.

[Sky59] T. H. R. Skyrme, *The effective nuclear potential*, Nucl. Phys. **9** (1959) 615.

[SR07] J. R. Stone and P.-G. Reinhard, *The Skyrme interaction in finite nuclei and nuclear matter*, Prog. Part. Nucl. Phys. **58** (2007) 587, nucl-th/0607002.

[VB72] D. Vautherin and D. M. Brink, *Hartree-Fock calculations with Skyrme's interaction. I. Spherical nuclei*, Phys. Rev. **C5** (1972) 626.

[VDPR93] B. E. Vonderfecht, W. H. Dickhoff, A. Polls, and A. Ramos, *Influence of tensor and short-range correlations on nucleon properties in the nuclear medium*, Nucl. Phys. **A555** (1993) 1.

[vHK02] H. van Hees and J. Knoll, *Renormalization in self-consistent approximation schemes at finite temperature. III. Global symmetries*, Phys. Rev. **D66** (2002) 025028, hep-ph/0203008.

[VW91] U. Vogl and W. Weise, *The Nambu and Jona-Lasinio model: Its implications for hadrons and nuclei*, Prog. Part. Nucl. Phys. **27** (1991) 195.

[Wel83] H. A. Weldon, *Simple rules for discontinuities in finite-temperature field theory*, Phys. Rev. **D28** (1983) 2007.

[Wir88] R. B. Wiringa, *Single-particle potential in dense nuclear matter*, Phys. Rev. **C38** (1988) 2967.

[Y+06] W. M. Yao et al. (Particle Data Group), *Review of particle physics*, J. Phys. **G33** (2006) 1, http://pdg.lbl.gov/pdg.html.

[Yam54] Y. Yamaguchi, *Two-nucleon problem when the potential is nonlocal but separable. I*, Phys. Rev. **95** (1954) 1628.

[ZW92] W. M. Zhang and L. Wilets, *Transport theory of relativistic heavy-ion collisions with chiral symmetry*, Phys. Rev. **C45** (1992) 1900.

Deutsche Zusammenfassung

Wir wissen aus unserer täglichen Erfahrung, dass die Eigenschaften eines Gegenstandes durch seine Umgebung beeinflusst werden. Ein typisches Beispiel dafür ist das unterschiedliche Gewicht eines Objekts in Luft oder in Wasser. Auch der Widerstand, den Luft und Wasser der Bewegung des Objekts entgegensetzen, lassen das Objekt unterschiedlich schwer erscheinen. Solche Effekte entstehen durch die Wechselwirkung mit dem Medium und spielen auch in mikroskopischen Vielteilchensystemen eine wichtige Rolle. In dieser Arbeit untersuchen wir den Einfluss dynamischer Korrelationen auf die Eigenschaften von Quarks in Quarkmaterie und Nukleonen in Kernmaterie. Wir konzentrieren uns dabei auf die Effekte, die durch kurzreichweitige Wechselwirkungen entstehen. Im Vergleich zu den – gut verstandenen – langreichweitigen Korrelationen, die globale Eigenschaften wie effektive Massen und Bindungsenergien festlegen, haben diese Wechselwirkungen einen subtileren Einfluss auf die In-Medium-Eigenschaften der Teilchen.

Den Unterschied zwischen lang- und kurzreichweitigen Korrelationen können wir an einem einfachen Beispiel verdeutlichen (Abb. 1.1): ein Spaziergänger, der an einem normalen Wochentag durch eine Fußgängerzone läuft, sieht andere Personen schon von weitem. Er kann diesen Personen durch kleine Richtungsänderungen ausweichen, ohne dass er seine Geschwindigkeit verändern muss. Im dichten Gedränge an einem Samstag kurz vor Weihnachten ändert sich die Situation. Die Bewegung der anderen Personen ist nicht immer vorhersehbar. Der Spaziergänger muss sich daher auf einer unregelmäßigen Bahn bewegen und immer wieder seine Geschwindigkeit anpassen (gelegentliche Zusammenstöße sind nicht ausgeschlossen). Die Wahrscheinlichkeit, dass der Spaziergänger sich zu einer bestimmten Zeit mit einer bestimmten Geschwindigkeit bewegt, ist nun nicht mehr durch einen scharfen Peak bei einer festen Geschwindigkeit, sondern durch eine breite Verteilung gegeben.

Die Wechselwirkungen zwischen Fußgängern lassen sich natürlich nicht direkt mit denen zwischen Quarks oder Nukleonen vergleichen. Die beobachteten Effekte dagegen schon. In Quark- und Kernmaterie beschreiben wir die Eigenschaften der Teilchen durch Spektralfunktionen. Diese Spektralfunktionen geben die Wahrscheinlichkeit an, dass ein Teilchen mit einer bestimmten Energie einen bestimmten Impuls hat. Daher sind sie sind eng mit der Geschwindigkeitsverteilung der Fußgänger verwandt. Solange wir nur langreichweitige Korrelationen zwischen den Quarks oder Nukleonen betrachten, finden wir in der Spektralfunktion einen scharfen Peak ohne Breite, den sogenannten Quasiteilchenpeak. Kurzreichweitige Wechselwirkungen, bei denen die Teilchen Energie und Impuls austauschen, führen dagegen – wie in Abb. 1.1 gezeigt – zu einer Verbreiterung der Peaks. Die Existenz von (Off-Shell-)Zuständen, die weit

vom Maximum des Peaks entfernt sind, führt zu interessanten Effekten, die in dieser Arbeit diskutiert werden.

Quarks in Quarkmaterie

Der erste Teil dieser Arbeit geht der Frage nach, welche Rolle kurzreichweitige Korrelationen in kalter und dichter Quarkmaterie spielen. Unser Ansatz beruht auf Methoden, die sich bei der Untersuchung von Kernmaterie als sehr erfolgreich erwiesen haben. Selbstkonsistente Rechnungen haben gezeigt, dass sich Punktwechselwirkungen gut für die Beschreibung von kurzreichweitigen Korrelationen in Kernmaterie eignen. Die mittlere Stärke der Wechselwirkung ist in diesem Fall wichtiger als ihre genaue Struktur. Unter der Annahme, dass ähnliche Bedingungen für die kurzreichweitigen Korrelationen in Quarkmaterie gelten, haben wir die Nambu–Jona-Lasinio-Wechselwirkung (NJL-Wechselwirkung) [NJL61b, Kle92] als Ausgangspunkt für unser Modell gewählt.

Ausgehend von einer Entwicklung bis zur zweiten Ordnung in der inversen Zahl der Quarkfarben ($1/N_c$), konstruieren wir ein vollständig selbstkonsistentes Modell, das die engen Beziehungen zwischen Spektralfunktionen und Selbstenergien ausnutzt. In Rechnungen bei endlichem chemischen Potential und Temperatur Null untersuchen wir die Off-Shell-Struktur der Kollisionsbreite, die Stärke der kurzreichweitigen Korrelationen und ihren Einfluss auf den chiralen Phasenübergang. Wir vergleichen die Ergebnisse mit der Loop-Entwicklung aus [FLM03b, FLM03c] und den Ergebnissen aus Rechnungen für Kernmaterie [FLM03a].

In Kapitel 2 stellen wir das NJL-Modell in seiner SU(2)-Version vor. Das Modell basiert auf einer Punktwechselwirkung, die alle relevanten Symmetrien der Quantenchromodynamik (QCD) berücksichtigt. Aufgrund der – wie in der QCD bei niedrigen Energien – großen Kopplungskonstanten ist nicht klar, ob eine diagrammatische Entwicklung in der Kopplungskonstanten (Loop-Entwicklung) in diesem Modell zulässig ist. Daher führen wir das Konzept der Entwicklung in der inversen Zahl der Quarkfarben ein und diskutieren die Unterschiede zur Loop-Entwicklung. Die Sortierung von Selbstenergiediagrammen nach ihrer Ordnung in $1/N_c$ motiviert die Einführung von dynamisch generierten Mesonen: Quark–Antiquark-Streuprozesse werden in einer „Random-Phase-Approximation“ (RPA) aufsummiert und generieren effektive Mesonpropagatoren. Die effektiven RPA-Mesonen setzten sich aus gebundenen $q\bar{q}$-Zuständen – den eigentlichen Mesonen – und einem Kontinuum aus ungebundenen $q\bar{q}$-Zuständen zusammen. Die dynamisch generierten Mesonen erlauben es uns, alle Beiträge zur Quarkselbstenergie der Ordnung $\mathcal{O}(1/N_c)$ – beispielsweise das Fock-Diagramm und das direkte Born-Diagramm – in einem einzigen Meson-Austausch-Diagramm zusammenzufassen.

Der Mesonaustausch führt zu einer Rückkopplung der RPA-Meson-Eigenschaften an die Eigenschaften der Quarks. In der Hartree+RPA-Näherung, dem Standardzugang zum NJL-Modell, existiert diese Verbingung nicht, da dort nur Selbstenergiediagramme in führender Ordnung in $1/N_c$, d.h. $\mathcal{O}(1)$, berücksichtigt werden. Die Quarkpropagatoren in den gekoppelten Dyson–Schwinger-Gleichungen, die wir in Ka-

pitel 2 konstruieren (Abb. 2.11), sind volle In-Medium-Propagatoren. Der nichtlokale Mesonaustausch führt zu einer endlichen Breite in den Propagatoren. Diese Kollisions- und Zerfallsbreite wird in unseren Rechnungen konsequent berücksichtigt. Im Gegensatz zur Hartree+RPA-Näherung, die wir im Anhang B kurz diskutieren, sind die Quarks in unserem Ansatz keine Quasiteilchen. Eine selbstkonsistente Lösung der Dyson–Schwinger-Gleichungen kann deshalb nur numerisch bestimmt werden.

Wir können die RPA-Pionen unseres $\mathcal{O}(1/N_c)$-Ansatzes nicht mit Goldstone-Bosonen identifizieren. Die gebundenen $q\bar{q}$-Zustände haben eine erhebliche Masse – ein Problem, das wir bereits in Mean-Field-Modellen beobachten können. In einer diagrammatischen Entwicklung werden die chiralen Theoreme (Goldstone, Goldberger–Treiman, Gell-Mann–Oakes–Renner) nur dann erfüllt, wenn sich die Beiträge verschiedener Diagramme gegenseitig aufheben. Um die chiralen Theoreme nicht zu stören, ist daher nötig, die Diagramme sorgfältig auszuwählen. Unser Ansatz basiert auf einer Entwicklung der Quarkselbstenergie bis zur zweiten Ordnung. Durch die selbstkonsistente Rechnung mit vollen Propagatoren werden automatisch Beträge in beliebig hohen Ordnungen zu den RPA-Polarisationen erzeugt. Dabei handelt es sich aber nur um einen Teil der Diagramme, die nötig wären, um die chiralen Eigenschaften in höheren Ordnungen zu erhalten.

In Abschnitt 2.5 diskutieren wir eine chiral invariante $1/N_c$-Erweiterung des Hartree+RPA-Schemas für Quasiteilchen [DSTL95]. Dieser Ansatz basiert auf einem Satz von Polarisationsdiagrammen mit der Struktur von Vertexkorrekturen für die Quark–Meson-Wechselwirkung (Abb. 2.14). Diese Diagramme werden nur genutzt, um *nach* der selbstkonsistenten Rechnung, die $1/N_c$-korrigierte Quarkpropagatoren und (massive) RPA-Propagatoren liefert, $1/N_c$-korrigierte Mesonpropagatoren zu bestimmen. Im Prinzip könnten wir die Polarisationskorrekturen auch in unserem Modell zur Verbesserung der Mesoneigenschaften nutzen.Dieses Vorgehen hätte aber keinen Einfluss auf die Eigenschaften der Quarks, die nach wie vor in einer Rechnung mit massiven RPA-Pionen bestimmt werden. Erst wenn die Vertexkorrekturen in die Dyson–Schwinger-Gleichungen aufgenommen würden, hätte das Einfluss auf die Quarkeigenschaften. Ein solcher Ansatz, der aber auch nicht die chiralen Eigenschaften der Pionen (gebundene $q\bar{q}$-Zustände) in allen Ordnungen von $1/N_c$ wiederherstellt, ist technisch äußerst anspruchsvoll. Daher diskutieren wir in dieser Arbeit zwar die Auswirkungen der Vertexkorrekturen, ignorieren sie aber in unseren Rechnungen.

Wir zeigen in Kapitel 3, wie sich die Kollisionsselbstenergie und -polarisationen durch Integrale über Spektralfunktionen sowie Bose- und Fermiverteilungen beschreiben lassen. Aus diesen Integralen berechnen wir die Quark- und Mesonbreiten. Die wichtigsten Probleme, die bei der numerischen Rechnung auftreten, diskutieren wir in Anhang H. Um die Analytizität von Quarkselbstergie und Mesonpolarisationen zu erhalten, berechnen wir deren Realteile nicht direkt, sondern über Dispersionrelationen aus den Breiten. Dieses Vorgehen erfordert eine gründliche Auswertung der analytischen Ausdrücke, um alle energieunabhängigen Terme zu isolieren, die nicht von Dispersionsintegralen erfasst werden können. Wir zeigen, dass die RPA-Polarisationen in unserem Modell (Polarisationsdiagramm mit vollen Quarkpropaga-

toren) sich (fast) genauso zerlegen lassen wie in der Hartree+RPA-Näherung. Den Term, der zur Verletzung des Goldstone-Theorems führt, können wir nutzen, um die RPA-Pion-Masse abzuschätzen. Die Zerlegung der Quarkselbstenergie liefert einen nichtdispersiven Term, der der Fock-Selbstenergie ähnelt – lediglich die konstante NJL-Kopplung wird durch den $k_0^2 \to \infty$ Grenzwert des RPA-Propagators ersetzt. Dieses Ergebnis ist nicht überraschend, da die Fock-Selbstenergie Bestandteil des Meson-Austausch-Selbstenergiediagramms ist.

Um die Struktur der Quarkbreite besser zu verstehen, bestimmen wir in Kapitel 4 alle Zerfalls- und Streuprozesse, die zur Kollisionsselbstenergie beitragen. Die Beiträge der gebundenen $q\bar{q}$-Zustände und des Off-Shell-Kontinuums zu den Zerfalls- und Streuraten betrachten wir in dieser Untersuchung getrennt. Auf der Basis einer Quasiteilchennäherung bestimmen wir die Energieschwellen, an denen sich der Phasenraum für jeden der gefundenen Prozesse öffnet und schließt. Außerdem schätzen wir die Dichteabhängigkeit der Prozesse ab und bestimmen die Prozesse, die Beiträge zur On-Shell-Breite der Quarks und Antiquarks liefern. Aus diesen Überlegungen ergibt sich, dass die Quarkbreite eine komplizierte Struktur hat, die wir anhand der Eigenschaften der verschiedenen Prozesse in den Abbildungen 4.1 und 4.3 verstehen können.

Die Analyse der On-Shell-Breite zeigt, dass die relativ hohe Masse der RPA-Pionen unseres Modells eingeschränkten Einfluss auf die Eigenschaften der besetzten Quarkzustände hat. Die Prozesse, in denen die gebundenen $q\bar{q}$-Zustände der RPA-Propagatoren auftreten, können nicht zur Quarkbreite in den On-Shell-Bereichen beitragen, wenn die RPA-Pionen eine endliche Masse haben – unabhängig davon, ob es sich um eine Masse von 100 oder 400 MeV handelt. Die raumartigen Off-Shell-Komponenten der RPA-Propagatoren, die für die größten Beiträge zur On-Shell-Quarkbreite verantwortlich sind, sind allerdings nicht unabhängig von der Pion-Masse. In einer genaueren Untersuchung haben wir herausgefunden, dass es durch die zu große Masse in der chiral gebrochenen Phase zu einer Unterdrückung von Beiträgen zur On-Shell-Breite der Quarks kommt. Im Durchschnitt werden die Beiträge um deutlich weniger als eine Größenordnung unterdrückt. Das bedeutet, dass unsere Ergebnisse nur eine konservative Abschätzung der kurzreichweitigen Korrelationen (in der chiral gebrochenen Phase) repräsentieren.

In unseren numerischen Rechnungen untersuchen wir die Eigenschaften von kalter Quarkmaterie (Temperatur Null) für verschiedene chemische Potentiale. Die Ergebnisse sind in Kapitel 5 dargestellt. Die gekoppelten Dyson–Schwinger-Gleichungen lösen wir in einem iterativen Verfahren. Der Einfluss der kurzreichweitigen Korrelationen macht es erforderlich, die üblichen Mean-Field-Parametersätze des NJL-Modells neu zu justieren. Um in unseren Rechnungen ein vernünftiges Ergebnis für das Quarkkondensat zu erhalten, genügt es, bei festem Cutoff die Kopplungskonstante für Rechnungen in der Hartree-Näherung um 22 Prozent zu reduzieren (dieses Vorgehen entspricht dem Übergang von der Hartree- zur Hartree–Fock-Näherung).

Die Quarkbreite kann bei höheren Energien beachtliche Werte annehmen. Bei niedrigen und mittleren Energien bleibt sie aber klein. Die qualitative Struktur der Breite,

die wir in Kapitel 5 diskutieren, passt sehr gut zu den Quasiteilchenabschätzungen aus Kapitel 4. Die On-Shell-Peaks der Quarkspektralfunktion zeigen eine deutliche Kollisionsverbreiterung. In den Off-Shell-Bereichen spiegelt die Spektralfunktion die Struktur der Breite wider. Aufgrund der Anwesenheit eines Mediums mit endlichem chemischen Potential ist die Symmetrie zwischen den Quark- und den Antiquarkzuständen gebrochen. Ein Vergleich mit unseren älteren Rechnungen zeigt, dass eine konsistente Entwicklung in $1/N_c$ zu Breiten führt, die eine ähnliche Struktur haben, aber um eine Größenordnung höher ausfallen als in einer Loop-Entwicklung. Die $q\bar{q}$-Komponenten der RPA-Breiten und Spektralfunktionen sind den Ergebnissen aus Mean-Field-Rechnungen in Form und Stärke sehr ähnlich. Ein kleiner, konstanter Beitrag zum Realteil der RPA-Polarisationen, der in Mean-Field-Rechnungen (Hartree-Näherung) nicht auftritt, führt zum erwarteten Anstieg der Masse des gebundenen $q\bar{q}$-Zustands in der RPA-Pion-Spektralfunktion. Auf die Masse des RPA-Sigmas hat der konstante Betrag kaum Einfluss. Das RPA-Sigma wird nur geringfügig schwerer.

Die Untersuchung des chiralen Phasenübergangs zeigt, dass die kurzreichweitigen Korrelationen in unserem $\mathcal{O}(1/N_c)$-Ansatz bei Temperatur Null nicht stark genug sind, um den Phasenübergang erster Ordnung in einen kontinuierlichen Übergang („Crossover“) umzuwandeln. Im Vergleich zu Rechnungen mit Quasiteilchen fallen die Sprünge der Masse und der Dichte am Phasenübergang allerdings um $40-50$ Prozent kleiner aus. Unterhalb des Phasenübergangs hängt die Quarkdichte stark vom chemischen Potential ab. Qualitativ zeigen die Quark- und die RPA-Sigma-Massen in unseren Rechnungen das gleiche Verhalten wie in der Hartree+RPA-Näherung. In der chiral restaurierten Phase gilt das auch für die Masse des RPA-Pions. Wenn wir einen Parametersatz im chiralen Limes ($m_0 = 0$) verwenden, dann verschwindet die Lorentz-skalare Komponente der Quarkselbstenergie oberhalb des chiralen Phasenübergangs. Die chirale Symmetrie wird vollständig wiederhergestellt und die Quarks werden masselos. Im Gegensatz zu den chiralen Eigenschaften des Pions wird dieses Verhalten nicht durch die $1/N_c$-Erweiterungen unseres Ansatzes gestört.

Eine genauere Untersuchung der On-Shell-Quarkselbstenergie führt zu interessanten Erkenntnissen. Die effektive Quarkmasse behält in unserem $\mathcal{O}(1/N_c)$-Modell eine einfache Struktur, sie bleibt nahezu energie- und impulsunabhängig. Der Realteil der Kollisionsselbstenergie ersetzt lediglich die Beiträge der Mean-Field-Selbstenergie, die durch die Reduktion der Kopplung – im Vergleich zur Hartree-Näherung – verloren gehen.

Die On-Shell-Breite zeigt in der chiral gebrochenen Phase eine starke Dichteabhängigkeit. Oberhalb des Phasenübergangs, in der chiral restaurierten Phase, beobachten wir eine Sättigung der Korrelationen. Um die Dichteabhängigkeit der Breite besser zu verstehen, haben wir die mittlere Breite der besetzten Quarkzustände und die mittlere Breite aller Quarkzustände (ohne die Antiquarkzustände bei negativen Energien, siehe Anhang E) untersucht. Unterhalb des Phasenübergangs ist die Dichteabhängigkeit direkt mit der Dichte der verfügbaren Streupartner aus dem Medium verknüpft. Oberhalb des Phasenübergangs nähert sich die mittlere Breite der besetzten Zustände einem konstanten Wert, während die Breite aller Quarkzustände

– nach dem Überschreiten eines Maximums – abnimmt. Die beobachteten Effekte sind Konsequenzen des Pauli-Prinzips („Pauli-Blocking“) und des Impuls-Cutoffs der NJL-Wechselwirkung, der in die Streuprozesse eingeht. Vergleichbare Effekte beobachten wir in der Untersuchung von Kernmaterie in Kapitel 6. Unsere Rechnungen zeigen, dass die mittlere Breite der besetzten Quarkzustände auch quantitativ mit der mittleren Breite von Nukleonen in Kernmaterie vergleichbar ist. Dieses Ergebnis sollte allerdings schon wegen der unterschiedlichen Massen von Quarks und Nukleonen nicht überbewertet werden.

Wir schließen unsere Untersuchung der Quarks mit der Bestimmung ihrer Impulsverteilung im Medium ab. Die Impulsverteilung erlaubt es uns, die Bedeutung der Off-Shell-Zustände abzuschätzen, die einen Teil der Stärke der (normierten) Spektralfunktion weg von den On-Shell-Peaks verlagern. Im Vergleich zur Impulsverteilung eines freien Fermigases (Quasiteilchen), die am Fermiimpuls von 1 auf 0 abfällt, treten zwei Effekte auf, die auf kurzreichweitige Korrelationen zurückzuführen sind: bei Impulsen unterhalb des Fermiimpulses beobachten wir eine Reduktion der Impulsverteilung um ca. 10 Prozent. Oberhalb des Fermiimpulses verschwindet die Impulsverteilung nicht, stattdessen erzeugen besetzte Off-Shell-Zustände einen sogenannten Hochimpulsschwanz. In der chiral restaurierten Phase sind die Effekte quantitativ vergleichbar mit den Ergebnissen für Nukleonen in Kernmaterie. Genau wie bei der Untersuchung der Breite stellen wir fest, dass die kurzreichweitigen Effekte in unserer Entwicklung in $1/N_c$ um eine Größenordnung größer ausfallen als in einer Entwicklung in der Kopplung (Loop-Entwicklung).

Zusammenfassend können wir feststellen, dass unsere ursprüngliche Loop-Entwicklung [Frö01, FLM03b] wichtige Beiträge zur Quarkselbstenergie ignoriert hat. Die Effekte, die sich aus den kurzreichweitigen Korrelationen ergeben, sind daher klein ausgefallen. Die wesentlich größeren Effekte, die wir der vorliegenden Arbeit beobachten, sind realistischer, da sie sich aus einer konsistenten Entwicklung in $1/N_c$ ergeben. Abgesehen von den Problemen mit der Masse des RPA-Pions repräsentiert unser $\mathcal{O}(1/N_c)$-Ansatz eine natürliche Weiterentwicklung des etablierten Hartree+RPA-Schemas. Der Vergleich der Ergebnisse für Quarkmaterie mit den Ergebnissen für Kernmaterie zeigt, dass die kurzreichweitigen Korrelationen in beiden Systemen von ähnlicher Bedeutung sind. In Kernmaterie spielen kurzreichweitige Effekte eine wichtige Rolle – eine vollständige Beschreibung, auch von endlichen Kernen, ist nur möglich, wenn diese Effekte berücksichtigt werden. Daher sollte der Einfluss der kurzreichweitigen Korrelationen auf die Quarks (und die dynamisch generierten Mesonen) ebenfalls nicht ignoriert werden.

Um diese Aussage zu verdeutlichen, betrachten wir das QCD-Phasendiagramm (Abb. 1.2): Es ist nicht möglich, den chiralen Phasenübergang bei beliebigen Dichten und Temperaturen in einer exakten Rechnung im Rahmen der QCD zu untersuchen. Eine numerische Untersuchung im Rahmen der Gitter-QCD ist gegenwärtig ebenfalls nicht realisierbar. Daher kommen effektive Modelle zum Einsatz, um die Eigenschaften des Phasenübergangs zu bestimmen. Die meisten dieser Modelle deuten darauf hin, dass der chirale Phasenübergang an einem kritischen Punkt von einem Übergang

erster Ordnung zu einem kontinuierlichen Übergang („Crossover“) wechselt. Wie wir in dieser Arbeit sehen, ändern die kurzreichweitigen Korrelationen die Eigenschaften des Phasenübergangs im Vergleich zu den Ergebnissen einer Quasiteilchenrechnung. Rechnungen für Kernmaterie deuten an, dass die kurzreichweitigen Korrelationen bei endlichen Temperaturen an Stärke zunehmen (vgl. Abb. 6.17). Daraus folgt, dass Mean-Field-Modelle mit hoher Wahrscheinlichkeit eine falsche Position des kritischen Punktes vorhersagen (bei einer zu hohen Temperatur). Rechnungen mit einer realistischeren Pion-Masse sollten sogar noch deutlicher von den Mean-Field-Rechnungen abweichen.

Nukleonen in Kernmaterie

Im zweiten Teil dieser Arbeit stellen wir ein Modell zur Untersuchung kurzreichweitiger Korrelationen in Kernmaterie bei endlichen Temperaturen und hohen Dichten vor. Ausgehend von dem Modell von Lehr et al. [LEL$^+$00, LLLM02] konstruieren wir in Kapitel 6 ein einfaches, aber selbstkonsistentes Modell. Die kurzreichweitigen Wechselwirkungen zwischen den Nukleonen beschreiben wir durch ein konstantes Matrixelement in Verbindung mit einem Formfaktor, der den Energie- und Impulstransfer in Stößen begrenzt. In [LEL$^+$00, LLLM02] haben Rechnungen mit einer gemittelten Kopplungskonstanten bei Temperatur Null zu hervorragenden Ergebnissen geführt. Die dichte- und temperaturabhängigen Beiträge des Mean-Fields zur Nukleonselbstenergie bestimmen wir mit Hilfe eines Skyrme-Modells für Quasiteilchen. Dieses Vorgehen garantiert uns ein realistisches, thermodynamisches Verhalten des chemischen Potentials.

Wir berechnen die Nukleonspektralfunktion in Kernmaterie für Temperaturen von 0 bis 70 MeV und für Dichten von ρ_0 (Sättigungsdichte) bis $3\rho_0$. Das ist gerade der Temperatur- und Dichtebereich, der in Supernovaexplosionen und in Schwerionenkollisionen, wie sie für das CBM-Experiment bei der GSI geplant werden, relevant ist. Zum ersten Mal wird damit ein so großer Bereich konsistent im Rahmen eines einheitlichen Modells untersucht.

Unsere Ergebnisse befinden sich in guter Übereinstimmung mit den Ergebnissen anderer Rechnungen [ARFdCO96, Bòz99], die für Temperaturen bis 20 MeV und Dichten bis $2\rho_0$ vorliegen. Wir nutzen die mittlere Breite der Spektralfunktion, um die Dichte- und Temperaturabhängigkeit der kurzreichweitigen Korrelationen zu bestimmen. Es zeigt sich, dass die Korrelationen nahezu linear mit der Temperatur skalieren. Bei Dichten oberhalb von $2\rho_0$ tritt allerdings eine Sättigung der Korrelationen auf. In einem naiven Bild würde man diese Sättigung in Abhängigkeit von der Dichte nicht erwarten. Wir können dieses Verhalten jedoch einfach erklären. Pauli-Blocking, ein rein quantenmechanischer Effekt, reduziert die Zahl der freien Endzustände in Streuprozessen und führt so zur beobachteten Sättigung.

Danksagung

An erster Stelle möchte ich mich bei Prof. Dr. Ulrich Mosel bedanken. Seine Anregungen – aber auch seine kritischen Fragen – haben maßgeblich zum Gelingen dieser Arbeit beigetragen. Andererseits war es durch die von ihm gewährten Freiräume möglich, viele eigene Ideen in die Arbeit einfließen zu lassen. Besonders bedanken möchte ich mich für seine wohlwollende Förderung, die mir die Teilnahme an mehreren internationalen Konferenzen und Workshops sowie einen dreimonatigen Aufenthalt am Helsinki Institute of Physics in Finnland ermöglicht hat.

Größten Dank bin ich auch PD Dr. Stefan Leupold schuldig. Seine vielfältigen Vorschläge haben diese Arbeit ganz wesentlich geprägt. Ich danke ihm für unzählige, hilfreiche Diskussionen, in denen er für jedes Problem eine Lösung fand. Es sei ihm dafür gedankt, dass er nicht die Geduld mit mir verloren hat wenn er eine Frage zum wiederholten Male beantworten musste. Ich habe viel von ihm gelernt.

Bei Prof. Dr. Horst Lenske bedanke ich mich nicht nur für die gute Zusammenarbeit bei der Untersuchung der Nukleonen, sondern auch für Anregungen und Gespräche, die über dieses Thema hinausgingen. Außerdem danke ich ihm dafür, dass er mir die Teilnahme an einem sehr interessanten Workshop vermittelt hat. Für wertvolle Beträge zu dieser Arbeit und interessante Diskussionen, bei denen es nicht immer um Physik ging, danke ich auch Professor Dr. Carsten Greiner und Dr. Marcus Post sowie Patrick Konrad.

I thank Prof. Dr. Dan-Olof Riska and Dr. Bruno Juliá-Díaz for their hospitality. They have made my stay in Helsinki a very pleasant and fruitful one. I have enjoyed our lunchtime excursions to the sea as well as the discussions on physics.

Meinen Zimmerkollegen Pascal Mühlich, Robert Würfel und Dr. Kai Gallmeister danke ich für die angenehme Gesellschaft. Besonders Kai danke ich für seine Gesprächsbereitschaft und für seine Mitarbeit bei vielen kleinen Projekten. Seine profunden Programmierkenntnisse haben sich oft als nützlich erwiesen.

Bei der Betreuung der Instituts-IT habe ich viel von Dr. Christoph Keil gelernt. Mittlerweile befindet sich dieses Wissen bei Oliver Buß in guten Händen. Beiden danke ich für die gute Zusammenarbeit im täglichen Betrieb und bei größeren Aktionen.

Ich danke allen Institutsmitgliedern für die gute und produktive Stimmung. Auch an die vielen gemeinsamen Erlebnisse bei „Lectureweeks“ und Frühjahrstagungen werde ich mich gerne erinnern. Neben den bereits erwähnten Personen möchte ich in diesem Zusammenhang noch Dr. Thomas Falter, Dr. Jürgen Lehr, Tina Leitner und Dr. Gunnar Martens hervorheben.

Elke Jung danke ich für ihr Engagement bei der Bewältigung aller administrativen Angelegenheiten. Ohne sie würde ich wohl heute noch auf meine erste Reisekostener-

stattung warten.

Schließlich möchte ich mich ganz herzlich bei meinen Eltern bedanken. Auch in Zeiten, in denen sie andere Sorgen geplagt haben, konnte ich mich immer auf ihre Unterstützung verlassen. Der Rückhalt, den sie mir über die letzten Jahre gegeben haben, war für das Gelingen dieser Arbeit unerlässlich.

Ein Teil der Rechnungen, deren Ergebnisse in dieser Arbeit präsentiert werden, sind am Center for Scientific Computing (CSC) in Frankfurt durchgeführt worden. The package CUBPACK by R. Cools and A. Haegemans [CH03] has been used for the numerical calculation of multidimensional integrals.